Numerical Modelling of Gas Production and CO_2 Injection in Tight Shale Reservoirs for Enhanced Gas Recovery

by

Dhruvit Satishchandra Berawala

Thesis submitted in fulfilment of
the requirements for the degree of
PHILOSOPHIAE DOCTOR
(PhD)

Faculty of Science and Technology
Department of Energy and Petroleum Engineering
2020

University of Stavanger
NO-4036 Stavanger
NORWAY
www.uis.no

ISBN: 978-82-7644-968-6
ISSN: 1890-1387
PhD: Thesis UiS No. 560

This dissertation is dedicated to my parents and my wife who instilled in me the virtues of perseverance and commitment and relentlessly encouraged me to strive for excellence.

Acknowledgements

I would like to express my sincere gratitude to everyone who helped and encouraged me in various ways in carrying out my PhD work. Their contributions are sincerely appreciated and gratefully acknowledged.

First and foremost, I would like to thank my supervisor Dr. Pål Østebø Andersen for his guidance, advices and suggestions throughout the term of my PhD. Without his valuable assistance, always generously and unstintingly given, the completion of this work would have been immeasurably more difficult. His support to me and encouragement in work apart from PhD project has made me a more skillful and knowledgeable on different topics.

I would also like to give my special thanks to Dr. Zhixin Yu for taking administrative responsibility of the project until a permanent main supervisor was established and to Dr. Jann Rune Ursin for providing me the opportunity to pursue PhD at University of Stavanger. During this work, the constant association with all my PhD colleagues, especially Jaspreet Singh Sachdeva, Muhammad Awais Alvi, Abhinav Bhaskar, Alireza, Emanuella Kallesten and Rockey Abhishek, and their valuable suggestions are highly appreciated.

My special thanks go to my parents Mr. Satish Berawala and Mrs. Pratima Berawala and my wife Mrs. Neelam Shah for their continuous encouragement, love and support during my thesis work. Their morale boosting support during these years cannot be described in words. I also express my gratitude to my brother Mr. Krunal Berawala, my sister-in-law Mrs. Payal Berawala and my cute nephew Kabir Berawala for continuously inspiring me to achieve new heights.

I would also like to thank everyone at the Department of Energy and Petroleum Engineering and the Department of Energy Resources, University of Stavanger, for their support and cooperation. I am also

indebted to The National IOR Centre of Norway for introducing me to so many industry stalwarts and helping me enhance my skills more than what I had wished for at the start of my PhD.

Finally and most importantly, I would like to acknowledge the Research Council of Norway and the industry partners, ConocoPhillips Skandinavia AS, Aker BP ASA, Eni Norge AS, Total E&P Norge AS, Equinor ASA, Neptune Energy Norge AS, Lundin Norway AS, Halliburton AS, Schlumberger Norge AS, Wintershall Norge AS, and DEA Norge AS, of The National IOR Centre of Norway for support.

I, once again, thank everyone for their never-ending support and encouragement that they have provided me at various stages of my PhD period.

Dhruvit Satishchandra Berawala

Summary

Natural gas production from shales has become exceedingly important in satisfying the ever-growing global energy demands. This unconventional hydrocarbon system is globally abundant, with large technically recoverable resources reported in China (1115 tcf), Argentina (802 tcf), US (665 tcf) and Canada (573 tcf). Commercial exploitation of shale resources has led to a shale energy revolution in the last decade. Successful implementation of large-scale horizontal drilling and hydraulic fracturing techniques made this possible and is attributed to collaborative efforts by the natural gas industry (notably Mitchell Energy) and the U.S. Department of Energy (DOE) from the 1980s.

A typical gas shale system is a blend of organic-rich deposition and complex mineralogy that forms a fine-grained clastic sedimentary rock with a unique geological framework where the shale independently exists as source, trap and reservoir. Low intrinsic matrix permeability (e.g. 0.1 μD for Huron shales) coupled with structural heterogeneity and complex pore networks complicates fluid transport and storage within the formation and poses tremendous challenges to technical evaluation and effective development. Technological advances in hydraulic stimulation of shale reservoirs have caused a fundamental shift to the exploration-and-production industry. These unconventional reservoirs typically have extremely low matrix permeability (10 to 100 nD) and exhibit gas stored both in free and adsorbed form. Gas flows from the nanopores in the matrix to the hydraulic fractures and then to the horizontal wells. This transport of gas comprises several flow mechanisms as investigated by a large number of scientists and engineers over many years.

The first part of the project deals with numerical modelling of shale gas production. **Paper I** and P**aper II** presents a mathematical 1D+1D model which involves a high-permeable fracture extending from a well

perforation, through symmetrically surrounding shale matrix with low permeability. Gas in the matrix occurs in the form of adsorbed material attached to kerogen (modeled by a Langmuir isotherm) and as free gas in the nano-pores. The pressure gradient towards the fracture and well perforation causes the free gas to flow. With pressure depletion, gas desorbs out of the kerogen into the pore space and then flows to the fracture. When the pressure has stabilized, desorption and production stop. The production of shale gas and mass distributions indicate the efficiency of species transfer between fracture and matrix. The model is then scaled, and production is characterized by applying input parameters from experimental and field data in the literature. Properties of fracture and matrix are varied systematically to understand the role of the fracture matrix interaction during production. **Paper I** investigate the main controlling factors during continuum flow regime in shale gas production in the context where well-induced fractures, extending from the well perforations, improve reservoir conductivity and performance. While **Paper II** focuses on the transition in non-Darcy flow regimes near fracture-matrix interfaces using mathematical modelling. Especially, we investigate conditions at which these effects vanish, and Darcy flow assumptions become reasonable. Investigated Non-Darcy mechanisms include apparent permeability, Knudsen diffusion, gas desorption and Forchheimer flow.

Paper I showed that the production behavior can be scaled and described according to the magnitude of two characteristic dimensionless numbers: the ratio of diffusion time scales in shale and fracture α, and the pore volume ratio between the shale and fracture domains β. The product $\alpha\beta$ expresses how much time it takes to diffuse the gas in place through the fracture to the well compared to the time it takes to diffuse that gas from the matrix to the fracture. For $\alpha\beta \ll 1$ the residence time in the fracture is of negligible importance and fracture properties such as shape, width and permeability can be ignored. However, if $\alpha\beta \approx 1$ the residence time

in the fracture becomes important and variations in all those properties have significant effects on the solution.

Scaling the model in **Paper II** showed that recovery of gas depends on two dimensionless number that incorporates geometry relations, time scales of flow, intrinsic parameters of the porous media, non-Darcy constants, adsorption and boundary conditions. The dimensionless numbers define respectively if 1) the fracture or matrix limit the gas production rate 2) if non-Darcy flow is significant in the fracture or matrix. When one of the media limit production, the non-Darcy flow in the other medium has reduced importance and can be excluded from the model. Non-Darcy flow is important if it limits flow in the medium limiting the production. By checking the magnitude of the selected dimensionless numbers, the modelling approach can be determined in advance and significant computational time can be saved.

The second part of the project (**Paper III** and **Paper IV**) deals with CO_2 injection in shale gas reservoirs for enhanced recovery. Although current technological advancements in horizontal drilling and fluid fracturing have contributed to primary production, only 5 – 10 % of the original gas in place (OGIP) is estimated to be recovered economically leaving a high potential for enhanced recovery methods. The gas stored by sorption in the shale matrix is estimated to account for 20 – 80 % of the total gas fraction. Desorption is triggered by pressure reduction and/or presence of a favorably adsorbing gas. Experimental studies have demonstrated that shale kerogen/organic matter has higher affinity for CO_2 than methane, CH_4, which opens possibilities for carbon storage and new production strategies.

Paper III presents a new multicomponent adsorption isotherm which is coupled with a flow model for evaluation of injection-production scenarios. The isotherm is based on the assumption that different gas species compete for adsorbing on a limited specific surface area. Rather than assuming a capacity of a fixed number of sites or moles this finite

surface area is filled with species taking different amount of space per mole. The final form is a generalized multicomponent Langmuir isotherm. Experimental adsorption data for CO_2 and CH_4 on Marcellus shale are matched with the proposed isotherm using relevant fitting parameters. The isotherm is first applied in static examples to calculate gas in place reserves, recovery factors and enhanced gas recovery potential based on contributions from free gas and adsorbed gas components. The isotherm is further coupled with a dynamic flow model with application to CO_2-CH_4 substitution for CO_2-ESGR, assuming only gas phase exists in the system. The paper presents the feasibility and effectiveness of CO_2 injection in tight shale formations in an injection-production setting representative of lab and field implementation and compare with regular pressure depletion.

Paper IV reviews the state of research on CH_4 and CO_2 sorption in shale. It presents the interaction of CO_2 and CH_4 with shale rocks and discuss the dependence of gas sorption on shale properties including organic matter content, kerogen type, mineralogy, moisture and temperature as well as shale selectivity for either species. Dynamic CO_2-CH_4 exchange studies are also summarized together with the geochemical and mechanical impact of gas sorption in shales. We note that most experimental work is still performed on crushed samples rather than whole cores. Also, CO_2 is preferentially adsorbed over CH_4 when both species co-exist in shale. Both gases are in supercritical state at typical reservoir conditions. Especially CO_2 adsorption is not well described by standard isotherm models in this state.

Abbreviations and Symbols

Roman:

a_i	=	Adsorbed component, mol / m^3 rock
$\hat{a}_i$	=	Adsorbed component, Pa
A	=	Specific surface area, m^2 / m^3 rock
A_i	=	Adsorbed specific surface area by component, m^2 / m^3 rock
a_g	=	Adsorbed gas, kg/m3
a_{max}	=	Max capacity adsorbed gas, kg/m3
$\hat{a}_g$	=	Adsorbed gas, Pa
$\hat{a}_{max}$	=	Max capacity adsorbed gas, Pa
b	=	Fracture half-width, m
b_0	=	Average fracture half-width, m
b_{max}	=	Max half width (at well), m
b_{min}	=	Min half width (end of fracture), m
b_g	=	Inverse gas volume factor, m^3 gas at standard conditions / m^3 gas at reservoir conditions
b_g'	=	Inverse gas volume factor differentiated with respect to total pressure, Pa^{-1}
B_i	=	Coefficient to relate $\hat{a}_i$ and A_i, Pa m^3 rock / m^2
C_i	=	Component molar concentration, mol / m^3 gas
D_i	=	Diffusion coefficient, m^2/s
C_β	=	Non-Darcy flow constant, $m^{-2.5}$
f	=	Transition factor, -
h	=	Fracture height, m
K	=	Absolute permeability, m^2
k, K_a	=	Apparent permeability, m^2
k_f	=	Fracture permeability, m^2
K_n	=	Knudsen number, -
L	=	System length, m
L_x	=	Matrix half-length, m
L_y	=	Fracture length, m
M	=	Gas molecular weight, g/mol
M_i	=	Conservation variable for each component, Pa
$M_{w,i}$	=	Molar weight gas component, kg / mol

$M_{w,g}$	=	Molar weight gas, kg / mol
n_i	=	Ratio of moles of component adsorbed in multilayer mode to monolayer mode, dimensionless
N_i	=	# moles of component, mol
N_t	=	# moles of gas, mol
P_i	=	Partial pressure of component, Pa
P_t	=	Total pressure, Pa
p_g	=	Gas pressure, Pa
p_L	=	Langmuir half capacity pressure, Pa
R	=	Gas constant, J/mol
r, r_e	=	Pore radius, nm
RF	=	Methane recovery factor, dimensionless
$S_{m,i}$	=	Moles that adsorb per area during monolayer adsorption at full capacity, mol / m^2
T	=	Temperature, K
u	=	Gas flux, m/s
V_g	=	Gas volume, m^3
V	=	Volume, m^3
W_i	=	Adsorbed mass of component per volume dry rock, kg / m^3 rock
x	=	Spatial coordinate, m
x_i	=	Mole fraction, dimensionless
Z	=	Gas compressibility factor, -

Greek:

α_K	=	Rarefraction parameter, -
γ	=	Forchheimer's constant, -
μ_g	=	Gas viscosity, Pa s
ρ_g	=	Gas molar density, mol/m^3 gas
$\rho_{g,sc}$	=	Surface gas molar density, mol/m^3 gas
τ	=	Tortuosity, -
ϕ^m	=	Matrix Porosity, -
ϕ^f	=	Fracture porosity, -

Indices:

atm	=	Atmospheric conditions
base	=	Under pressure depletion condition

c	=	Carbon dioxide CO2
f	=	Fracture
i	=	Component;
init	=	Initial conditions
inj	=	Under CO2 injection conditions
m	=	Methane CH4
sc	=	Surface conditions
well	=	Well conditions

Abbreviations:

EOR	=	Enhanced oil recovery
ESGR	=	Enhance shale gas recovery
GOIP	=	Gas originally in place, kg
GCIP	=	Gas currently in place, kg
NFR	=	Naturally fractured reservoir
TOC	=	Total organic content

List of publications

Paper I:

Berawala, D. S., Andersen, P. Ø., & Ursin, J. R. (2019). Controlling Parameters During Continuum Flow in Shale-Gas Production: A Fracture/Matrix-Modelling Approach. *SPE Journal*, 24(3), 1378-1394. https://doi.org/10.2118/190843-PA

Paper II:

Berawala, D. S., & Østebø Andersen, P. (2020). Numerical Investigation of Non-Darcy Flow Regime Transitions in Shale Gas Production. Submitted to *Journal of Petroleum, Science and Engineering,* 20, 107114. https://doi.org/10.1016/j.petrol.2020.107114

Paper III:

Berawala, D. S., & Andersen, P. Ø. (2020). Evaluation of Multicomponent Adsorption Kinetics for Carbon Dioxide Enhanced Gas Recovery from Tight Shales. *SPE Reservoir Evaluation & Engineering*, 23(03), 1060-1076. https://doi.org/10.2118/195536-PA

Paper IV:

Klewiah, I., Berawala, D. S., Walker, H. C. A., Andersen, P. Ø., & Nadeau, P. H. (2020). Review of experimental sorption studies of CO_2 and CH_4 in shales. *Journal of Natural Gas Science and Engineering*, 73, 103045. https://doi.org/10.1016/j.jngse.2019.103045

Additional publications

Berawala, D. S., & Østebø Andersen, P. (2020). Fracture-Matrix Modelling of CO_2 Enhanced Shale Gas Recovery in Compressible Shale. Paper SPE 202222-MS presented at *SPE Asia Pacific Oil & Gas Conference and Exhibition,* Brisbane, Australia, 17-19 November.

Kallesten, E., Østebø Andersen, P., Berawala, D. S., Korsnes, R. I., Vadla Madland, M., Omdal, E., & Zimmermann, U. (2020). Modelling of Permeability and Strain Evolution in Chemical Creep Compaction Experiments with Fractured and Unfractured Chalk Cores Conducted at Reservoir Conditions. *SPE Journal*, preprint. https://doi.org/10.2118/197371-PA

Berawala, D. S., & Østebø Andersen, P. (2019). Numerical Investigation of Non-Darcy Flow Regime Transitions and Geomechanical Effects in Shale Gas Production. Paper SPE 197133-MS presented at *SPE Abu Dhabi International Petroleum Exhibition & Conference*, Abu Dhabi, UAE, 11-14 November. https://doi.org/10.2118/197133-MS

Kallesten, E., Berawala, D. S., Andersen, P., Korsnes, R., Madland, M., Omdla, E., Zimmermann, U. (2019). Modelling of Permeability Evolution in Shear Failing Chalk Cores Under Thermochemical Influence. Paper SPE 197371-MS presented at *SPE Abu Dhabi International Petroleum Exhibition & Conference*, Abu Dhabi, UAE, 11-14 November. https://doi.org/10.2118/197371-MS

Berawala, D. S., Østebø Andersen, P. (2019). Evaluation of Multicomponent Adsorption Kinetics for CO2 Enhanced Gas Recovery from Tight Shales. Paper SPE 195536-MS presented at *SPE featured at 81st EAGE Europec Conference and Exhibition*, London, United Kingdom, 3-6 June. https://doi.org/10.2118/195536-MS

Andersen, P. Ø., & Berawala, D. S. (2019). Modelling of Creep-Compacting Outcrop Chalks Injected with Ca-Mg-Na-Cl Brines at

Reservoir Conditions. *SPE Journal,* 24(6), 2889-2910. https://doi.org/10.2118/192018-PA

Berawala, D. S., Andersen, P. Ø., & Ursin, J. R. (2018). Controlling Parameters for Shale Gas Production into a Well-Induced Fracture: A Fracture-Matrix Modelling Approach. Paper SPE 190843-MS presented at *SPE featured at 80th EAGE Europec Conference and Exhibition*, Copenhagen, Denmark, 11-14 June. https://doi:10.2118/190843-MS

Andersen, P. Ø., & Berawala, D. S. (2018). Analytical and Numerical Solutions for Interpretation of Chemical Compaction in Chalk. Paper SPE 192081-MS presented at *SPE Asia Pacific Oil and Gas Conference and Exhibition*, Brisbane, Australia, 23-25 October. https://doi:10.2118/192018-MS

Nadeau, P.H., Andersen, P. Ø., Berawala, D. S. (2019). Towards zero carbon emission power via CO_2 increased shale energy recovery. Poster presented at *Euroclay Conference,* Paris, France, 1-5 July.

Berawala, D. S., Andersen, P. Ø. (2019). Core-Scale Modelling of CO2 Injection in Tight Shale Formations for Enhanced Gas Recovery. Poster presented at *IOR Norway*, Stavanger, Norway.

Klewiah, I., Berawala, D. S., Walker, H. C. A., Andersen, P. Ø., & Nadeau, P. H. (2019). Opportunities for increased energy recovery and carbon sequestration in shales - reversing climate change? Poster presented at *IOR Norway*, Stavanger, Norway.

Berawala, D. S., Andersen, P. Ø. (2018). Modelling of CO_2 Injection in Shale Gas Reservoirs-Improved Recovery and CCS**.** Poster presented at *IOR Norway*, Stavanger, Norway.

Berawala, D. S., Ursin, J. R., & Slijepcevic, O. (2017). Sphere in Cube Grid Approach to Modelling of Shale Gas Production Using Non-Linear Flow Mechanisms. *International Journal of Geological and Environmental Engineering*, **11**(9), 889-898**.** https://doi:10.1999/1307-6892/10008359

Table of Contents

List of Figures

List of Tables

Chapter 1 - Introduction

Shale gas is the most rapidly growing energy resource in the United States in recent years. This unconventional resource is stored densely packed into the shale matrix through adsorption, in addition to occurring as free gas in the pores, which increases the storativity of gas. Gas production from these low permeable deposits is made possible by drilling horizontal wells and hydraulically fracturing the reservoir to establish high permeable fractures that improve well productivity. In spite of technological advancements, there is little understanding in mechanisms for shale gas production and predictions have proved to be very pessimistic and inaccurate. Shale formations, which in the past were considered only as potential source rocks, are today being actively pursued as potential reservoirs. The success of the Barnett Shale of central Texas, USA, initiated the recent interest in developing shale as producing reservoirs. This fundamental shift has attracted many companies and brought a revolution in the E&P industry, which was evident from the decline in crude oil prices in 2014-2015.

When considering unconventional resource plays, the focus is on finding organic shales (Alexander et al. 2011). Shale gas reservoirs differ from the conventional gas reservoirs by two important characteristics. Firstly, they have extremely low matrix permeability, typically 10 to 100 nanodarcies (10^{-6} mD) (Cipolla et al. 2010). Secondly, in some instances they contain organic-rich rocks where gas is adsorbed on the surface of matrix pores (Arogundade and Sohrabi 2012; Hill and Nelson 2000). The amount of adsorbed gas can vary between 5-80% of total gas-in-place volumes (Curtis 2002). The amount of gas in place is strongly affected by the total organic carbon content, clays and the adsorption ability of methane on the internal surface of the solid (Martin et al. 2010). Gas shale consists of a solid matrix and fractures that contribute to the natural permeability pathway for gas flow.

Production from these reservoirs requires stimulation by drilling long horizontal wells with multistage hydraulic fracture treatments to create extensive artificial fracture networks near the wellbore. The stimulation effectiveness is often measured in terms of Stimulated Reservoir Volume SRV (Mayerhofer et al. 2010). Gas flows from the nanopores in the matrix to the hydraulic fractures and then to the horizontal well. This transport phenomenon is a combination of several flow mechanisms investigated by several scientists over the past couple of decades (Beskok and Karniadakis 1999; Bird 2002; Civan 2010; Civan et al. 2011; Javadpour 2009; Javadpour et al. 2007). Moridis et al. (2010) and Blasingame (2008) provided a comprehensive review of flow mechanisms in shale and mentioned that significant gas adsorption-desorption mechanisms occur in the pore surfaces. Civan (2010) used Beskok and Karniadakis (1999) model of rarefied gas flow in microchannels, ducts and pipes to describe gas transport in tight porous media. The co-existence of severe heterogeneity, Klinkenberg or slippage effects (Klinkenberg, 1941) and geomechanical effects further complicates the flow behavior.

Bird (2002) suggested that gas transport in nanopores is a combination of viscous flow, Knudsen diffusion and molecular diffusion. Javadpour (2009) also presented a gas transport flow model considering viscous flow and Knudsen diffusion. Molecular diffusion refers to the relative motion of different gas species and occurs when the mean free path of gas molecules is at least one order larger than the pore diameter of the porous media (Ho and Webb, 2006). Viscous flow generates through collision between molecules whereas Knudsen diffusion generates from collision between molecules and pore walls. Among these mechanisms, which one is dominant depends on the relationship between mean free path of gas and the pore size of the porous media. If the mean free path of gas is much smaller than the pore size, the probability of collision between molecules is much higher than the collision between molecules and the pore walls. Thus, in such case, gas transport is mainly governed

by viscous flow and Knudsen diffusion can be ignored. As the pore diameter gets smaller, reaching the same order as the gas molecular mean free path, collisions between molecules and the pore walls become more prominent with gas transport mainly governed by Knudsen diffusion. Knudsen (1909) gave a widely recognized dimensionless parameter, Knudsen number K_n, which is defined as the ratio of the molecular mean free path λ to the characteristic length scale L. Based on the magnitude of Knudsen number, gas transport in porous media can be divided into four flow regimes (as shown in **Table 1**) (Javadpour et al. 2007):

Table 1 Classification of gas flow regimes based on the Knudsen number.

$K_n < 0.001$	$0.001 < K_n < 0.1$	$0.1 < K_n < 10$	$K_n > 10$
Mean free path << pore radius	Mean free path < pore radius	Mean free path ≈ pore radius	Mean free path > pore radius
Continuum flow regime	Slip flow regime	Transition flow regime	Free molecular regime

In the continuum flow regime ($K_n < 0.001$), the mean free path of gas molecules is much smaller than the pore size of the porous media, therefore the probability of collision between molecules is much higher than that of collisions between molecules and the pore walls. The gas transport is mainly governed by viscous flow and Knudsen diffusion can be ignored. In this regime, conventional Darcy's law equation with conventional no-slip boundary conditions can describe the gas flow in porous media. Gas transport governed by Knudsen diffusion becomes important when the pore size is of the same order of magnitude or smaller than the mean free path of gas molecules. Such transport refers to transition or free molecular flow regime with $K_n > 0.1$. The mean free path of gas molecules in the matrix is usually of the same order of magnitude or larger than the size of pore throat. This may cause acceleration of gas molecules along the flow path leading to an increase in the apparent permeability (Tang et al. 2017). Wang and Reed (2009) observed slippage effect in Marcellus shale, where they reported that permeability increases from 19.6 μD at 1000 psi to 54 μD at 80 psi. The

gas flow in matrix is further complicated by gas adsorption/desorption and geomechanical effects. The adsorbed gas layer on the pore surface occupies the pore space, resulting in variations of the gas apparent permeability (Xiong et al. 2012; Cao et al. 2016). The adsorbed gas is mostly produced in the latter stages of production when a considerable amount of free gas has been depleted and the well undergoes boundary dominated flow (Mengal and Wattenbarger, 2011).

Another key mechanism in shale gas production is the non-Darcy flow; the traditional linear equation for flow in porous media based on Darcy's law is not enough for accurately describing high-rate flows. Non-Darcy flow occurs when inertial forces may no longer be neglected compared with viscous forces (Hagoort 2004). That is very common near gas production wells or in the near-wellbore region, especially in fractures where local velocities can be very high. Bybee (2006) suggested that in hydraulic fracture stimulation, non-Darcy flow can have a major effect on reduction of a propped half-length to a considerably shorter "effective" half-length, thus lowering the productive capability of the well and overall reserves recovery. Moreover, flow-capacity can reduce by 5 % to 30 % in low-rate wells due to non-Darcy effects (Bybee 2006). To account for this nonlinear behavior, an inertial term called the Forchheimer term is added to Darcy's equation. Forchheimer (1901) gave the empirical Forchheimer equation to model gas flow more accurately at high flow rates (Mustapha et al. 2015; Li and Engler 2001; Belhaj et al. 2003; Jones 1987; Ling et al. 2013; Barree and Conway 2005; Zeng and Zhao 2008). Al-Rbeawi (2018) showed that non-Darcy flow has a significant effect on the pressure profile of unconventional gas reservoirs, especially at early production time. Luo and Tang (2015) through semi-analytical modelling concluded that non-Darcy flow in the fracture mainly reduces the effective conductivity. This varying conductivity and non-Darcy flow in the fracture make the pressure curves deviate from the type curves. Several efforts have been made over the past 10 years to identify the effects of non-Darcy flow on overall gas

production from shale reservoirs (Wang and Marongiu-Porcu 2015; Fan et al. 2019; Al-Rbeawi 2019; Luo and Tang 2015; Sun et al. 2015; Pang et al. 2018; Wang et al. 2017). However, there appears to lack a clear understanding on exactly where the transition from Darcy to non-Darcy flow occurs, quantifying this transition and assessing how its importance can be estimated a priori.

The gas flow in shale reservoirs is further complicated by geomechanical effects. Geomechanical effect, in form of stress-dependent matrix properties, such as permeability, volumetric strain and porosity can vary as a function of confining pressure and pore pressure. The pore pressure reduction leads to a rise in the effective stress, which subsequently compacts pore-structure geometry and reduces formation porosity and intrinsic permeability (Ren et al. 2016). Moreover, gas desorption triggers matrix shrinkage, whose effect is contrary to the pore pressure decrease (Cui and Bustin 2005; Zhang et al. 2008). The pore size reduction caused by compaction also influences the gas slippage process as it is related to the size of pore throat. It has been proved by coal experiments that a strong coupling effect exists between the pore compressibility and the gas slippage (Tang et al. 2017; Gensterblum et al. 2014). Consequently, the net change in porosity and permeability accompanying gas extraction is controlled by the several competing processes (Jiang and Yang, 2018). All these effects increase with production as the drawdown pressure is decreased and may result in significantly lowered overall gas recovery in many shale gas reservoirs (Yu and Sepehrnoori, 2014).

In addition to the matrix flow, the fracture flow is also critically important in unconventional reservoirs which takes place on the centimetre scale. The conductivities of fractures were found to be very sensitive to the applied effective stress based on the experiment results. Proppants are utilized for holding fractures open after the treatment as well as forming conduits for fluid flow into the wellbore (Zendehboudi and Bahadori, 2016). The stress-dependence of hydraulic fractures in

shale gas reservoir have been discussed in the literature, whilst the stress-dependence of matrix pores and natural fractures have been mostly ignored. Another complexity in modelling shale gas flow is how to handle fracture flow, its geometry and fracture-matrix interactions. Currently, there is limited understanding of how these complicated flow mechanisms impact gas flow and the ultimate gas recovery in such reservoirs and what are the parameters that control the production.

To improve this understanding, we present in part one of this work a simplistic numerical modelling approach of a 1D+1D combined fracture-matrix model that characterizes fracture-matrix interactions and defines controlling parameters for the flow of free and desorbed gas from shale matrix to the well-induced fracture. The model consists of a high-permeable hydraulic fracture extending from a well perforation, through symmetrically surrounding shale matrix of fixed length with low permeability. The fracture is modeled with variable width depicting a real-field scenario. By assuming the matrix has finite length, we are implicitly assuming equally spaced perforation intervals. This is a good assumption if the well has a fixed pressure and the perforations and fractures have identical properties. The free gas present in the nano-pores diffuses towards the fracture and well perforation due to pressure gradients. With pressure depletion, gas adsorbed onto the kerogen material desorbs into the pore space and then flows to the fracture. This system is solved numerically using an operator splitting approach. The commonly used approach to model fracture-matrix flow is based on the dual-porosity methodology (Warren and Root, 1963) for naturally fractured reservoirs (NFRs) where the geometry of fracture and matrix are represented by average properties (Du et al. 2010; Hoteit and Firoozabadi 2008; Karimi-Fard et al. 2003; Samandarli et al. 2011). A transfer term takes care of the communication between fracture and matrix. Here we do not study a full network of fractures, but rather an individual hydraulic fracture induced at a well perforation and its surrounding shale volume. Further, contrary to the models for NFRs that

address advection-diffusion flows, this system is based on solving a pressure diffusion equation for the fracture coupled with a pressure diffusion equation in the matrix where free gas and adsorbed gas reside. Instead of advection-diffusion system, we have a diffusion-diffusion system where the fracture is open only from one side. The work is an adaptation of the single fracture-matrix system methodology from NFRs studied in (Mainguy and Ulm 2001; Tecklenburg et al. 2013; Andersen et al. 2014, 2015; Andersen and Evje 2016) where characteristic flow regimes and dimensionless numbers could be derived for spontaneous imbibition and reactive flow processes. A similar geometry is now considered in the context of shale gas production.

We consider this system geometry and further extend it to two different sets of cases accounting for different flow mechanisms:

System 1- Darcy Flow: Flow is governed by conventional Darcy's equation. Only continuum flow regime is assumed, i.e. mean free path of gas molecules is much smaller than pore size of the shale matrix.

System 2- Non-Darcy Flow: Flow is governed by non-Darcy flow due to high velocity of gas. Apparent permeability is used to account for gas slippage effects, effective stress, adsorption and flow regimes relevant due to the nano-pore structure of the shale matrix.

In second part of the thesis, we extend our understanding of numerical modelling of shale gas production to CO_2 injection for enhanced shale gas recovery. In-spite of technological advancements and extensive efforts by researchers and engineers, the ultimate recovery from shale gas reservoirs is considerably low (3-10%). A significant portion (20-85 %) of the CH_4 is stored as an adsorbed phase (Hill and Nelson 2000; Vermylen 2011), and only a relatively small portion of this produced during the lifetime of a shale gas well (Cipolla et al. 2010). The gas production rate decreases rapidly after a few years of production so that estimated ultimate recovery is poorly constrained in early stages of field

development (Weijermars 2013). Consequently, interest in enhanced shale gas recovery (ESGR) from these reservoirs has grown recently (Kim et al. 2017). CO_2-EOR and storage in conventional oil and gas reservoirs is proven effective, the potential to sequester in unconventional organic-rich shales (oil/gas) is even more promising and economical, yet there has been minimum attention given to these vast resources (Sherifa and Reza 2018).

Experimental results have shown that shales have greater adsorption affinity for CO_2 than CH_4 (Weniger et al. 2010; Heller and Zoback, 2014). CO_2 is also favorably adsorbed over CH_4 when both gas species co-exist within the shale (Pino et al., 2014; Cancino et al., 2017; Ma et al., 2018). A huge potential for enhanced shale gas recovery (ESGR) is therefore feasible through injection of CO_2 (Blok et al., 1997; Oldenburg et al., 2001) which can stimulate the desorption of pre-adsorbed methane through an in-situ molecular swapping mechanism at the sorption sites, releasing the otherwise trapped methane into the porous system to increase the rate and volume of CH_4 recovered (Regan, 2007). This technique is referred to as CO_2 enhanced shale gas recovery, CO_2-ESGR and is considered a viable means for simultaneous CO_2 storage in the shale formations with recent reviews provided by Liu et al. (2019) and Rani et al. (2019). This concept of CO_2 utilization in shales is illustrated in **Figure 1**. Godec et al. (2013) demonstrated through simulation that at optimal operational conditions, 7% incremental CH_4 production could be obtained through CO_2 injection in the Marcellus Shale in Eastern United States. They estimated 12 trillion cubic meters of methane to be technically recoverable with an associated storage of 55 billion tonnes of CO_2. Khosrokhavar (2015) demonstrated that for an approximate storage of 12 kg of CO_2 in a characteristic gas shale system, 1 kg of CH_4 can be produced and yield 55 MJ energy while spending 12 MJ energy for compression. They noted that the energy gain was still substantial when accounting for CO_2 capture and storage (CCS) as quantified by Iijima et al. (2011). Logistically, in most cases, a surface gas pipeline distribution

network could easily be modified to transport CO_2 to the wellhead whereas the cost of CO_2 injection into the subsurface formation is drastically minimized by repurposing the available well infrastructure to accommodate CO_2 injection (Tao et al., 2014).

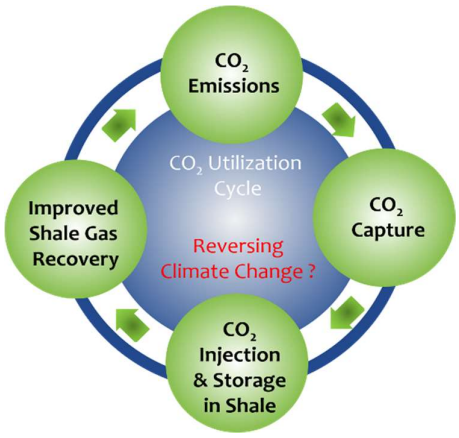

Figure 1 Concept of CO2 capture and utilization for enhanced shale gas recovery and carbon sequestration.

Over the past decade in US, shale gas production has increased significantly from about 6.16 trillion cubic feet to exceeding 20 trillion cubic feet in 2020 and is expected to reach about 35 trillion cubic feet in 2050 (Fatah et al., 2020). Out of these, 49% of the total US gas production is expected to come from shale reservoirs, providing the potential for CO_2 storage projects. Thus, CCS applications hold good promise in reducing CO_2 emissions in the coming decades, despite the increase in energy demands. Effective utilization of these depleted gas formations as storage sites for CO_2 can significantly contribute to minimizing CO_2 emissions, assuming good connectivity between induced and existing fractures and no pore space collapse. Tao and Clarens (2013) estimated that Marcellus shale alone has the storage capacity ranging between 10.4 and 18.4 Gt (1 Gt = 10^{12} kg) which has the potential equivalent to around 50% of CO_2 emissions in the US by 2030 (Middleton et al., 2015). Similarly, Barnett shale has a CO_2 storage

capacity ranging between 2.1 to 3.1 Gt. These studies direct towards the strong foundation and high possibility of storage capacity in shale formations. However, there is still a gap in understanding of CO_2-shale interaction and more investigations are needed to successfully apply CCS technology in shale formations technically and economically. It is crucial to address the potential interactions between CO_2 and shale formation, and their influence on CCS to ensure the longevity of CO_2 containment (Liu et al., 2016, Fatah et al., 2013).

To understand efforts made by different engineers and scientist, we also present a detailed literature review and results and summarize our findings on key parameters/mechanisms in CO_2 enhanced shale gas recovery (**Paper IV**). The review focuses on the related literature of CO_2/shale interaction and its effect on shale, to gain a wide understanding of the effect of CO_2 injection on shale properties. Moreover, we derived a new a multi-component adsorption isotherm with application to CH_4-CO_2 substitution (**Paper III**). The basics for the derivation are the principle that different molecules can occupy a surface, but not necessarily take the same space. Area, rather than moles, is therefore treated as the conserved capacity of the surface. The implications of isotherm are demonstrated, first in various static settings where we fit the isotherm to experimental data and predict adsorption behaviour under other conditions. Next, we apply the isotherm in a dynamic CO_2-EGR setting on lab scale. A shale core initially saturated with both free and adsorbed CH_4 is produced by sequentially depleting the pressure and re-pressurizing the core with CO_2 injection. Optimal configurations of gas production and CO_2 injection are evaluated, for a base case and at conditions more comparable to field where permeability is reduced, and spatial dimensions increase. The role of substitution and molecular diffusion are emphasized.

1.1 Objectives

The thesis is essentially divided into two parts: 1) numerical modelling of shale gas production using fracture-matrix modelling approach and 2) review of key mechanisms and modelling of CO_2 injection for enhanced shale gas production.

The proposed model for part one which is further subdivided into system 1 and 2 focuses on addressing some questions of practical importance:

- Which properties of the fracture are important for overall gas recovery? Length, width, volume, permeability?
- What is the impact of having a variable fracture width versus a uniform fracture width?
- What is the role of matrix permeability and adsorption parameters?
- How is end recovery affected by the well bottom hole pressure and how is that linked to adsorption properties?
- How can the flow be characterized into fracture dominated or matrix dominated and in under what conditions?
- How can we quantify the flow transition from Darcy to non-Darcy (using Forchheimer equation)?
- What are the conditions under which non-Darcy effects in the matrix become significant for gas recovery?
- How does non-Darcy flow affect flow regimes in shale gas production?
- Most importantly, what is the advantage and potential of this model?

We answer these questions (1) by showing a sensitivity analysis of the model behavior in terms of pressure and gas recovery, parameterized using experimental and literature data and (2) by interpreting the results using dimensionless numbers derived from the model. A scaling number is suggested that controls flow in the considered fracture-matrix geometry. It is shown that the behavior can be described according to the magnitude of two characteristics dimensionless numbers alone: the ratio

of diffusion time scales in the fracture and matrix and the pore volume ratio between shale matrix and fracture. This formulation provides an intuitive interpretation of the complex shale gas production system. A further advantage of the model is that it creates a base, which can easily incorporate additional mechanisms including non-linear flow, geomechanics and enhanced gas recovery studies that are not readily found in standard commercial software. The model can be further extended to field scale application.

Objectives for second part of the thesis focusing on CO_2 injection for enhanced shale gas production are:

- Evaluate the state of experimental findings regarding gas sorption in shales.
- Present a new multicomponent adsorption isotherm based on area rather than moles as in the case of Langmuir isotherm.
- Couple the adsorption model with flow model for evaluation of injection-production scenarios.
- Identify optimal configurations for gas production and CO_2 injection at lab and field scale conditions.

Along with these objectives, we also determine gaps in experimental research for CO_2 enhanced shale gas recovery that should be addressed.

1.2 Thesis Outline

This thesis is divided into five main chapters. They are:

Chapter 2 covers the definitions related to processes and flow mechanisms that has been applied in this work. It includes the basics of gas adsorption on shale, apparent permeability variations, non-Darcy flow and density-pressure relations used for modelling gas production and CO_2 injection. Chapter 3 presents the numerical modelling approach used is this work while chapter 4 presents the main results from the work

performed and the discussion and limitations of these models. The last chapter, chapter 5, provides the concluding remarks and the scope of future work.

Four journal papers (**Paper I**, **Paper II**, **Paper III** and **Paper IV**), that document the main body of this PhD thesis, are attached in the end.

Chapter 2 - Flow Mechanism Definitions

In this chapter, the key underlying processes and flow mechanisms used in this study to model shale gas production and CO_2 enhanced shale gas recovery are presented.

2.1 Density-Pressure Relationships

For simplicity in modelling, we have considered shale gas (mainly comprising of methane, CH_4) as an ideal gas. Introduce the inverse gas volume factor b_g, using the ideal gas law, we can write mass density as a function of pressure:

$$\rho_g(p_g) = b_g(p_g)\rho_{gs}, \qquad b_g = \frac{T^{atm}}{T p_g^{atm}}\, p_g. \tag{1}$$

Further, we can write this as:

$$\rho_g(p_g) = \rho_{gs} b_g' p_g, \qquad b_g' = \frac{T^{atm}}{T p_g^{atm}}, \tag{2}$$

where b_g' is the inverse volume factor differentiated with respect to pressure, which, as seen, is constant and has unit of inverse pressure. The density-pressure relation described by (2) helps us to formulate the transport equation in terms of pressure as the gas in the shale reservoir is transported by pressure diffusion.

2.2 Gas Adsorption on Shale

Adsorption can be defined as a process in which material (adsorbate) travels from a gas or liquid phase and forms a superficial monomolecular layer on a solid or liquid condensed phase (substrate) (Artioli, 2008). It is a surface process that leads to transfer of a molecule from a fluid bulk to solid surface. This can occur because of physical forces or by chemical bonds. Usually it is reversible (the reverse process is called desorption); then it is responsible not only for a subtraction of substances but also for release. In most of the cases, this process is described at the equilibrium

by means of some equations that quantify the amount of substance attached on the surface given the concentration in the fluid. These equations are called isotherms because of the dependence of their parameters on the temperature, which is one of the most important environmental factors affecting adsorption (Artioli, 2008).

The total or absolute amount adsorbed is computed by mathematical modelling, before fitting the data to one of many available mathematical isotherm models (e.g. Henry, Langmuir, BET, DR, Pore-filling). It is suspected that adsorption occurs as a monolayer at low pressures and as multilayers at higher pressures. The adsorption behaviour of the gas in shale gas reservoirs is normally described by the monolayer Langmuir isotherm. This means a single layer of molecules covering the solid surfaces. The Langmuir isotherm assumes that the adsorbed gas behaves as an ideal gas under isothermal conditions. Hence, there is a dynamic equilibrium at constant pressure and temperature between the adsorbed and non-adsorbed gas (Gholinezhad et al. 2018). Another widely used isotherm is BET isotherm which assumes that the adsorption layers on the surface of the organic carbon were infinite (Brunauer et al. 1938). Unlike the Langmuir isotherm which assumed a monolayer adsorption, BET isotherm extended Langmuir's application to include multi-layer adsorption. BET isotherm is considered a better fit to describing the adsorption processes in shale gas reservoirs (Gholinezhad et al. 2018). However, the acceptance of a single model for universal description of sorption in shales is still contended amongst researchers.

The pressure dependency of adsorbed gas (mass per solid volume), a_g, in this study is described by a Langmuir isotherm:

$$a_g = a_{max} \frac{p_g}{p_g + p_L}, \tag{3}$$

where a_{max} is the max capacity of the shale (in mass per solid volume) to store gas on the surface and p_L is the pressure at which half this capacity has been obtained.

Using density-pressure relationship given by (2), we can write (3) in terms of pressure unit by introducing following notation:

$$\hat{a}_g = \frac{(1-\phi)}{\phi \rho_{gs} b'_g} a_g = \hat{a}_{max} \frac{p_g}{p_g + p_L}, \qquad \hat{a}_{max} = \frac{(1-\phi)}{\phi \rho_{gs} b'_g} a_{max}. \tag{4}$$

Note that $\hat{a}_g$ and $\hat{a}_{max}$ have the units of pressure.

2.2.1 *Multi-component Adsorption*

The presence of CO_2 with methane during CO_2-ESGR process makes the gas desorption behaviour and measurements more difficult. Thus, presence of more than one component within the pore network means that a better and more representative isotherm model will have to be taken into account.

Ruthven (1984) proposed a general equation that represents the extended Langmuir isotherm as:

$$V_{ads,i} = \frac{V_{L,i}\left(\frac{p_i}{p_{L,i}}\right)}{1 + \sum\left(\frac{p_i}{p_{L,i}}\right)}, \tag{5}$$

where $V_{L,i}$ the Langmuir volume for component i, $p_{L,i}$ is the Langmuir pressure component for i and $\sum\left(\frac{p_i}{p_{L,i}}\right)$ is the summation of all component pressure ratios i and L, i, p_i is the partial pressure of component i (Gholinezhad et al. 2018).

Kim et al. (2017) developed a field scale CO_2 injection model for Barnett shale, Marcellus shale and New Albany shale considering this multi-component adsorption and concluded substantial increase in gas recovery and potential for CO_2 sequestration. Liu et al. (2017) also used this multi-adsorption phenomenon to analyse CO_2-ESGR potential for Yanchang shale in China.

Sorption of CO_2 or CH_4 onto shale matrix is frequently examined in the laboratory by construction of sorption isotherms, which involves measuring the uptake or release of either gas species on a shale sample at controlled temperature and pressure conditions. The measured sorption is a combination of adsorption, absorption or capillary condensation which individually are difficult to distinguish. Although these mechanisms are characteristically different, the net result is a storage of gas molecules in a denser phase relative to the bulk (free gas) phase in the open pores (Ross & Bustin, 2009). The experimental procedures to measure sorption vary but can be categorized into mass-based or volumetric-based. In the mass-based method the change in sample mass associated with adsorption at each fixed pressure and temperature condition is measured with a microbalance of high accuracy. The volumetric technique is based on Boyle's law, where the adsorption isotherms are constructed by computing the amount of adsorbed gas using the real gas equation, which accounts for the gas compressibility factor at each equilibrium pressure (Heller & Zoback, 2014). The former approach is limited to the use of very small sample sizes whereas the latter can satisfactorily accommodate different sample sizes.

The reviewed literature depicts tremendous challenge with performing experimental flow-through tests due to the characteristically ultra-low permeability of shale rocks. Hence most experimental evaluations of gas sorption have been conducted with crushed samples as opposed to whole cores. Likely sources of experimental errors and uncertainties in these tests are discussed by Fraissard and Conner (1997); Busch and Gensterblum (2011). In general, high-pressure isotherm experiments determine sorption capacity, whereas structural properties (e.g. specific surface area, pore size distribution, nano-, micro- or mesopore volumes) are evaluated via low-pressure (< 1 MPa) sorption tests.

The majority of shale formations have temperatures ranging from 96 – 122 °C, with pore pressures in the range of 15 – 25 MPa (Lu et al., 2016). The subsurface sorption phenomenon will most likely proceed as a

supercritical adsorption-desorption process (Menon, 1968) since both CH_4 and CO_2 will typically exist in the supercritical state (CH_4: T_{cr} = -82°C and P_{cr} = 4.64 MPa; CO_2: T_{cr} = 31°C and P_{cr} = 7.38 MPa). A peculiar feature in adsorption isotherms of supercritical fluids is the possible occurrence of a peak in adsorption with pressure (Aranovich & Donohue, 1995, 1996). Its occurrence will depend on the gas type, the proximity of pressure and temperature conditions to the supercritical ('sc') state of the gas, the void volume determination technique, and the sample properties (e.g, pore size distribution) (Murata et al., 2001; Gumma & Talu, 2003; Herrera et al., 2011; Gasparik et al., 2012). Laboratory experiments thus should be performed at relevant subsurface pressure and temperature conditions, but often the experimental literature is restricted to lower pressures due to available equipment and experimental constraints.

In that context, CH_4-CO_2-shale adsorption processes are conveniently divided into three stages owing to the pressure range and adsorption rate: low pressure (< 3 MPa; below supercritical conditions), intermediate pressure (3-10 MPa; transition into supercritical conditions) and high-pressure (> 10 MPa; supercritical state) adsorption stages that vary depending on the gas species and sample properties. The low-pressure stage is characterized by sorption on the sites with highest adsorption energy (i.e. the smallest pores) first, and progression towards larger pores (as pressure increases) which causes gradual reduction in the isosteric heat of adsorption (Stoeckli, 1990). This is indicative of physisorption by pore-filling as originally suggested by (Dubinin, 1975) for gas sorption in microporous materials. Further increase in pressure will eventually cause only small changes in the adsorption content. The isosteric heat of adsorption reduces with pressure until equilibrium is established, and no more gas can adsorb.

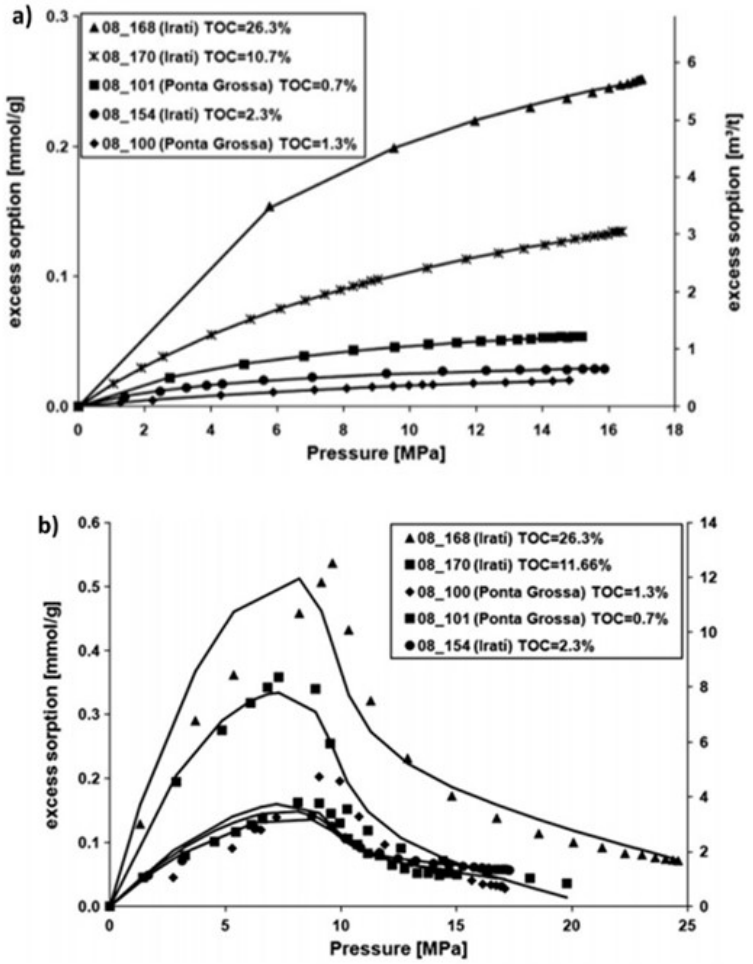

Figure 2: Comparison of adsorption isotherm (excess sorption vs pressure) for CH_4 (a) and CO_2 (b) on gas shale samples of the Paraná Basin in Brazil (Weniger et al., 2010). Experiment was conducted on crushed dry samples at a fixed temperature of 45°C.

In the reviewed literature, CH_4 excess adsorption (the difference between the amount of CH_4 in the system and the amount that would be present at the same temperature and pressure in the absence of adsorption) on gas shales is reported to increase monotonously with pressure (in both gaseous and supercritical states) and gradually reach a constant value at

high pressures (Bi et al., 2016; Wang et al., 2016; Li et al., 2017). Gas-phase CO_2 adsorption also increases monotonously with pressure to the supercritical transition point, however adsorption of CO_2 in supercritical state causes the adsorption profile to reach a maximum, after which further increase in pressure will cause CO_2 to desorb monotonically. Typical sorption behavior for both CH_4 and CO_2 is depicted in **Figure 2** for sorption experiments on crushed Devonian shale samples at a fixed temperature of 45 °C and pressures ranging up to 25 MPa. The characteristic difference in the adsorption of either gas is clearly revealed, with maxima observed only for CO_2. The same trend in experimental profiles of CO_2-CH_4 sorption is reported by Strubinger et al. (1991); Sudibandriyo et al. (2003); Busch et al. (2008); Weniger et al. (2010); Schaef et al. (2013); Gasparik et al. (2014); Schaef et al. (2014); Lu et al. (2016); Merey and Sinayuc (2016) on either gas shale samples of original composition or pure inorganic minerals.

In shales, the gradual increase in CO_2 adsorption near supercritical conditions has been attributed to the sharp change (i.e. increase) in fluid density when gaseous CO_2 is converted to supercritical fluid. This favors overall CO_2-shale interaction by increased (binding) energy and more molecular layers are attached onto the surfaces. For CO_2, Schaef et al. (2013) observed that with continued adsorption, the cross-over point (**Figure 2b**) is reached because the stabilization energy ($E_{inter\text{-}ad}$) of the supercritical CO_2 molecules increases as the pressurized system brings the gas molecules closely together. Meanwhile, the adsorbate-adsorbent adsorption energy (E_{ads}) decreases (becomes less negative). This could drive the adsorbent-adsorbent binding energy (E_b) to negative ranges and thereafter desorption dominates as the principal mechanism and a decline is observed in the isotherm curve. Recently, Jia et al. (2018) reported a similar trend of CO_2 adsorption behavior, where a crossover region was observed before and after the critical pressure point, through sorption measurements from low- to high-pressure conditions (temperature was kept constant at 30 °C) in a shale core from the Green River Formation

in Colorado. The discontinuity of CO_2 adsorption at pressures above CO_2-P_{cr} may have crucial implications on CO_2-ESGR and CO_2 storage. It must be noted that the occurrence of an adsorption peak has also been reported in some cases for CH_4, although mostly for dried overmatured gas shales (Moffat & Weale, 1955; Gasparik et al., 2012; Merkel et al., 2015; Zhou et al., 2018) and pure carbon adsorbents (Xiong et al., 2017). Most single- and multi-component adsorption isotherms are monotonous; showing no distinct peaks even at relatively high pressures (e.g. the Langmuir type). Capturing physical behavior at reservoir conditions may require more general isotherm approaches, especially when significant peaks and declines are demonstrated in lab measurements.

2.3 Non-Darcy Flow

In gas reservoirs, gases generally have very high velocity due to their low viscosity. This is especially true for near well-bore region. The traditional linear equation for flow in porous media based on Darcy's law is not sufficient for accurately describing high-rate flows. Non-Darcy flow occurs when inertial forces may no longer be neglected compared with viscous forces (Hagoort 2004). Flow-capacity can reduce by 5 % to 30 % in low-rate wells due to non-Darcy effects (Bybee 2006). To account for this nonlinear behavior, an inertial term called the Forchheimer term is added to Darcy's equation. Forchheimer (1901) gave the empirical Forchheimer equation to model gas flow more accurately at high flow rates (Mustapha et al. 2015; Li and Engler 2001; Belhaj et al. 2003; Jones 1987; Ling et al. 2013; Barree and Conway 2004; Zeng and Zhao 2008; Berawala et al. 2020).

Forchheimer's equation is defined by (Forchheimer, 1901):

$$\partial_x p = -u\left(\frac{\mu}{k} + \gamma\rho|u|\right), \tag{6}$$

where γ is Forchheimer's constant. When $\gamma = 0$ the formula reduces to Darcy's equation:

(7) $$\partial_x p = -u\frac{\mu}{k}$$

This coefficient γ is usually obtained from experimental data. However, there are several correlations available in the literature to evaluate the Forchheimer's constant. In this paper, we use the correlation given by Tek et al. (1962):

(8) $$\gamma = \frac{C_\beta}{k^{1.25}\phi^{0.75}},$$

where C_β is non-Darcy flow constant and k is the apparent permeability.

It is useful that:

(9) $$u|u| = s(u)u^2$$

where $s(\cdot)$ denotes the sign function with value ± 1. We further have that:

(10) $$\partial_x p = s(\partial_x p)|\partial_x p|, \qquad s(u) = -s(\partial_x p)$$

To get velocity in a form comparable with Darcy's law ($u = -\frac{k}{\mu}\partial_x p$) we write:

(11) $$u = -\frac{k}{\mu}\partial_x p \left(\frac{-1 + \sqrt{1 + 4\frac{k^2}{\mu^2}\gamma\rho|\partial_x p|}}{2\frac{k^2}{\mu^2}\gamma\rho|\partial_x p|} \right)$$

The latter term is in the form:

(12) $$f(z) = \frac{-1 + \sqrt{1 + 2z}}{z},$$

where

(13) $$z = \frac{k^2}{\mu^2}\gamma\rho|\partial_x p|,$$

which has a limit $f \to 1$ when $z \to 0$ and $f \to 0$ when $z \to \infty$. We name $f(z)$ the transition factor as it denotes the transition of flow from Darcy

to non-Darcy. In other words, the velocity is always less or equal to the velocity from Darcy's law. The value of $f(z) = 1$ would indicate Darcy flow and $f(z) < 1$ would mean non-Darcy flow.

2.4 Apparent Permeability

Due to the nano-pore structure of the shale matrix, Darcy's law with constant permeability cannot describe the actual gas behaviour and transport phenomena. Fluid flow departs from the continuum flow regime, in favour of other flow mechanisms such as slip flow, transition flow and free molecular conditions. The Knudsen number (Knudsen, 1909) which is a dimensionless parameter is used to differentiate between these flow regimes, for conduit with effective radius r_e, it is defined as:

$$K_n = \frac{\mu_g Z}{p_g r_e}\sqrt{\frac{\pi RT}{2M}}, \tag{14}$$

where T is absolute temperature, Z is gas compressibility factor, r_e is effective radius of flow path, R is the universal gas constant and M is gas molecular weight.

The apparent permeability of shale matrix can be represented by the following general form that relies only on Knudsen number K_n, and the effective intrinsic permeability $k_{\infty e}$ (Karniadakis et al., 2001):

$$k = k_{\infty e} f(K_n) \tag{15}$$

Florence et al. (2007) extended this derivation to characterize the non-Darcy gas flow in shale formations:

$$k = k_{\infty e}(1 + \alpha_K K_n)\left(1 + \frac{4K_n}{1 + K_n}\right) \tag{16}$$

where α_K is the rarefraction parameter:

$$\alpha_K = \frac{128}{15\pi^2}\tan^{-1}(4K_n^{0.4}) \tag{17}$$

Considering the effect of matrix compaction and adsorbed layer on the nanopore geometry, the effective intrinsic permeability is given as (Jiang and Yang, 2018):

$$k_{\infty e} = \frac{r_e^2}{8}\frac{\phi}{\tau} \tag{18}$$

where r_e is the effective radius of flow path and τ is the tortuosity of rock.

Huang and Ghassemi (2015) and Cao et al. (2016) gave generalized formulation that incorporates the overall contribution from effective stress, adsorption and flow regimes for the apparent gas permeability:

$$k = \frac{r_e^2}{8}\frac{\phi}{\tau}\,(1 + \alpha_K K_n)\left(1 + \frac{4K_n}{1 + K_n}\right) \tag{19}$$

Chapter 3 - Modelling Approach

This chapter presents the mathematical modelling approach used in this study to investigate and understand role of various complex flow mechanisms and their effects on shale gas production. For modelling purposes, we use the definitions presented in Chapter 2 - .

3.1 Part one- Numerical Modelling of Shale Gas Production

As an analysis tool, we consider a 1D+1D combined fracture/matrix model that allows systematic evaluation of the role and magnitude of the different mechanisms. Similar to the works by Mainguy and Ulm (2001) and Andersen et al. (2014, 2015) the model consists of a high-permeable fracture (length L_y) with width $2b$. This depicts a typical hydraulic fracture in a real-field scenario. The fracture can have non-uniform width and is symmetrically surrounded by shale matrix of fixed length L_x and low permeability as shown in **Figure 3**. We implicitly assume equally spaced perforation intervals by assuming fixed matrix length. The gas is stored densely in the matrix by adsorption (modeled by a Langmuir isotherm), in addition to free gas in the pores. Apparent permeability is used (only in system 2) to account for gas slippage effects, effective stress, adsorption and flow regimes relevant due to the nano-pore structure of the shale matrix. The pressure gradient towards the fracture and the well causes free gas from the matrix nanopores to flow. With pressure depletion, gas adsorbed onto the kerogen material desorbs into the pore space where it can flow as free gas to the fracture. A transfer term takes care of the communication between the fracture and the matrix. The system consists of a pressure-diffusion equation for the fracture which is coupled with a pressure-diffusion equation in the matrix. The model is scaled to derive dimensionless numbers that characterize the model.

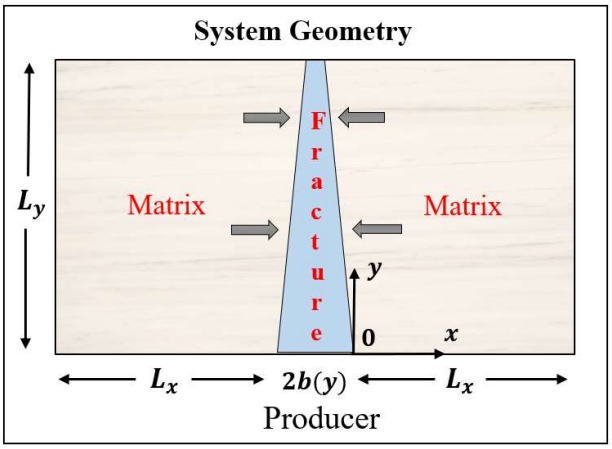

Figure 3 System geometry (left): the near well reservoir is seen from above where a fracture with variable width extends from a well perforation with length L_y. Shale matrix surrounds the fracture on both sides with total length $2L_x$ (typical perforation interval).

Assume a fracture that goes perpendicularly from the well. Define the positive y-axis along the fracture pointing away from the well perforation, where $y = 0$. The fracture has length L_y and varying width $2b(y)$. The fracture recovers gas from the matrix in the direction perpendicular to the fracture (x-direction). We define $x = 0$ at the right-hand side fracture-matrix interface. The fracture and matrix domains are given by:

$$\Omega^f = \{(x,y): -2b(y) < x < 0;\ 0 < y < L_y\},$$
$$\Omega^m = \{(x,y): -2b(y) - L_x < x < -2b(y);\ 0 < x < L_x;\ 0 < y < L_y\} \quad (20)$$

Assuming that the given system is repetitive (equally spaced fractures) we obtain a natural no-flow boundary at $x = L_x$ (the matrix half-(symmetry) length). Due to symmetry around the fracture, we will end up with and solve equations for only one side of the system, but account for production from both sides.

3.1.1 List of Assumptions

We seek a simplified model that can represent important aspects of shale gas production. The main assumptions on the fracture and matrix domains are:

1. A single fracture drains gas from surrounding shale matrix.
2. Gas is produced from the fracture to the well at constant well pressure.
3. Variable fracture width is considered.
4. Rock properties (porosity, permeability) are homogeneous within matrix and fracture.
5. Single-phase flow of gas is considered, i.e., it is assumed that the reservoir is a dry gas or that it contains insignificant amount of water.
6. Desorption of gas is pressure dependent which is defined by Langmuir's isotherm.
7. The composition and flow properties of free gas and desorbed gas are the same.
8. The gas is ideal and has constant viscosity.
9. The model is considered to be horizontal with constant height h.

3.1.2 Transport Equation

Consider a domain Ω with volume V containing shale gas in free and adsorbed form. The mass of gas in the porous media volume changes due to flow in and out of the interface $\partial\Omega$ with area A as expressed by the mass balance equation (LeVeque 2002):

$$\partial_t \int_{\Omega} \left(\phi\rho_g + (1-\phi)a_g\right) dV = -\int_{\partial\Omega} \left(\rho_g \boldsymbol{u}\right) \cdot \boldsymbol{n}\, dA, \tag{21}$$

where ϕ is porosity, $\rho_g(p_g)$ gas density, a_g adsorbed gas (mass per solid volume), $\boldsymbol{u}$ Darcy mass flux vector, $\boldsymbol{n}$ is the unit normal vector pointing out of Ω, and p_g is the gas pressure.

Fracture domain

In the fracture, gas adsorption is negligible, i.e., $a_g^f = 0$. The fracture width, denoted $2b(y)$, can vary with distance from the well. Considering a volume $dV = 2b(y)\ h\ dy \to 0$ we get from (21):

$$\partial_t(\phi\rho_g 2b) = \partial_y(\rho_g u 2b) + (\rho_g u)_{x=-2b,y} - (\rho_g u)_{x=0,y}. \tag{22}$$

Since the fracture is surrounded by matrix symmetrically, the two source terms contribute identically:

$$(\rho_g u)_{x=-2b,y} = -(\rho_g u)_{x=0,y}, \tag{23}$$

and we obtain:

$$\partial_t(\phi\rho_g b) = -\partial_y(\rho_g u b) - (\rho_g u)_{x=0,y}. \tag{24}$$

Matrix domain

In the matrix, it is assumed that all flow is directed in the x-direction (towards the fracture), while flow in the *y*-direction is ignored. Considering a volume $dV = dx\ h\ dy \to 0$ we get from (21):

$$\partial_t(\phi\rho_g + (1-\phi)a_g) = -\partial_x(\rho_g u). \tag{25}$$

Equation (24) and (25) represent the transport equations for the flow of gas in fracture and matrix domain respectively. These equations are further expanded and solved in the following sections depending on the flow mechanisms considered.

3.1.3 *System 1- Darcy flow*

The flux vector $\boldsymbol{u}$ is here assumed related to pressure through Darcy's law:

$$\boldsymbol{u} = -\frac{K}{\mu_g}\nabla p_g. \tag{26}$$

In addition to assumptions listed in section 3.1.1, we also assume only continuum flow regime i.e., $K_n < 0.001$ and mean free path of gas

molecules is much smaller than pore size of the shale matrix. The flow is then governed by conventional Darcy's equation. Also, the permeability and porosity are assumed to remain constant during the production.

Substituting (2)-(4)-(26) into (24) and (25), we summarize the system for the flow of gas in the fracture-matrix system:

$$\phi^f b(y)\partial_t p_g = \frac{K^f}{\mu_g}\partial_y\left(p_g b(y)\partial_y p_g\right) + \frac{K^m}{\mu_g}\left(p_g\partial_x p_g\right)_{x=0,y}, \qquad (x, y \in \Omega^f), \tag{27}$$

$$\phi^m\partial_t\left(p_g + \hat{a}_g\right) = \frac{K^m}{\mu_g}\partial_x\left(p_g\partial_x p_g\right), \qquad (x, y \in \Omega^m). \tag{28}$$

$$\hat{a}_g = \hat{a}_{max}\frac{p_g}{p_g + p_L} \tag{29}$$

These flow equations must be solved together with the initial and boundary conditions.

<u>Scaling and Reduced 1D+1D Model</u>

We now scale the system by introducing the following dimensionless variables:

$$p' = \frac{p_{well} - p_g}{\Delta p}, \qquad y' = \frac{y}{L_y}, \qquad x' = \frac{x}{L_x}, \qquad b' = \frac{b}{b_0}, \qquad D'(p') = \frac{p_g(p')}{p_{avr}}, \qquad \hat{a}_g' = \frac{\hat{a}_g}{\Delta p}, \tag{30}$$

where we have defined the pressure change and average pressure during the process as:

$$\Delta p = p_{well} - p_{init} < 0, \qquad p_{avr} = \frac{1}{2}(p_{well} + p_{init}). \tag{31}$$

$2b_0$ is the average width of the fracture, i.e. $2b_0 = \frac{1}{L_y}\int_{y=0}^{L_y} 2b(y)dy$. D' represents the part of the gas diffusion coefficient resulting from the absolute pressure and is thus scaled by the average pressure. The scaled

coordinates obey $0 \leq x', y' \leq 1$. The scaled pressure p' takes an initial value of 1 and decreases to 0 (corresponding to the well pressure in absolute terms). Applying the above to equations (27) and (28), we can naturally define two-time scales:

- τ^f representing diffusion of gas from the fracture to the well,
- τ^m representing diffusion of free and adsorbed gas from the matrix to the fracture, given as follows:

$$\tau^f = \frac{\mu_g \phi^f L_y^2}{K^f p_{avr}}, \quad \tau^m = \frac{\mu_g \phi^m R_p L_x^2}{K^m p_{avr}}, \qquad R_p = 1 + \frac{\hat{a}_g(p_{init}) - \hat{a}_g(p_{well})}{p_{init} - p_{well}}. \tag{32}$$

Note that we have introduced $R_p \geq 1$ which denotes both a retardation factor in terms of the increased time it takes to produce gas from the matrix due to adsorption, but also the increased quantity of gas that is released from adsorption during the pressure reduction. If $R_p \approx 1$, negligible amounts of adsorbed gas are released compared to production of free gas, while $R_p > 1$ means production of adsorbed gas is significant. In the following we scale time with respect to the fracture diffusion time scale:

$$t' = \frac{t}{\tau^f}. \tag{33}$$

After scaling, the coupled transport system (27) and (28) can be expressed in the following form:

$$b' \partial_{t'} p' = \partial_{y'}\left(D' b' \partial_{y'} p'\right) + \alpha\beta (D' \partial_{x'} p')_{x'=0,y'}, \quad (x', y' \in \Omega^f), \tag{34}$$

$$\partial_{t'}\left(p' + \hat{a}_g'\right) = \alpha \partial_{x'}(D' \partial_{x'} p'), \qquad (x', y' \in \Omega^m) \tag{35}$$

We have collected all constant terms into the two following dimensionless numbers:

$$\alpha = \frac{\tau^f}{\tau^m} = \frac{\phi^f L_y^2 K^m}{\phi^m L_x^2 K^f R_p}, \qquad \beta = \frac{\phi^m L_x R_p}{\phi^f b_0}. \tag{36}$$

α represents the ratio of the time scales involved in gas diffusion from the fracture and gas diffusion from the matrix (including desorption),

respectively. β denotes the capacity ratio of the matrix relative to the fracture and consists of the product of pore volume ratio and the increased amount of gas produced from the matrix due to adsorption, indicated by R_p.

3.1.4 *System 2- Non-Darcy flow*

In this section, we extend the model (24)-(25) to account for non-Darcy flow. We also incorporate apparent permeability relations in the model. Substituting (6)-(19) in (24)-(25), we can summarize the system for the flow of gas in fracture-matrix system as:

$$\phi^f b(y)\partial_t(p) = -\partial_y\big(pub(y)\big) - (pu)_{x=0,y}, \quad \big(x, y \in \Omega^f\big) \tag{37}$$

$$\phi^m \partial_t\big(p + \hat{a}_g(p)\big) = -\partial_x(pu), \quad \big(x, y \in \Omega^m\big) \tag{38}$$

$$u = -\frac{k}{\mu_g} f\, \partial_x P \tag{39}$$

Scaling and Reduced 1D+1D Model

After scaling, the coupled transport system (37)-(38) can be expressed in the following form:

$$\begin{aligned} B\partial_t P &= \partial_y\big(DBK^f F^f \partial_y P\big) \\ &\quad + \alpha\beta(DK^m F^m \partial_X P)_{x=0,y}, \quad \big(x, y \in \Omega^f\big) \\ \frac{1}{(G')_{ref}}\partial_T\big(P + \hat{A}_g(P)\big) &\\ &= \alpha\beta\partial_X(DK^m F^m \partial_X P), \qquad \big(x, y \in \Omega^m\big) \end{aligned} \tag{40}$$

All the constant terms are collected into the two following dimensionless variables α and β:

$$\begin{aligned} \alpha = \frac{\tau^f}{\tau^m} &= \frac{\phi^f L_y^2}{f_{ref}^f k_{ref}^f}\frac{f_{ref}^m k_{ref}^m}{(G')_{ref} L_x^2 \phi^m}, \\ \beta &= \frac{(G')_{ref} L_x^2 \phi^m}{\phi^f b_0}, \end{aligned} \tag{41}$$

$$\alpha\beta = \frac{f_{ref}^{m} k_{ref}^{m} L_y^2}{f_{ref}^{f} k_{ref}^{f} L_x b_0}.$$

where α and β consists of the additional amount of gas produced from the matrix due to adsorption, indicated by $(G')_{ref}$. The apparent permeability is scaled using a reference permeability defined as:

$$k_{ref}^{i} = \frac{2}{\left(\frac{1}{k^i(p_{init})} + \frac{1}{k^i(p_{well})}\right)}, \qquad (i = m, f). \tag{42}$$

Accordingly, we scale the transition factor $f(z)$ using the k_{ref} and Δp:

$$f_{ref}^{i} = \frac{-1 + \sqrt{1 + 2z_{ref}^{i}}}{z_{ref}^{i}}, \tag{43}$$

$$z_{ref}^{i} = 2\frac{\left(k_{ref}^{i}\right)^2}{\mu^2 L_i}\gamma_{ref}^{i}\rho_{gs}b_g' p_{avr}|\Delta p|, \qquad (i = m, f)$$

Where

$$\gamma_{ref}^{i} = \frac{C_\beta}{\left(k_{ref}^{i}\right)^{1.25}\phi_i^{0.75}}, \qquad (i = m, f) \tag{44}$$

Comparing to Darcy flow model (section 3.1.3), the updated model represented by (37)-(38) now consists of non-Darcy flow velocity u represented in a form comparable to Darcy flow through a transition factor f. It also accounts for permeability variation in the matrix due to gas slippage effects, adsorption and effective stresses. The scaling of model also leads to new definitions of dimensionless variables. However, it is important to note that diffusion time scale of matrix τ_m comprises of reference transition factor f_{ref}^{m} whose value changes with matrix non-Darcy flow constant from case to case.

3.1.5 *Initial and boundary conditions*

Transport equations presented in 3.1.3 and 3.1.4 are solved using following initial and boundary conditions.

At initial conditions ($t = 0$) the fracture and matrix have the same pressure, P_{init}. The adsorbed gas in the matrix is in equilibrium with this initial pressure:

(45) $$P_g(t = 0) = P_{init} \qquad \hat{a}_g(t = 0) = \hat{a}_{max}\left(\frac{P_{init}}{P_{init}+P_L}\right)$$

The perforation is defined at $y = 0$ and has a known pressure, P_{well}:

(46) $$P_g^f(y = 0) = P_{well} \qquad (x \in \Omega^f)$$

There is pressure and mass flux continuity across the fracture-matrix boundary:

(47) $$P_g\big|_{x=0^-} = P_g\big|_{x=0^+} \qquad (\rho_g u)_{x=0^-} = (\rho_g u)_{x=0^+}$$

The fracture is closed (or has negligible production) from the matrix in the y-direction. Similarly, the matrix has no flow at its outer boundary, due to symmetry:

(48) $$\delta_y P_g\big|_{y=L_y} = 0 \qquad \delta_x P_g\big|_{y=L_x} = 0$$

3.2 Part two- Modelling of CO_2 injection for enhanced shale gas recovery

In this work, we derive a multi-component adsorption isotherm with application to CH_4-CO_2 substitution. The basics for the derivation, as stated in Chapter 1 - are the principle that different molecules can occupy a surface, but not necessarily take the same space. Area, rather than moles, is therefore treated as the conserved capacity of the surface. The production scenario we consider is a 1D shale core or matrix system intitally saturated with free and adsorbed CH_4 gas with only left side (well) boundary open. During primary depletion, gas is produced from the shale to the well by advection and desorption. This process tends to give low recovery and is entirely dependent on the well pressure. Stopping production and then injecting CO_2 into the shale leads to increase in pressure where CO_2 gets preferentially adsorbed over CH_4.

The injected CO_2 displaces, but also mixes with the in situ CH_4. Restarting production from the well then allows CH_4 gas to be produced in the gas mixture. Diffusion allows the CO_2 to travel further into the matrix while keeping CH_4 accessible to the well. Surface substitution further reduces the CO_2 content and increases the CH_4 content in the gas mixture that is produced to the well. A result of the isotherm and its application of Marcellus experimental data is that adsorption of CO_2 with resulting desorption of CH_4 will lead to a reduction in total pressure if the CO_2 content in the gas composition is increased. That is in itself an important drive mechanism since the pressure gradient driving fluid flow is maintained (pressure buildup is avoided). This is because CO_2 takes ~24 times less space per mol than CH_4.

3.2.1 *Geometry and variables*

Consider a 1D shale matrix system (e.g. a core sample) with length L, where all flow is taking place in the x-direction, see Figure 4. The left-hand side boundary $x = 0$ is considered open to mass flow, while the right-hand side boundary at $x = L$ is closed. We track the components methane CH_4 (m) and carbon dioxide CO_2 (c); both appearing in gaseous form with partial pressures P_m, P_c and in adsorbed form denoted a_m, a_c.

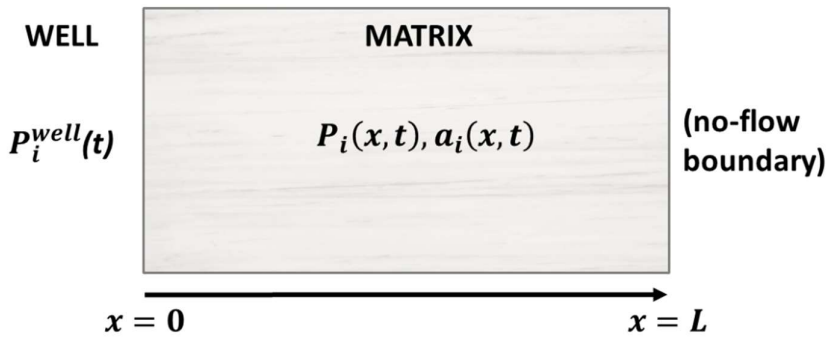

Figure 4 System geometry. A 1D system with an open boundary at $x = 0$ and a closed boundary at $x = L$. The model is studied in terms of gas partial pressures P_i and adsorbed content in the matrix a_i.

3.2.2 List of assumptions

1. Porosity and characteristic pore radius are homogeneous within matrix, i.e. compaction effects are not considered.
2. The shale matrix initially contains methane (CH_4) component only, in form of free and adsorbed gas phases.
3. Carbon dioxide (CO_2) is injected as a gaseous phase but can appear in both free and adsorbed gas phases in the matrix.
4. The composition of free and adsorbed gas phases is assumed to be the same.
5. Other phases (e.g. water or oil) are assumed not present.

3.2.3 Transport description

A general transport description of compressible compositional gas flow involving advection, diffusion and adsorption is given by (modified from Chen et al. (2006)):

$$\begin{aligned} &\partial_t\left(\phi\rho_g x_i + (1-\phi)a_i\right) \\ &\qquad = -\partial_x\left(\rho_g x_i u\right) + \partial_x\left(D_{i,e}\phi\partial_x C_i\right), \\ &\qquad (i = m, c), \\ &D_{i,e} = \frac{D_{i,f}}{\tau} \quad (i = m, c). \end{aligned} \tag{49}$$

where ϕ is rock porosity, ρ_g gas molar density (moles of gas phase per volume gas mixture), x_i mole fraction of component $i(= c, m)$, a_i is amount adsorped component i (in moles component per volume matrix rock) and C_i is the concentration of gas component i (in mol per volume gas mixture). $D_{i,e}$ is the effective molecular diffusion coefficient of gas components and depends on the free molecular diffusion coefficient $D_{i,f}$ and the tortuosity τ of the porous medium as follows (He et al. 2014). u is the Darcy flux of the gas phase which is assumed related to the total pressure (P_t) gradient through Darcy's law:

$$u = -\frac{K_a}{\mu_g}\nabla P_t, \qquad P_t = P_m + P_c. \tag{50}$$

K_a is the apparent permeability of gas in the matrix and μ_g the gas viscosity, which is set constant. The partial pressure P_i associated with N_i moles of component residing in the gas volume V_g (which can be shared with other components is described by the real gas law (Chen et al. 2006):

$$P_i V_g = zN_i RT, \qquad P_t V_g = zN_t RT. \tag{51}$$

The latter formula follows directly from the first and concerns the total pressure from the gas mixture. z denotes the deviation factor from ideal gas, R is the gas constant and T is absolute temperature. Molar gas phase density at reservoir and surface conditions (*sc*) follow directly as:

$$\rho_g = \frac{N_g}{V_g} = \frac{P_t}{zRT}, \qquad \rho_{g,sc} = \frac{N_g}{V_{g,sc}} = \frac{P_{sc}}{RT_{sc}}. \tag{52}$$

z is assumed constant at reservoir conditions and unity at standard conditions. From this we define the inverse gas volume factor b_g as the ratio of the volume taken by a gas mixture at standard conditions to the volume it takes at reservoir conditions:

$$b_g(P_t) = \frac{\rho_g}{\rho_{g,sc}} = P_t \frac{T_{sc}}{P_{sc} zT}, \qquad b_g'(P_t) = \frac{T_{sc}}{P_{sc} zT}, \tag{53}$$
$$\rho_g(P_t) = \rho_{g,sc} b_g' P_t.$$

In the above we have used that the derivative of b_g with respect to P_t is a constant (with unit of inverse pressure) to write a compact relation between gas density and total pressure. Mole fractions x_i and molar concentrations C_i of the gas components follow directly from the gas law (51):

$$x_i = \frac{N_i}{N_t} = \frac{P_i}{P_t}, \qquad C_i = \frac{N_i}{V_g} = \frac{P_i}{zRT}, \qquad (i = m, c). \tag{54}$$

3.2.4 *Proposed Adsorption Model*

Let A be the total surface area available for adsorption, A_f the area of free sites, A_m the area occupied by methane and A_c the area occupied

by CO_2, all per volume matrix rock (note that A is the specific surface area). Then we have:

$$A = A_f + A_m + A_c \tag{55}$$

The following reactions can describe the substitution of CH_4 by CO_2:

$$(\mathrm{CH_4})_{n_m}\mathrm{X} \leftrightarrow n_m\,\mathrm{CH_4}(g) + \mathrm{X} \tag{56}$$

$$(\mathrm{CO_2})_{n_c}\mathrm{X} \leftrightarrow n_c\,\mathrm{CO_2}(g) + \mathrm{X} \tag{57}$$

X denotes a site occupied by a mole of a given component during monolayer adsorption. n_m and n_c denote multipliers indicating if more than monolayer capacity is spent by the component. Hence, in monolayer adsorption we have $n_m = n_c = 1$ and. If multilayer adsorption takes place both n_m and n_c are greater than unity and more moles of component can fill that same space. Note also, that different components can take up a different area when they adsorb, hence if large molecules occupy the surface it will adsorb fewer moles (on fewer sites) before the surface is saturated. Equilibrium of the above reactions is described as follows:

$$K_m = \frac{[CH_4]^{n_m}[X]}{[(CH_4)_{n_m}X]} = \frac{P_m^{n_m}\,{A_f}/{A}}{{A_m}/{A}} = \frac{P_m^{n_m}(A - A_m - A_c)}{A_m}, \tag{58}$$

$$K_c = \frac{[CO_2]^{n_c}[X]}{[(CO_2)_{n_c}X]} = \frac{P_c^{n_c}\,{A_f}/{A}}{{A_c}/{A}} = \frac{P_c^{n_c}(A - A_m - A_c)}{A_c}. \tag{59}$$

In the above we have assumed that the activity of the gas components and surface species is approximated by their partial pressures and the area fraction they occupy, respectively. K_m and K_c are thermodynamical equilibrium constants with dimensions of Pa^{n_m} and Pa^{n_c}, respectively. They will be considered constant for a given temperature. Rearranging terms in (58) and (59), results in the area per volume rock A_i occupied by CH_4 or CO_2:

$$A_c = A\frac{K_m P_c^{n_c}}{K_c P_m^{n_m} + K_c K_m + K_m P_c^{n_c}}, \qquad A_m = A\frac{K_c P_m^{n_m}}{K_c P_m^{n_m} + K_c K_m + K_m P_c^{n_c}}. \tag{60}$$

For application of these parameters in the mole balance calculations, e.g. in (49), we make the following conversion:

$$a_i\left[\frac{mol}{vol\ dry\ rock}\right] = A_i\left[\frac{area}{vol\ dry\ rock}\right] S_{m,i}\left[\frac{mol\ monolayer}{area\ monolayer}\right] n_i\left[\frac{mol\ multilayer}{mol\ monolayer}\right] \tag{61}$$

We note that the above requires information about the factors $S_{m,i}$ telling how many moles adsorb per area during monolayer adsorption (implicitly how much area is taken by a site where a gas component has adsorbed). The three factors above indicate the capacity and relative preference among the components for adsorption. Particularly, the latter two factors indicate how densely a component can adsorb thus permitting a greater number of moles to be stored. Similarly, the adsorbed mass per volume W_i can be calculated as follows:

$$W_i\left[\frac{mass}{vol\ dry\ rock}\right] = a_i\left[\frac{mol}{vol\ dry\ rock}\right] M_{w,i}\left[\frac{mass}{mol}\right] \tag{62}$$

where $M_{w,i}$ is the (familiar) molar weight of CH_4 or CO_2.

3.2.5 *Application of the Isotherm*

The unknown parameters in the isotherm and adsorption terms (60) and (61) are $A, K_c, K_m, n_c, n_m, S_{m,m}$ and $S_{m,c}$. To determine their individual values, we proceed as follows:

- For a given sample the specific surface area A can be measured independently using the BET procedure (Brunauer et al. 1938).
- Consider an adsorption experiment where only CH_4 is present, i.e. $P_c = 0$. Then the methane isotherm (either of A_m, a_m and W_m) depends only on the unknowns K_m, n_m and $S_{m,m}$. The max level of adsorption is directly proportional to $S_{m,m}n_m$, while the parameters K_m and n_m affect

the pressure sensitivity in approaching that maximum.

- The same procedure can be performed with a CO_2 experiment without CH_4, i.e. $P_m = 0$. In this case the isotherm (either of A_c, a_c and W_c) depends only on the unknowns K_c, n_c and $S_{m,c}$ which can be determined in the same way.

It should be noted that the isotherms (60) take the same functional shape as the multicomponent Langmuir isotherm when $n_i = 1$. In that case K_i takes the role of the Langmuir pressure (the pressure where half the capacity is adsorbed). The comparison between two isotherms is described in detail in **Appendix B)**.

3.2.6 *Initial and Boundary Conditions*

Initially, at $t = 0$, the matrix contains free CH_4 gas with initial pressure P_{m0}:

$$P_m(t = 0) = P_{m0}, \qquad P_c(t = 0) = P_{c0} = 0. \tag{63}$$

The adsorbed gas is in equilibrium with this composition:

$$a_m(t = 0) = a_m(P_{m0}, P_{c0}), \qquad a_c(t = 0) = 0. \tag{64}$$

The open boundary at $x = 0$ operates with defined partial pressures as function of time. The flux between matrix and well is associated with advection only and not diffusion (which is only considered in the matrix):

$$P_m(x = 0, t) = P_{mb}(t), \qquad P_c(x = 0, t) = P_{cb}(t), \qquad \partial_x C_i|_{x=0} = 0. \tag{65}$$

The matrix has no flow at its outer boundary $x = L$:

$$\partial_x P_i|_{x=L} = 0, \qquad \partial_x C_i|_{x=L} = 0. \tag{66}$$

3.2.7 *Summary of the model*

After simplification we obtain the following transport equations:

$$\partial_t(P_i + \hat{a}_i) = \frac{1}{\phi\mu_g}\partial_x(P_i K_a \partial_x P_t) + \widehat{D}_i \partial_{xx} P_i, \quad (i = m, c), \tag{67}$$

where we have introduced the following notations to simplify the adsorption and diffusion terms.

$$\hat{a}_i = \frac{(1-\phi)}{\phi\rho_{g,sc}b'_g}\, a_i(P_m, P_c) = \frac{(1-\phi)}{\phi\rho_{g,sc}b'_g}\, S_{m,i} n_i A_i(P_m, P_c) = B_i A_i(P_m, P_c), \tag{68}$$

$$\widehat{D}_i = \frac{1}{\rho_{g,sc}b'_g}\,\frac{D_{i,f}}{\tau z R T}, \qquad B_i = \frac{(1-\phi)S_{m,i}n_i}{\phi\rho_{g,sc}b'_g}. \tag{69}$$

These flow equations must be solved together with the initial and boundary conditions (63) to (66).

3.3 Solution Approach

The system is solved by an operator splitting approach, similar to that described in Andersen et al. (2014, 2015). This means that for fracture-matrix system, we alternate between solving for flow in *y*-direction (fracture diffusion) and flow in *x*-direction (fracture-matrix diffusion and desorption). The operator splitting time step was selected at least 20 times lower than the time scale of fracture diffusion τ^f in order to switch sufficiently frequent between the two solvers. The numerical solution procedure is described in detail in **paper I, paper II** and **paper III**. The *y*-axis was discretized into 20 equal cells, while the (positive) *x*-axis was discretized into 40 equal cells in addition to the fracture cell. Gas recovery factor RF is reported as the produced fraction of the mass initially in the reservoir. We also define RF_{ob} as the mass fraction of the gas that *can* be produced by lowering the reservoir pressure uniformly from p_{init} to p_{well}.

For CO_2 injection system, we 1) solve for advective and diffusive transport of CO_2 and CH_4 without surface effects (adsorption/desorption)

and then 2) adjust the variables by distributing the local masses between free gas and adsorbed form. Switching between these processes is done frequently to assure the coupling between the mechanisms is captured. The x-axis was discretized into 30 equal cells for all the simulation cases.

Chapter 4 - Results and Discussions

Part one- Numerical Modelling of shale gas production

4.1 System 1- Darcy flow

In this section, we explore the behaviour of the model (34)-(36) by considering its sensitivity to different input parameters. Particularly we see how distributions of pressure and relative amount of adsorbed gas, reservoir pressure and gas recovery profiles are affected by matrix, fracture and gas parameters. Gas recovery factor RF is reported as the produced fraction of the mass initially in the reservoir. We also define RF_{ob} as the mass fraction of the gas that can be produced by lowering the reservoir pressure uniformly from p_{init} to p_{well}. We refer to **Appendix A)** for mathematical definitions.

4.1.1 *Model input parameters*

The model input parameters used for the reference case are described in **Table 2**. The Langmuir isotherm parameters are representative of Marcellus shale and taken from Yu et al. (2016). Unless otherwise is stated, any unvaried parameter is held constant equal to the reference case. Further, the fracture will in the reference case be assumed to have constant width. We will also consider cases where the fracture shape varies. We then consider that the fracture width decreases linearly in width with distance from the well and is defined by three parameters; the length L_y, the average half-width b_o and the max-to-min width ratio b_{max}/b_{min}:

$$b(y) = 2b_0\left(\frac{b_{max}/b_{min}}{(b_{max}/b_{min}+1)} - \frac{(b_{max}/b_{min}-1)}{(b_{max}/b_{min}+1)}\frac{y}{L_y}\right). \quad (70)$$

Note that for a uniform fracture width, i.e. $b_{max}/b_{min} = 1$, we get $b(y) = 2b_0$.

Table 2 Input parameters used for reference case simulations (1Yu et al. (2016)). The Knudsen number K_n is calculated using $K_n = \frac{\mu_g Z}{p_{init} r_e}\sqrt{\frac{\pi RT}{2M}}$ (Knudsen, 1909).

Parameters	Value	Units
Average fracture half-width, b_0	0.02	m
Bottom hole well pressure, p_{well}	17.24	Bar
Fracture length, L_y	7	m
Fracture permeability, K^f	10	mD
Fracture porosity, ϕ^f	0.60	–
Fracture height, h	1	m
Gas compressibility factor (ideal gas), Z	1	–
Gas constant, R	8.314	J/mol
Gas density at standard condition, ρ_{gs}	0.7	kg/Sm^3
Gas viscosity, μ_g	0.0184	cP
[1]Initial reservoir pressure, p_{init}	344.7	Bar
Knudsen number, K_n	0.00274	–
[1]Langmuir max adsorption capacity, a_{max}	5.023	kg/m^3
[1]Langmuir half capacity pressure, p_L	27.58	Bar
Matrix permeability, K^m	10	μD
Matrix half length, L_x	25	m
[1]Matrix porosity, ϕ^m	0.15	–
Mean pore radius, r_e	100	nm
Molar mass of methane, M	16.04	g/mol
Max-to-min fracture width ratio, $\frac{b_{max}}{b_{min}}$	1	-
[1]Reservoir temperature, T	323.15	K

4.1.2 *Reference Case Demonstration*

Using the reference case parameters listed in **Table 2,** we present distributions of scaled pressure $p'(x', y')$ and mass fraction of adsorbed gas relative to total mass $\frac{\hat{a}(p_g)}{\hat{a}(p_g)+p_g}$ at different stages of recovery, see **Figure 5**.

At production start the pressure declines quickly in the fracture, followed by pressure decline in the surrounding matrix. As pressure depletes, gas desorbs out of the kerogen into the pore space, which then flows to the fracture. At $RF_{ob} = 15\ \%$ (5.6 days) gas is mainly produced from the near fracture region where the pressure gradients are the sharpest. Gas flows comparably towards the fracture although the production is somewhat higher near the well. At later times, for $RF_{ob} = 50\ \%$ (40 days) and $RF_{ob} = 85\ \%$ (198 days), the same trends are observed. The production of free and adsorbed gas stops when the pressures have stabilized.

At $RF_{ob} = 15\ \%$ the fraction of adsorbed mass is still close to its initial value of 0.12 and is uniformly distributed along the *x*-axis, except near the fracture. The fraction is zero in the fracture as no adsorption is considered there. A key observation is that the adsorbed mass fraction increases towards the fracture region ($x \approx 0$) at a given time and increases with time. This can be explained mathematically below from the use of the Langmuir isotherm:

$$\frac{\hat{a}(p_g)}{\hat{a}(p_g) + p_g} = \frac{\hat{a}_{max}}{\hat{a}_{max} + p_L + p_g}. \tag{71}$$

This relation is also illustrated in **Figure 6** (right) for the reference case. Clearly, the fraction will increase when the pressure is reduced, explaining the trends towards the fracture and with time. At low pressures, i.e. if $p_g << \hat{a}_{max} + p_L$, the fraction is approximately constant. Looking at the isotherm in **Figure 6** (left) this behaviour follows due to that an increase of pressure will add free gas linearly due to ideal compressibility and adsorb linearly due to the linear shape of the isotherm at low pressure. When increasing pressure, the amount of free gas increases more rapidly than the amount of adsorbed gas. Therefore, the adsorbed fraction decreases.

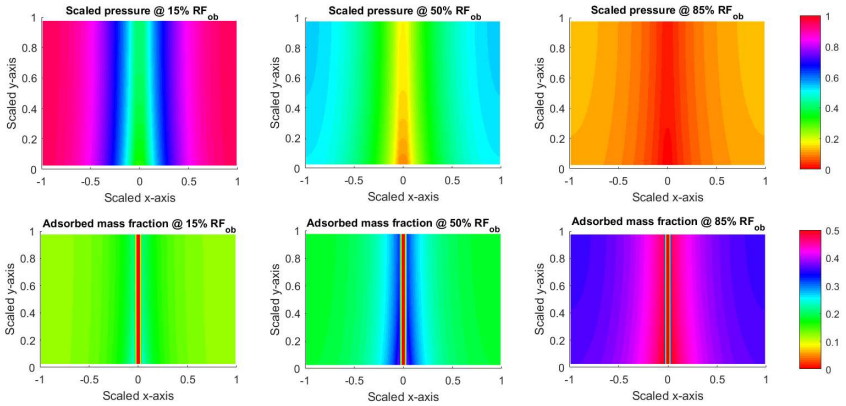

Figure 5 Distribution of scaled pressure (top) and adsorbed mass fraction (bottom) for the reference case after 15% (5.6 days) (left), 50% (40 days) (middle) and 85% (198 days) (right) obtainable recovery RF_{ob}.

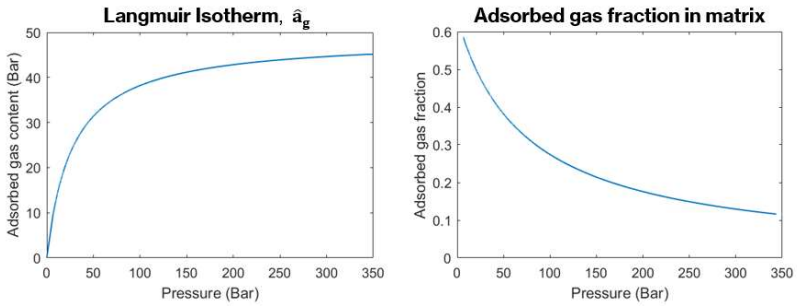

Figure 6 Langmuir isotherm $\hat{a}(p_g)$ (left) and adsorbed gas fraction $\frac{\hat{a}(p_g)}{\hat{a}(p_g)+p_g}$ (right) for the reference case.

4.1.3 *Numerical Solution Validation*

We assess the performance of the numerical model (developed on Matlab) by comparing results with the established industry software Eclipse (Geoquest, 2009). We consider a case with negligible amount of adsorbed gas in the matrix and a fracture with uniform width. The input parameters defined in **Table 2** are used for comparison. The full system (both sides of matrix surrounded by fracture) is modelled in Eclipse

using $80 \cdot 20 \cdot 1 = 1600$ number of blocks. **Figure 7** shows the average scaled pressure from each model with time. The numerical solution gives results in agreement with the Eclipse model.

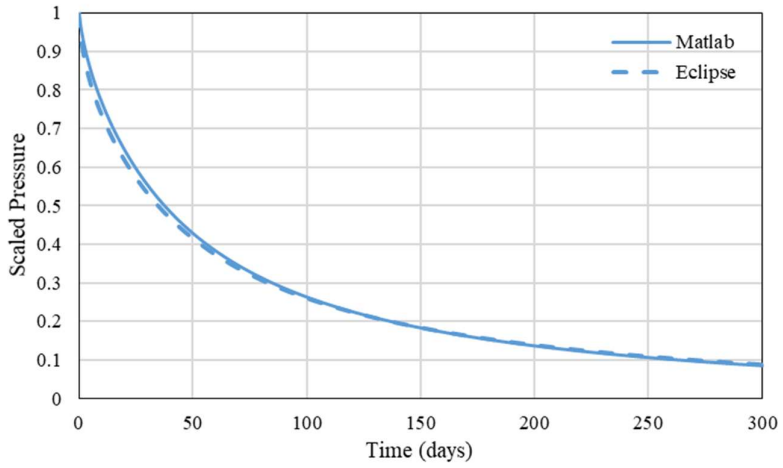

Figure 7 Comparison of scaled average pressure profile between the numerical model and Eclipse.

We further compare the block pressure profiles for four different blocks: fracture block closest to the well (40,20), near fracture matrix block (38,15), block at intermediate distance from fracture (30,10) and block far away from fracture (10,5). As shown in **Figure 8**, the numerical solution of this paper is consistent with Eclipse, therefore our model and its numerical solution is reliable and feasible. The difference in pressures initially may be due to the no flow in y-direction in the matrix is considered in our model which is not the case in Eclipse. It could also be due to discretization and convergence issues.

4.1.4 *Role of Fracture Properties and Shape*

We compare three cases with average fracture width (b_0) 0.05 m, 0.02 m (reference), and 0.009 m to evaluate the effect of fracture size. Further for each of these cases, we use three subcases with $\frac{b_{max}}{b_{min}}$ ratio of 1

(reference), 3 and 10 to evaluate the effect of fracture shape. The $\frac{b_{max}}{b_{min}}$ ratio of 1 indicates a uniform fracture width along the y-axis whereas a ratio of 10 indicates that the fracture is 10 times narrower at $y = L_y$ compared to at $y = 0$, as illustrated in **Figure 3**. **Figure 9** shows the simulated scaled average gas pressure p' (left) and gas recovery RF (right) up to 300 days for all the cases.

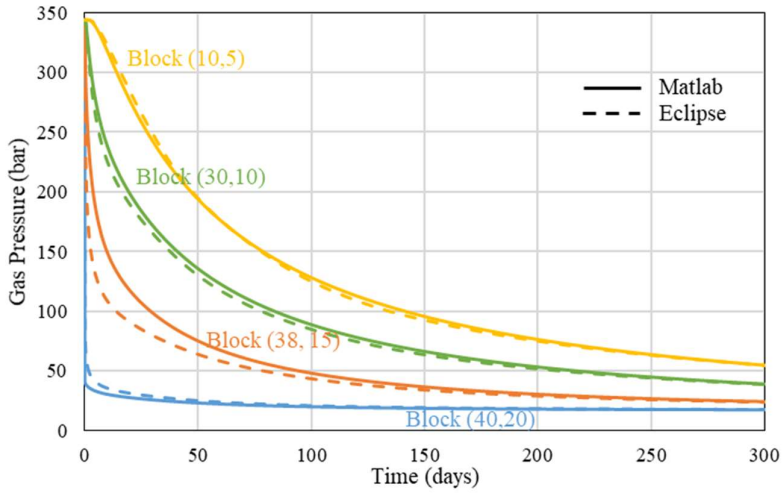

Figure 8 Block pressure comparison between the numerical model and Eclipse for blocks number (10,5), (30,10), (38,15) and (40,20)

As seen from **Figure 9**, the recovery process goes faster compared to the reference case $b_0 = 0.02$ m if the average fracture width is higher, given by $b_0 = 0.05$ m. Production takes longer time for $b_0 = 0.009$ m. This indicates that the size of the fracture affects recovery and production rate. Berawala et al. (2017) presented the effect of fracture width on time to reach the critical desorption pressure in the matrix. They found that with narrower fracture width it takes longer time to reach critical desorption pressure, resulting in significant drop in the production rate before getting stabilized by the desorbed gas. The slow pressure decline at narrow width is in agreement with our findings.

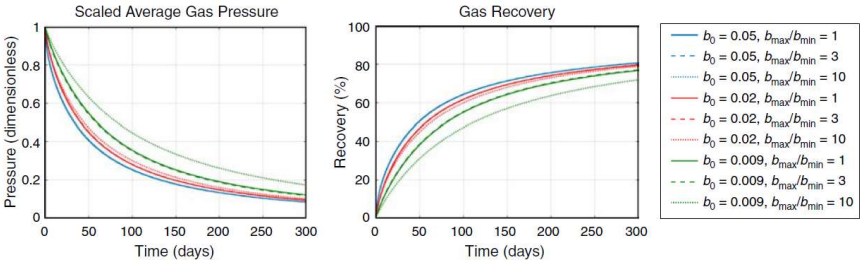

Figure 9 Effect of fracture shape $\frac{b_{max}}{b_{min}}$ and size b_0 on scaled average gas pressure p' and gas recovery RF.

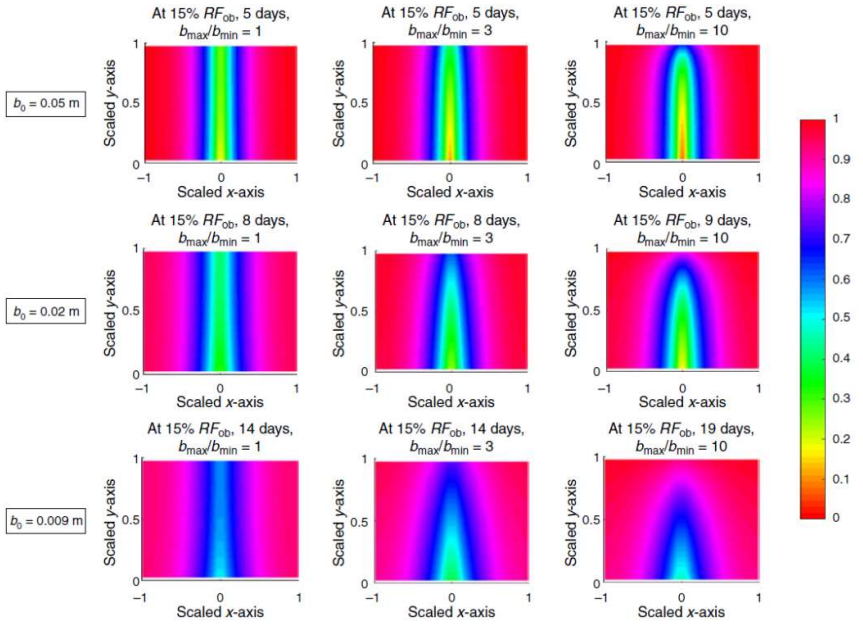

Figure 10 Scaled pressure distribution $p'(x', y')$ after $RF_{ob} = 15$ % for different fracture shape $\frac{b_{max}}{b_{min}} = 1, 3, 10$ and size $b_0 = 0.05, 0.02, 0.009$ m.

The role of fracture width also reflected in **Figure 10** where scaled gas pressure is plotted after $RF_{ob} = 15$ %. In the left column the three cases with uniform fracture width are shown. It takes longer time for the narrow fracture case ($b_0 = 0.009$ m, 14 d) to obtain the same recovery

as the wide fracture case ($b_0 = 0.05$ m, 5 d). The narrow fracture case displays a higher fracture pressure ($p' \approx 0.5$) compared to the case with widest fracture ($p' \approx 0.25$). Since the fracture gas has less space to diffuse, it maintains a higher pressure (right) reducing the driving force of gas production from the matrix.

When we look at recovery and pressure curves (**Figure 9**) for b_0 = 0.05 and 0.02 we note that they are very weakly sensitive to the $\frac{b_{max}}{b_{min}}$ ratio, i.e. very similar profiles are seen. This indicates that we have similar inflow of gas to the well irrespective of the shape of the fracture. However, for comparatively narrower fracture width b_0 = 0.009, we observe that production takes more time with increasing $\frac{b_{max}}{b_{min}}$ ratio. This implies that the shape of the fracture becomes more important at narrower fracture width.

To further understand the role of fracture shape we again turn to **Figure 10** where $\frac{b_{max}}{b_{min}}$ has been varied systematically with values 1, 3 and 10 for different fixed half widths $b_0 = 0.05, 0.02, 0.009$ m. For each fracture width we note that the more narrow the fracture is at the end (higher $\frac{b_{max}}{b_{min}}$), the less space does the gas have to diffuse towards the well resulting in a local pressure buildup. Since the fracture is assumed widest near the well a lower pressure is seen there, and more gas is produced from the matrix in the near well region compared to the regions at the far end of the fracture. In the widest fractures the difference is not significant and a close to uniform production is seen along the fracture.

In **Figure 11** we demonstrate the role of varying the fracture permeability K^f over several orders of magnitude, while also varying the fracture shape. At sufficiently high fracture permeability the pressure and recovery profiles are very similar and do not differ with permeability or shape (the time profiles of the 10 and 1000 mD cases are comparable). Going to low permeabilities does however result in delayed production

and also greater sensitivity to fracture shape. Interestingly, at low permeability, high fracture width ratio results in faster production compared to a uniform fracture. The wide fracture region near the well allows more efficient production of the matrix in this region. **Figure 12** shows scaled pressure distribution for fracture permeability 1 mD and 1000 mD with uniform fracture width ($\frac{b_{max}}{b_{min}} = 1$) after $RF_{ob} = 50\%$. We see that low fracture permeability (1 mD) gives lower matrix-to-fracture pressure gradient, restricting the flow from matrix, resulting in lower recovery rate compared to the case with much higher fracture permeability (1000 mD). After 50 % RF_{ob}, most of the remaining gas is located in matrix at the far end of the fracture for the 1 mD permeability case. The gas has been produced more equally for the case with 1000 mD permeability. In the former case, the slow production from matrix at the far end of the fracture will constrain the recovery rate. Fracture permeabilities can be associated with the fracture width or fracture porosity, see e.g. Carman (1937) or van Golf-Racht (1982). Such relations are not considered presently.

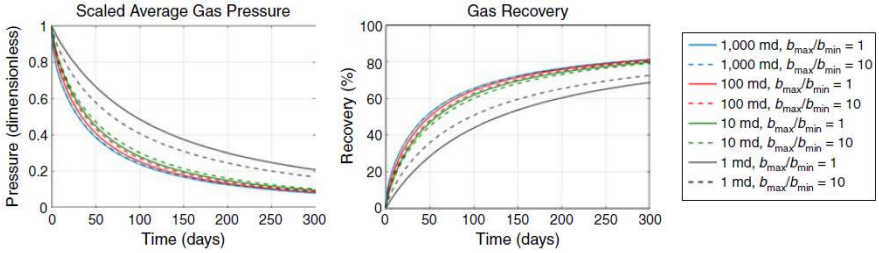

Figure 11 Effect of fracture permeability and shape on scaled average gas pressure (left) and gas recovery (right).

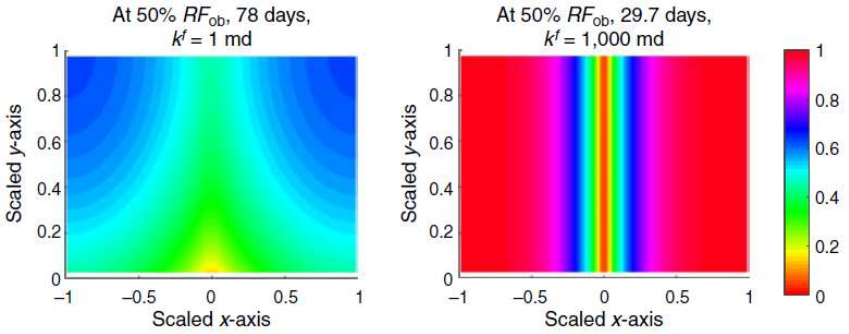

Figure 12 Scaled pressure distribution after $RF_{ob} = 50\%$ for fracture permeability 1 mD (left) and 1000 mD (right), both with $\frac{b_{max}}{b_{min}} = 1$.

4.1.5 *Role of Matrix Properties*

In the following we consider the role of the matrix permeability K^m and matrix dimension L_x (corresponding to half the fracture spacing). As seen in **Figure 13**, lowering the permeability or increasing L_x increases the time required to recover gas from the matrix. However, the recovery is more sensitive to L_x than K^m, as a shale with 100 times lower permeability can be produced in the same time by perforating 10 times as frequently. This is reflected directly in the time scale of gas diffusion from the matrix, see (32)-(33), to be discussed later.

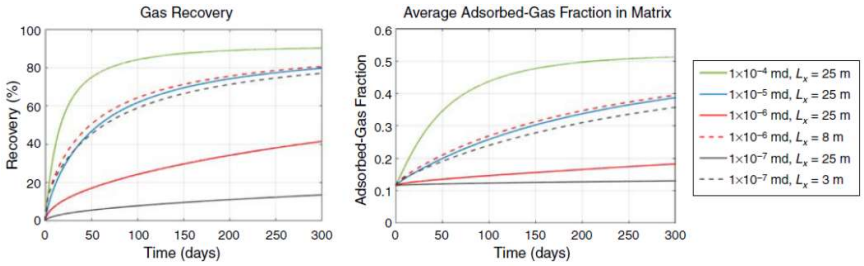

Figure 13 Effect of matrix permeability and perforation interval on recovery and adsorbed gas fraction.

4.1.6 *Interpretation of Results using Dimensionless Numbers*

In the above discussion we have demonstrated that matrix and fracture properties can affect the production of shale gas. In particular at low fracture permeability or narrow fracture width the system can depend more strongly on the fracture properties, including its shape. In the following we interpret this behavior by means of the scaled model (34) and (35).

Assume that the fracture has an initial scaled pressure $p' = 1$ diffusing towards 0. For a uniform fracture this process will require a time of approximately τ^f. Similarly, diffusing free and adsorbed gas out of the matrix from $p' = 1$ to 0 given that the open boundary (to the fracture) has 0 scaled pressure, will be reflected by the time scale τ^m. Since all the matrix gas has to flow through the fracture the process will require at least a time of $(\beta + 1)\tau^f$, where the factor $(\beta + 1)$ denotes that there is β times as much gas in the matrix as in the fracture in addition to the (1) fracture volume. If this time is significant compared to the time it takes for gas to diffuse out of the matrix, the process may be delayed. Noting that $\beta \gg 1$ we introduce the ratio ω of these times as:

$$\omega = \frac{(\beta + 1)\tau^f}{\tau^m} \approx \alpha\beta = \frac{L_y^2 K^m}{L_x b_0 K^f}. \tag{72}$$

If $\omega \ll 1$ the gas has negligible residence time in the fracture and is completely controlled by the time scale of diffusion from the matrix. For these cases we can expect a unique behavior when plotting recovery vs. time scaled against τ^m. For larger ω the residence time in the fracture is significant and further delays the process. From (72), we note that under the stated assumptions the only parameters affecting this process are the absolute permeabilities, the perforation interval, fracture (half) width and fracture length. However, properties such as Langmuir adsorption and compressibility can challenge this claim. The role of the scaling number and the mentioned nonlinear effects are explored in the following.

4.1.6.1 Systematic variations of α and β

In this section, we present a vast set of simulation cases of gas recovery and interpret the tests according to the dimensionless number $\omega = \alpha\beta$. Both linear and non-linear parameters are varied as explained in **Table 3** and reference parameters described in **Table 2** are used unless specified. The simulation cases are selected to give specific values of the product $\alpha\beta = 10^{-3}, 10^{-2}, 10^{-1}, 10^{0}$. For each of these $\alpha\beta$ values, we vary constant-in-time parameters appearing in these terms (absolute permeabilities K^m, K^f, the perforation interval $2L_x$, fracture width $2b_0$ and fracture length L_y) and parameters that vary spatially or during the recovery process and are represented by reference values in α and β, such as adsorption properties (represented by the retardation factor R_p), fracture shape (given by $\frac{b_{max}}{b_{min}}$) and compressibility (represented using the average pressure P_{avr}).

In particular, we compare with three scenarios: 1) Increased adsorption given by increasing $\hat{a}_{max}$, effectively accounted for by a high retardation factor, $R_p = 1.46, 1.81$ compared to the reference value $R_p = 1.081$; 2) High fracture width ratio, $\frac{b_{max}}{b_{min}} = 10$ compared to 1 (uniform width). This effect is not included in α or β; 3) Low pressure interval due to a high well pressure $P_{well} = 125, 250$ bar compared to the reference case $P_{well} = 17$ bar. The parameter p_{avr} will be affected. Further, a higher well pressure results in lower end recovery. All the given simulation cases (ca. 21 in total) are presented in terms of gas recovery vs time in **Figure 14** (inside figure). It is seen that the simulations span a wide range of time scale (hence the logarithmic time axis) and also three end recovery scenarios are considered ($\approx 25, 50$ and 90 %). The same simulations are also presented in terms of obtainable recovery RF_{ob} vs scaled time t/τ^m in **Figure 14** (main figure) from which we make the following observations:

- The different simulation cases group well according to the value of

$\alpha\beta$: simulations with same value are indicated by the same color. The main trend is that cases with lower value of the product $\alpha\beta$ give higher RF_{ob} when plotted against t/τ^m.

- Cases where only constant-in-time parameters appearing in α, β were varied (while others were kept constant to their reference values) are indicated by full lines. They gave a unique behavior with completely overlapping curves for the same $\alpha\beta$. Only at high $\alpha\beta = 1$ (blue lines) was there a noticeable difference. At sufficiently low $\alpha\beta$ all these curves overlapped also, e.g. $\alpha\beta = 10^{-3}$ (black lines) and 10^{-2} (red lines) corresponded to the same behavior, i.e. the highest recovery. This reflects that the residence time of the gas in the fracture is not significant compared to that in the matrix and the recovery only depends on matrix properties.
- Cases where the fracture shape was changed to give $\frac{b_{max}}{b_{min}} = 10$ are indicated by dotted lines. The adsorption and pressure interval parameters are kept the same, while constant parameters in α and β are varied. For the case $\alpha\beta = 0.1$ (green dotted line) the wider fracture near the well results in faster production in the early phase (compared to the cases with uniform width, and any combination of constant parameters). However, the correspondingly narrow width in the end of the fracture gives slower production at late times. Looking at low values of $\alpha\beta = 10^{-3}$ (black dotted line), using $\frac{b_{max}}{b_{min}} = 10$ shows identical behavior as the uniform width simulations, namely because the fracture residence time and thus the fracture properties do not affect the solution in this range.
- Finally, we consider the role of changing non-constant matrix parameters such as adsorption and compressibility. P_{well} was increased for four cases with $\alpha\beta = 10^{-3}, 10^{-2}, 10^{-1}, 1$. As before, we see that when the matrix properties are the same and P_{well} was the same, the behavior converges when $\alpha\beta$ is sufficiently low (10^{-3} and 10^{-2}), hence the two leftmost curves (black and red dashed lines) seen in **Figure 14** (main figure) are almost identical. The non-constant compressibility and variation from the reference does however induce a noticeable difference compared to the full line cases (where only constant parameters were varied). The green dashed line corresponding to $\alpha\beta = 10^{-1}$ is more similar to the

reference case behavior, which is reasonable as the fracture flow plays a greater role in that situation.

- In three cases, the retardation factor R_p was increased by variation of $\hat{a}_{max}$. These cases are represented by dash-dot lines for cases with $\alpha\beta = 10^{-3}, 10^{-1}$ and 1 (black, green and blue dash-dot lines respectively). For all three cases it is seen that the strong change in adsorbed content is not scaled as well as the other simulations and that a more optimal choice can be made for incorporating this parameter.

Table 3 Input parameters for simulation cases selected such that $\omega = \alpha\beta$ is constant for 4 values: $\omega_i = 10^{-3}, 10^{-2}, 10^{-1}$ and 10^{0}. $L_y = 10\ m$ and $L_x = 18.8\ m$ is used for all cases. Other unspecified parameters are given by reference case values in Table 2.

	$\alpha\beta$ (-)	α (-)	β (-)	K_m (mD)	$b0$ (m)	b_{max}/b_{min} (-)	R_p (-)	P_{well} (bar)
	1e-3	1e-6	1e3	1e-8	5e-3	1	1.08	17.2
	1e-3	1e-5	1e2	1e-7	5e-2	1	1.08	17.2
	1e-3	1.1e-5	0.95e2	1e-7	5e-2	1	1.08	125
	1e-3	1.12e-5	0.94e2	1e-7	5e-2	1	1.08	250
	1e-3	1e-5	1e2	1e-7	5e-2	10	1.08	17.2
	1e-3	7.7e-6	1.35e2	1e-7	5e-2	1	1.46	17.2
	1e-3	6.2e-6	1.68e2	1e-7	5e-2	1	1.81	17.2
	1e-2	1e-5	1e3	1e-7	5e-3	1	1.08	17.2
	1e-2	1e-4	1e2	1e-6	5e-2	1	1.08	17.2
	1e-2	1.1e-4	0.95e3	1e-6	5e-2	1	1.08	125
	1e-2	1.12e-4	0.94e2	1e-6	5e-2	1	1.08	250
	1e-1	1e-4	1e3	1e-6	5e-3	1	1.08	17.2
	1e-1	1e-3	1e2	1e-5	5e-2	1	1.08	17.2
	1e-1	1.12e-3	0.94e2	1e-5	5e-2	1	1.08	250
	1e-1	1e-3	1e2	1e-5	5e-2	10	1.08	17.2
	1e-1	6.2e-4	1.68e2	1e-5	5e-2	1	1.81	17.2
	1	1e-3	1e3	1e-5	5e-3	1	1.08	17.2
	1	1e-2	1e2	1e-4	5e-2	1	1.08	17.2
	1	1.12e-2	0.94e2	1e-4	5e-2	1	1.08	250
	1	7.7e-3	1.35e3	1e-4	5e-2	1	1.46	17.2
	1	6.2e-3	1e2	1e-4	5e-2	1	1.81	17.2

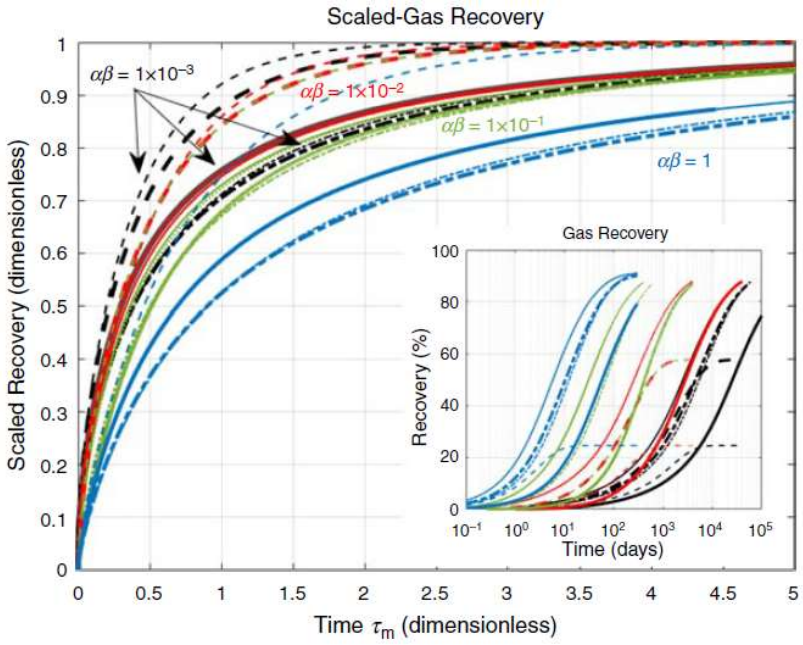

Figure 14 Scaled (main figure) gas recovery vs scaled time and absolute gas recovery vs time (inside the main figure). Comparative test where $\omega = \alpha\beta$ is constant for 4 values: $\omega_i = 10^{-3}, 10^{-2}, 10^{-1}$ and 10^{0}. Parameters α, β, R_p and b_{max}/b_{min} are varied in 21 tests as described in table 3. ω seems to characterize the flow regime of the fracture-matrix system. Unspecified parameters are given by reference case values in Table 2.

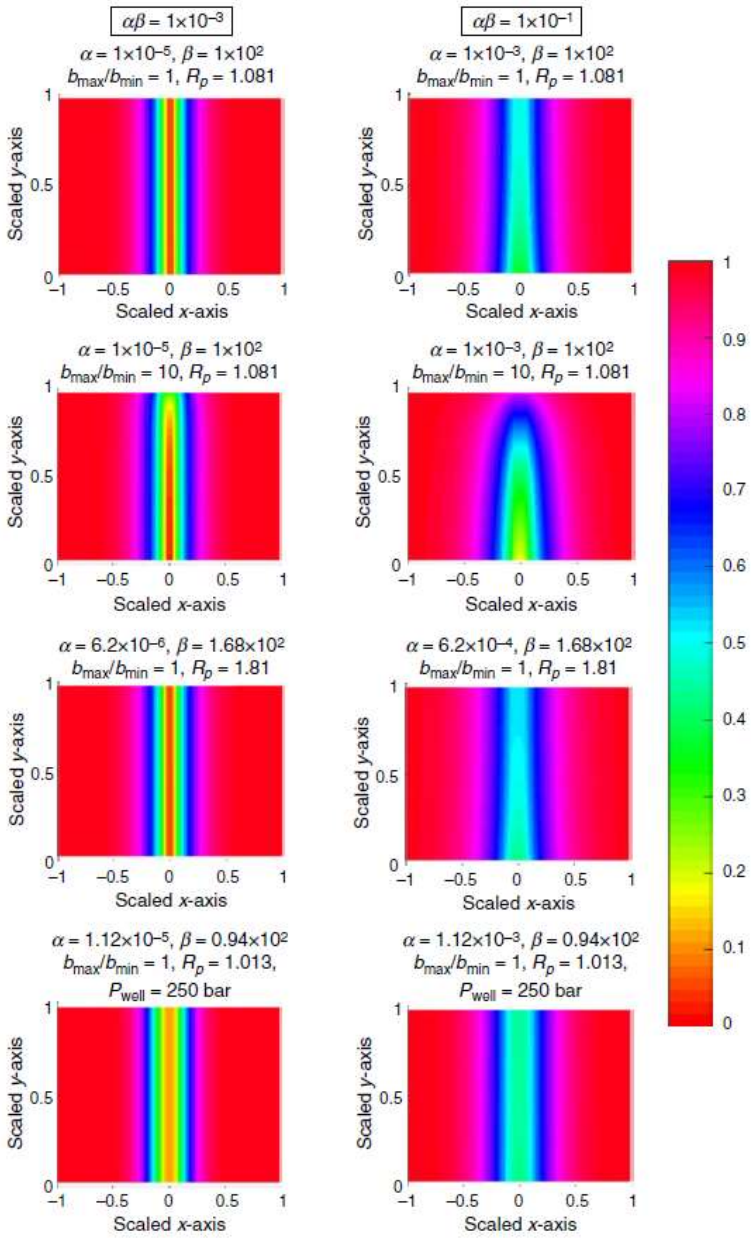

Figure 15 Scaled pressure distribution after $RF_{ob} = 15$ % for $\alpha\beta = 10^{-3}$ (left) and 10^{-1} (right). Unspecified parameters are given by the reference case.

4.1.6.2 Identification of flow regimes

From the previous identification of $\alpha\beta$ as an indicator of whether fracture flow was significant, we plot in **Figure 15** distributions of scaled pressure after $RF_{ob} = 15\,\%$ for two values $\alpha\beta = 10^{-3}, 10^{-1}$ while varying parameters such as width ratio, retardation factor and well pressure. It is seen that the distributions bear strong similarity if they have same value of $\alpha\beta$. In particular, if $\alpha\beta = 10^{-3}$ (a low value) then we are in a *matrix-controlled regime* where the gas entering the fracture is instantly produced to the well. We thus see a zero-scaled pressure in the fracture for these cases and uniform pressure distribution surrounding the fracture. In the case with $\alpha\beta = 10^{-1}$ (a high value), the gas requires some time to leave the fracture and a significant pressure and pressure gradient is observed in the fracture. The high pressure reduces the production rate from the matrix and the pressure gradient leads to more non-uniform production from the matrix. Since the time required to transport through the fracture controls the process, we can call this a *fracture-controlled regime* where the gas has a significant residence time.

4.2 System 2- Non-Darcy flow

In this section, we study the behavior of the model (40)-(41) by considering Marcellus shale Langmuir isotherm parameters defined in **Table 4**. We also perform sensitivity analysis to various input parameters to identify the conditions under which the non-Darcy effect becomes significant. In particular, we plot overall gas recovery vs time and show distributions of scaled pressure, transition factor and the relative amount of total mass in the system at 15% production of the mass initially in the reservoir, denoted by RF_{ob}.

Mean pore radius of shale matrix is usually in the range of 1-100 nm (Javadpour et al. 2007, Loucks et al. 2009, Zou et al. 2012, Yao et al. 2013), we use a representative value 14 nm for simulation. Using the

input parameters defined in **Table 4**, we get Knudsen number (K_n) in the range of 0.01 to 0.1 which indicates slip-flow or transition flow regime (refer **Table 1**). This implies the mean-free path of gas molecule is less or of the same magnitude as pore size of the matrix. In this regime, the gas transport is mainly governed by Knudsen diffusion and the conventional Darcy's law equation with no-slip boundary conditions cannot be applied. The permeability described by (19) takes into account this slippage effect. The corresponding apparent permeability for the reference case parameters is shown in **Figure 16(b)**.

Table 4 Input parameters used for reference case simulations.

Parameters	Value	Units
Average fracture half-width, b_0**	0.02	m
Bottom hole well pressure, p_{well}*	17.24	Bar
Fracture length, L_y**	7	m
Fracture permeability, k^f**	10	mD
Fracture porosity, ϕ^f**	0.60	–
Fracture height, h**	1	m
Gas compressibility factor (ideal gas), Z	1	–
Gas constant, R	8.314	J/mol
Gas density at standard condition, ρ_{gs}**	0.7	kg/Sm^3
Gas viscosity, μ_g**	0.0184	cP
Initial reservoir pressure, p_{init}*	344.7	Bar
Langmuir max adsorption capacity, a_{max}*	5.023	kg/m^3
Langmuir half capacity pressure, p_L*	27.58	Bar
Matrix half length, L_x	15	m
Matrix porosity, ϕ^m**	0.15	–
Mean pore radius, r_e	14	nm
Molar mass of methane, M	16.04	g/mol
Max-to-min fracture width ratio, $\frac{b_{max}}{b_{min}}$	1	-
Reservoir temperature, T*	323.15	K
Non-Darcy flow constant, C_β	$1e-6$	m$^{-2.5}$

*Yu et al. (2016), ** Berawala et al. (2019)

Eq. (12) described in section 2.3 denotes the transition factor f which is a function of non-Darcy flow velocity z. The transition factor will always be less or equal to 1. $f(z) = 1$ indicates Darcy flow and a value less than 1 would indicate how significant the non-Darcy effect is. We plot the transition factor f against z as shown in **Figure 17**. We see that the gas

transport is governed by non-Darcy effects when $z > 10^{-1}$. To establish the conditions under which this can happen, we perform sensitivity analyses (**4.2.1 - 4.2.5**) on various input parameters such as non-Darcy flow constant (C_β), pore size (r_m), fracture permeability (k^f), and shape (b_0) and size. Further, we also compare how each of these parameters affect gas recovery with/without non-Darcy flow in the matrix and fracture.

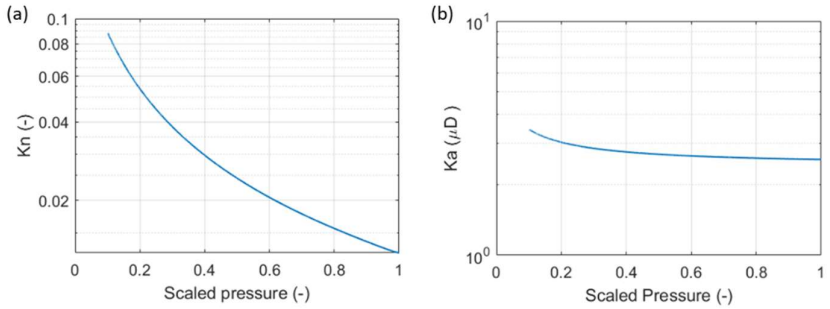

Figure 16 Knudsen number (a) and apparent permeability (b) vs scaled pressure for reference case input parameters defined in Table 4.

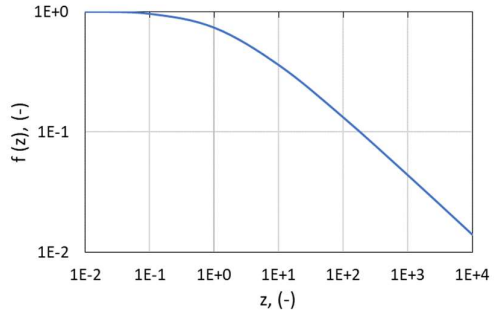

Figure 17 Transition factor $f(z)$ vs z indicating Darcy to non-Darcy flow transiton.

4.2.1 *Reference case demonstrations*

Using the reference case parameters listed in **Table 4**, we present scaled average gas pressure and recovery profiles against time for four

systematically varied non-Darcy flow constants C_β, see **Figure 18**. The same values are applied to fracture and matrix. The $C_\beta = 0$ case indicates that Darcy flow is considered both in matrix and fracture. As seen from **Figure 18**, the recovery process goes much faster for Darcy flow $C_\beta = 0$ compared to the non-Darcy cases $C_\beta = 1e-6, 3e-6$ and $9e-6$ m$^{-2.5}$. This indicates that with increasing the magnitude of non-Darcy flow constant, the gas is produced at a much slower rate. To report how significant the non-Darcy effect for individual cases is, we report the reference transition factor f_{ref} values for both fracture and matrix, denoted by f_{ref}^f and f_{ref}^m in **Table 5**. The reference values are calculated using the pressure gradient between initial reservoir and well pressure divided over the entire length of the matrix (refer to Eq. (43)). For $C_\beta = 1e-6$ m$^{-2.5}$, we get $f_{ref}^f = 0.11$ and $f_{ref}^m = 0.87$, which indicates that the flow is reduced by 89% and 13% compared to Darcy flow for the same pressure gradient in fracture and matrix respectively. Also, from (11), we see that for the same pressure gradient, non-Darcy flow will give lower velocities than Darcy. In general, both Darcy and non-Darcy Forchheimer models predict the same behavior at low velocity. But at high velocities like in fracture, non-Darcy models results in reduced velocities limiting the overall gas recovery.

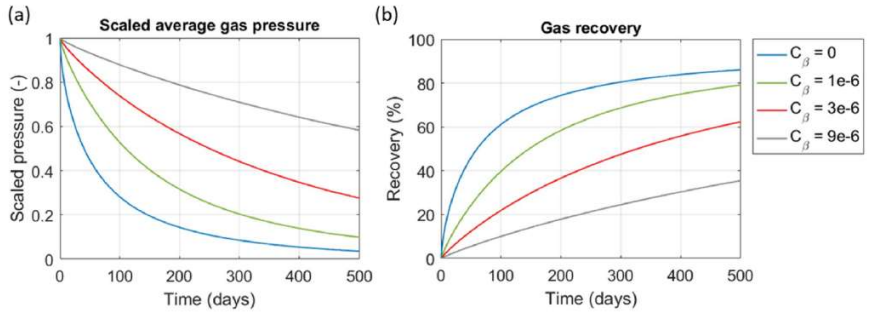

Figure 18 Scaled average pressure (a) and gas recovery (b) profiles for four systematically varied non-Darcy flow constant, C_β.

Table 5 Reference transition factor values of fracture and matrix for systematically varied four non-Darcy flow constants.

C_β ($\mathrm{m}^{-2.5}$)	f_{ref}^{f} (-)	f_{ref}^{m} (-)
0	1	1
$1e-6$	0.11	0.87
$3e-6$	0.07	0.73
$9e-6$	0.04	0.54

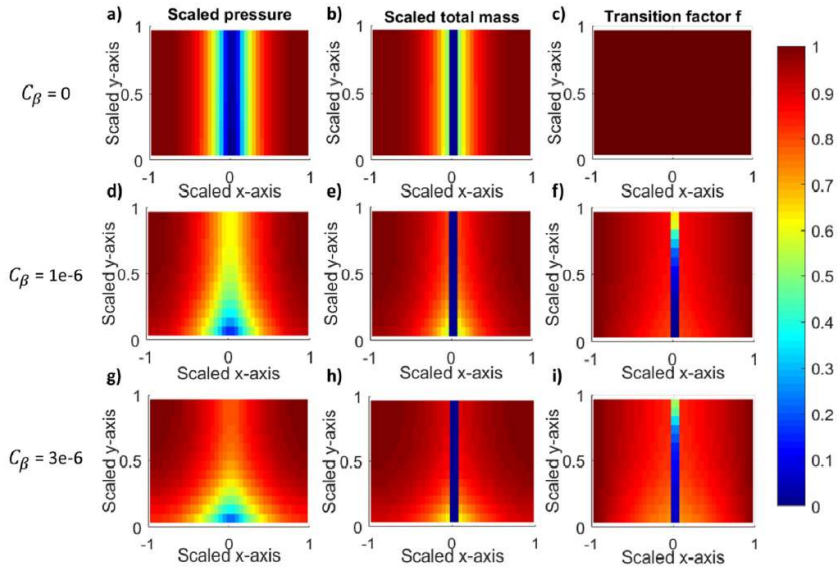

Figure 19 Scaled pressure, scaled total mass and transition factor distribution for different non-Darcy flow constants after $RF_{ob} = 15\%$.

To further understand as to why non-Darcy effects limits the production, we plot in **Figure 19** distributions of scaled pressure, total mass and transition factor after $RF_{ob} = 15\%$ for three values $C_\beta = 0, 1e-6$ and $3e-6$ $\mathrm{m}^{-2.5}$. Scaled total mass is defined as the relative amount of gas currently in place to initial mass of gas in matrix and fracture (refer to **Appendix A)**, Eq. (93). If $C_\beta = 0$ (Darcy flow), we see that the gas entering the fracture is instantly produced to the well. A zero-scaled

pressure in the fracture for this case and uniform pressure and total mass distribution surrounding the fracture is observed. The flow here is mainly governed by matrix and we are in a *matrix-controlled regime.* In the case with $C_\beta = 1e-6, 3e-6$ $\mathrm{m}^{-2.5}$ (non-Darcy flow), the gas requires some time to leave the fracture and a significant pressure is observed in the fracture. This high-pressure gradient reduces the production rate from the matrix and leads to more non-uniform production around the fracture. We can thus say that non-Darcy effects leads to significant residence time in the fracture and controls the rate of recovery. The flow becomes more fracture-dominated or *fracture-controlled regime*. Inspired by works on spontaneous imbibition (Rangel-German and Kovscek 2002; Andersen et al. 2014); Berawala et al. (2019) showed that also the production of shale gas can be classified into matrix- or fracture-controlled. A similar approach is applied here with respect to the role of non-Darcy flow.

4.2.2 *Role of individual fracture and matrix non-Darcy flow constants*

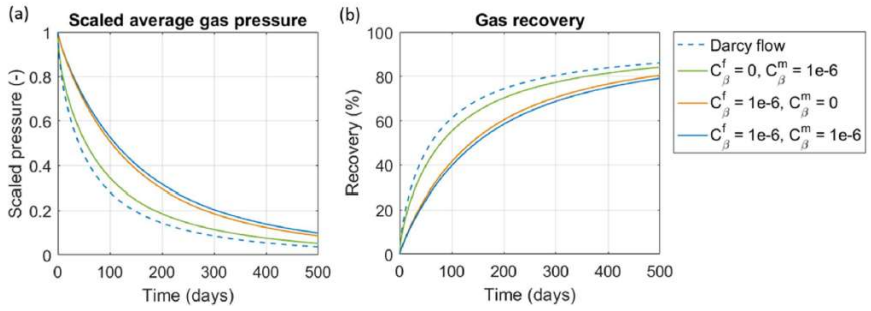

Figure 20 Scaled gas pressure (a) and gas recovery (b) vs time for different C_β in fracture and matrix.

In order to understand the importance of non-Darcy flow in the fracture and matrix domains, we consider two cases where we turn off the non-Darcy effect alternately in each domain and plot scaled pressure and gas

recovery versus time. These two cases are compared against Darcy flow denoted by dashed line in **Figure 6** and against the reference case where we used same $C_\beta = 1e-6$ m$^{-2.5}$ for both fracture and matrix.

For the case where non-Darcy flow is considered only in the matrix ($C_\beta^f = 0, C_\beta^m = 1e-6$ m$^{-2.5}$, green line), we obtain similar recovery as in the case of Darcy flow. This shows that for the input parameters mentioned in **Table 4**, non-Darcy effects in the matrix do not play a significant role. When $C_\beta^f = 1e-6, C_\beta^m = 0$ m$^{-2.5}$ (orange line), we get much lower recovery compared to the Darcy flow. The gas transport from matrix to the well is then fracture dominated, i.e. the time scale of transporting gas through the fracture limits the gas production compared to producing the gas from the matrix. This also follows from the mathematical formulation of diffusion time scale for fracture (Eq. (41)). High C_β in fracture and its intrinsic properties give very low f_{ref}^f resulting in higher diffusion time for gas in fracture compared to matrix.

4.2.3 *Effect of pore size*

In this section, we investigate the role of matrix pore size r_m on gas recovery. We consider four pore radii $r_m = 10,\ 20, 40, 80$ nm and plot Knudsen number, apparent permeability in **Figure 21(a)** & **(b)**. As seen from the figure, increasing pore radii in the matrix, increases the Knudsen number. For higher pore radii, pore size becomes comparatively larger than the mean-free path of gas molecules and gas is mainly driven by viscous forces. Apparent permeability is proportionally linked to the Knudsen number (refer Eq. (19)). Increase in Knudsen number with increasing pore size gives higher apparent permeability as shown in **Figure 21(b)**.

Figure 21(c) shows the recovery profile when only Darcy flow is considered in the system. It can be seen that at higher pore radii, gas travels from matrix to the fracture at much faster rate due to high

apparent permeability, which is then produced from the fracture instantaneously. However, when the same cases are plotted in presence of non-Darcy effects both in matrix and fracture (**Figure 21(d)**), we see delay in production. As seen in **4.2.1**, non-Darcy effect also here cause a shift from matrix-controlled flow regime towards fracture-controlled flow regime. A high-pressure gradient is created in the matrix due to which gas is not uniformly produced from fracture surroundings. The fracture then limits the flow of gas and thus; the gas is not instantaneously produced to the well. Interestingly, for cases with sufficiently low pore radii ($r_m < 40$ nm), gas recovery seems to be less sensitive in the presence of non-Darcy effects as compared to Darcy flow in the system. This is because non-Darcy effects incurs residence time in the fracture in addition to increase travel time for gas to flow from matrix to the fracture.

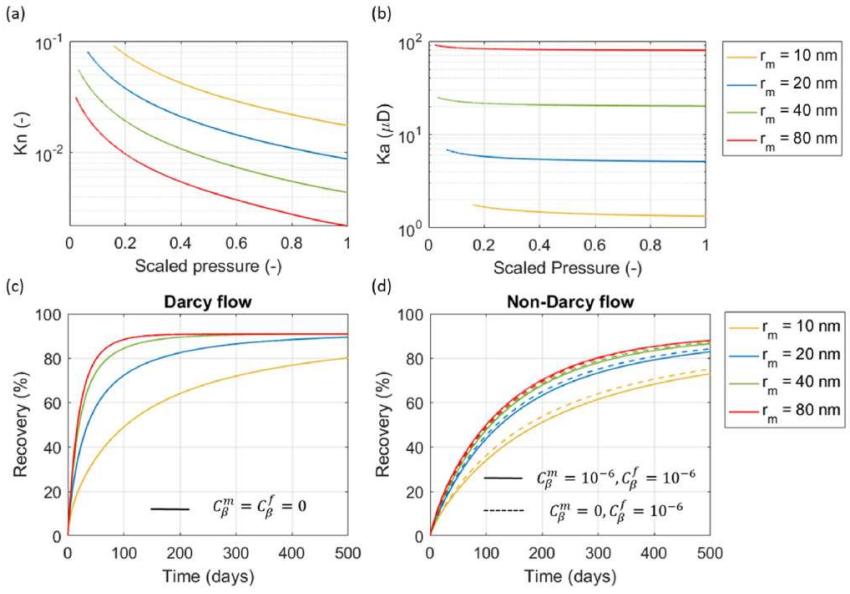

Figure 21 Effect of matrix pore size on Knudsen number (a), apparent permeability (b), gas recovery with only Darcy flow (c) and with non-Darcy flow (d) in the system.

4.2.4 *Effect of fracture permeability*

In the following, we consider the role of fracture permeability k^f by plotting gas recovery for the system with/without non-Darcy effects. The fracture permeability is varied between 1 mD and 1000 mD. As seen in **Figure 22(a)**, fracture permeability barely has any influence on gas recovery for Darcy flow. The effect is dominant only when k^f is very low (~1mD). Low fracture permeability gives lower matrix-to-fracture pressure gradient, resulting in lower recovery rate compared to the case with much higher recovery (1000 mD). This was also observed by Berawala et al. (2019).

For non-Darcy flow (**Figure 22(b)**), we see that fracture permeability becomes very important and the production is limited by the fracture until k^f ~100 mD, a fracture controlled regime. However, when non-Darcy effects are turned off in the matrix, the recovery becomes more sensitive with increasing fracture permeability. The effect of non-Darcy flow in matrix becomes more important at higher fracture permeability.

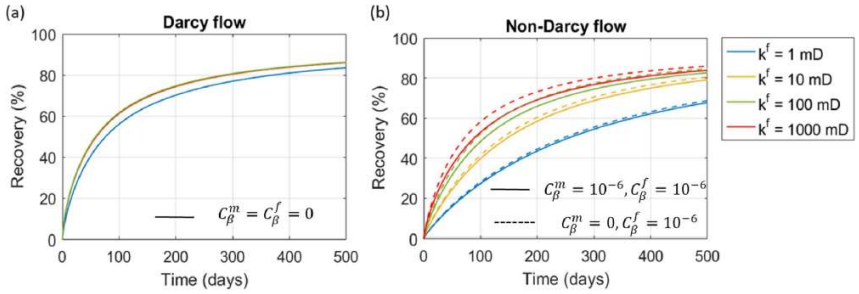

Figure 22 Effect of fracture permeability on gas recovery with Darcy flow (a) and with non-Darcy flow (b) in the system.

4.2.5 *Interpretation using dimensionless numbers*

In the above discussion, we have demonstrated how non-Darcy flow constants, matrix pore radius and fracture properties affect the production of shale gas with/without non-Darcy effects. In particular, we

observed that non-Darcy effects typically shifts the flow towards fracture-controlled regime as compared to matrix-controlled regime with Darcy flow. In this section, we demonstrate the cases where matrix properties become dominant as compared to fracture properties in the presence of non-Darcy effects. We do this by interpreting the results with the help of two dimensionless numbers α and β defined in Eq. (41).

Berawala et al. (2019) showed that the production of shale gas can be classified into matrix-controlled or fracture-controlled based on the magnitude of the product of α and β (this was first demonstrated for advection-spontaneous imbibition flow in Andersen et al. (2014)). They coined the parameter ω given by:

$$\omega = \frac{(\beta + 1)\tau^f}{\tau^m} \approx \alpha\beta \tag{73}$$

From (41), we get:

$$\omega = \frac{(\beta + 1)\tau^f}{\tau^m} \approx \alpha\beta = \frac{f_{ref}^m k_{ref}^m L_y^2}{f_{ref}^f k_{ref}^f L_x b_0}. \tag{74}$$

If $\omega \ll 1$, the flow of gas is completely controlled by the time scale of diffusion from the matrix. For larger ω, the residence time in the fracture is significant and further delays the process. Thus, when gas recovery is plotted for the cases with low ω and high non-Darcy flow constant for matrix and fracture, we expect to see matrix-controlled flow regime. To perform this test, we present eight simulation cases of gas recovery to give approximate values of the product $\omega = \alpha\beta = 1e-3, 1e-2, 1e-1, 1e0$. Both linear and non-linear parameters are varied as explained in **Table 6**. Other parameters are kept constant as listed in **Table 4** unless otherwise is specified. All the simulation cases are presented in terms of gas recovery vs time in **Figure 23**.

In particular, we compare two scenarios: 1) Increased non-Darcy flow effects both in matrix and fracture by considering high C_β^m and C_β^f values. This will give low f_{ref}^m indicating significantly high non-Darcy

effect in the matrix (indicated by solid lines). 2) Compare 1) with non-Darcy effects only in the fracture, by assigning $C_\beta^m = 0$ giving $f_{ref}^m = 1$ (indicated by dashed lines). We do this for all values of $\omega = 1e-3, 1e-2, 1e-1, 1e0$. Note: assigning $C_\beta^m = 0$ would affect the ω value. In such cases, all the other parameters defined in **Table 6** are kept constant so that the recovery is only affected by the matrix non-Darcy effect. Logarithmic time axis is used in **Figure 23** since the simulations span over a wide range of time scale.

We observe that for cases with low value of ω (1e-1), gas recovery is strongly sensitive to non-Darcy effects in the matrix. Only at high $\omega = 1$ (grey lines), we see negligible effect of non-Darcy flow in matrix. This is because at high ω, flow is dominatd by fracture properties and residence time for the flow of gas in fracture plays a key role. On the other hand, for high ω, flow is controlled by the residence time in matrix and the recovery only depends on matrix properties.

We repeat the simulation cases described in **Table 6** and plot them against the time scaled against τ_m. However, this time for cases with no non-Darcy effect in matrix, we vary the other input parameters and adjust them in such a way that we get same ω as their corresponsing pair with non-Darcy effect in both fracture and matrix. These changes are reflected in **Table 7**. As demonstrated by Berawala et al. (2019), we expect that the different simulation cases group well according to the value of ω. However, from **Figure 24**, we see that a unique behavior with completely overlapping curve is not observed. This discrepancy is due to the fact that diffusion time scale of matrix τ_m comprises of reference transition factor f_{ref}^m whose value changes with matrix non-Darcy flow constant from case to case. Thus, the case with $\omega = 1e-2, 1e-1$ (red and green lines) show similar trend as they have similar f_{ref}^m values. The cases with $\omega < 1e-1$ still show similar behavior and maximum recovery is obtained for those cases compared to $\omega = 1e0$.

Table 6 Input parameters for simulation cases shown in Figure 23, selected such that $\omega = \alpha\beta$ is nearly constant for 4 values: $\omega_i = 10^{-3}, 10^{-2}, 10^{-1}$ and 10^{0}. Other unspecified parameters are given by reference case values in Table 4.

	$\omega = \alpha\beta$ (-)	α (-)	β (-)	f^m_{ref} (-)	f^f_{ref} (-)	C^m_β ($m^{-2.5}$)	C^f_β ($m^{-2.5}$)	k^f (mD)	L_x (m)	L_y (m)	ϕ_m (-)	ϕ_f (-)	r_m (nm)
———	1e-3	5.2e-5	22.4	0.18	0.018	1.5e-4	1.5e-4	2000	15	6	0.01	0.6	10
- - -	6e-3	3.9e-5	30	1	0.018	0	9e-6	2000	15	6	0.01	0.6	10
———	1e-2	4e-4	22.4	0.16	0.005	9e-6	9e-6	1500	15	4	0.01	0.8	100
- - -	6e-2	2.8e-4	22.4	1	0.005	0	9e-6	1500	15	4	0.01	0.8	100
———	1e-1	5.4e-3	19.5	0.15	0.016	9e-6	9e-6	150	13	7	0.01	0.8	100
- - -	7e-1	3.6e-3	19.5	1	0.016	0	9e-6	150	13	7	0.01	0.8	100
———	1e0	0.014	70	0.26	0.037	9e-6	9e-6	10	10	5	0.1	0.8	34
- - -	4e0	0.056	70	1	0.037	0	9e-6	10	10	5	0.1	0.8	34

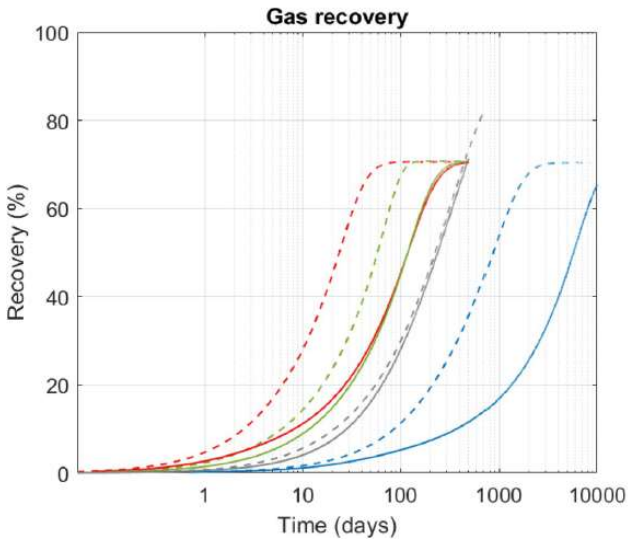

Figure 23 Absolute gas recovery vs scaled time. Comparative test where $\omega = \alpha\beta$ is approximately for 4 values: $\omega_i = 1e-3, 1e-2, 1e-1$ and $1e0$. Input parameters are varied in 8 tests as described in Table 6. ω seems to characterize the flow regime of the fracture-matrix system. Unspecified parameters are given by reference case values in Table 4.

Table 7 Input parameters for simulation cases shown in Figure 24, selected such that $\omega = \alpha\beta$ is constant for 4 values: $\omega_i = 10^{-3}, 10^{-2}, 10^{-1}$ and 10^{0}. Other unspecified parameters are given by reference case values in Table 4.

	$\omega = \alpha\beta$ (-)	α (-)	β (-)	f^m_{ref} (-)	f^f_{ref} (-)	C^m_β ($m^{-2.5}$)	C^f_β ($m^{-2.5}$)	k^f (mD)	L_x (m)	L_y (m)	ϕ_m (-)	ϕ_f (-)	r_m (nm)
———	1e-3	5.2e-5	22.4	0.49	0.005	9e-6	9e-6	1500	15	5	0.01	0.6	14
- - -	1e-3	4.6e-5	30	1	0.005	0	9e-6	1500	15	5	0.01	0.6	10
———	1e-2	4e-4	22.4	0.16	0.005	9e-6	9e-6	1500	15	4	0.01	0.8	100
- - -	1e-2	2.8e-4	30	1	0.005	0	9e-6	2000	20	4	0.01	0.8	50
———	1e-1	5.4e-3	19.5	0.15	0.016	9e-6	9e-6	150	13	7	0.01	0.8	100
- - -	1e-1	3.6e-3	30	1	0.016	0	9e-6	150	20	7	0.01	0.8	46
———	1e0	0.01	100	0.09	0.564	9e-6	9e-6	10	10	5	0.1	0.8	34
- - -	1e0	0.01	176	1	0.564	0	9e-6	10	25	5	0.1	0.6	27

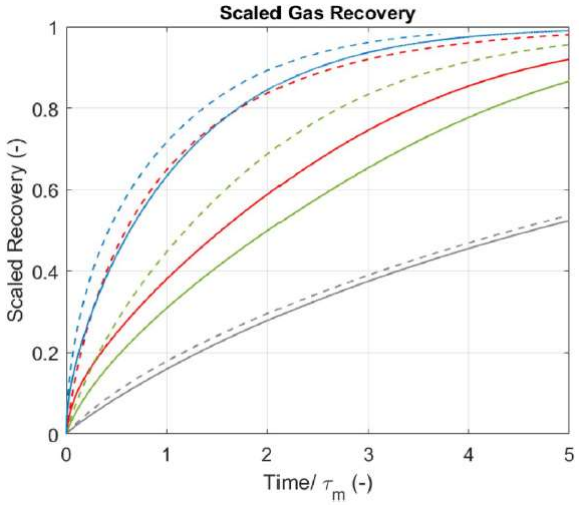

Figure 24 Scaled gas recovery vs scaled time. Comparative test where $\omega = \alpha\beta$ is constant for 4 values: $\omega_i = 1e-3, 1e-2, 1e-1$ and $1e0$. Input parameters are varied in 8 tests as described in Table 7. ω seems to characterize the flow regime of the fracture-matrix system. Unspecified parameters are given by reference case values in Table 4.

The extended 1D+1D model is a useful tool to evaluate sensitivity of input parameters, to understand the role of non-Darcy effects in matrix and fracture and to qualitatively study the shale gas production system. However, the model does not consider changes in effective stresses during production. The resulting changes in fracture or matrix porosity

and permeability due to geomechanical effects might alter some of the results discussed in this paper. Moreover, the model considers flow of gas only from stimulated reservoir volume, i.e. the domain affected by the hydraulic fracture. However, flow of gas from beyond the tip of fracture and crossflow could also contribute to overall recovery. These effects should be evaluated before extending the model to field scale application.

Part two- CO_2 injection for enhanced shale gas recovery

4.3 CO_2 injection

In this section, we explore the behaviour of the model (67)-(69) by considering its sensitivity to different input parameters. Particularly we see how distributions of pressure and relative amount of adsorbed gas, reservoir pressure and gas recovery profiles are affected by matrix and injected CO_2 gas parameters. Gas recovery factor RF is reported as the produced fraction of the mass initially in the reservoir. Please refer to **paper III** for mathematical definitions.

The system is solved by an operator splitting approach, similar to that described in Andersen et al. (2014); Berawala et al. (2019) and Agista et al. (2019). This means that we 1) solve for advective and diffusive transport of CO_2 and CH_4 without surface effects (adsorption/desorption) and then 2) adjust the variables by distributing the local masses between free gas and adsorbed form. Switching between these processes is done frequently to assure the coupling between the mechanisms is captured. The x-axis was discretized into 30 equal cells for all the simulation cases.

4.3.1 *Model Input*

The base case parameters for simulations are presented in **Table 8** and include gas, rock and transport properties. To parameterize the multi-

component adsorption model, adsorption measurements of CH_4 and CO_2 taken from Marcellus, Barnett and Eagle Ford shale (Godec et al. 2013; Heller and Zoback 2014) were matched using the approach previously described in 3.2.5. A typical specific surface area $A = 4.6e7$ m^2/m^3 was applied for all the shale types. See Tang et al. (2016) or Kuila & Prasad (2013) for more information on typical values and factors determining this property. The ability of the isotherm to match the experimental data is illustrated for the three shale types in **Figure 25**. Notably, both CH_4 and CO_2 measurements were well captured. It was possible to match the data using $n_i = 1$ in most cases, except for Barnett shale where $n_c = 2$. This suggests that a traditional multicomponent Langmuir isotherm with associated monolayer adsorption is a sufficient description in two of the tests. The Marcellus shale isotherm will be used as base case.

Table 8 Input parameters used for reference case simulations. Reservoir pressure and temperature are representative of Marcellus shale (Godec et al. 2013).

Parameters	Value	Units
CH_4 well pressure, $P_{m,well}^{inj}$	0	bar
CO_2 well injection pressure, $P_{c,well}^{inj}$	550	bar
Well production pressure $P_{t,well}^{prod}$	150	bar
Initial CH_4 matrix pressure, P_{m0}	350	bar
Initial CO_2 matrix pressure, P_{c0}	0	bar
Real gas deviation factor (ideal gas), Z	1	–
Gas constant, R	8.314	J/mol
CH_4 viscosity, μ_m	0.0184	cP
CO_2 viscosity, μ_c	0.0184	cP
Matrix length, L	0.07	m
Matrix porosity, ϕ	0.1	–
Mean pore radius, r_e	100	nm
Reservoir temperature, T	323.15	K
Tortuosity of rock, τ	1.51	-
Molar weight of CH_4	$16.04x10^{-3}$	kg/mol
Molar weight of CO_2	$44.01x10^{-3}$	kg/mol
CH_4 Diffusion coefficient, D_m	$1x10^{-8}$	m^2/s
CO_2 Diffusion coefficient, D_c	$1x10^{-8}$	m^2/s

Table 9 Adsorption isotherm matching parameters for three different shale types: Marcellus, Barnett and Eagle Ford. For all shale types the value for specific surface area, $A = 4.6x10^7$ m^2/m^3 was used.

	K_m	K_c	$S_{m,m}$	$S_{m,c}$	n_m	n_c
	bar^{n_m}	bar^{n_c}	mol/m^2	mol/m^2	-	-
Marcellus (base case)	50	18	$3.04x10^{-6}$	$7.43x10^{-5}$	1	1
Barnett	50	280	$2.09x10^{-6}$	$9.57x10^{-6}$	1	2
Eagle Ford	80	40	$4.35x10^{-7}$	$9.57x10^{-6}$	1	1

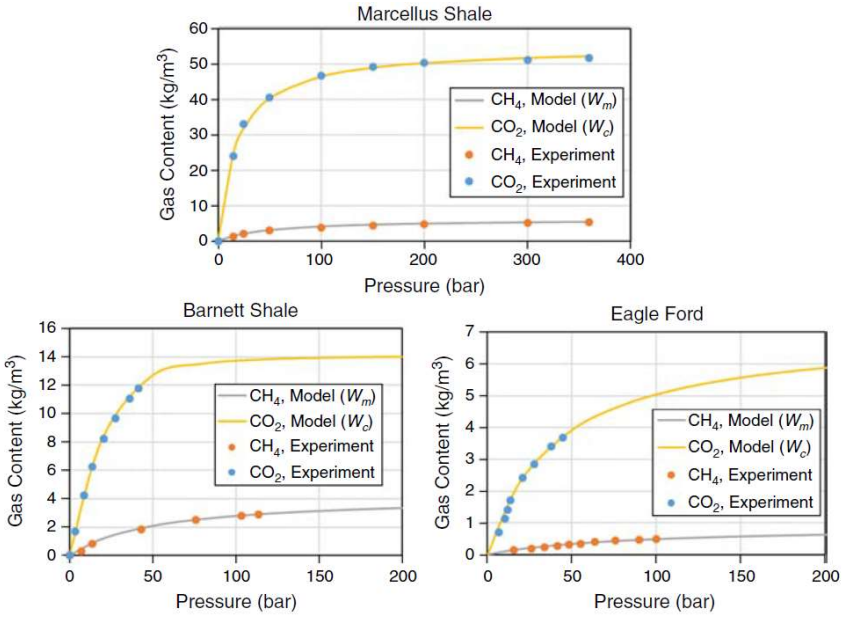

Figure 25 Simulated and Experimental adsorption isotherms in terms of W_i (kg / m^3) for Marcellus (top), Barnett (left) and Eagle Ford (right) shales. Experimental data for Marcellus shale is taken from Godec et al. (2013), Barnett and Eagle Ford shale data are from Heller and Zoback (2014).

4.3.2 *Adsorption isotherm behaviour*

With Marcellus shale parameters as base case, we systematically vary the input parameters $K_i, S_{m,i}$ and n_i to study their effect on CH_4 adsorption ($i = m$) and CO_2 adsorption ($i = c$) in **Figure 26** left and

right, respectively. It is noted that in both considered cases the partial pressure P_i of the considered component is varied while the partial pressure of the other component is zero. The results are plotted in terms of W_i (mass per volume), but the same trends apply for $\hat{a}_i$ (Pa), a_i (mol per volume) or A_i (area per volume) by proportionality.

When component i reacts with the surface with the other component present, a lower value of K_m or K_c implies that the reaction (56) or (57) is moved to the left, respectively, and more of that component will be adsorbed. The implication is that the surface gets saturated on the component at relatively low pressures when K_i is low. Increasing $S_{m,i}$ by definition increases how many moles are stored per area but does not change the functional relation with pressure. As seen, the function shape is similar, but the capacity is increased with larger $S_{m,i}$. The parameter n_i also affects the storage capacity since an increased value further increases the number moles being stored per area. However, not only the capacity, but the functional relation with pressure is affected and lets that higher capacity be reached at lower pressures.

In **Figure 27** the adsorption behavior of a component is illustrated for cases where the partial pressure of the other component is systematically varied. As seen, for a given methane pressure P_m, increased levels of P_c leads to less adsorbed content of CH_4. This captures that CO_2 is able to displace CH_4 from the surface. Similarly, for lower methane pressures P_m more CO_2 is adsorbed giving a synergetic effect where CO_2 is stored while methane is produced.

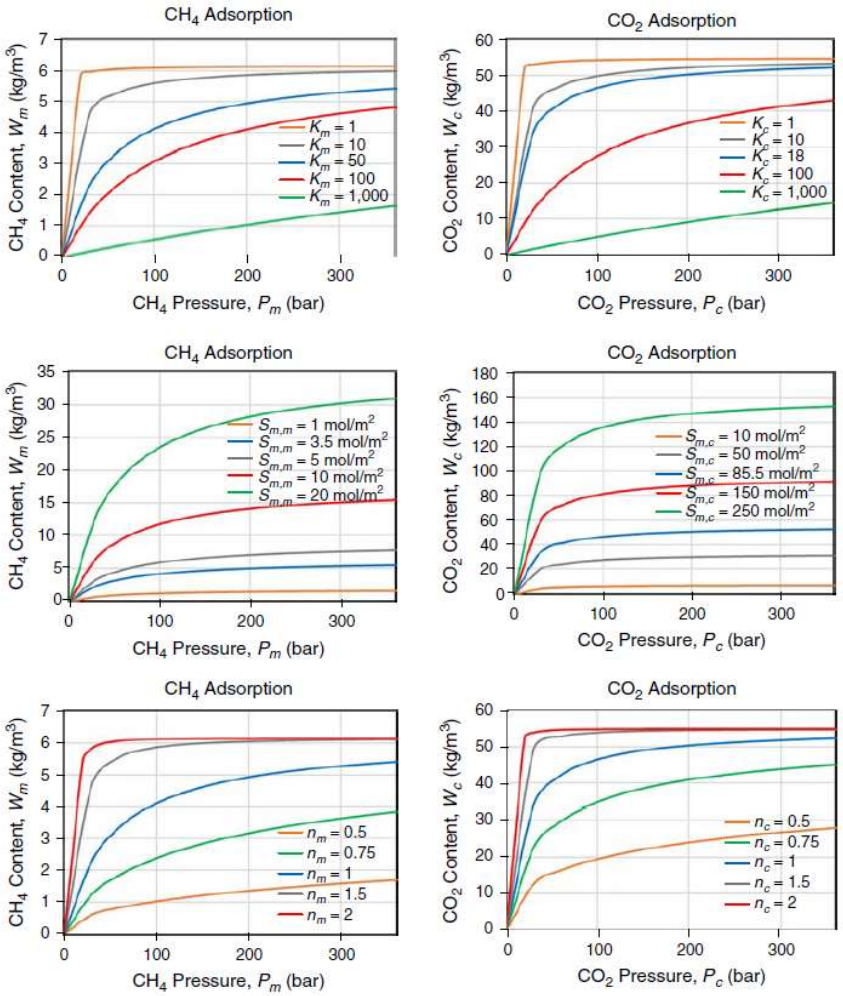

Figure 26 Adsorption content of CH4 (left) and CO2 (right) as function of that components partial pressure. It is here assumed the other component is not present (zero partial pressure). Relevant isotherm parameters are systematically varied from the base case.

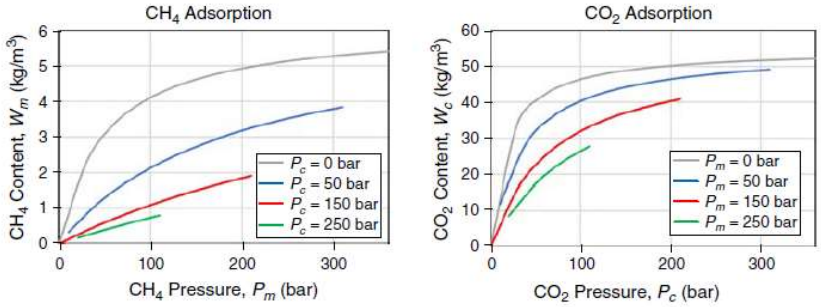

Figure 27 Adsorption behaviour of CH_4 (left) and CO_2 (right) when the partial pressure of the opposite component is systematically varied with a constant value.

The previous cases have considered how changes in adsorbed content changes when partial pressures in a surrounding gas phase and isotherm parameters are varied. During injection we are interested in how the surface interactions can affect the mass balance and flow of gas components. For this reason, we assume a closed porous medium with, for simplicity, equal masses of CH_4 and CO_2 as defined by the conserved property (with units of pressure) $M_i = P_i + \hat{a}_i = 3.0e7$ Pa. It is assumed that the methane first was in equilibrium with the surface before CO_2 was made present defining an initial methane pressure according to:

$$M_m^{GOIP} = P_{m0} + \hat{a}_m(P_{m0}; P_c = 0), \tag{75}$$

where necessarily $0 < P_{m0} < M_m^{GOIP}$ and M_m^{GOIP} denotes the gas originally in place expressed by the variable M_m. The CO_2 was assumed to enter in gas phase with $P_{c0} = M_c$ (and $\hat{a}_{c0} = 0$). The initial pressure of this system will then be $P_{t0} = P_{m0} + P_{c0}$. We then wish to see how this system changes when it gets to its equilibrium state defined by pressures P_m, P_c such that:

$$M_m = P_m + \hat{a}_m(P_m; P_c), \qquad M_c = P_c + \hat{a}_c(P_m; P_c). \tag{76}$$

In **Figure 28** we vary the 7 parameters $K_i, S_{m,i}, n_i$ and A and present equilibrium results for the fractions of M_i that are in form of free gas or

adsorbed form and the ratio of total pressure to initial total pressure P_t/P_{t0}.

As seen, the total pressure (blue curve) is, for a wide range of parameter cases, much lower than the initial value. It is clear that P_c should decrease from its initial value due to adsorption, however interestingly that reduction is not fully compensated by desorbed methane. As long as the surface is not fully saturated initially it is reasonable that the added pressure of CO_2 will lead to a net increase of adsorbed gas. This implies that the surface can act as a buffer for pressure buildup and allow gas to be injected with less resistance. For parameter choices where the surface does not attract CO_2, or adsorption at all, i.e. $\frac{\hat{a}_c}{M_c} = 0$, the presence of CO_2 does not cause desorption of CH_4 and hence the total pressure stays the same $\left(\frac{P_t}{P_{t0}} = 1\right)$. That is the case for high n_m, low n_c, S_{mc} and A.

When CO_2 fully replaces CH_4 on the surface $\frac{P_m}{M_{m0}} = 1$ and the surface is fully saturated by CO_2, the amount of moles able to be stored per area for CO_2 vs CH_4 will determine if a net number of moles are added or removed from the surface. That is given by the ratio $(S_{m,c}n_c)/(S_{m,m}n_m)$ which if greater than 1 will cause more moles of CO_2 to be adsorbed than there were moles of CH_4 originally attached. Considering the Marcellus base case parameters in

Table 9 we get a value of 24.4. Hence, in most cases where we see $\frac{P_m}{M_{m0}} = 1$ together with stable values of P_t, the total pressure has decreased, i.e. $\frac{P_t}{P_{t0}} < 1$. An interesting, but theoretical example is also seen for low values of $S_{m,c}$ where adsorption has caused the pressure to increase.

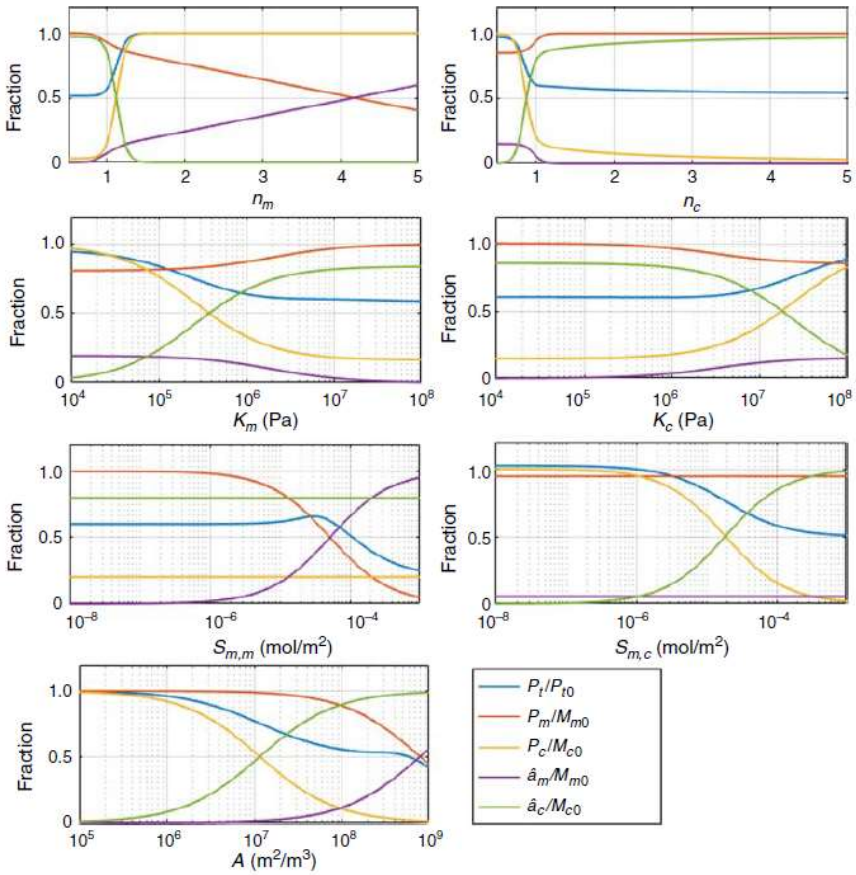

Figure 28 Responses in total pressure and contents of free and adsorbed carbon and methane in a constant mass test. Relevant parameters are varied in each figure.

For CO_2 storage and EGR purposes we are interested in cases where adsorption is important, i.e. much of the gas initially stored is in adsorbed form and where the presence of CO_2 is able to convert that into free gas while adsorbing as much of the CO_2 as possible. We do however note that a surface that is able to store a lot of CH_4 at a given pressure must also have great affinity for CH_4 which will limit how easily it is desorbed. If under these conditions the surface affinity for CO_2 can compensate for

this by lowering the CH_4 isotherm and effectively fill the surface capacity, optimal conditions are defined. To explore this mathematically we note that CH_4 storage at a given initial reservoir pressure P_m is linearly increasing with the adsorbed content, as repeated from (75):

$$M_m^{GOIP} = P_{m0} + \hat{a}_m(P_{m0}; P_c = 0). \tag{77}$$

By simple pressure depletion (no CO_2 involved) to the pressure P_{well} the gas currently in place would be:

$$M_{m-base}^{GCIP} = P_{well} + \hat{a}_m(P_m = P_{well}; P_c = 0). \tag{78}$$

The base recovery factor RF_{base} from pressure depletion is then simply:

$$RF_{base} = \frac{M_m^{GOIP}(P_{m0}) - M_{m-base}^{GCIP}(P_{m0}, P_{well})}{M_m^{GOIP}(P_{m0})} \tag{79}$$

$$RF_{base} = \frac{[P_{m0} + \hat{a}_m(P_{m0}; P_c = 0)]}{P_{m0} + \hat{a}_m(P_{m0}; P_c = 0)} - \frac{[P_{well} + \hat{a}_m(P_m = P_{well}; P_c = 0)]}{P_{m0} + \hat{a}_m(P_{m0}; P_c = 0)} \tag{80}$$

For comparison, if CO_2 is injected and the gas mixture is produced to the (same) well pressure P_{well} we get a gas currently in place of

$$M_m^{GCIP} = P_m + \hat{a}_m(P_m; P_c), \qquad P_m + P_c = P_{well}, \tag{81}$$

where the latter equation denotes that the total pressure must add to P_{well} after production to have comparable conditions. The individual values of P_m, P_c will depend on the manner of injection; if a high volume of CO_2 has been injected that will likely let more CH_4 be produced before the low well pressure is obtained, while adding only a minor amount of CO_2 to the system will remove little CH_4 to get the well pressure. For this reason, we treat $\frac{P_c}{P_m}$ as an independent variable. The methane currently in place M_{m-inj}^{GCIP} and recovery factor RF_{inj} after CO_2-EGR, are then calculated as:

$$M_{m-inj}^{GCIP}(P_m, P_c) = P_m + \hat{a}_m(P_m; P_c = P_{well} - P_m), \tag{82}$$

$$RF_{inj} = \frac{M_m^{GOIP}(P_{m0}) - M_{m-inj}^{GCIP}(P_m, P_c)}{M_m^{GOIP}(P_{m0})} \tag{83}$$

$$RF_{inj} = \frac{[P_{m0} + \hat{a}_m(P_{m0}; P_c = 0)]}{P_{m0} + \hat{a}_m(P_{m0}; P_c = 0)} - \frac{[P_m + \hat{a}_m(P_m; P_c = P_{well} - P_m)]}{P_{m0} + \hat{a}_m(P_{m0}; P_c = 0)} \tag{84}$$

To evaluate the benefit of CO_2 injection we define the EGR potential F_{inj} as the factor gas recovery increases by when CO_2 injection is applied:

$$F_{inj} = \frac{RF_{inj}}{RF_{base}} = \frac{M_m^{GOIP} - M_{m-inj}^{GCIP}}{M_m^{GOIP}(P_{m0}) - M_m^{GCIP}(P_{m0}, P_{well})} = \frac{[P_{m0}+\hat{a}_m(P_{m0};P_c=0)]-[P_m+\hat{a}_m(P_m;P_c=P_{well}-P_m)]}{[P_{m0}+\hat{a}_m(P_{m0};P_c=0)]-[P_{well}+\hat{a}_m(P_m=P_{well};P_c=0)]} \tag{85}$$

Note that despite the complexity of this equation the main components determining the EGR potential is how much methane is adsorbed before and after production and how much free methane constitutes the composition in the end. Setting $\hat{a}_m = 0$, implies:

$$F_{inj} = \frac{P_{m0} - P_m}{P_{m0} - P_{well}}\ , \qquad (P_{well} < P_m < P_{m0}), \tag{86}$$

that simply increasing the fraction of CO_2 in the free gas composition may contribute but relies on the compositional gradients to disperse effectively.

In **Figure 29** it is seen that the GOIP (in terms of M_m^{GOIP}) increases both with initial pressure and surface area. Naturally, more gas is stored in free form when compressed, and more gas is adsorbed at higher pressures. Increasing the specific surface area increases the amount stored in adsorbed form at a given pressure. When reducing the reservoir pressure to that of the well pressure from the initial 350 bar recovery increases, see **Figure 29** right, in an almost linear trend. At high pressures the isotherm is relatively flat and hence the recovery factor is slightly less sensitive to pressure for higher surface capacities. By

reducing to a zero pressure all the gas will be recovered. In terms of time and practice that is only a theoretical limit.

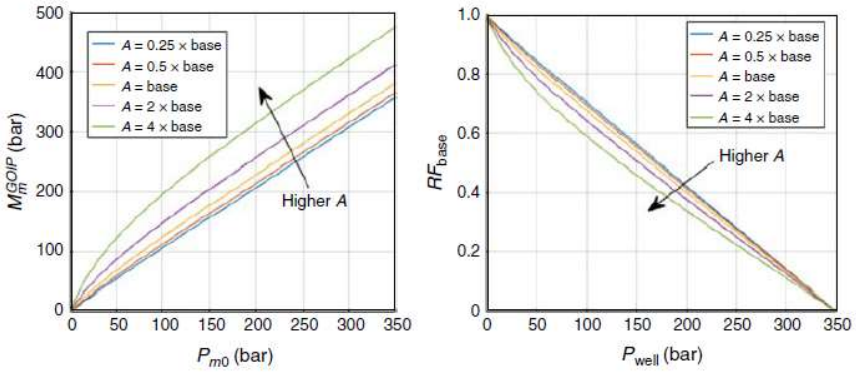

Figure 29 Left: Gas originally in place, as expressed by M_m^{GOIP} (unit of pressure) as function of initial pressure P_{m0} at different values of specific surface area A. Right: Recovery factor RF_{base} evaluated by pressure depletion (without CO_2 injection) as function of well pressure and A.

In **Figure 30** the role of CO_2 injection is studied. Clearly, if more CO_2 is present in the final gas composition it has also displaced more of the CH_4 originally adsorbed and in the limit all the CH_4 is recovered, regardless of well pressure. That is a clear distinction from regular pressure depletion where only pressure depletion to zero pressure could give such a high value. Lowering the well pressure (and thus the final matrix pressure) still has a main effect on increasing recovery. At low P_c the recovery approaches that of regular pressure depletion without any CO_2 injection and thus a minimum. At a very low specific surface area, the recovery is mainly improved by mixing the methane with CO_2 and reducing the CH_4 content by producing the mixture to the specified pressure. Increased specific surface area A increases the original methane in place in adsorbed form. At a high P_c the methane pressure will be correspondingly low and adsorbed methane will also be low. Although

more mass is recovered, there is more to recover in the first place and the net effect appears to be a less effective recovery.

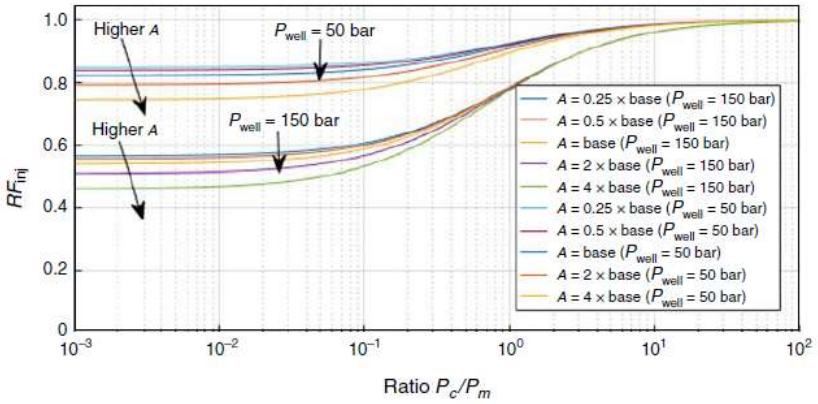

Figure 30 Recovery factor RF_{inj} for different gas compositions and well pressures.

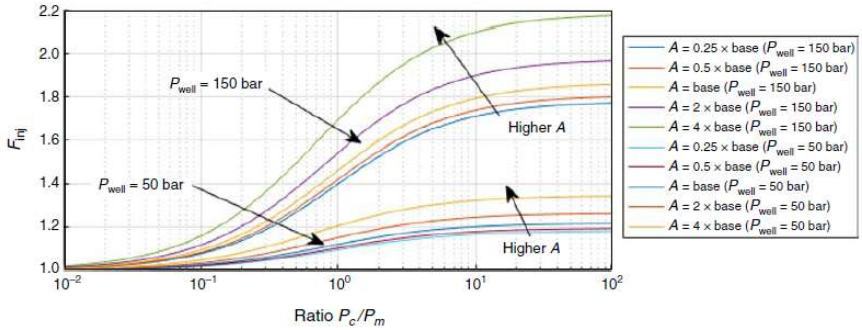

Figure 31 EGR potential factor F_{inj} for different gas composition, well pressure and specific surface area.

The improvement in recovery when using CO_2 (indicated by the composition P_c/P_m) over simple pressure depletion to P_{well} is shown by the EGR potential factor F_{EGR} in **Figure 31**. For negligible amounts of CO_2 present there is no improvement over regular pressure depletion, giving $F_{inj} = 1$, however, as the CO_2 content increases it is seen that recovery is improved by factors as high as 2. At high well pressure of

150 bar we have seen that little gas is produced by regular pressure depletion, hence there is greater potential for EGR. At a low well pressure of 50 bar much more of the gas can be produced by pressure depletion and there is less to gain from CO_2 injection. We also see that specific surface area is of key importance and that recovery by CO_2 injection improves much more in cases with high specific surface area.

4.3.3 *Dynamic simulations*

In this section, we investigate the dynamic CO_2-CH_4 interplay and its influential using simulations at core scale and field scale. At core scale a pore radius of 100 nm is assumed, since shale samples then are often crushed and compacted to obtain homogeneity and reproducibility of measurements. At field scale a pore radius of 20 nm is assumed. The Knudsen number K_n as function of the relevant pressures is shown in **Figure 32** (left). The resulting apparent permeability at these pressures is shown in **Figure 32** (right) with relatively constant values of 2.5 µD for field scale and 85 µD at core scale.

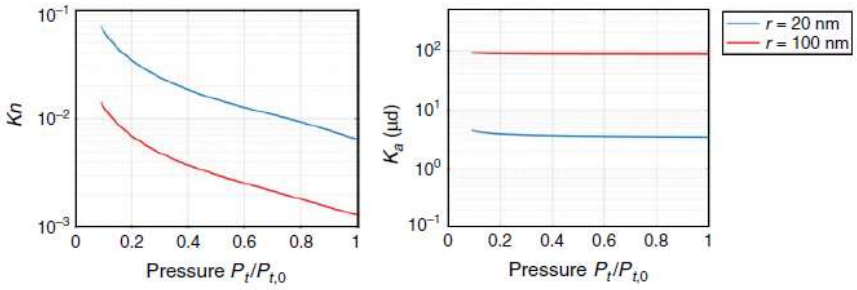

Figure 32 Knudsen number (left) and apparent permeability (right) vs scaled total pressure for two pore radii related to core scale and field scale simulations.

4.3.3.1 Core-scale simulations

Considering the standard dimensions of a core, $L = 0.07$ m, the input parameters listed in **Table 8** are applied, except for a lower initial

pressure of $P_{m0} = 250$ bar compared to real Marcellus reservoir conditions (350 bar). At $t = 0$; CO_2 is injected at various pressures $P_{well} > P_{m0}$ until $t = 0.05$ d. The well pressure is then lowered to $P_{well} = 50$ bar and gas mixture is produced from the core the remaining time. Note that one of the injection pressures equals P_{m0} meaning no injection occurs and only pressure depletion is considered after 0.05 d.

As seen in **Figure 33**, during the injection stage the total pressure increases to that of the well pressure. Recovery does not change in this period and remains zero since CH_4 is not leaving the system. Once the well pressure is lowered after 0.05 d, the total pressure of the system follows. Gas then flows out, carrying both CH_4 and CO_2 and recovery increases.

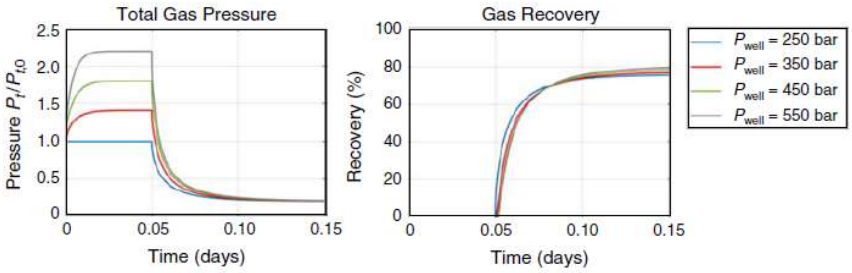

Figure 33 Total pressure (left) and CH_4 recovery (right) vs time. CO_2 is injected from 0 to 0.05 d and gas is recovered the rest of the time. Core scale parameters are assumed.

The distribution of scaled total pressure $P_t/P_{t,0}$ after the end of the CO_2 injection period (0.05 d) is shown top left in **Figure 34**. In agreement with total pressures having stabilized with time; the total pressure is uniform along the core at this time. The partial pressures and adsorbed content distributions (middle and right columns, top) are however not uniform. Free CH_4 pressure P_m has been reduced near the inlet due to CO_2 injection which has pushed CH_4 towards the right boundary of the core. The space initially occupied by CH_4 is now dominated by CO_2 near the inlet of the core as seen from the CO_2 gas partial pressure P_c. As seen by (67) advection mainly works to stabilize total pressure, but beyond

that partial pressures are distributed only by diffusion. The importance of molecular diffusion as a limiting factor in enhanced recovery settings has previously been underlined by Stoll et al. (2008) and Andersen et al. (2015). At higher P_{well} more CO_2 is injected and displaces CH_4 further into the matrix.

An interesting observation is that for all injection pressures the compositional distribution is such that the methane is predominantly in free gas form, while the injected CO_2 is mainly in adsorbed form (ca 4 times more moles are adsorbed than free gas). This demonstrates the efficiency of CO_2 to release CH_4 while itself is stored.

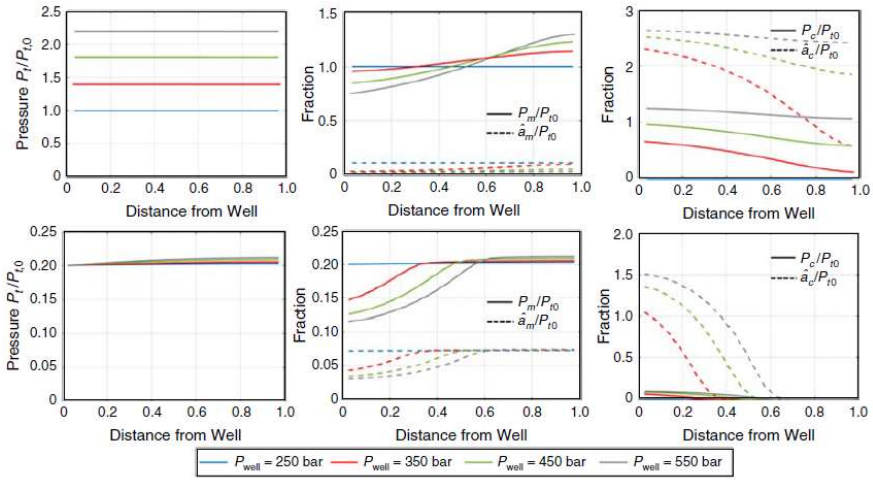

Figure 34 Total pressure distribution (left), CH_4 free and adsorbed content distribution (middle) and CO_2 free and adsorbed content distribution (right) along the core at different CO_2 injection pressures. Upper row: distributions after 0.05 d (end of injection period). Lower row: distributions after 0.15 d (end of production period).

After 0.15 days, the total pressure drop has stabilized after production and the distributions of total pressure and species at that time are shown in the bottom row of **Figure 34**. Again, it is seen that although the total pressure is uniform and advective flow thus has stopped, the compositional distributions are non-uniform. The mixing of the gas

components and the preferential adsorption of CO_2 has caused CO_2 to remain in the matrix in gas phase and adsorbed phase when the total pressure has stabilized. Accordingly, CH_4 has followed the gas mixture out of the system during pressure depletion.

To examine the role of diffusion on CO_2-EGR the previous example was repeated with the diffusion coefficient D_i being varied from 10^{-8} to 10^{-6} m^2/s. The injection well pressure was the same in all cases; $P_{well} = 350$ bar, while the initial and production pressures were as before $P_{m0} = 250$ bar and $P_{well} = 50$ bar. The effect of diffusion on total pressure vs time is relatively small as seen by **Figure 35** (left). However, at larger values of the diffusion coefficient a positive effect is seen on recovery (right in **Figure 35**). That is explained by examining the compositional distributions seen in **Figure 36**. At higher diffusion coefficients CO_2 is able to migrate deeper into the system and reduce compositional gradients in the system. CH_4 displaced from the inlet region retains a higher partial pressure compared to cases with less significant diffusion. When production starts less of the CH_4 is then located at the outermost boundary of the system. More of the produced gas composition will be composed of CH_4 and subsequently recovery increases.

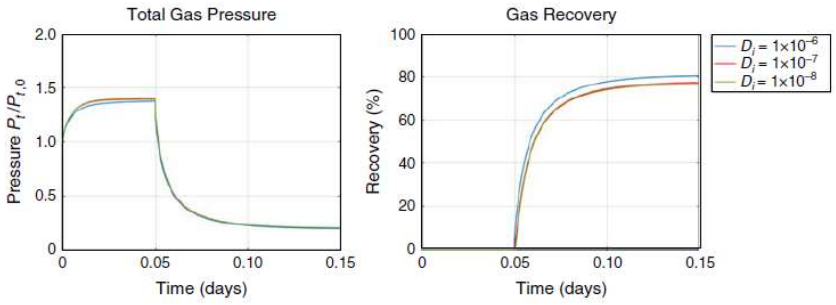

Figure 35 Total pressure (left) and CH_4 recovery (right) vs time after injecting CO_2 from t=0 to t=0.05 d and then producing the remaining time. Diffusion coefficients D_i (in m^2/s) are varied.

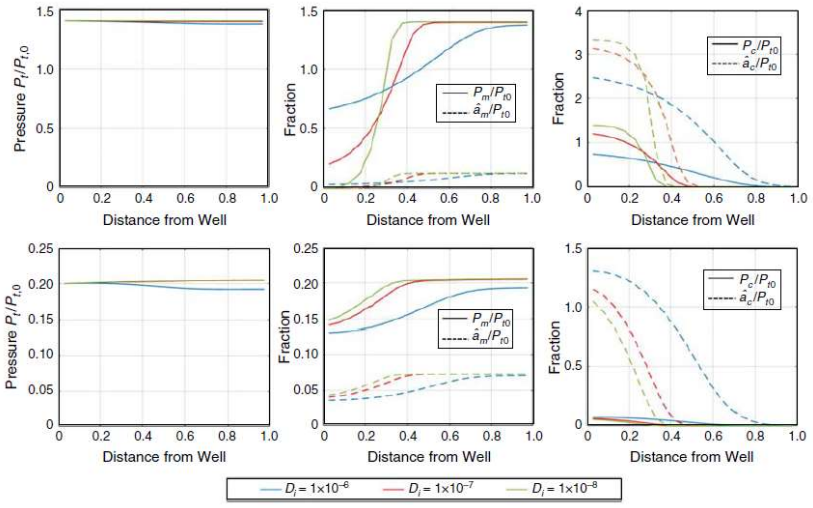

Figure 36 Total pressure distribution (left), CH_4 free and adsorbed content distribution (middle) and CO_2 free and adsorbed content distribution (right) along the core at different diffusion coefficients D_i (in m^2/s). Upper row: distributions after 0.05 d (end of injection period). Lower row: distributions after 0.15 d (end of production period).

4.3.3.2 Field scale

In this section, we investigate the effect of CO_2 injection on enhanced CH_4 recovery in a field scale scenario. We consider a system with matrix length $L = 20$ m and narrow pore radii of 20 µm. Marcellus reservoir pressure of $P_{m0} = 350$ bar is used as initial value. Cyclic production and injection is performed as follows: First P_{well} is set to 150 bar (less than P_{m0}) to produce for 250 d; then P_{well} is increased above P_{m0} to 350 bar where CO_2 is injected for a following 250 d. This cycle is repeated.

The total pressure vs time is shown in **Figure 37** together with gas recovery. In addition to the base case, run in the described scenario, we compare with corresponding cases for different specific surface areas and where, instead of cyclic injection-production, strictly pressure depletion to $P_{well} = 150$ bar is applied. In all cases, changing the well pressure correspondingly lowers or raises the reservoir pressure to the

same levels defined by the well (350 or 150 bar). Note that greater length dimension and lower matrix apparent permeability (see **Figure 32**) compared to the core scale has increased the time scale of injection/production from 0.05 to 300 d.

Increasing the specific surface area A increases the time needed to establish the well pressure in the matrix. Adsorption increases the capacity of the matrix to store CO_2 and delays its propagation. As shown by Berawala et al. (2019) in a single component setting; adsorption processes increase the time scale for gas pressure to establish. As shown in **Figure 29** increased specific surface area increases the GOIP, but the overall recovery factor is reduced during pressure depletion. That is also seen in **Figure 37** for the dashed lines.

At each cycle where CO_2 is injected, and gas is produced to total pressure equilibration; recovery increases incrementally. That is a result of increasing the compositional content of CO_2 every time CO_2 is injected, which releases CH_4 in the produced mixture. By comparison with **Figure 30**, a higher recovery is obtained as P_c/P_m increases for each cycle.

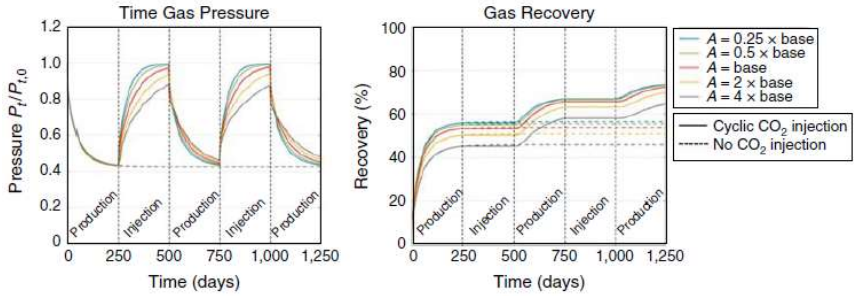

Figure 37 Total pressure (left) and gas recovery (right) vs time for field scale simulation cases; cyclic CO_2 injection – gas production is compared with regular pressure depletion. Specific surface area is varied.

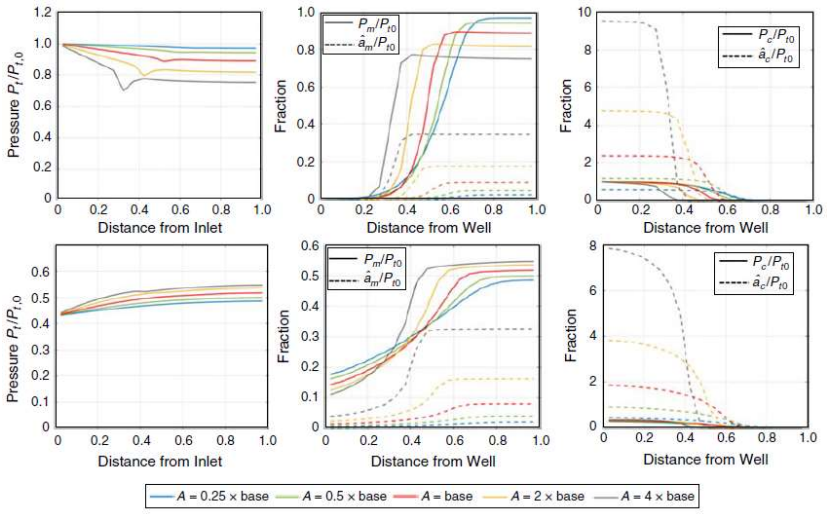

Figure 38 Total pressure distribution (left), CH_4 free and adsorbed content distribution (middle) and CO_2 free and adsorbed content distribution (right) along the matrix at different CO_2 injection pressures. Top row – distributions after 400 days (first injection cycle). Bottom row- during production period after 650 days.

The distributions of total pressure and components are shown in **Figure 38** after 400 d (in the middle of the first injection period) and 650 d (in the middle of the second production period). The cases with higher specific surface area A have not stabilized at that time and show less uniform total pressure profiles. At increased A a higher amount of CO_2 is stored (seen by comparison of the areas under $\frac{P_c}{P_{to}} + \frac{\hat{a}_c}{P_{to}}$ in the right figure in top row) although injection has happened during the same period of time. That is the case because CO_2 adsorption is predicted to lower the total pressure compared to if adsorption was not taking place and thus the injection rate, driven by the (total) pressure difference between well and matrix is increased. More CO_2 is also stored when reducing the well pressure, since the surface has great affinity for this component. Although more CO_2 is stored and CH_4 is produced at higher specific surface area, that is strongly associated with the higher capacity

and the efficiency of the process is expected to be lower; considering **Figure 37** the recovery is lower when specific surface area increases.

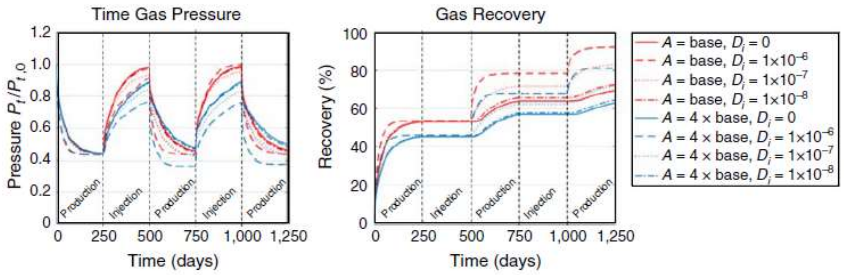

Figure 39 Cyclic CO_2 injection – gas production for different specific surface area and diffusion coefficients.

Finally, the role of diffusion in the cyclic injection-production scenario is considered. **Figure 39** shows total pressure and recovery as function of time for different diffusion coefficients at the base (red color) and 4xbase (blue color) value of specific surface area A. At base A the total pressure response to changes in diffusion coefficient is not very noticeable. Diffusion can determine how easily CO_2 spreads. If there is little diffusion the surface capacity near the inlet is quickly equilibrated and any loss in total pressure is associated with a small portion of the system. However, if CO_2 manages to spread over a great part of the system by diffusion the surface will take up much of the CO_2 and reduce the total pressure to greater extent. For this reason, we see total pressure being lower with a high diffusion coefficient than a high diffusion coefficient in the first injection cycle (the remaining cycles are history dependent and more difficult to interpret). For a system with little capacity for adsorption this difference will be minor, but significant when the surface capacity increases. For that reason, there is more sensitivity in the $A = 4\text{xbase}$ cases than the $A = \text{base}$ cases.

The effect diffusion has on recovery is mainly positive. A higher diffusion coefficient raises the end recovery factor obtained in a given

cycle. Primarily that is due to applying the storage capacity across the matrix and making CH_4 accessible to the well.

4.4 Review results – parameters influencing gas sorption on shale

This section summarizes the important findings and literature review results on parameters influencing gas sorption in shale reservoirs. Most sorption studies are available on gas shale samples of original composition or pure individual shale components. The literature indicates that shale adsorption capacity correlates directly to factors that can generate more micropores, but inversely to factors that reduce or plug micropores. This is because small pores generate larger surface area and stronger adsorbate-adsorbent interaction energy which results in greater adsorption. Sorption experiments on samples from across the world (see **Figure 40**) have been reviewed in this section to gain insight into the relationship between sorption, rock compositional and geological features to outline the major factors that controls gas sorption capacity of shales.

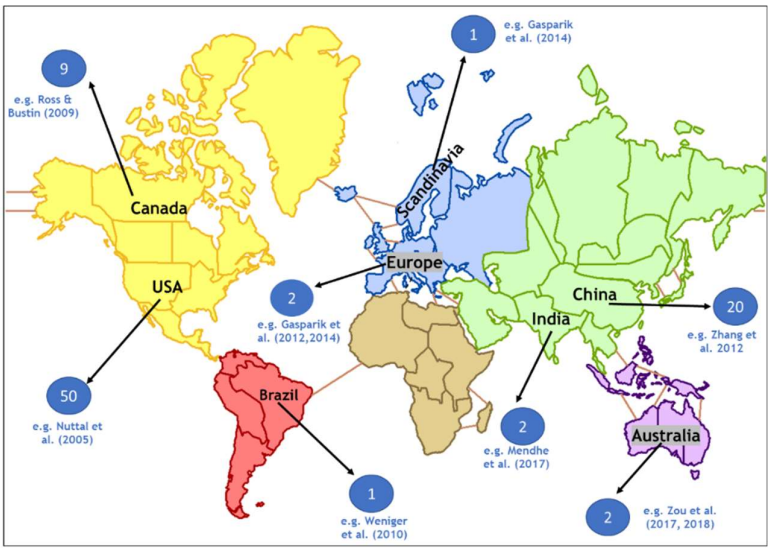

Figure 40 : Worldwide illustration of shale formations actively investigated by researchers. The numbers are purely based on the literature reviewed in this study with focus particularly on CH_4 and CO_2, sorption tests and auxiliary evaluations relevant to CO_2-ESGR.

4.4.1 *Influence of organic matter (richness) on gas sorption*

The shale organic matter (OM), also known as kerogen, is associated with the in-situ generation of hydrocarbons. The organic richness is frequently expressed by the Total Organic Carbon (TOC). It is primarily responsible for the microporous nature of shale and is the main contributor to the surface area and total pore volume (Cao et al., 2015; Zhou et al., 2018). The TOC wt% of the shale varies substantially among shale reservoirs and within a formation itself. **Table 10** shows the TOC content reported for some shale gas plays. Although these values may not exactly be large, the microporosity associated with the organic fraction is the principal control on CH_4 and CO_2 sorption; there the trapping forces are enhanced due to coalescing of molecules and overlap of interaction energies between the sorbed gas molecules (Thommes, 2010). In stark contrast, immature gas shales with appreciable matrix bituminite can store gas by dissolution and may demonstrate large sorbed gas capacities that are unrelated to micropore volume (Ross & Bustin, 2009). Bituminite, originally described by Teichmüller (1971), could be considered as a semi-solid portion of degrading organic matter that lacks definite shape or form (Kus et al., 2017). It is often present in immature source rocks and may have a dominantly fluidal or granular internal structure within which gases could be stored by dissolution.

Table 10: Typical TOC of some shale plays and formations (fm.) adapted from Chalmers and Bustin (2007); Ross and Bustin (2007a, 2008); Ambrose et al. (2010); Zhang et al. (2012); Wang et al. (2013).

Region	***Shale/Play***	***TOC (wt%)***
North – American Shale systems, U.S	Barnett	2.5 -7.9
	Marcellus	1-10
	Haynesville	0 – 8
	Horn River	3
	Woodford	5
Northeastern British Columbia region, Canada	Lower Jurassic fm.	0.8 – 11.8
	Lower cretaceous fm.	0.53 – 17
	Poker Chip fm.	0.8 – 2.2
Western Canada Basin	Besa River fm.	0.9 – 5.7
	Horn River fm.	2.5 – 3.5
	Muskwa fm.	0.4 – 3.6
	Fort Simpson fm.	< 1
	Mattson	< 1.2
Sichuan Basin, China	Qiong-zhu-si fm.	0.5 – 4
	Long-ma-xi fm.	0.5 – 2.3
	Da-long and Long-tan fm.	1.0 – 10

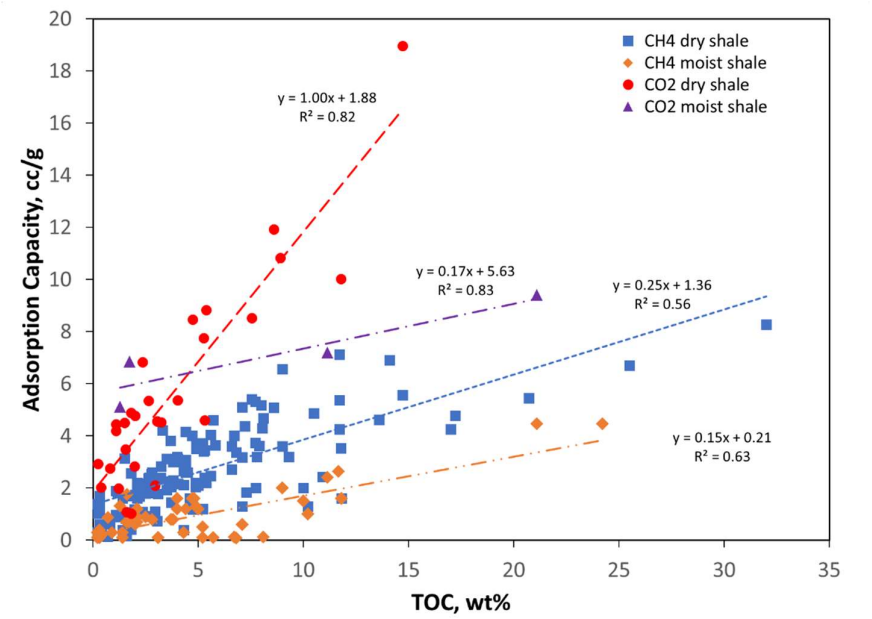

Figure 41: Correlation between TOC and CH_4, CO_2 sorption capacity of dry and moisture equilibrated shales. Data points are representative of langmuir volume reported in the evaluations of (Nuttal et al., 2005; Ross & Bustin, 2009; Weniger et al., 2010; Zhang et al., 2012; Wang et al., 2013; Gasparik et al., 2014; Heller & Zoback, 2014; Luo et al., 2015; Hong et al., 2016; Cancino et al., 2017; Pozo et al., 2017; Zhou et al., 2018).The regression constants of both species are relatively high and extrapolation to zero TOC content shows impact of auxillary sorption sites.

The reviewed literature confirms that CH_4 and CO_2 sorption capacities on shale is strongly correlated with TOC. A strong positive linearity is observed for CH_4 and CO_2 sorption datasets (Ross & Bustin, 2007a, 2008, 2009; Zhang et al., 2012; Wang et al., 2013; Heller & Zoback, 2014; Hong et al., 2016; Cancino et al., 2017; Zhou et al., 2018) sourced from experimental measurements on a wide range of shale samples (**Figure 41**). The regression factors for both CH_4 and CO_2 are relatively high under both dry and moist conditions and demonstrate the shale TOC to have primary control on adsorption of either gas species. It is interesting to note that the regression constants for both species is higher for moisture-equilibrated samples relative to dry samples. This implies a

much stronger correlation of gas adsorption to TOC in the presence of water and could infer that water adsorbs primarily to water-wet inorganic (i.e. clay) mineral phases within the shale formation.

It is noted that extrapolating the regression lines to TOC concentrations of zero reveals the influence of other non-organic adsorption sites, hence significant deviations from this trend could be observed for individual samples depending on the compositional makeup. High-pressure gas sorption isotherms reported by Tan et al. (2014) showed sorption capacities of samples with similar clay content, thermal maturity and moisture content to exhibit even stronger positive linear correlations with TOC. The dependence of gas adsorption on TOC content has been reported by many other researchers (Manger et al., 1991; Schettler Jr & Parmely, 1991; Lancaster & Hill, 1993; Lu et al., 1995; Zuber et al., 2002; Chalmers & Bustin, 2007; Ross & Bustin, 2007a; Chalmers & Bustin, 2008; Ruppel & Loucks, 2008; Beaton et al., 2010; Strapoc et al., 2010; Weniger et al., 2010; Chareonsuppanimit et al., 2012; Wei et al., 2012; Gasparik et al., 2014; Rexer et al., 2014; Bi et al., 2016; Wang et al., 2016; Yang et al., 2016; Chang et al., 2017; Mendhe et al., 2017; Xia et al., 2017; Sharma & Galvis-Portilla, 2018). There are however existing studies that have reported little to no correlation between TOC and adsorption capacity (Gasparik et al., 2012; Zou et al., 2017). This trend is particularly notable in shales with low organic matter content and high clay content.

4.4.2 *Influence of thermal maturity*

Thermal maturity describes the heat-driven diagenetic changes of organic matter in sedimentary source rocks to generate hydrocarbons. Vitrinite reflectance, V_r, is widely used as indication of thermal maturity in shale analysis. It is measured by optical microscopy and reported by $\%R_o$ (where high $\%R_o$ indicates high maturity), the percentage of incident light reflected from the surface of vitrinite particles in the shale rock. In shales, thermal maturity of organic matter can generate

additional micropores (Bae & Bhatia, 2006; Jarvie et al., 2007; Chalmers & Bustin, 2008; Loucks et al., 2009; Ambrose et al., 2010; Sondergeld et al., 2010; Curtis et al., 2011; Bernard et al., 2012; Ma et al., 2015; Wu et al., 2017; Delle Piane et al., 2018; Zheng et al., 2018). This is due to the structural transformation of organic matter during maturation that generates smaller (nano-micro scale) pores as kerogen is thermally converted. The generation of more micropores with organic matter maturity increases the adsorption capacity.

It was previously suggested (Ramos, 2004) that the strong correlation between sorption and TOC masks the relationship between adsorption capacity and thermal maturation. However, Ross and Bustin (2009) found the sorption capacities of low TOC (0.2 – 4.9 wt%) overmature D-M shale samples ($1.6\% < R_o < 2.5\%$) to be higher than for high TOC (1.4 – 11.8) immature Jurassic shales ($R_o < 1.2\%$). This was qualitatively attributed to creation of sorption sites, and/or opening up microporosity onto which gas could sorb from structural transformations of the organic matter during thermal maturation. Nonetheless, other researchers have found concomitant decrease in CH_4 sorption capacity with increasing maturity (Chalmers & Bustin, 2007, 2008). This suggests, as previously pointed out by Schieber (2010) that intraparticle OM pore generation in thermally matured rocks may depend on the OM type. Loucks et al. (2012) also reported absence of OM pores in a matured (R_o of 0.89%) shale sample from the Atoka formation in the Midland Basin. The relationships established for any specific shale system, therefore, may not be directly applied elsewhere. But in general, the reviewed literature indicates that overmature and high TOC samples will show higher sorption capacity for both CH4 and CO_2 than the low mature and low TOC shales.

Some literature also reports thermal maturity to have noticeable effect on the shape of excess isotherms. Zhang et al. (2012) reported the methane Langmuir pressure, P_L of three Barnett shale samples ($\%R_o$ = 0.58, 0.81, 2.01) to distinctly shift towards lower pressures from the

immature to overmature gas shale samples under the same temperature conditions. Similar trends have been reported by Gasparik et al. (2014) and Tan et al. (2014). In a related study, Gasparik et al. (2012) also found positive correlation between TOC-normalized sorption capacities and maturity for black shales, but the trend became negative for over matured samples with R_o in a range of 2.8 – 3.3%.

4.4.3 *Influence of Kerogen Type*

Although TOC content has a superior control on gas sorption in shales, another key factor is kerogen type. Kerogen is the fraction of organic matter in sedimentary rocks (in this case, shale rocks) that is insoluble in organic solvents. It is formed from the decomposition of organic matter and is the precursor of hydrocarbon generation in source rocks. Kerogen is categorized as either Type I, which consists mainly of algal and amorphous kerogen and is highly likely to generate oil; Type II, which is formed from mixed terrestrial and marine source materials and can generate both oil and gas (but mostly waxy oil); and Type III, which is formed from terrestrial plant debris and typically generates gas upon maturation. In essence, the kerogen type depends on the source rock material and the deposition environment (Seewald, 2003; Boyer et al., 2006; Vandenbroucke & Largeau, 2007; Glorioso & Rattia, 2012).

Chalmers and Bustin (2008) investigated CH_4 sorption capacity for the Lower Cretaceous Buckinghorse Formation in Canada and found that per unit TOC volume basis, the capacity trend was Type II/III mixtures > Type III > Type II > Type I. They attributed this to Type III kerogen being more mature and generating more hydrocarbons and micropores at a given temperature compared to the other kerogen types. Zhang et al. (2012) conducted high pressure (0-16 MPa) methane sorption tests on organic-rich bulk shale samples and their isolated kerogens, with thermal maturity and kerogen type being the main variation in the samples. At all temperature conditions (35, 50, 65 °C), the CH_4 sorption capacity was in the order of Type III > Type II > Type I (**Figure 42**). The trend was

attributed to extensive aromatization from immature (Type I) to overmature (Type III) organic matter. They indicated that the progression from kerogen Type I to Type III, represents an increase in the relative fraction of aromatic hydrocarbons compared to the aliphatic and naphthenic hydrocarbons, as reported by other researchers (Tissot & Welte, 1984; Helgeson et al., 2009). The findings of Zhang et al. (2012) depict methane adsorption to be influenced by the chemical structure of the organic matter. The details and concept of the effects exerted by organic functional groups on gas adsorption, particularly CO_2 is not well addressed in the literature and deserves further investigation. We also note, as indicated by Loucks et al. (2012) that different kerogen types exhibit differing propensities to the development of intraparticle OM pores. The storage capacity trend reported for a shale Basin system based on kerogen types may therefore not be applicable to shales from different Basins. This complicates the generalization of the effects that kerogen type exerts on adsorption capacity. We recommend further studies on the association of OM pores and kerogen type to elucidate this phenomenon.

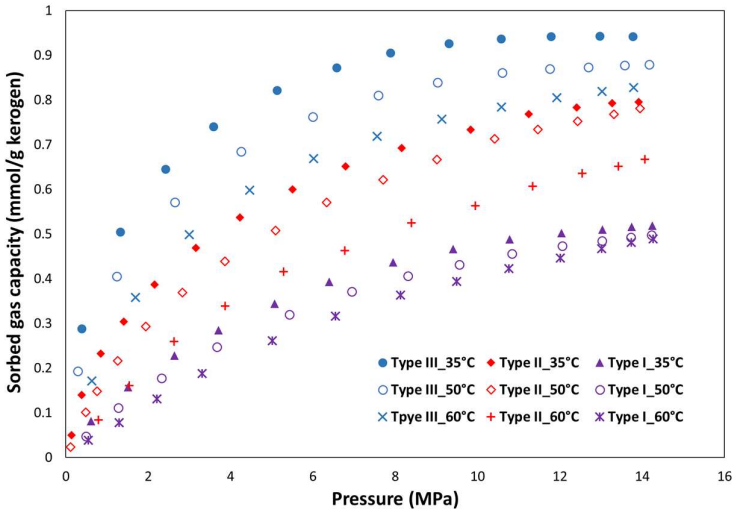

Figure 42 Effect of kerogen type on methane sorption capacity at different temperatures (Zhang et al., 2012).

4.4.4 *Influence of Inorganic components*

Shale usually contains clay, quartz or carbonate mineral phases with trace amounts of albite and pyrite. These inorganic constituents contribute enormously to the surface area and influence pore size, cumulative porosity and sorption properties. Particularly, the clay minerals are reported (Slatt & O'Brien, 2011; Milliken et al., 2013) to contribute to the shale micropore volume. In contrast to coals, where mineral matter seems to have little influence on CH_4 sorption capacity (e.g. Faiz et al., 1992; Rice et al., 1993; Bustin & Clarkson, 1998) but significantly affects CO_2 sorption (e.g. Karacan & Mitchell, 2003; Weniger et al., 2010), mineral components in gas shale systems have been proven to have appreciable sorption capacity for both gases (Aylmore, 1974; Heller & Zoback, 2014).

Preliminary adsorption studies on Devonian gas shale samples by Schettler Jr and Parmely (1991); Lu et al. (1995) exclusively highlighted the inorganic clay minerals to contribute as sorption sites in shale systems due to their microporous nature. Schettler Jr and Parmely (1990) originally postulated TOC to be of secondary importance in shale systems with low organic content. This conclusion was later reiterated by Busch et al. (2008) who attributed the high CO_2 sorption capacity of Muderong shales (TOC < 0.5%) entirely to its clay mineral constituents. The strong positive correlation of shale clay content to sorption capacity is emphasized in other reports (Chalmers & Bustin, 2008; Gasparik et al., 2012; Luo et al., 2015; Wang & Yu, 2016; Lutyński et al., 2017) where low TOC shale samples demonstrated high sorption due to their high clay contents. The specific influence of clay on shale sorption, however, is less evident in shales with high TOC content (Wang et al., 2013; Gasparik et al., 2014; Tan et al., 2014; Bi et al., 2016).

The microporous crystal layers of clay serve as ideal adsorption sites due to the large surface area (Venaruzzo et al., 2002). The contributions differ with clay type. Ross and Bustin (2009) reported clay-rich (low

Si/Al ratio) shales to have superior gas storage capacities over their silica-rich (high Si/Al ratio) counterparts. Ji et al. (2012) conducted sorption experiments (up to 15MPa) on dried clay-rich rocks at varying temperatures (35 – 65 °C) to shed light on the relative influence of clay type on methane adsorption. They established physisorption as the dominant mechanism for CH_4 adsorption on clay and noted sorption capacity to proceed in the order of montmorillonite > illite/smectite mixed layers > kaolinite > chlorite > illite. High-pressure CO_2 sorption experiments on pure clay minerals showed Ca-rich montmorillonite to have greater storage capacity than Na-rich montmorillonite (Busch et al., 2008). Gas shale reservoirs are dominated by illite (Jarvie et al., 2001; Gasparik et al., 2012), possibly due to the illitization of kaolinite and smectite which occurs at temperatures between 80 and 120 °C (Pytte & Reynolds, 1989). The temperatures of high organic content shale systems is in the range 96 to 277 °C (Lu et al., 2016). It is likely that at adequate conditions (especially in tropical zones) a blend of chemical and temperature gradient change could trigger a transition from illite to smectite (Eberl, 1984). This may occur particularly for uplifted shales exposed to weathering (e.g. shallow reservoir sections and outcrops). Since smectite has larger surface area (Šucha et al., 2001) and thus greater sorption, this could lead to potential overestimation of gas storage capacity during shale gas exploration. Additional study is recommended to understand the possibility of illite-smectite reversal transformation in clays found in shale formations.

It must be pointed out that clays are naturally hydrophilic and may present experimental challenges when correlating shale sorption capacity to clay content. For example, Chalmers and Bustin (2008) observed that the TOC-normalized CH_4 sorption capacity in dry samples from the Bucking horse formation in Canada positively correlated with clay content whereas no correlation existed for moisture equilibrated samples. Data obtained from as received or moisture equilibrated, and dried

samples should therefore be evaluated carefully to accommodate this fundamental clay-water affiliation.

4.4.5 *Influence of moisture*

Moisture is reported to correlate positively with organic matter and clay content in shale formations (Chalmers & Bustin, 2007; Passey et al., 2010) which makes it a crucial subsurface component to be analyzed in sorption experimental procedures. Many authors have addressed the effect of moisture on gas adsorption by comparing the adsorption capacity of dry samples and moisture equilibrated samples (Lu et al., 1995; Ross & Bustin, 2007a; Busch et al., 2008; Ross & Bustin, 2009; Gasparik et al., 2012; Aljamaan, 2013; Gasparik et al., 2014; Tan et al., 2014; Yuan et al., 2014; Yang et al., 2016; Zou et al., 2018) The result indicates that sorption capacity decreases with increasing moisture content until a certain equilibrium (critical) moisture content is attained for the sample. This equilibrium moisture content is representative of the maximum moisture saturation that can adsorb on the shale surfaces.

When present, water sorbs strongly on organic functional groups containing oxygen via hydrogen bonding (Dubinin, 1980) and has secondary tendencies to interact with pre-adsorbed water and charged surfaces of mineral matter (especially chemisorptive clay). Thus, besides attaching to primary (water-wet) sorption sites in the clay matrix, molecular water also competes with CO_2 and CH_4 for adsorption sites and causes a reduction in the gas sorption capacity. In shales, besides attaching onto surfaces, water molecules can condense in inorganic pores, occupying the smaller capillaries first before filling the larger pores as relative humidity increases (Zolfaghari et al., 2017a; Zolfaghari et al., 2017b). The water molecules can also aggregate as clusters at high pressure (Aljamaan, 2013; Yang et al., 2016; Huang et al., 2018) to block gas-enterable pores and serves as an added negative effect on gas sorption capacity.

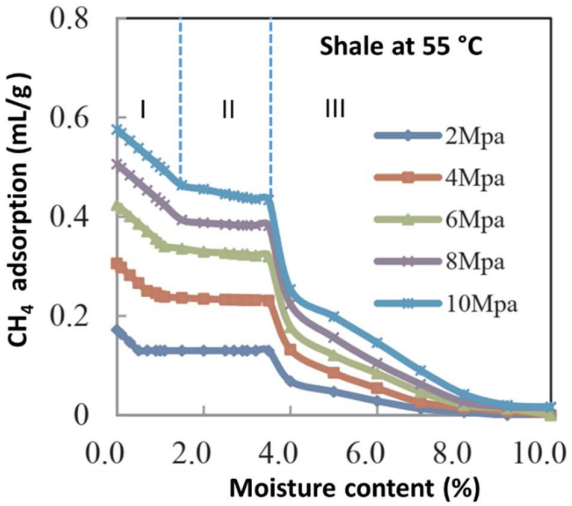

Figure 43 Effects of moisture content on methane maximum sorption capacity at 55°C (Fan et al., 2018).

The equilibrium moisture content depends on the shale maturity, organic richness and organic type (Chalmers & Bustin, 2008). The value for selected European gas shale samples was estimated (Gasparik et al., 2014) to be at or below 75% relative humidity (RH). Merkel et al. (2015) reported similar values for the moisture saturation threshold (50 – 75% RH) of Bossier and Haynesville shales from the U.S. A recent report by Fan et al. (2018) indicated that the methane sorption capacity versus moisture content exhibited three distinct decreasing stages separated by two threshold moisture contents (**Figure 43**). They performed CH_4 sorption experiments on gas shale samples from the Sichuan Basin in China at 35, 45 and 55 °C and pressures up to 10MPa. They attributed the initial reduction (stage I) to competitive adsorption between water and methane until an extended stagnant period (stage II) where all possible hydrophilic sites are filled. They postulated that water condensation in the clay pores and some organic hydrophobic pores was responsible for the late convex-like decrease (stage III) in the adsorption capacity. The moisture effect is however reported to be masked in high

TOC and over mature gas shales (Ross & Bustin, 2007a; Wang & Yu, 2016).

4.4.6 *Influence of temperature*

Thermodynamically, adsorption is an exothermic process and the effect of changing the equilibrium temperature is hinged to the Le Châtelier principle. Therefore, less adsorption is expected with increasing temperature. This relation was first reported for shales by Lu et al. (1995) who investigated sorption as a function of both pressure and temperature on Devonian shales and showed the sorption capacity to decrease with temperature. Recently, Merey and Sinayuc (2018) confirmed through adsorption measurements at 25, 50 and 75 °C that adsorption capacity increases for both CH_4 and CO_2 when temperature is decreased. This concurs with other experimental evaluations (Guo, 2013; Guo et al., 2013; Hao et al., 2013; Fan et al., 2014; Duan et al., 2016; Chang et al., 2017; Pozo et al., 2017; Zou et al., 2017; Liu et al., 2018).

Zhang et al. (2012) reported that the decrease in sorptive capacity with temperature occurred on both bulk gas shale samples (of original composition) and their isolated kerogens. Gasparik et al. (2014) constructed methane isotherms at experimental temperatures ranging up to 100 °C for immature (V_r=0.5) and mature (V_r=0.9) shale samples and up to 150 °C for over-mature (V_r=1.5) samples and reported that besides reduction in sorptive capacity, this sorption capacity was reached at a higher pressure when the temperature was increased. This implies that for the same sample, adsorption capacity decreases with temperature and that less gas can adsorb at lower pressures. The interrelation of adsorbed gas amount with temperature and pressure is depicted in **Figure 44.**

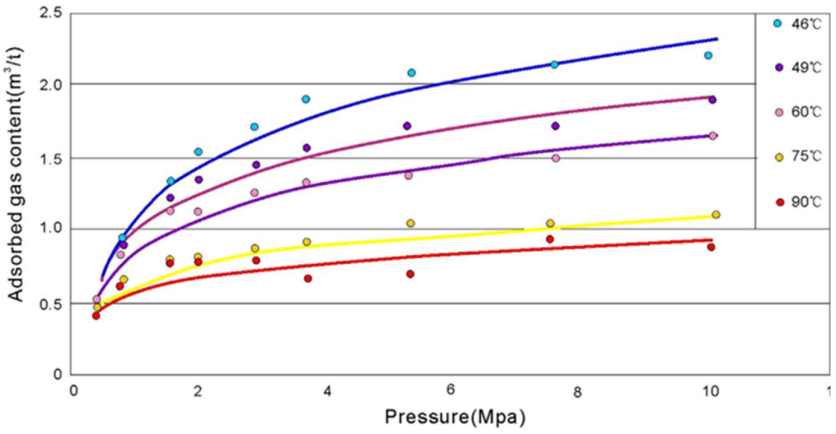

Figure 44 Variation of adsorbed CH4 amount with temperature performed on gas shale samples of the Ordos Basin in China (Guo, 2013).

4.4.7 *CO_2 versus CH_4 sorption on shale*

The first investigation of CO_2 and CH_4 sorption on the same shale material was conducted by Nuttal et al. (2005). They measured isothermal CH_4 and CO_2 adsorption on several Devonian black shales from Kentucky and found CO_2 absolute mass adsorption to be approximately 5 times greater than that of CH_4 at the same pressure. Following their report, several authors (Weniger et al., 2010; Kang et al., 2011; Chareonsuppanimit et al., 2012; Aljamaan, 2013; Heller & Zoback, 2014; Luo et al., 2015; Charoensuppanimit et al., 2016; Hong et al., 2016; Cancino et al., 2017; Pozo et al., 2017) have performed CO_2 and CH_4 gas sorption measurements on the same gas shale sample under controlled experimental conditions and reported consistently higher CO_2 sorption relative to CH_4. The reported CO_2/CH_4 absolute mass sorption ratio ranges between 1.3 to 10 for dry shale samples (**Figure 45**). The ratio is expected to be relatively lower at moist conditions for the same shale sample since sorption capacity in general is lower for moist shales (see **Figure 41**). There is limited data in the literature that compares the

CO_2/CH_4 sorption ratio for the same sample at dry and moist conditions. Such an experimental study would be relevant to confirm this trend.

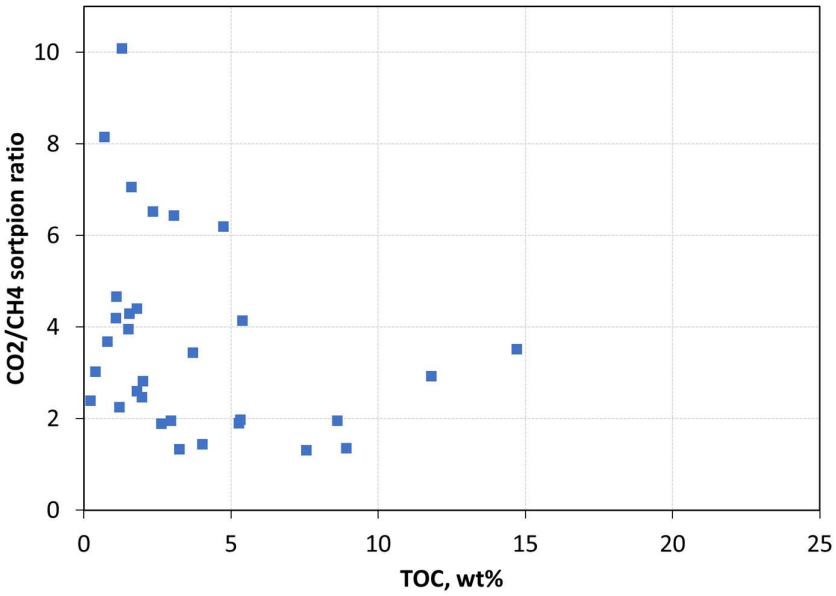

Figure 45 CO2/CH4 sorption ratio for different dry shale samples as a function of total organic carbon content. Data sets are taken from Langmuir volumes reported in the evaluations of Nuttal et al. (2005); Heller and Zoback (2014); Luo et al. (2015); Hong et al. (2016); Cancino et al. (2017); Pozo et al. (2017).

The relative sorption capacity of gas shale materials for either CO_2 or CH_4 is controlled by the respective interaction energy (thermodynamic forces), molecular size and accessibility of each gas type to the microporous network of the shale matrix system (steric forces). The tetrahedral molecular geometry of CH_4 is somewhat rounded, compared to CO_2 which has a linear molecular geometry. The dynamic diameter of CO_2 is about 0.33 nm as compared to 0.38 for CH_4 (Duan et al., 2016). The effective size of CO_2 is therefore smaller and can access narrower pores in the shale matrix and contacts a greater volume of the shale system (Kang et al., 2011). The reviewed experimental results depict that the steric and thermodynamic controlling parameters favor adsorption of

CO_2 over CH_4 in gas shales. The mechanism of CO_2 accessibility is reportedly enhanced at supercritical conditions where gaseous CO_2 transitions to supercritical CO_2 (Sc-CO_2). Sc-CO_2 is completely wetting to the shale rock, with liquid-like density, but with viscosity and diffusive properties close to gas behaviour (Wang et al., 2012). This unique physicochemical feature can improve the volumetric sweep during CO_2 injection and potentially increase the CO_2 subsurface storage amount by allowing Sc-CO_2 to contact more available sorption sites deeper within the formation.

Binary CO_2-CH_4 and mixed-gas sorption experiments evaluating the selectivity of gas shales for either gas species under the same pressure and temperature conditions have also been recently reported on the same shale sample in the literature. In these tests, a gas detection device (e.g. gas chromatograph) supplements the conventional sorption experimental setup that allows the determination of the gas mole fraction of each species in the mixture. During the tests, the shale samples are initially saturated with varied molar ratios of CO_2 and CH_4 at the desired experimental conditions. The majority of these authors (Pusch et al., 2012; Luo et al., 2015; Duan et al., 2016; Cancino et al., 2017; Huang et al., 2018; Ma et al., 2018) observed preferential adsorption of CO_2 over CH_4. It is reported that the selectivity of CO_2 in a gas mixture experiment evolves with pressure and is significantly higher at low pressures (Cancino et al., 2017) most likely due to the dominance of micropore filling associated with low temperatures. The adsorption selectivity parameter (represented as α) is frequently used to evaluate the competitive adsorption between CO_2 and CH_4 and given as (Duan et al., 2016):

$$\propto_{CO_2/CH_4} = \frac{x_{CO_2} y_{CH_4}}{x_{CH_4} y_{CO_2}} = \frac{V_{LCO_2}/P_{LCO_2}}{V_{LCH_4}/P_{LCH_4}} \quad (87)$$

where x and y variables are the molar fractions of the gas species in the adsorbed phase and free gas phase respectively for gas mixture evaluations and V_L, P_L are the Langmuir parameters. A value of

$\propto_{CO_2/CH_4} > 1$ suggests that adsorbed CH_4 can be displaced by CO_2. Larger values represent stronger displacement capacity of CO_2 over CH_4. The CO_2 selectivity over CH_4 depends on shale matrix composition and pore structure. For iso-TOC samples, high clay content and micropores favours higher $\propto_{CO_2/CH_4}$ (Duan et al., 2016). The variation of $\propto_{CO_2/CH_4}$ for some selected shales in China and the U.S are shown in **Figure 46** where the selectivity is seen to decrease with increasing TOC.

In coals, preferential adsorption of CH_4 over CO_2 in mixed-gas sorption experiments has been reported, particularly at low pressures (Crosdale, 1999; Busch et al., 2003; Busch et al., 2006; Majewska et al., 2009). In shale samples, however, consistent CO_2 preferential adsorption in the entire pressure range has been experimentally proven and verified by simulation studies (e.g Merey and Sinayuc 2016). These experiments are however limited, and further studies of multi-component sorption in gas shales is recommended to validate the trend.

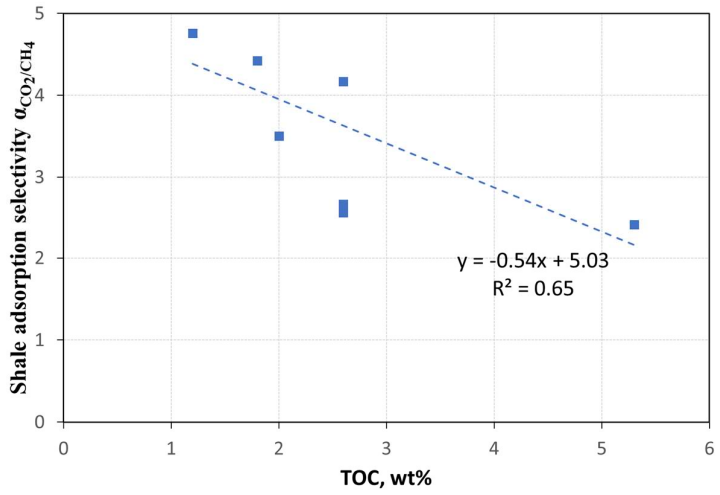

Figure 46 Variation of shale adsorption selectivity $\propto_{CO_2/CH_4}$ different dry shale samples from China and the U.S. as a function of total organic carbon content (Heller & Zoback, 2014; Pei et al., 2015; Duan et al., 2016; Cancino et al., 2017).

4.4.8 *Current practice of dynamic CO_2-CH_4 exchange*

In gas shales, the experimental approaches to evaluate CO_2-CH_4 exchange and gas recovery have been conducted implicitly by measuring how effectively CO_2 can replace already adsorbed CH4 in a closed system. The procedures differentiate between the CO_2 and CH_4 molecules existing as adsorbed or free phase throughout the dynamic CO_2-CH_4 exchange within the shale sample at specific time steps. During these tests, usually shale material (which is often crushed) is initially saturated with CH_4 at desired experimental conditions and allowed to equilibrate before CO_2 is injected at specified criteria. The CH_4 recovery yield is quantified by the resulting amount of originally adsorbed CH_4 released from the adsorbed state.

Some authors have employed the usual Gibbsian surface excess (GSE) variable for computations through the application of conventional sorption techniques, whereas others have used fluid detection techniques, like Nuclear Magnetic Resonance (NMR), for evaluation. NMR characterizes the existing states of hydrogen (^1H) proton-containing fluids existing within a porous media (Coates et al., 1999). NMR-based techniques have been used successfully for petrophysical characterization of nano-porous structures in coal and gas shale (Mullen, 2010; Jin et al., 2017; Yin et al., 2017b; Zhou et al., 2018), monitoring flow and dispersion in porous media (Manz et al., 1999), evaluating CO_2 and CH_4 self-diffusion (Pusch et al., 2012) and CO_2 sorption on rock surfaces (Bernin & Hedin, 2018). A summary of the various findings from CO_2-CH_4 exchange tests are presented in **Table 11**.

Table 11 : Experimental studies of CO_2-CH_4 dynamic exchange conducted on shales.

Author (s)	Location	Procedure	Operating Conditions	Findings	Cons
Huo et al. (2017)	Longmaxi shales, China	Volumetric-based method applied to dried crushed samples	Fixed temperature of 45 °C. Constant initial equilibrium pressure of CH4 of 4.5MPa. CO_2 injection at varied pressures of 5.2, 6.3, 7.3, 8.4, and 9.3 MPa. Final system equilibrium pressures ranged were 4..7, 5.6, 6.5, 7.5 and 8.4 MPa respectively	The amounts of recovered CH_4 and stored CO_2 increase with CO_2 injection pressure. CH_4 recovery yield was higher for shales with smaller micropores (i.e. having lower CH_4 adsorption performance)	Inherent uncertainties of evaluating excess sorption measurements. Final system equilibrium pressure not allowed to reach injection value. It is unclear what determined when to stop the test for each injection pressure step
Liu et al. (2017)	Longmaxi shales, China	Nuclear Magnetic Resonance (NMR) based method on dried crushed samples	Fixed temperature of 35 °C. Varied initial equilibrium pressure of CH_4-saturated sample of 0.1MPa and 1.5MPa. CO_2 injected at constant pressure of 4.5MPa	CO_2 injection improved recovery yield of CH_4 in the adsorbed phase by an additional ~25%.	Rather simplified laboratory conditions devoid of relevant in situ reservoir complexities (e.g High temperature, high pressure, presence of water). Uncertainties

Zhao and Wang (2018)	Longmaxi shales, China	NMR-based technology on dried crushed samples	Fixed temperature of 25 °C. Initial equilibrium pressures of the CH_4-saturated sample was ~10MPa. CO_2 injection pressure not specified. Final equilibrium system pressures varied between 11.8 to 12.5 MPa.	Decreased adsorbed molar amounts of CH_4 due to CO_2 injection. They suggested the inclusion of secondary stimulating (e.g. hydraulic fracturing) methods in the design of shale CO_2 injection since the CH_4 was predominantly restricted to the pore center after desorption by CO_2 exchange.	in NMR detection capabilities, particularly in the presence of e.g. moisture, pyrite

4.5 Discussions and limitations

In part one of this project, we have presented a mathematical model for production of shale gas by considering shale matrix with an induced fracture extending from a well perforation. Shale gas is stored in the matrix as free gas and in adsorbed form, the latter modelled by a Langmuir isotherm. The extended model accounting for non-Darcy flow, gas slippage, apparent permeability is also presented. The role of geometrical and intrinsic properties of the fracture-matrix system were investigated and further interpreted by dimensionless numbers. The proposed 1D+1D model is a useful tool to evaluate sensitivity of parameters such as fracture and matrix permeability, perforation interval, fracture geometry, adsorption and compressibility on shale gas production. The model is simple enough to allow for qualitative understanding of the role of these parameters individually. However, the model presented in 3.1.3 is limited to continuum and slip flow regime

where the gas transport is governed by viscous forces and Knudsen diffusion is neglected. This assumption is valid for gas transport from near well and well-induced fracture region where perforations and jetting of high viscous fluid causes pore size to be sufficiently large. Yao et. al. (2013) showed that for a mean equivalent pore radius equal to or greater than 0.1 µm, the production predicted by the Darcy equation is very close to that predicted by other models considering Knudsen diffusion. The model (3.1.3 to 3.1.4) considers flow of gas only from stimulated reservoir volume, i.e. the domain affected by the hydraulic fracture. However, flow of gas from beyond the tip of fracture and crossflow could also contribute to overall recovery. Moreover, the model assumes ideal gas with constant viscosity. The density and viscosity of shale gas varies significantly due to the associated high pressures. These effects should be evaluated before extending the model to field scale application.

The model can further be extended to account for geomechanical effects. The changes in porosity and permeability with effective stress can be captured and scaled in a similar way as presented giving rise to new dimensionless numbers. One such model was developed and presented in master thesis by Negård (2018) which we had supervised as part of this project.

The CO_2 injection model presented in 3.1.5 examines CO_2-ESGR during huff-and-puff injection to better understand the parameters controlling its feasibility and effectiveness. The mathematical model is presented where the CO_2-CH_4 substitution mechanism is implemented in an injection-production setting representative of field implementation. Experimental adsorption data were used to quantify the substitution parameters while typical field data were used for the operating and geometrical conditions. Through a series of simulations, the most amenable characteristics of the system are identified with emphasis on the critical parameters that control the success of CO_2 injection as an ESGR process. However, the presented model has some limitations.

Only gas phase is considered in the model. More viscous and dense water is often used as the major source of fracturing fluid and its influence generally needs to be evaluated. If the water is at immobile saturations, the presented single-phase model can still be applied if effective permeability and adsorption measurements are available for input. Secondly, ideal gas behavior ($Z = 1$) is considered for both CO_2 and CH_4 gases for simplicity in the model. The gas deviation factor for the CO_2-CH_4 mixture varies in the range of 0.6 to 1.1 for pressures and temperature relevant to our study; 5 to 350 bars and 50°C (Adisoemarta et al. 2004). The use of accurate Z-values in the model might affect the results quantitatively. However, we still expect to see similar trends as already presented. Moreover, the effect of changing stresses in the matrix due to injection of CO_2 and production of CH_4 on reservoir properties and gas recovery should be evaluated.

Another aspect which is not considered in the model is the CO_2 transmissivity or how fast can CO_2 be injected through the well. Gas reservoirs are generally well above the critical point of CO_2 (pressure of 73.7 bar and temperature of 31°C and hence CO_2 will be in its supercritical state and will exhibit certain behavior which deviates from a normal gas and will impact the injectivity. Also, gravity will play a role at the flow rates considered in the model and hence affects the flow behavior of the supercritical CO_2 during ESGR. Through a series of experiments, Abba et al. (2018) showed that gravity is more dominant at lower injection rates. Also, they concluded that CO_2 injectivity may significantly be affected by the orientation of the injection into the displacing reservoir. Such effects are difficult to characterize using a 1D model and hence are not considered in this thesis.

A vast amount of investigations has been carried out to study the effectiveness and feasibility of CO_2-ESGR. However, some key research issues should be looked into:

- The majority of experimental work reported in the literature is conducted on crushed samples. To our knowledge, only Nuttal et al. (2003) reported adsorption data acquisition using an intact core. Their report highlighted the experimental difficulty involved since they only managed to capture CO_2 adsorption isotherm data for a single whole core out of twenty-six Devonian black shale samples. Using crushed samples is a quick and convenient means to perform measurements on shales, but an obvious trade-off is uncertainty in whether the data would be representative of actual reservoir conditions since it alters the structure of the porous medium (e.g. micro-fractures) and could lead to misrepresentative estimates of formation characteristics.

- The impact on gas sorption (i.e. isotherm shape) from organic matter content (TOC) and maturity, temperature and pressure and clay and moisture content are all relations that deserve attention. Particularly, lowered P_L values (associated with decreasing temperature or higher maturity) indicate that CH_4 will desorb more readily at lower pressures on higher maturity shales. Such affinity to remain sorbed in matured shales indicates that a greater reduction in CH_4 partial pressure will be required to desorb CH_4 during production. The selectivity of the surface towards CO_2 can be the solution to release the strongly sorbed CH_4 and is in such cases even more important to measure. The question of how significant adsorbed gas will be to overall production is a key concept and further investigation is required to properly correlate the P_L reduction to these parameters. Furthermore, measuring the density of the adsorbed gas phases is a key parameter in the commonly used modelling approaches that has not received much attention in experimental assessments.

- A notable concern for CO_2-ESGR is the impact of moisture which preferentially binds to hydrophilic clay surfaces and reduces sorption (and hence CO_2 sequestration) potential. Dried samples may overestimate the adsorption capacity. Although water in principle

like CO_2 can substitute CH_4 by adsorbing to hydrophilic surfaces and give EGR, water will usually exist also in aqueous phase and cause mobility issues related to presence of multiple phases and water blocking effects near the wellbore or macro-fractures. Pressurized fracking fluids are essential for creating flow paths in the reservoir. The standard is use of water, but there is potential in using water-free fracking methods (e.g. propane-gel, supercritical CO_2). Gas soluble fracking fluids should be positive for recovery as well as the environment (reduction of produced water).

- Reports (Heller & Zoback, 2014; Lu et al., 2016; Yin et al., 2016) indicate crushed shale to swell (especially for high clay-content shales) during gas adsorption which changes both the pore structure and roughness. The degree of adsorption-induced swelling is shown to vary depending on the shale composition and pore characteristics and achieves a stable state when adsorption equilibrium is attained. The extent to which swelling during CO_2 injection impacts sorption isotherms, rock mechanical and hydrological (permeability, porosity) properties is crucial.

- Mechanical weakening of organic-rich gas shales by CO_2 saturation has been reported, especially for supercritical CO_2 (Lyu et al., 2016a; Lyu et al., 2016b; Yin et al., 2017a; Lyu et al., 2018a; Lyu et al., 2018b) This is attributed to the modification of in-situ acid-base equilibria that triggers precipitation and dissolution of minerals (Liu et al., 2012; Carroll et al., 2013) and the ability of supercritical CO_2 to act as an organic solvent to extract non-polar aliphatic and polycyclic aromatic hydrocarbons from shale (Jiang et al., 2016; Yin et al., 2016). This could expand originally present gas seepage channels or generate flow channels with influence on the safety of sequestered CO_2. Most of the experimental results are reported for gas saturated shale samples monitored over a couple of days.

- Geochemical alterations of Australian Muderong shales were suggested to explain differences in specific surface areas before and after CO_2 sorption experiments conducted at reservoir conditions (T = 45–50 °C; P < 20 MPa) (Busch et al., 2008). The inferred geochemical changes however could not be quantified and seemed to occur only at high pressures. In a subsequent study, Busch et al. (2009) assessed the interrelation of CO_2-mediated reactions and transport properties in the Muderong shale by exposing crushed samples to CO_2 in the presence of water at 15 MPa and 50 °C for different equilibration time periods. They reported significant changes (equilibration times < 1 month) in mineralogical composition, particularly with the increase of smectite and K-feldspar contents and reduction in illite content. Mineral changes in shale sample plugs have also been reported in the literature (Wollenweber et al., 2009; Battistutta et al., 2010). The extent to which these changes could influence storage integrity needs further investigation. Available data (Angeli et al., 2009; Busch et al., 2010; Wollenweber et al., 2010; Edlmann et al., 2013) indicates shale cap rocks to be adequately resilient towards CO_2 leakage and demonstrates an encouraging note for the sequestration of CO_2 in gas shale systems.

As seen, production and enhanced recovery of gas from shales is a complex process. Sorption is a central mechanism in this interplay. Despite this complexity, promising results have been achieved at lab and field scales (Louk et al., 2017) and CO_2 injection for ESGR is becoming a better understood process.

4.6 Implications on the industry

The proposed 1D+1D model provides a tool for interpretation of complex shale gas production systems. Characterizing the shale gas production based on two dimensionless numbers, simplifies the complexity and helps to provide intuitive understanding of flow

mechanisms and fracture-matrix interaction. It can be used for screening of flow regimes at different operational configurations and hence appropriate modelling approaches. The model, via the number ω and fracture geometry, can be used to optimize fracture network design and potentially in identifying stimulation operations that may significantly improve production rates and ultimate recovery from unconventional gas reservoirs. Furthermore, the model with non-Darcy flow and the introduction of transition factor $f(z)$ provides a clear understanding on exactly where the transition from Darcy to non-Darcy flow occurs between matrix to fracture. The transition factor quantifies this transition and helps to assess the significance of it on flow performance.

The second part of the thesis examines CO_2-ESGR during huff-and-puff injection and provides better understanding of the parameters controlling its feasibility and effectiveness. The proposed adsorption isotherm provides an alternative way of modelling adsorption based on specific surface area rather than number of moles. The strength of the given formulation is that we generalize to multilayer adsorption, assign more direct physical meaning to the involved parameters and preserve parameters such as the total surface area. The isotherm thus helps to quantify adsorption behavior under various conditions. The proposed model is a useful tool to evaluate both static multicomponent adsorption for CO_2-CH_4 substitution as well as dynamic implementation of CO_2 injection for enhanced gas recovery by coupling the adsorption model to relevant transport mechanisms in shale such as diffusion, advection and gas slippage. Moreover, the review of the state of research on CH_4 and CO_2 sorption in shale determines gaps in experimental research that should be addressed. This work thus enables the industry to identify ideal candidates for enhanced gas recovery by CO_2 injection and screen available gas reservoirs for CO_2 storage. Such technology would create symbiotic economic drivers for carbon capture, leading towards carbon neutral energy production with strategic environmental benefits.

Chapter 5 - Conclusions and future work

5.1 Conclusions

In this thesis, we have presented a 1D+1D mathematical model for production of shale gas by considering shale matrix with an induced fracture extending from a well perforation. From the numerical investigations presented, we draw the following conclusions:

- The shape of the fracture only matters for narrower average fracture width. At high width, no effect of fracture shape was seen on production rate and recovery. A wider fracture near the well and narrow fracture at its end can increase the early phase production but give lower production rates at late times.
- At sufficiently high fracture permeability, and width the pressure and recovery profiles are very similar and do not differ with permeability or shape. However, low fracture permeabilities resulted in delayed production and greater sensitivity to fracture shape.
- Scaling the model allowed derivation of two important dimensionless numbers controlling the shale gas production; the ratio of gas diffusion time scale of the fracture to that of the matrix α, and the ratio of capacity to store gas (free and adsorbed) in the matrix to that in the fracture β.
- The product $\alpha\beta$ expresses how much time it takes to diffuse the gas in place through the fracture to the well compared to the time it takes to diffuse that gas from the matrix to the fracture. For $\alpha\beta \ll 1$ the residence time in the fracture is of negligible importance and fracture properties such as shape, width and permeability can be ignored. However, if $\alpha\beta \approx 1$ the residence time in the fracture becomes important and variations in all those properties have significant effects on the solution.
- Due to the parameters appearing in $\alpha\beta$ we can state that the fracture properties will have no effect on the production if the matrix is much less permeable than the fracture, the fracture is short (low volume) and wide and the fracture spacing is large.
- The case with $\alpha\beta \ll 1$ can be referred to as *matrix-dominated*. All

the fracture gas is instantly produced giving a minimum pressure in the fracture and uniform gas production from the matrix along the entire fracture. The case with $\alpha\beta \approx 1$ can be referred to as *fracture-dominated* since the residence time in the fracture controls the rate of recovery. This scenario can be observed even when the fracture is many orders of magnitude more permeable than the matrix since the high-volume ratio β typically compensates for the low time scale ratio α.

- Shale gas production can be optimized by designing the fracture properties to be in the range $\alpha\beta < 10^{-2}$ such that there are no limiting effects from the fracture on production. Note in particular that if the fractures are placed closer (more frequent perforations) it is more likely that the fractures can become a limiting factor.
- Non-Darcy flow shifts the flow regime towards fracture dominated. The non-Darcy effects are more pronounced in fracture than matrix and cause greater increase in fracture diffusion time than matrix diffusion time.
- Theoretical and numerical results indicated that the model cases could be classified according to *matrix-dominated* for $\omega \ll 1$ (the matrix then limits the gas production) and *fracture-dominated* where $\omega \approx 1$ (the fracture limits the gas production).
- Non-Darcy flow in the matrix is significant when the flow regime is matrix dominated and non-Darcy flow in matrix significantly reduces matrix flow rate. When any of these conditions is not met, non-Darcy flow in the matrix is not relevant. This is mathematically equivalent to the dimensionless number $\omega \ll 1$ and $f_{ref}^{m} \ll 1$ as expressed in our model.
- At sufficiently high fracture permeability (k^f>100 mD for our base case), diffusion time in the fracture reduces. Recovery profiles then become very similar and unchanging with permeability both for Darcy and non-Darcy flow. The impact of non-Darcy flow in the matrix becomes more sensitive at high fracture permeability.
- The magnitude of the f-factor helps to quantify the transition of Darcy flow to non-Darcy flow. At high non-Darcy flow constant C_β, non-Darcy effects in the matrix show greater sensitivity due to lower f_{ref}^{m} value and should be considered for evaluation of shale gas

production.

- Because of the parameters appearing in ω, we can conclude that matrix properties will control the production if f_{ref}^{m} is low, matrix is much less permeable than fracture, the fracture volume is low and the fracture spacing is large.

We have also investigated a new multicomponent isotherm for shale gas enhanced gas recovery by CO_2 injection under static and dynamic conditions. The model is based on assuming a fixed specific surface area that directly determines the surface capacity rather than assuming that the surface can store a fixed maximum number of moles or has a fixed number of sites. The adsorption of different species then depends on how much many moles are adsorbed per area at full capacity and how much of the capacity (area) is covered by adsorbed species. The static conditions considered either fixed gas composition or fixed mass systems. The dynamic conditions considered cyclic gas production – CO_2 injection. The effects on methane and carbon dioxide storage, gas recovery and enhanced gas recovery potential were investigated.

- Under the assumption of ideal CO_2 and CH_4 gas phase behavior, our model indicates that injection of CO_2 into a shale with unsaturated surface (remaining capacity) will lead to a net adsorption and reduction of the total pressure. The adsorption processes thus resist pressure buildup and mitigate CO_2 injection.
- When CO_2 fully replaces CH_4 on a fully saturated surface, the amount of moles able to be stored per area for CO_2 vs CH_4 will determine if a net number of moles are added or removed as determined by the ratio $S_{m,c}n_c/S_{m,m}n_m$. For Marcellus shale that ratio was ~24 which means also in this case pressure will decline spontaneously by adsorption.
- Key parameters determining recovery during pressure depletion are initial pressure and isotherm parameters (determining gas in place) and well pressure. At zero well pressure, full recovery can theoretically be obtained.
- Enhanced gas recovery can be obtained by CO_2 injection if the CO_2 is able to effectively mix with the methane in place. The mixture will

then dilute the methane and replace it with higher concentrations of CO_2 in every cycle. The repressurization boosts the driving force. Hence, even without adsorption, there is an EGR effect of CO_2.

- Adsorption will improve the potential of CO_2 EGR further since more adsorbed CH_4 is released at same total pressure and since injection will go faster due to pressure reduction in the adsorption process. Diffusion of CO_2 into the matrix is a key parameter determining the effectiveness of the EGR method. That will depend on matrix spatial dimension, diffusion time, matrix tortuosity and permeability. If diffusion is strongly limited, there is little benefit of regular pressure depletion.

The key takeaways from review of experimental sorption studies of CO_2 and CH_4 in shales are:

- Both CH_4 and CO_2 exist in critical thermodynamical state for most relevant reservoir conditions. CH_4 sorption increases monotonously with pressure from pressures near ambient to reservoir and can in most cases be described by a Langmuir isotherm. CO_2 however changes sorption behavior at the critical pressure. At lower pressures, the sorption increases monotonously, while near the critical pressure a peak in adsorption is reached and desorption occurs with increased pressure. This is not captured in low pressure experiments and standard isotherm models, e.g. multicomponent Langmuir models, are not sufficient. Extended isotherms or PVT-relations that treat both the gas and sorbed phases accurately should be applied.
- CH_4 and CO_2 adsorption storage capacity have a strong positive correlation with Total Organic Carbon, where a greater capacity is measured for CO_2.
- More mature shales tend to have higher storage capacity, but also lower Langmuir pressure indicating that the gas desorbs less easily on pressure reduction.
- Kerogen type also influences storage capacity of CH_4 with capacity trend as Type III > Type II > Type I. More experimental data is suggested to fully support this trend. Especially, there seems to be

little or no data on the correlation between CO_2 storage capacity and kerogen type.

- Clays can increase the storage capacity for gas adsorption, but they strongly associate with water. Measurements on dry samples are therefore likely to yield higher capacity than original state or moisture equilibrated samples.
- Adsorption is an exothermic process and the heat of adsorption for CO_2 is greater than for CH_4 in shales. CO_2 is therefore more favorably adsorbed. Increased temperature opposes the adsorption reaction and explains observed trends; both gases adsorb less at higher temperature.

5.2 Future Work

This study opens the scope for a detailed future work. The current model creates a base which can easily incorporate non-linear flow mechanisms, geo-mechanical effects and other complex flow mechanisms that are not readily found in standard commercial software, and further be extended to field scale application.

Some of the planned works and ongoing activities (in terms of master/bachelor thesis and/or paper publications) include:

a) Developing analytical solution for production of shale gas in a fracture-matrix geometry. In line with previous work, the system behaves either as fracture or matrix dominated in terms of what limits production rate. Simplified versions of the solution can be derived for cases where either time scale becomes dominating. Shale gas production represents a complex system which can benefit from comparison with analytical solutions.
b) Investigating the influence of adsorption layer thickness and compressibility of shale matrix on ultimate recovery both with/without CO_2 injection for enhanced recovery.

c) Extending the proposed adsorption model to fracture-matrix settings for CO_2 enhanced shale gas recovery along with hysteretic compaction.
d) Study and incorporate the role of proppants and its influence on fracture-matrix interactions and gas production.
e) Upscaling of the model to multi-scale fractures for real field applications.

References

1. Abba, M., Abbas, A., Saidu, B., Nasr, G., & Al-Otaibi, A. (2018). Effects of gravity on flow behaviour of supercritical CO2 during enhanced gas recovery (EGR) by CO_2 injection and sequestration. In *Fifth CO_2 Geological Storage Workshop (Vol. 2018, No. 1, pp. 1-5). European Association of Geoscientists & Engineers*.
2. Adisoemarta, P., Frailey, S. M., & Lawal, A. S. (2004). Measurement of Z-factors for carbon dioxide sequestration. In *2004 AIChE Annual Meeting*.
3. Agista, M. N., Andersen, P. Ø., & Yu, Z. (2019). Modelling nanofluid injection in porous media. *Journal of Petroleum Science and Engineering*, **176**, 836-849.
4. Ahsan, R. and Fabricius, I.L. (2010). Sorption of magnesium and sulfate ions on calcite. *In 72nd EAGE Conference and Exhibition incorporating SPE EUROPEC 2010*, Extended Abstracts, SP13.
5. Alam, M.M., Ahsan, R., Shaik, A.K., and Fabricius, I.L. (2010). Surface charge of calcite and its influence on the electrical conductivity in chalk. In 80th Annual International Meeting, Society of Exploration Geophysicists, Expanded Abstracts, 2686-2691.
6. Alexander, T., Baihly, J., Boyer, C., Clark, B., Waters, G., Jochen, V., . . . Thaeler, J. (2011). Shale gas revolution. *Oilfield review,* **23**(3), 40-55.
7. Aljamaan, H. (2013). Petrophysical Investigation on Gas Transport Properties of the Barnett. Paper presented at the *SPE Annual Technical Conference and Exhibition*.
8. Al-Rbeawi, S. (2019). Flow-Regime-Based Inflow-Performance Relationships of Unconventional Fractured Reservoirs. *SPE Production & Operations*, preprint.
9. Al-Rbeawi, S. (2018). Performance-Based Comparison for Hydraulically Fractured Tight and Shale-Gas Reservoirs With and Without Non-Darcy-Flow Effect. *SPE Reservoir Evaluation & Engineering*, **21**(04), 981-1.

10. Ambrose, R. J., Hartman, R. C., Diaz Campos, M., Akkutlu, I. Y., & Sondergeld, C. (2010). New Pore-scale Considerations for Shale Gas in Place Calculations. Paper presented at the *SPE Unconventional Gas Conference*, Pittsburgh, Pennsylvania, USA.
11. Andersen, P., Evje, S., Kleppe, H. (2014). A model for spontaneous imbibition as a mechanism for oil recovery in fractured reservoirs. *Transport in Porous Media,* **101**(2), 299-331.
12. Andersen, P. Ø., Evje, S., Kleppe, H., Skjæveland, S. M. (2015). A Model for Wettability Alteration in Fractured Reservoirs. *SPE Journal*, **20**(6), 1-261.
13. Andersen, P. Ø., Evje, S. (2016). A model for reactive flow in fractured porous media. *Chemical Engineering Science*, **145**, 196-213. Angeli, M., Soldal, M., Skurtveit, E., & Aker, E. (2009). Experimental percolation of supercritical CO2 through a caprock. *Energy Procedia*, **1**(1), 3351-3358.
14. Artioli, Y. (2008). Adsorption. *Encyclopedia of Ecology*, pg. 60-65.
15. Arogundade, O., Sohrabi, M. (2012). A review of recent developments and challenges in shale gas recovery. Paper presented at the *SPE Saudi Arabia Section Technical Symposium and Exhibition*.
16. Aylmore, L. A. G. (1974). Gas sorption in clay mineral systems. *Clays and clay minerals*, **22**(2), 175-183.
17. Bae, J.-S., & Bhatia, S. K. (2006). High-Pressure Adsorption of Methane and Carbon Dioxide on Coal. *Energy & Fuels*, **20**(6), 2599-2607.
18. Battistutta, E., van Hemert, P., Lutynski, M., Bruining, H., & Wolf, K.-H. (2010). Swelling and sorption experiments on methane, nitrogen and carbon dioxide on dry Selar Cornish coal. *International Journal of Coal Geology*, **84**(1), 39-48.
19. Beaton, A. P., Pawlowicz, J. G., Anderson, S. D. A., Berhane, H., & Rokosh, C. D. (2010). Total organic carbon and adsorption isotherms of the duvernay and muskwa formations in alberta: shale gas data release. Energy Resources Conservation Board /Alberta Geological Survey: Edmonton, Alberta, Canada.
20. Belhaj, H. A., Agha, K. R., Nouri, A. M., Butt, S. D., Vaziri, H. F.,

& Islam, M. R. (2003). Numerical Simulation of Non-Darcy Flow Utilizing the New Forchheimer's Diffusivity Equation. Paper presented at *Middle East Oil Show*, Bahrain.

21. Berawala, D. S., & Andersen, P.Ø. (2019). Evaluation of Multicomponent Adsorption Kinetics for CO_2 Enhanced Gas Recovery from Tight Shales. Paper presented at *SPE Europec featured at 81st EAGE Conference & Exhibition, United Kingdom.*
22. Berawala, D. S., & Andersen, P.Ø. (2020). Evaluation of Multicomponent Adsorption Kinetics for CO_2 Enhanced Gas Recovery from Tight Shales. *SPE Reservoir Evaluation & Engineering,* preprint.
23. Berawala, D. S., Andersen, P. Ø., & Ursin, J. R. (2019). *Controlling Parameters During Continuum Flow in Shale-Gas Production: A Fracture/Matrix-Modeling Approach*. SPE Journal, **24**(03), 1378 – 1394.
24. Berawala, D. S., Ursin, J. R., & Slijepcevic, O. (2017). Sphere in Cube Grid Approach to Modelling of Shale Gas Production Using Non-Linear Flow Mechanisms. *World Academy of Science, Engineering and Technology, International Journal of Geological and Environmental Engineering*, **4**(9).
25. Bernard, S., Horsfield, B., Schulz, H.-M., Wirth, R., Schreiber, A., & Sherwood, N. (2012). Geochemical evolution of organic-rich shales with increasing maturity: A STXM and TEM study of the Posidonia Shale (Lower Toarcian, northern Germany). *Marine Petroleum Geology*, **31**(1), 70-89.
26. Bernin, D., & Hedin, N. (2018). Perspectives on NMR studies of CO2 adsorption. *Current Opinion in Colloid & Interface Science*, **33**, 53-62.
27. Beskok, A., Karniadakis, G. E. (1999). Report: a model for flows in channels, pipes, and ducts at micro and nano scales. *Microscale Thermophysical Engineering,* **3**(1), 43-77.
28. Bi, H., Jiang, Z., Li, J., Li, P., Chen, L., Pan, Q., & Wu, Y. (2016). The Ono–Kondo model and an experimental study on supercritical adsorption of shale gas: A case study on Longmaxi shale in southeastern Chongqing, China. *Journal of Natural Gas Science and Engineering*, **35**, 114-121.
29. Billemont, P., Coasne, B., & De Weireld, G. (2014). Adsorption of

carbon dioxide-methane mixtures in porous carbons: effect of surface chemistry. *Adsorption*, **20**(2-3), 453-463.

30. Bird, R. B. (2002). Transport phenomena. *Applied Mechanics Reviews,* **55**(1), R1-R4.
31. Blasingame, T. A. (2008). The characteristic flow behavior of low-permeability reservoir systems. Paper presented at the *SPE Unconventional Reservoirs Conference*.
32. Blok, K., Williams, R. H., Katofsky, R. E., & Hendriks, C. A. (1997). Hydrogen production from natural gas, sequestration of recovered CO2 in depleted gas wells and enhanced natural gas recovery. *Energy*, **22**(2), 161-168.
33. Boyer, C., Kieschnick, J., Suarez-Rivera, R., Lewis, R. E., & Waters, G. (2006). Producing gas from its source. Oilfield Review, **18**(3), 36-49.
34. Brunauer, S., Emmett, P. H., & Teller, E. (1938). Adsorption of gases in multimolecular layers. *Journal of the American chemical society*, **60**(2), 309-319.
35. Busch, A., Krooss, B. M., Gensterblum, Y., Van Bergen, F., & Pagnier, H. J. M. (2003). High-pressure adsorption of methane, carbon dioxideand their mixtures on coals with a special focus on the preferential sorption behaviour. *Journal of Geochemical Exploration*, **78-79**, 671-674.
36. Busch, A., Gensterblum, Y., Krooss, B. M., & Siemons, N. (2006). Investigation of high-pressure selective adsorption/desorption behaviour of CO2 and CH4 on coals: An experimental study. *International Journal of Coal Geology*, **66**(1), 53-68.
37. Busch, A., Alles, S., Gensterblum, Y., Prinz, D., Dewhurst, D. N., Raven, M. D., Stanjek, H., & Krooss, B. M. (2008). Carbon dioxide storage potential of shales. *International Journal of Greenhouse Gas Control*, **2**(3), 297-308.
38. Busch, A., Alles, S., Krooss, B. M., Stanjek, H., & Dewhurst, D. (2009). Effects of physical sorption and chemical reactions of CO2 in shaly caprocks. *Energy Procedia*, **1**(1), 3229-3235.
39. Busch, A., Amann-Hildenbrand, A., Bertier, P., Waschbuesch, M., & Krooss, B. M. (2010). The Significance of Caprock Sealing Integrity for CO2 Storage. Paper presented at the *SPE*

International Conference on CO2 Capture, Storage, and Utilization, New Orleans, Louisiana, USA.

40. Bustin, R. M., & Clarkson, C. R. (1998). Geological controls on coalbed methane reservoir capacity and gas content. *International Journal of Coal Geology*, **38**(1-2), 3-26.
41. Busch, A., Alles, S., Gensterblum, Y., Prinz, D., Dewhurst, D. N., Raven, M. D., . . . Krooss, B. M. (2008). Carbon dioxide storage potential of shales. *International Journal of Greenhouse Gas Control,* **2**(3), 297-308.
42. Bybee, K. (2006). Non-Darcy Flow in Hydraulic Fractures. *Journal of Petroleum Technology*. **58**(03), 58-59.
43. Cancino, O. P. O., Pérez, D. P., Pozo, M., & Bessieres, D. (2017). Adsorption of pure CO2 and a CO2/CH4 mixture on a black shale sample: Manometry and microcalorimetry measurements. *Journal of Petroleum Science Engineering*, **159**, 307-313.
44. Cao, P., Liu, J., & Leong, Y. K. (2016). Combined impact of flow regimes and effective stress on the evolution of shale apparent permeability. *Journal of Unconventional Oil and Gas Resources*. **14**, 32-43.
45. Cao, T., Song, Z., Wang, S., Cao, X., Li, Y., & Xia, J. (2015). Characterizing the pore structure in the Silurian and Permian shales of the Sichuan Basin, China. *Marine and Petroleum Geology*, **61**, 140-150.
46. Carman, P. C. (1937). Fluid flow through granular beds. *Trans. Inst. Chem. Eng.*, **15**, 150-166.
47. Carroll, S. A., McNab, W. W., Dai, Z., & Torres, S. C. (2013). Reactivity of Mount Simon Sandstone and the Eau Claire Shale Under CO2 Storage Conditions. Environmental Science & Technology, **47**(1), 252-261. Chareonsuppanimit, P., Mohammad, S. A., Robinson Jr, R. L., & Gasem, K. A. (2012). High-pressure adsorption of gases on shales: Measurements and modeling. *International Journal of Coal Geology*, **95**, 34-46.
48. Chen, Z., Huan, G., & Ma, Y. (2006). Computational methods for multiphase flows in porous media (Vol. 2). SIAM.
49. Chalmers, G. R., & Bustin, R. M. (2007). The organic matter distribution and methane capacity of the Lower Cretaceous strata

of Northeastern British Columbia, Canada. *International Journal of Coal Geology*, **70**(1-3), 223-239.

50. Chalmers, G. R., & Bustin, R. M. (2008). Lower Cretaceous gas shales in northeastern British Columbia, Part I: geological controls on methane sorption capacity. *Bulletin of Canadian petroleum geology*, **56**(1), 1-21.
51. Chang, T., Shu, Y., Ma, Y., Xu, X., & Niu, Y. (2017). Isothermal Adsorption and Desorption Properties of Marine Shales on Longmaxi Shale in South China. *Open journal of geology,* 7(12), 1819-1835.
52. Chareonsuppanimit, P., Mohammad, S. A. R., Robert L., Robinson, R. L., & Gasem, K. A. M. (2012). High-pressure adsorption of gases on shales: Measurements and modeling. *International Journal of Coal Geology*, **95**, 34-46.
53. Charoensuppanimit, P., Mohammad, S. A., & Gasem, K. A. M. (2016). Measurements and Modeling of Gas Adsorption on Shales. *Energy & Fuels*, **30**(3), 2309-2319.
54. Cipolla, C. L., Lolon, E. P., Erdle, J. C., Rubin, B. (2010). Reservoir modeling in shale-gas reservoirs. *SPE Reservoir Evaluation & Engineering,* **13**(4), 638-653.
55. Civan, F. (2010). Effective correlation of apparent gas permeability in tight porous media. *Transport in Porous Media,* **82**(2), 375-384.
56. Civan, F., Rai, C. S., Sondergeld, C. H. (2011). Shale-gas permeability and diffusivity inferred by improved formulation of relevant retention and transport mechanisms. *Transport in porous media,* **86**(3), 925-944.
57. Coates, G. R., Xiao, L., & Prammer, M. G. (1999). NMR logging: principles and applications (Vol. 234): Haliburton Energy Services Houston.
58. Crosdale, P. J. (1999). Mixed methane/carbon dioxide sorption by coal: new evidence in support of pore-filling models. Paper presented at the Proceedings of the *1999 International Coalbed Methane Symposium*, Tuscaloosa, Alabama
59. Curtis, M. E., Ambrose, R. J., Sondergeld, C. H., & Rai, C. S. (2011). Investigation of the relationship between organic porosity

and thermal maturity in the Marcellus Shale. Paper presented at the *North American unconventional gas conference and exhibition*.

60. Curtis, J. B. (2002). Fractured shale-gas systems. *AAPG bulletin*, **86**(11), 1921-1938.
61. Delle Piane, C., Bourdet, J., Josh, M., Clennell, M. B., Rickard, W. D., Saunders, M., Sherwood, N., Li, Z., Dewhurst, D. N., & Raven, M. D. (2018). Organic matter network in post-mature Marcellus Shale: Effects on petrophysical properties. *AAPG Bulletin*, **102**(11), 2305-2332.
62. Denney, D. (2005). Beyond beta factors: A model for darcy, forchheimer, and trans-forchheimer flow in porous media. *Journal of petroleum technology*, **57**(03), 43-45.
63. Dreisbach, F., Staudt, R., & Keller, J. U. (1999). High pressure adsorption data of methane, nitrogen, carbon dioxide and their binary and ternary mixtures on activated carbon. *Adsorption*, **5**(3), 215-227.
64. Du, C. M., Zhang, X., Zhan, L., Gu, H., Hay, B., Tushingham, K., Ma, Y. Z. (2010). Modeling hydraulic fracturing induced fracture networks in shale gas reservoirs as a dual porosity system. Paper presented at the *International Oil and Gas Conference and Exhibition in China*.
65. Duan, S., Gu, M., Du, X., & Xian, X. (2016). Adsorption Equilibrium of CO2 and CH4 and Their Mixture on Sichuan Basin Shale. *Energy & Fuels*, **30**(3), 2248-2256.
66. Dubinin, M. M. (1980). Water vapor adsorption and the microporous structures of carbonaceous adsorbents. *Carbon*, **18**(5), 355-364.
67. Eberl, D. (1984). Clay mineral formation and transformation in rocks and soils. Philosophical Transactions of the Royal Society of London. *Series A, Mathematical and Physical Sciences*, **311**(1517), 241-257.
68. Edlmann, K., Haszeldine, S., & McDermott, C. I. (2013). Experimental investigation into the sealing capability of naturally fractured shale caprocks to supercritical carbon dioxide flow. *Environmental earth sciences*, **70**(7), 3393-3409.
69. Edwards, R. W., Celia, M. A., Bandilla, K. W., Doster, F., &

Kanno, C. M. (2015). A model to estimate carbon dioxide injectivity and storage capacity for geological sequestration in shale gas wells. *Environmental science & technology*, **49**(15), 9222-9229.

70. Faiz, M., Aziz, N., Hutton, A., & Jones, B. (1992). Porosity and gas sorption capacity of some eastern Australian coals in relation to coal rank and composition. Paper presented at the *Coalbed Methane Symposium*, Townsville
71. Fan, E., Tang, S., Zhang, C., Guo, Q., & Sun, C. (2014). Methane sorption capacity of organics and clays in high-over matured shale-gas systems. *Energy Exploration & Exploitation*, **32**(6), 927-942.
72. Fan, K., Li, Y., Elsworth, D., Dong, M., Yin, C., Li, Y., & Chen, Z. (2018). Three stages of methane adsorption capacity affected by moisture content. *Fuel*, **231**, 352-360.
73. Fan, M., McClure, J., Han, Y., Ripepi, N., Westman, E., Gu, M., & Chen, C. (2019). Using an Experiment/Simulation-Integrated Approach To Investigate Fracture-Conductivity Evolution and Non-Darcy Flow in a Proppant-Supported Hydraulic Fracture. *SPE Journal*, preprint.
74. Fatah, A., Bennour, Z., Ben Mahmud, H., Gholami, R., & Hossain, M. (2020). A Review on the Influence of CO2/Shale Interaction on Shale Properties: Implications of CCS in Shales. *Energies*, **13** (12), 3200.
75. Florence, F. A., Rushing, J., Newsham, K. E., & Blasingame, T. A. (2007). Improved permeability prediction relations for low permeability sands. Paper presented at *Rocky Mountain Oil & Gas Technology Symposium*, USA.
76. Forchheimer, P. (1901). Wasserbewegung durch boden. Z. *Ver. Deutsch*, Ing. **45**, 1782-1788.
77. Gasparik, M., Ghanizadeh, A., Bertier, P., Gensterblum, Y., Bouw, S., & Krooss, B. M. (2012). High-pressure methane sorption isotherms of black shales from the Netherlands. *Energy & Fuels*, **26**(8), 4995-5004.
78. Gasparik, M., Bertier, P., Gensterblum, Y., Ghanizadeh, A., Krooss, B. M., & Littke, R. (2014). Geological controls on the

methane storage capacity in organic-rich shales. *International Journal of Coal Geology*, **123**, 34-51.

79. Gensterblum, Y.; Ghanizadeh, A.; Krooss, B.M. (2014). Gas permeability measurements on Australian subbituminous coals: Fluid dynamic and poroelastic aspects. *J. Nat. Gas Sci. Eng*. **19**, 202–214.
80. GeoQuest, S. (2009). ECLIPSE reservoir simulator. Technical description.
81. Glorioso, J. C., & Rattia, A. J. (2012). Unconventional Reservoirs: Basic Petrophysical Concepts for Shale Gas. Paper presented at the *SPE/EAGE European Unconventional Resources Conference and Exhibition*, Vienna, Austria.
82. Godec, M., Koperna, G., Petrusak, R., & Oudinot, A. (2013). Potential for enhanced gas recovery and CO2 storage in the Marcellus Shale in the Eastern United States. *International Journal of Coal Geology*, **118**, 95-104.
83. Guo, S. (2013). Experimental study on isothermal adsorption of methane gas on three shale samples from Upper Paleozoic strata of the Ordos Basin. *Journal of Petroleum Science and Engineering*, **110**, 132-138.
84. Guo, W., Xiong, W., Gao, S., Hu, Z., Liu, H., & Yu, R. (2013). Impact of temperature on the isothermal adsorption/desorption of shale gas. *Petroleum Exploration and Development*, **40**(4), 514-519.
85. Godec, M., Koperna, G., Petrusak, R., & Oudinot, A. (2013). Potential for enhanced gas recovery and CO2 storage in the Marcellus Shale in the Eastern United States. *International Journal of Coal Geology*, **118**, 95-104.
86. Hagoort, J. (2004). Non-Darcy Flow Near Hydraulically Fractured Wells. *SPE Journal*. **9**(02), 180-185.
87. Hao, F., Zou, H., & Lu, Y. (2013). Mechanisms of shale gas storage: Implications for shale gas exploration in ChinaMechanisms of Shale Gas Storage. *AAPG Bulletin*, **97**(8), 1325-1346.

88. He, W., Lv, W., & Dickerson, J. H. (2014). Gas diffusion mechanisms and models. In *Gas Transport in Solid Oxide Fuel Cells* (pp. 9-17). Springer, Cham.
89. Heller, R., & Zoback, M. (2014). Adsorption of methane and carbon dioxide on gas shale and pure mineral samples. *Journal of Unconventional Oil and Gas Resources*, **8**, 14-24.
90. Helgeson, H. C., Richard, L., McKenzie, W. F., Norton, D. L., & Schmitt, A. (2009). A chemical and thermodynamic model of oil generation in hydrocarbon source rocks. *Geochimica et Cosmochimica Acta*, **73**(3), 594-695.
91. Heller, R., & Zoback, M. (2014). Adsorption of methane and carbon dioxide on gas shale and pure mineral samples. *Journal of Unconventional Oil and Gas Resources*, **8**, 14-24.
92. Hill, D. G., Nelson, C. (2000). Gas productive fractured shales: an overview and update. *Gas Tips,* **6**(3), 4-13.
93. Ho, C. K., & Webb, S. W. (Eds.). (2006). Gas transport in porous media (Vol. 20). *Springer Science & Business Media*.
94. Hong, L., Jain, J., Romanov, V., Lopano, C., Disenhof, C., Goodman, A., Hedges, S., Soeder, D., Sanguinito, S., & Dilmore, R. (2016). An investigation of factors affecting the interaction of CO 2 and CH 4 on shale in Appalachian Basin. *Journal of Unconventional Oil Gas Resources*, **14**, 99-112.
95. Hoteit, H., Firoozabadi, A. (2008). An efficient numerical model for incompressible two-phase flow in fractured media. *Advances in Water Resources,* **31**(6), 891-905.
96. Huang, L., Ning, Z., Wang, Q., Zhang, W., Cheng, Z., Wu, X., & Qin, H. (2018). Effect of organic type and moisture on CO 2/CH 4 competitive adsorption in kerogen with implications for CO 2 sequestration and enhanced CH 4 recovery. *Journal of Applied Energy*, **210**, 28-43.
97. Huang, J., & Ghassemi, A. (2015). *A poroelastic model for evolution of fractured reservoirs during gas production*. Journal of Petroleum Science and Engineering. **135**, 626-644.
98. Huo, P., Zhang, D., Yang, Z., Li, W., Zhang, J., & Jia, S. (2017). CO_2 geological sequestration: displacement behavior of shale gas

methane by carbon dioxide injection. *International Journal of Greenhouse Gas Control*, **66**, 48-59.

99. Iijima, M., Nagayasu, T., Kamijyo, T., & Nakatani, S. (2011). MHI's energy efficient flue gas CO2 capture technology and large scale ccs demonstration test at coal-fired power plants in USA. *Mitsubishi Heavy Industries Technical Review*, **48**(1), 26-32.
100. Jarvie, D. M., Claxton, B. L., Henk, F., & T., B. J. (2001). Oil and Shale Gas from the Barnett Shale, Ft. Worth Basin, Texas. Paper presented at the *AAPG Annual Meeting Program*.
101. Jarvie, D. M., Hill, R. J., Ruble, T. E., & Pollastro, R. M. (2007). Unconventional shale-gas systems: The Mississippian Barnett Shale of north-central Texas as one model for thermogenic shale-gas assessment. *AAPG bulletin*, **91**(4), 475-499.
102. Javadpour, F. (2009). Nanopores and apparent permeability of gas flow in mudrocks (shales and siltstone). *Journal of Canadian Petroleum Technology,* **48**(8), 16-21.
103. Javadpour, F., Fisher, D., Unsworth, M. (2007). Nanoscale gas flow in shale gas sediments. *Journal of Canadian Petroleum Technology,* **46**(10).
104. Ji, L., Zhang, T., Milliken, K. L., Qu, J., & Zhang, X. (2012). Experimental investigation of main controls to methane adsorption in clay-rich rocks. *Applied Geochemistry*, **27**(12), 2533-2545.
105. Jiang, J., & Yang, J. (2018). Coupled fluid flow and geomechanics modeling of stress-sensitive production behavior in fractured shale gas reservoirs. *International Journal of Rock Mechanics and Mining Sciences*, **101**, 1-12.
106. Jiang, Y., Luo, Y., Lu, Y., Qin, C., & Liu, H. (2016). Effects of supercritical CO2 treatment time, pressure, and temperature on microstructure of shale. *Energy*, **97**, 173-181.
107. Jin, X., Wang, X., Liu, X., Jiao, H., Sun, L., Su, L., Bi, L., & Chen, Y. (2017). Low Field Cryoporometry NMR for Mesopores Distribution in Shale. Paper presented at the *SPE/IATMI Asia Pacific Oil & Gas Conference and Exhibition*, Jakarta, Indonesia.
108. Jones, S. C. (1987, January 1). Using the Inertial Coefficient, β, To Characterize Heterogeneity in Reservoir Rock. Paper presented at *SPE Annual Technical Conference and Exhibition*, USA.

109. Kang, S. M., Fathi, E., Ambrose, R. J., Akkutlu, I. Y., & Sigal, R. F. (2011). Carbon dioxide storage capacity of organic-rich shales. *SPE Journal*, **16**(04), 842-855.
110. Karacan, C. Ö., & Mitchell, G. D. (2003). Behavior and effect of different coal microlithotypes during gas transport for carbon dioxide sequestration into coal seams. *International Journal of Coal Geology*, **53**(4), 201-217. Karimi-Fard, M., Durlofsky, L. J., Aziz, K. (2003). An efficient discrete fracture model applicable for general purpose reservoir simulators. Paper presented at the *SPE Reservoir Simulation Symposium*.
111. Karniadakis, G., & Beşkök, A. (2001). Microflows: fundamentals and simulation. *Springer*.
112. Khosrokhavar, R. (2015). Sorption of CH4 and CO2 on Belgium Carboniferous Shale Using a Manometric Set-up. In Mechanisms for CO2 Sequestration in Geological Formations and Enhanced Gas Recovery (pp. 49-66): Springer International Publishing.
113. Kim, T. H., Cho, J., & Lee, K. S. (2017). Evaluation of CO2 injection in shale gas reservoirs with multi-component transport and geomechanical effects. *Applied Energy*, **190**, 1195-1206.
114. Klewiah, I., Berawala, D. S., Walker, H. C. A., Andersen, P. Ø., & Nadeau, P. H. (2019). Review of Experimental Sorption Studies of CO2 and CH4 in Shales. *Journal of Natural Gas Science and Engineering*, **73,** 103045.
115. Klinkenberg, L. (1941). The permeability of porous media to liquids and gases. Paper presented at the *Drilling and production practice*.
116. Knudsen, M. (1909). Die Gesetze der Molekularstro¨mung und der inneren Reibungsstro¨mung der Gase durch Ro¨hren (The laws of molecular and viscous flow of gases through tubes). *Annals of Physics.* **333**(1), 75–130.
117. Kus, J., Araujo, C. V., Borrego, A. G., Flores, D., Hackley, P. C., Hámor-Vidó, M., Kalaitzidis, S., Kommeren, C. J., Kwiecińska, B., Mastalerz, M., Mendonça Filho, J. G., Menezes, T. R., Misz-Kennan, M., Nowak, G. J., Petersen, H. I., Rallakis, D., Suárez-Ruiz, I., Sýkorová, I., & Životić, D. (2017). Identification of alginite and bituminite in rocks other than coal. 2006, 2009, and

2011 round robin exercises of the ICCP Identification of Dispersed Organic Matter Working Group. *International Journal of Coal Geology*, **178**, 26-38. https://doi.org/10.1016/j.coal.2017.04.013

118. Kuila, U., & Prasad, M. (2013). Specific surface area and pore-size distribution in clays and shales. *Geophysical Prospecting*, **61**(2), 341-362.
119. Kurniawan, Y., Bhatia, S. K., & Rudolph, V. (2006). Simulation of binary mixture adsorption of methane and CO2 at supercritical conditions in carbons. *AIChE Journal*, **52**(3), 957-967.
120. Lancaster, D., & Hill, D. (1993). A multi-laboratory comparison of isotherm measurements of Antrim shale samples. Paper presented at the *SCA Conference*, Otsego County, Michigan.
121. LeVeque, R. J. (2002). Finite volume methods for hyperbolic problems (Vol. 31): *Cambridge university press.*
122. Liu, D., Li, Y., Yang, S., & Agarwal, R. K. (2019). CO2 sequestration with enhanced shale gas recovery. *Energy Sources*, Part A: Recovery, Utilization, and Environmental Effects, 1-11.
123. Liu, D.; Li, Y.; Agarwal, R.K. (2016). Numerical simulation of long-term storage of CO2 in Yanchang shale reservoir of the Ordos basin in China. Chem. *Geol*., **440**, 288–305
124. Liu, F., Lu, P., Griffith, C., Hedges, S. W., Soong, Y., Hellevang, H., & Zhu, C. (2012). CO2–brine–caprock interaction: Reactivity experiments on Eau Claire shale and a review of relevant literature. *International Journal of Greenhouse Gas Control*, **7**, 153-167.
125. Liu, J., Yao, Y., Liu, D., & Elsworth, D. (2017). Experimental evaluation of CO2 enhanced recovery of adsorbed gas from shale. *International Journal of Coal Geology*, **179**, 211-218.
126. Liu, Y., Li, H. A., Tian, Y., Jin, Z., & Deng, H. (2018). Determination of the absolute adsorption/desorption isotherms of CH4 and n-C4H10 on shale from a nano-scale perspective. *Fuel*, **218**, 67-77.
127. Li, D., & Engler, T. W. (2001). Literature review on correlations of the non-Darcy coefficient. Paper presented in *SPE Permian Basin Oil and Gas Recovery Conference*, USA.

128. Ling, K., He, J., Wu, X., & Shen, Z. (2013). Determining Coefficient of Quadratic Term in Forchheimer Equation. *International Petroleum Technology Conference*, China.
129. Loucks R. G., Reed R. M., Ruppel S. C., Jarvie D. M. (2009). Morphology, genesis, and distribution of nanometer-scale pores in siliceous mudstones of the Mississippian Barnett Shale. *Journal of Sedimentary Research*, **79**(12), 848-861.
130. Loucks, R. G., Reed, R. M., Ruppel, S. C., & Hammes, U. (2012). Spectrum of pore types and networks in mudrocks and a descriptive classification for matrix-related mudrock pores. *AAPG bulletin*, **96**(6), 1071-1098.
131. Loucks, R. G., Reed, R. M., Ruppel, S. C., & Jarvie, D. M. (2009). Morphology, Genesis, and Distribution of Nanometer-Scale Pores in Siliceous Mudstones of the Mississippian Barnett Shale. *Journal of Sedimentary Research*, **79**(12), 1527-1404.
132. Louk, K., Ripepi, N., Luxbacher, K., Gilliland, E., Tang, X., Keles, C., Schlosser, C., Diminick, E., Keim, S., Amante, J., & Michael, K. (2017). Monitoring CO2 storage and enhanced gas recovery in unconventional shale reservoirs: Results from the Morgan County, Tennessee injection test. *Journal of Natural Gas Science and Engineering*, **45**, 11-25.
133. Lu, X. C., Li, F. C., & Watson, A. T. (1995). Adsorption studies of natural gas storage in Devonian shales. *SPE Formation evaluation*, **10**(02), 109-113.
134. Lu, Y., Ao, X., Tang, J., Jia, Y., Zhang, X., & Chen, Y. (2016). Swelling of shale in supercritical carbon dioxide. *Journal of Natural Gas Science and Engineering*, **30**, 268-275.
135. Luo, X., Wang, S., Wang, Z., Jing, Z., Lv, M., Zhai, Z., & Han, T. (2015). Adsorption of methane, carbon dioxide and their binary mixtures on Jurassic shale from the Qaidam Basin in China. *International Journal of Coal Geology*, **150-151**, 210-223.
136. Luo, W., & Tang, C. (2015). A Semianalytical Solution of a Vertical Fractured Well With Varying Conductivity Under Non-Darcy-Flow Condition. *SPE Journal*, **20**(05), 1-028.

137. Lutyński, M., Waszczuk, P., Słomski, P., & Szczepański, J. (2017). CO2 sorption of Pomeranian gas bearing shales – the effect of clay minerals. *Energy Procedia*, **125**, 457-466.
138. Lyu, Q., Long, X., Ranjith, P. G., & Kang, Y. (2016a). Unconventional gas: Experimental study of the influence of subcritical carbon dioxide on the mechanical properties of black shale. *Energies*, **9**(7), 516.
139. Lyu, Q., Ranjith, P. G., Long, X., & Ji, B. (2016b). Experimental investigation of mechanical properties of black shales after CO2-water-rock interaction. *Materials*, ***9***(8), 663.
140. Lyu, Q., Long, X., Ranjith, P., Tan, J., Zhou, J., Wang, Z., & Luo, W. (2018a). A laboratory study of geomechanical characteristics of black shales after sub-critical/super-critical CO 2+ brine saturation. *Geomechanics and Geophysics for Geo-Energy and Geo-Resources*, 1-16.
141. Lyu, Q., Long, X., Ranjith, P. G., Tan, J., Kang, Y., & Wang, Z. (2018b). Experimental investigation on the mechanical properties of a low-clay shale with different adsorption times in sub-/super-critical CO2. *Energy*, **147**, 1288-1298.
142. Ma, Y., Zhong, N., Li, D., Pan, Z., Cheng, L., & Liu, K. (2015). Organic matter/clay mineral intergranular pores in the Lower Cambrian Lujiaping Shale in the north-eastern part of the upper Yangtze area, China: A possible microscopic mechanism for gas preservation. *International Journal of Coal Geology*, **137**, 38-54.
143. Ma, Y., Yue, C., Li, S., Xu, X., & Niu, Y. (2018). Study of CH4 and CO2 Competitive Adsorption on Shale in Yibin, Sichuan Province of China. *Carbon Resources Conversion*.
144. Mainguy, M., Ulm, F. J. (2001). Coupled diffusion-dissolution around a fracture channel: the solute congestion phenomenon. *Transport in Porous Media*, **45**(3), 479-495.
145. Majewska, Z., Ceglarska-Stefańska, G., Majewski, S., & Ziętek, J. (2009). Binary gas sorption/desorption experiments on a bituminous coal: Simultaneous measurements on sorption kinetics, volumetric strain and acoustic emission. *International Journal of Coal*.

146. Manger, K. C., Oliver, S. J. P., Curtis, J., B, & Scheper, R., J. (1991). Geologic influences on the location and production of Antrim shale gas, Michigan Basin. Paper presented at the *Low Permeability Reservoirs Symposium*.
147. Manz, B., Gladden, L. F., & Warren, P. B. (1999). Flow and dispersion in porous media: Lattice-Boltzmann and NMR studies. *AlChE journal*, **45**(9), 1845-1854.
148. Martin, J. P., Hill, D. G., Lombardi, T. E., Nyahay, R. (2010). *A primer on New York's gas shales.* Paper presented at the *Field Trip Guidebook for the 80th Annual Meeting of the New York State Geological Association*.
149. Mayerhofer, M. J., Lolon, E., Warpinski, N. R., Cipolla, C. L., Walser, D. W., & Rightmire, C. M. (2010). What is stimulated reservoir volume? *SPE Production & Operations*, **25**(01), 89-98.
150. Mendhe, V. A., Mishra, S., Varma, A. K., Kamble, A. D., Bannerjee, M., & Sutay, T. (2017). Gas reservoir characteristics of the lower gondwana shales in Raniganj basin of eastern India. *Journal of Petroleum Science Engineering*, **149**, 649-664.
151. Merey, S., & Sinayuc, C. (2016). Analysis of carbon dioxide sequestration in shale gas reservoirs by using experimental adsorption data and adsorption models. *Journal of Natural Gas Science and Engineering*, **36**, 1087-1105.
152. Merey, S., & Sinayuc, C. (2018). Adsorption behaviour of shale gas reservoirs. International *Journal of Oil, Gas and Coal Technology*, **17**, 172.
153. Merkel, A., Fink, R., & Littke, R. (2015). The role of pre-adsorbed water on methane sorption capacity of Bossier and Haynesville shales. *International Journal of Coal Geology*, **147-148**, 1-8.
154. Middleton, R.S.; Carey, J.W.; Currier, R.P.; Hyman, J.D.; Kang, Q.; Karra, S.; Jiménez-Martínez, J.; Porter, M.L.; Viswanathan, H.S. (2015). Shale gas and non-aqueous fracturing fluids: Opportunities and challenges for supercritical CO2. *Appl. Energy*, **147**, 500–509.
155. Milliken, K. L., Rudnicki, M., Awwiller, D. N., & Zhang, T. (2013). Organic matter–hosted pore system, Marcellus Formation

(Devonian), PennsylvaniaGeohorizon. *AAPG Bulletin*, **97**(2), 177-200.

156. Moridis, G. J., Blasingame, T. A., Freeman, C. M. (2010). Analysis of mechanisms of flow in fractured tight-gas and shale-gas reservoirs. Paper presented at the *SPE Latin American and Caribbean Petroleum Engineering Conference.*
157. Mullen, J. (2010). Petrophysical Characterization of the Eagle Ford Shale in South Texas. Paper presented at the *Canadian Unconventional Resources and International Petroleum Conference*, Calgary, Alberta, Canada.
158. Mustapha, H., Langavant, L., Giddins, M. (2015). Darcy and non-Darcy Flows in Fractured Gas Reservoirs. Paper presented at *SPE Reservoir Characterisation and Simulation Conference and Exhibition*, UAE.
159. Newsham, K. E., & Rushing, J. A. (2001). An Integrated Work-Flow Model to Characterize Unconventional Gas Resources: Part I-Geological Assessment and Petrophysical Evaluation. In *SPE Annual Technical Conference and Exhibition*.
160. Nuttal, B. C., Eble, C., Bustin, R. M., & Drahovzal, J. A. (2005). Analysis of Devonian black shales in kentucky for potential carbon dioxide sequestration and enhanced natural gas production. *In Greenhouse Gas Control Technologies* 7 (pp. 2225-2228): Elsevier.
161. Oldenburg, C. M., Pruess, K., Benson, S. M., & Fuels. (2001). Process modeling of CO2 injection into natural gas reservoirs for carbon sequestration and enhanced gas recovery. *Energy & Fuels*, **15**(2), 293-298.
162. Ottiger, S., Pini, R., Storti, G., & Mazzotti, M. (2008). Competitive adsorption equilibria of CO 2 and CH 4 on a dry coal. *Adsorption*, **14**(4-5), 539-556.
163. Pang, Y., Soliman, M. Y., & Sheng, J. (2018). Investigating gas-adsorption, stress-dependence, and non-Darcy-flow effects on gas storage and transfer in nanopores by use of Simplified Local Density Model. *SPE Reservoir Evaluation & Engineering*, **21**(01), 73-95.

164. Passey, Q. R., Bohacs, K., Esch, W. L., Klimentidis, R., & Sinha, S. (2010). From oil-prone source rock to gas-producing shale reservoir-geologic and petrophysical characterization of unconventional shale gas reservoirs. Paper presented at the *International oil and gas conference and exhibition in China*.
165. Pei, P., Ling, K., He, J., & Liu, Z. (2015). Shale gas reservoir treatment by a CO2-based technology. *Journal of Natural Gas Science and Engineering*, **26**, 1595-1606.
166. Pino, D., Plantier, F., & Bessieres, D. (2014). Experimental determination of the adsorption isotherms in gas mixtures under extended pressure and temperature range. *Journal of Thermal Analysis Calorimetry*, **117**(3), 1469-1477.
167. Pozo, M., Pino, D., & Bessieres, D. (2017). Effect of thermal events on maturation and methane adsorption of Silurian black shales (Checa, Spain). *Applied Clay Science*, **136**, 208-218.
168. Pusch, A.-K., Splith, T., Moschkowitz, L., Karmakar, S., Biniwale, R., Sant, M., Suffritti, G. B., Demontis, P., Cravillon, J., & Pantatosaki, E. J. A. (2012). NMR studies of carbon dioxide and methane self-diffusion in ZIF-8 at elevated gas pressures. **18**(5-6), 359-366.
169. Pytte, A. M., & Reynolds, R. C. (1989). The thermal transformation of smectite to illite. In Thermal history of sedimentary basins (pp. 133-140): *Springer*.
170. Ramos, S. (2004). The effect of shale composition on the gas sorption potential of organic-rich mudrocks in the Western Canadian sedimentary basin. *University of British Columbia*.
171. Rangel-German, E. R., & Kovscek, A. R. (2002). Experimental and analytical study of multidimensional imbibition in fractured porous media. *Journal of Petroleum Science and Engineering*, **36**(1-2), 45-60.
172. Rani, S., Padmanabhan, E., & Prusty, B. K. (2019). Review of gas adsorption in shales for enhanced methane recovery and CO2 storage. *Journal of Petroleum Science and Engineering*, **175**, 634-643.

173. Regan, M. (2007). A Review of the potential for carbon dioxide (CO2) enhanced gas recovery in Australia
174. Rexer, T. F., Mathia, E. J., Aplin, A. C., & Thomas, K. M. (2014). High-pressure methane adsorption and characterization of pores in Posidonia shales and isolated kerogens. *Energy & Fuels*, **28**(5), 2886-2901.
175. Rice, D. D., Law, B. E., & Clayton, J. L. (1993). Coalbed gas: An undeveloped resource. *US Geological Survey Professional Paper*, **1570**, 389-404.
176. Ross, D. J. K., & Bustin, R. M. (2007a). Shale gas potential of the lower Jurassic Gordondale member, northeastern British Columbia, Canada. *Bulletin of Canadian Petroleum Geology*, **55**(1), 51-75.
177. Ross, D. J. K., & Bustin, R. M. (2008). Characterizing the shale gas resource potential of Devonian–Mississippian strata in the Western Canada sedimentary basin: Application of an integrated formation evaluation. *AAPG bulletin*, **92**(1), 87-125.
178. Ross, D. J. K., & Bustin, R. M. (2009). The importance of shale composition and pore structure upon gas storage potential of shale gas reservoirs. *Marine and Petroleum Geology*, **26**(6), 916-927.
179. Roy, S., Raju, R., Chuang, H.F., Cruden, B., and Meyyappan, M. (2003). Modeling gas flow through microchannels and nanopores. *Journal of Applied Physics*. **93** (8), 4870–4879.
180. Ruppel, S., & Loucks, R. (2008). Black mudrocks: lessons and questions from the Mississippian Barnett Shale in the southern Midcontinent. *The Sedimentary Record*, **6**(2), 4-8.
181. Samandarli, O., Al Ahmadi, H. A., Wattenbarger, R. A. (2011). A new method for history matching and forecasting shale gas reservoir production performance with a dual porosity model. Paper presented at the *North American Unconventional Gas Conference and Exhibition.*
182. Schettler Jr, P., & Parmely, C. (1990). The measurement of gas desorption isotherms for Devonian shale. GRI Devonian Gas Shale Technology Review, **7**(1), 4-9.

183. Schettler Jr, P., & Parmely, C. (1991). Contributions to total storage capacity in Devonian shales. Paper presented at the *SPE Eastern Regional Meeting*.
184. Schieber, J. (2010). Common Themes in the Formation and Preservation of Intrinsic Porosity in Shales and Mudstones - Illustrated with Examples Across the Phanerozoic. Paper presented at the *SPE Unconventional Gas Conference*.
185. Seewald, J. S. (2003). Organic–inorganic interactions in petroleum-producing sedimentary basins. *Nature*, **426**, 327.
186. Sharma, G., & Galvis-Portilla, H. (2018). Impact of Total Organic Carbon on Adsorption Capacity, In-Place Hydrocarbons, and Ultimate Recovery: A Case Study of the Duvernay Formation in Alberta, Canada. Paper presented at the *Abu Dhabi International Petroleum Exhibition & Conference*.
187. Sherifa, C., & Reza, B. (2018). Carbon Dioxide Utilization and Sequestration in Kerogen Nanopores. *In Carbon Capture, Utilization and Sequestration*. IntechOpen.
188. Slatt, R. M., & O'Brien, N. R. (2011). Pore types in the Barnett and Woodford gas shales: Contribution to understanding gas storage and migration pathways in fine-grained rocksGeohorizon. *AAPG Bulletin*, **95**(12), 2017-2030.
189. Soeder, D. J. (1988). Porosity and Permeability of Eastern Devonian Gas Shale. *SPE Formation Evaluation*, **3**(01), 116-124.
190. Sondergeld, C. H., Ambrose, R. J., Rai, C. S., & Moncrieff, J. (2010). Micro-structural studies of gas shales. Paper presented at the *SPE Unconventional Gas Conference.*
191. Stoll, M., Hofman, J., Ligthelm, D. J., Faber, M. J., & van den Hoek, P. (2008). Toward field-scale wettability modification—the limitations of diffusive transport. *SPE Reservoir Evaluation & Engineering*, **11**(03), 633-640.
192. Strapoc, D., Mastalerz, M., Schimmelmann, A., Drobniak, A., & Hasenmueller, N. R. (2010). Geochemical constraints on the origin and volume of gas in the New Albany Shale (Devonian–Mississippian), eastern Illinois Basin. *AAPG bulletin*, **94**(11), 1713-1740.

193. Šucha, V., Środoń, J., Clauer, N., Elsass, F., Eberl, D., Kraus, I., & Madejová, J. (2001). Weathering of smectite and illite-smectite under temperate climatic conditions. *Clay Minerals*, **36**(3), 403-419.
194. Tan, J., Weniger, P., Krooss, B., Merkel, A., Horsfield, B., Zhang, J., Boreham, C. J., van Graas, G., & Tocher, B. A. (2014). Shale gas potential of the major marine shale formations in the Upper Yangtze Platform, South China, Part II: Methane sorption capacity. *Fuel*, **129**, 204-218.
195. Tang, H. M., Wang, J. J., Zhang, L. H., Guo, J. J., Chen, H. X., Liu, J., ... & Feng, Y. T. (2016). Testing method and controlling factors of specific surface area of shales. *Journal of Petroleum Science and Engineering*, **143**, 1-7.
196. Tao, Z., Bielicki, J. M., & Clarens, A. F. (2014). Physicochemical factors impacting CO2 sequestration in depleted shale formations: The case of the Utica shale. *Energy Procedia*, **63**, 5153-5163.
197. Tao, Z.; Clarens, A. (2013). Estimating the carbon sequestration capacity of shale formations using methane production rates. *Environ. Sci. Technol*., **47**, 11318–11325.
198. Teichmüller, M. (1971). Anwendung kohlenpetrographischer Methoden bei der Erdöl-und Erdgasprospektion. *Erdöl Kohle*, **24**, 69-76.
199. Tecklenburg, J., Neuweiler, I., Dentz, M., Carrera, J., Geiger, S., Abramowski, C., Silva, O. (2013). A non-local two-phase flow model for immiscible displacement in highly heterogeneous porous media and its parametrization. *Advances in Water Resources,* **62**, 475-487.
200. Tek, M.R., Coats, K.H., Katz, D.L. (1962). The Effects of Turbulence on Flow of Natural Gas through Porous Reservoirs. J. Pet. Technol. Trans. AIME **222**, 799–806.
201. Thommes, M. (2010). Physical adsorption characterization of nanoporous materials. *Chemie Ingenieur Technik*, **82**(7), 1059-1073.
202. Tissot, B. P., & Welte, D. H. (1984). Petroleum Formation and Occurrence. In: *Springer-Verlag*, Berlin-Heidelberg.
203. van Golf-Racht, T. D. (1982). Fundamentals of fractured reservoir

engineering (Vol. 12). *Elsevier*.
204. Vandenbroucke, M., & Largeau, C. (2007). Kerogen origin, evolution and structure. *Organic Geochemistry*, **38**(5), 719-833.
205. Vermylen, J. P. (2011). Geomechanical studies of the Barnett shale, Texas, USA. *Stanford University*.
206. Wang, J., Luo, H., Liu, H., Cao, F., Li, Z., & Sepehrnoori, K. (2017*)*. An integrative model to simulate gas transport and production coupled with gas adsorption, non-Darcy flow, surface diffusion, and stress dependence in organic-shale reservoirs. *SPE Journal*, **22**(01), 244-264.
207. Wang, H., & Marongiu-Porcu, M. (2015). Impact of shale-gas apparent permeability on production: combined effects of non-darcy flow/gas-slippage, desorption, and geomechanics. *SPE Reservoir Evaluation & Engineering*, **18**(04), 495-507.
208. Wang, F. P., Reed, R. M. (2009). Pore networks and fluid flow in gas shales. Paper presented at the *SPE annual technical conference and exhibition*.
209. Wang, H., Li, G., & Shen, Z. (2012). A feasibility analysis on shale gas exploitation with supercritical carbon dioxide. Energy Sources, Part A: Recovery, Utilization, and Environmental Effects, **34**(15), 1426-1435.
210. Wang, L., & Yu, Q. (2016). The effect of moisture on the methane adsorption capacity of shales: A study case in the eastern Qaidam Basin in China. *Journal of Hydrology*, **542**, 487-505.
211. Wang, S., Song, Z., Cao, T., & Song, X. (2013). The methane sorption capacity of Paleozoic shales from the Sichuan Basin, China. *Marine Petroleum Geology*, **44**, 112-119.
212. Wang, Y., Zhu, Y., Liu, S., & Zhang, R. (2016). Methane adsorption measurements and modeling for organic-rich marine shale samples. *Fuel*, **172**, 301-309.
213. Warren, J., Root, P. J. (1963). The behavior of naturally fractured reservoirs.
214. Weijermars, R. (2013). Economic appraisal of shale gas plays in Continental Europe. *Applied Energy*, **106**, 100-115.
215. Weniger, P., Kalkreuth, W., Busch, A., & Krooss, B. M. (2010). High-pressure methane and carbon dioxide sorption on coal and shale samples from the Paraná Basin, Brazil. *International Journal*

of Coal Geology, **84**(3-4), 190-205.

216. Wei, X., Wei, G., Honglin, L., Shusheng, G., Zhiming, H., & Farong, Y. (2012). Shale reservoir characteristics and isothermal adsorption properties. *Natural Gas Industry*, **32**(1), 113-116.
217. Weniger, P., Kalkreuth, W., Busch, A., & Krooss, B. M. (2010). High-pressure methane and carbon dioxide sorption on coal and shale samples from the Paraná Basin, Brazil. *J International Journal of Coal Geology*, **84**(3-4), 190-205.
218. Wollenweber, J., Alles, S., Kronimus, A., Busch, A., Stanjek, H., & Krooss, B. M. (2009). Caprock and overburden processes in geological CO2 storage: An experimental study on sealing efficiency and mineral alterations. *Energy Procedia*, **1**(1), 3469-3476.
219. Wollenweber, J., Alles, S., Busch, A., Krooss, B. M., Stanjek, H., & Littke, R. (2010). Experimental investigation of the CO2 sealing efficiency of caprocks. *International Journal of Greenhouse Gas Control*, **4**(2), 231-241.
220. Wu, C., Tuo, J., Zhang, L., Zhang, M., Li, J., Liu, Y., & Qian, Y. (2017). Pore characteristics differences between clay-rich and clay-poor shales of the Lower Cambrian Niutitang Formation in the Northern Guizhou area, and insights into shale gas storage mechanisms. *International Journal of Coal Geology*, **178**, 13-25.
221. Xia, J., Song, Z., Wang, S., & Zeng, W. (2017). Preliminary study of pore structure and methane sorption capacity of the Lower Cambrian shales from the north Gui-zhou Province. *Journal of Natural Gas Science and Engineering*, **38**, 81-93.
222. Yang, F., Xie, C., Ning, Z., & Krooss, B. (2016). High-pressure methane sorption on dry and moisture-equilibrated shales. *Energy & Fuels*, **31**(1), 482-492.
223. Yao, J., Sun, H., Fan, D. Y., Wang, C. C., & Sun, Z. X. (2013). Numerical simulation of gas transport mechanisms in tight shale gas reservoirs. *Petroleum Science*, **10**(4), 528-537.
224. Yin, H., Zhou, J., Jiang, Y., Xian, X., & Liu, Q. (2016). Physical and structural changes in shale associated with supercritical CO2 exposure. *Fuel*, **184**, 289-303.

225. Yin, H., Zhou, J., Xian, X., Jiang, Y., Lu, Z., Tan, J., & Liu, G. (2017a). Experimental study of the effects of sub- and super-critical CO2 saturation on the mechanical characteristics of organic-rich shales. *Energy*, **132**, 84-95.
226. Yin, T., Liu, D., Cai, Y., Zhou, Y., & Yao, Y. (2017b). Size Distribution and Fractal Characteristics of Coal Pores through Nuclear Magnetic Resonance Cryoporometry. *Energy & Fuels*, **31**(8), 7746-7757.
227. Yuan, W., Pan, Z., Li, X., Yang, Y., Zhao, C., Connell, L. D., Li, S., & He, J. (2014). Experimental study and modelling of methane adsorption and diffusion in shale. **117**, 509-519.
228. Yu, W., Sepehrnoori, K., Patzek, T. W. (2016). Modeling gas adsorption in Marcellus shale with Langmuir and bet isotherms. *SPE Journal*, **21**(2), 589-600.
229. Zendehboudi, S., & Bahadori, A. (2016). Shale oil and gas handbook: theory, technologies, and challenges. *Gulf Professional Publishing*.
230. Zeng, F., & Zhao, G. (2008). SemiAnalytical Model for Reservoirs with Forchheimer's Non-Darcy Flow. *SPE Res Eval & Eng*, **11**(2), 280-291.
231. Zhang, T., Ellis, G. S., Ruppel, S. C., Milliken, K., & Yang, R. (2012). Effect of organic-matter type and thermal maturity on methane adsorption in shale-gas systems. *Organic geochemistry*, **47**, 120-131.
232. Zhao, G., & Wang, C. (2018). Influence of CO2 on the adsorption of CH4 on shale using low-field nuclear magnetic resonance technique. *Fuel*, **238**, 51-58.
233. Zheng, X., Zhang, B., Sanei, H., Bao, H., Meng, Z., Wang, C., & Li, K. (2018). Pore structure characteristics and its effect on shale gas adsorption and desorption behavior. *Marine and Petroleum Geology*, **100**, 165-178.
234. Zhou, S., Xue, H., Ning, Y., Guo, W., & Zhang, Q. (2018). Experimental study of supercritical methane adsorption in Longmaxi shale: Insights into the density of adsorbed methane. *Fuel*, **211**, 140-148.

235. Zolfaghari, A., Dehghanpour, H., & Holyk, J. (2017a). Water sorption behaviour of gas shales: I. Role of clays. *International Journal of Coal Geology*, **179**, 130-138.
236. Zolfaghari, A., Dehghanpour, H., & Xu, M. (2017b). Water sorption behaviour of gas shales: II. Pore size distribution. *International Journal of Coal Geology*, **179**, 187-195.
237. Zou, J., Rezaee, R., & Liu, K. (2017). Effect of Temperature on Methane Adsorption in Shale Gas Reservoirs. *Energy & Fuels*, **31**(11), 12081-12092.
238. Zou, J., Rezaee, R., Xie, Q., You, L., Liu, K., & Saeedi, A. (2018). Investigation of moisture effect on methane adsorption capacity of shale samples. *Fuel*, **232**, 323-332.
239. Zuber, M. D., Williamson, J. R., Hill, D. G., Sawyer, W. K., & Frantz Jr, J. H. (2002). A comprehensive reservoir evaluation of a shale reservoir-the New Albany shale. Paper presented at the *SPE Annual Technical Conference and Exhibition*.
240. Zou, C. N., Zhu, R. K., Wu, S. T., Yang, Z., Tao, S. Z., Yuan, X. J., ... & Bai, B. (2012). Types, characteristics, genesis and prospects of conventional and unconventional hydrocarbon accumulations: taking tight oil and tight gas in China as an instance. *Acta Petrolei Sinica*, **33**(2), 173-187.

Appendix

A) Initial and Current Gas in Place and Recovery Factor – for Darcy and Non-Darcy Flow Model

The gas currently in place (*GCIP*) is given by the addition of the mass of gas adsorbed in the matrix (M_1), free gas in the fracture (M_2) and free gas in the matrix (M_3). These masses are calculated over both sides of the fracture.

(88) $$GCIP = M_1 + M_2 + M_3$$

(89) $$GCIP = 2h\sum_{i=1}^{n_x}\sum_{j=1}^{n_y}(1-\phi^m)a_g\left(p_g(x_i,y_j)\right)\Delta x\Delta y + \phi^f\rho_{gs}b_g'h\sum_{j=1}^{n_y}p_g(y_j)2b(y_j)\Delta y + 2\phi^m\rho_{gs}b_g'h\sum_{j=1}^{n_y}p_g(x_i,y_j)\Delta x\Delta y.$$

The gas originally in place (*GOIP*) can be evaluated by using gas currently in place at initial reservoir pressure p_{init}:

(90) $$GOIP = GCIP(p_{init})$$

The recovery factor RF is then evaluated as:

(91) $$RF = 1 - \frac{GCIP}{GOIP} = 1 - \frac{GCIP}{GCIP(p_{init})}.$$

The obtainable recovery is defined by:

(92) $$RF_{ob} = \frac{RF}{RF_\infty} = \frac{GCIP(p_{init}) - GCIP}{GCIP(p_{init}) - GCIP(p_{well})}.$$

Scaled total mass in the matrix and fracture is mathematically defined as:

(93) $$M_T = \frac{GCIP}{GOIP(p_{init})} = \frac{M1 + M3}{M1(P_{init}) + M3(P_{init})} + \frac{M2}{M2(P_{init})}$$

B) Langmuir isotherm vs proposed adsorption isotherm

To compare the proposed adsorption model with the Langmuir isotherm, we assume a single component (CH_4) system. By substituting (15)-(16) into (17) and using $P_c = 0$ and $M_{w,m} = S_{m,m} = A = 1$, we get the CH_4 adsorbed mass per volume W_m as:

$$W_m = n_m \frac{{P_m}^{n_m}}{K_m + {P_m}^{n_m}} \tag{94}$$

The above expression takes the form of the Langmuir isotherm when $n_m = 1$, where K_m then represents Langmuir pressure. Thus, the Langmuir isotherm is a special case of the proposed adsorption isotherm with monolayer adsorption.

Plotting W_m/n_m (to normalize to a max adsorption of unity) against P_m gives direct comparison between the two isotherms at different values of n_m, as shown in **Figure 47** for two values of K_m. All the curves will pass through the same point at $P_m = 1$ defined by:

$$\left[\frac{W_m}{n_m}\right]_{P_m=1} = \frac{1}{K_m + 1} \tag{1}$$

As seen, the proposed model can capture more trends and shapes of adsorption experiment data than the Langmuir isotherm.

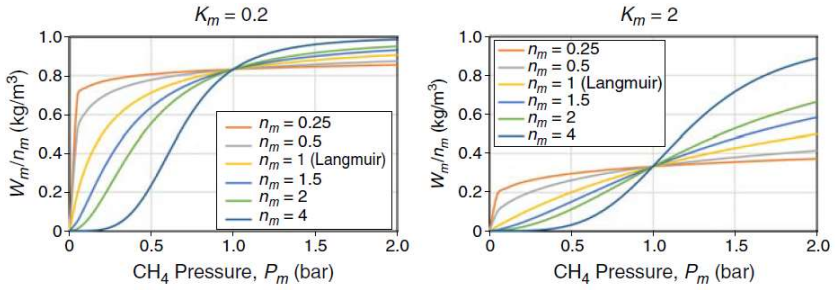

Figure 47 Adsorption content of CH4 (W_m/n_m) as function of CH4 partial pressure for $K_m = 0.2$ (left) and $K_m = 2$ (right) at different values of n_m.

Paper I

Berawala, D. S., Andersen, P. Ø., & Ursin, J. R. (2019). Controlling Parameters During Continuum Flow in Shale-Gas Production: A Fracture/Matrix-Modelling Approach. *SPE Journal, 24(3),* 1378-1394.
https://doi.org/10.2118/190843-PA

Paper II

Journal of Petroleum Science and Engineering 190 (2020) 107114

Contents lists available at ScienceDirect

Journal of Petroleum Science and Engineering

journal homepage: http://www.elsevier.com/locate/petrol

Numerical investigation of Non-Darcy flow regime transitions in shale gas production

Dhruvit S. Berawala [a,c,*], Pål Ø. Andersen [b,c]

[a] Department of Energy and Petroleum Engineering, University of Stavanger, Stavanger, Norway
[b] Department of Energy Resources, University of Stavanger, Stavanger, Norway
[c] The National IOR Centre of Norway, Stavanger, Norway

ARTICLE INFO

Keywords:
Shale gas production
Non-Darcy flow
Forchheimer equation
Fracture-matrix flow
Apparent permeability

ABSTRACT

Shale gas reservoirs are organic rich formations with often ultra-low permeability. Gas is stored in free and adsorbed form. Conventional Darcy flow cannot fully describe the gas transport in such porous media. It is thus crucial to study the shale gas production considering different flow regimes and time dependent permeability, which can improve well-induced fracture design and ultimate gas recovery. In particular, this paper will focus on the transition in non-Darcy flow regimes near fracture-matrix interfaces using mathematical modelling. Especially, we investigate conditions at which these effects vanish, and Darcy flow assumptions become reasonable.

The model describes a representative well-induced high permeability fracture surrounded by shale matrix. Investigated Non-Darcy mechanisms include apparent permeability, Knudsen diffusion, gas desorption and Forchheimer flow. Pressure depletion is the main driving force for single phase gas flow from the matrix to the fracture and from the fracture to the well. Pressure dependent gas desorption is defined by Langmuir isotherm and is a key production mechanism. This model is implemented in Matlab using Marcellus shale data.

Scaling the model shows that recovery of gas depends on two dimensionless number that incorporates geometry relations, time scales of flow, intrinsic parameters of the porous media, non-Darcy constants, adsorption and boundary conditions. The dimensionless numbers define respectively if 1) the fracture or matrix limit the gas production rate 2) if non-Darcy flow is significant in the fracture or matrix. When one of the media limit production, the non-Darcy flow in the other medium has reduced importance and can be excluded from the model. Non-Darcy flow is important if it limits flow in the medium limiting the production. By checking the magnitude of the selected dimensionless numbers, the modelling approach can be determined in advance and significant computational time can be saved.

The proposed model provides a tool for interpretation of complex shale gas production systems. It can be used for screening of flow regimes at different operational configurations and hence appropriate modelling approaches. The model can be used to optimise fracture network design and potentially in identifying stimulation operations that may significantly improve production rates and ultimate recovery from unconventional gas reservoirs.

1. Introduction

Technological advances in hydraulic stimulation of shale reservoirs have caused a fundamental shift to the exploration-and-production industry. These unconventional reservoirs typically have extremely low matrix permeability (10–100 nD, Cipolla et al., 2010) and exhibit gas stored both in free and adsorbed form. Gas flows from the nanopores in the matrix to the hydraulic fractures and then to the horizontal wells. This transport of gas comprises several flow mechanisms as investigated by a large number of scientists and engineers over many years (Bird, 2002; Javadpour et al., 2007; Javadpour, 2009; Civan, 2010; Civan et al., 2011; Beskok and Karniadakis, 1999; Blasingame, 2008; Moridis et al., 2010; Klewiah et al., 2019).

One of the key mechanisms is the non-Darcy flow; the traditional linear equation for flow in porous media based on Darcy's law is not sufficient for accurately describing high-rate flows. Non-Darcy flow occurs when inertial forces may no longer be neglected compared with viscous forces (Hagoort, 2004). That is very common near gas

* Corresponding author. Department of Energy and Petroleum Engineering, University of Stavanger, Norway.
E-mail address: dhruvit.s.berawala@uis.no (D.S. Berawala).

https://doi.org/10.1016/j.petrol.2020.107114
Received 22 November 2019; Received in revised form 9 February 2020; Accepted 21 February 2020
Available online 28 February 2020

production wells or in the near-wellbore region, especially in fractures where local velocities can be very high. Bybee (2006) suggested that in hydraulic fracture stimulation, non-Darcy flow can have a major effect on reduction of a propped half-length to a considerably shorter "effective" half-length, thus lowering the productive capability of the well and overall reserves recovery. Moreover, flow-capacity can reduce by 5%–30% in low-rate wells due to non-Darcy effects (Bybee, 2006). To account for this nonlinear behavior, an inertial term called the Forchheimer term is added to Darcy's equation. Forchheimer (1901) gave the empirical Forchheimer equation to model gas flow more accurately at high flow rates (Mustapha et al., 2015; Li and Engler, 2001; Belhaj et al., 2003; Jones, 1987; Ling et al., 2013; Barree and Conway, 2005; Zeng and Zhao, 2008).

Al-Rbeawi (2018) showed that non-Darcy flow has a significant effect on the pressure profile of unconventional gas reservoirs, especially at early production time. Luo and Tang (2015) through semianalytical modelling concluded that non-Darcy flow in the fracture mainly reduces the effective conductivity. This varying conductivity and non-Darcy flow in the fracture make the pressure curves deviate from the type curves. Several efforts have been made over the past 10 years to identify the effects of non-Darcy flow on overall gas production from shale reservoirs (Wang and Marongiu-Porcu, 2015; Fan et al., 2019; Al-Rbeawi, 2019; Luo and Tang, 2015; Pang et al., 2018; Wang et al., 2017). However, there appears to lack a clear understanding on exactly where the transition from Darcy to non-Darcy flow occurs, quantifying this transition and assessing how its importance can be estimated a priori. The objective of this work is to address these issues. As an analysis tool, we consider a 1D+1D combined fracture/matrix model that allows systematic evaluation of the role and magnitude of the different mechanisms. This extends work presented in Berawala et al. (2019) focusing on flow regime characterization to now also consider and focus on non-Darcy flow mechanisms. Similar to the works by Mainguy and Ulm (2001) and Andersen et al. (2014, 2015) the model consists of a high-permeable fracture (length L_y) with width $2b$. This depicts a typical hydraulic fracture in a real-field scenario. The fracture can have non-uniform width and is symmetrically surrounded by shale matrix of fixed length L_x and low permeability as shown in Fig. 1. We implicitly assume equally spaced perforation intervals by assuming fixed matrix length. The gas is stored densely in the matrix by adsorption (modelled by a Langmuir isotherm), in addition to free gas in the pores. Apparent permeability is used to account for gas slippage effects, effective stress, adsorption and flow regimes relevant due to the nano-pore structure of the shale matrix. The pressure gradient towards the fracture and the well causes free gas from the matrix nanopores to flow. With pressure depletion, gas adsorbed onto the kerogen material desorbs into the pore space where it can flow as free gas to the fracture. A transfer term takes care of the communication between the fracture and the matrix. The system consists of a pressure-diffusion equation for the fracture which is coupled with a pressure-diffusion equation in the matrix. The model is scaled to derive dimensionless numbers that characterize the model. The Forchheimer term is incorporated into the flow equations using a correction factor f denoting flux reduction compared to Darcy flow. The scaled system gives rise to non-linear partial differential equations which are solved numerically using an operator splitting approach. Using the scaled model we then address the following questions of practical importance:

- How can we quantify the flow transition from Darcy to non-Darcy?
- What are the conditions under which non-Darcy effects in the matrix become significant for gas recovery?
- How does non-Darcy flow affect flow regimes in shale gas production?

Marcellus field and literature data are used to parameterize the model. Sensitivity analysis is performed to see the effect on gas recovery with time and 2D distributions of scaled pressure, and the transition factor $f(z)$.

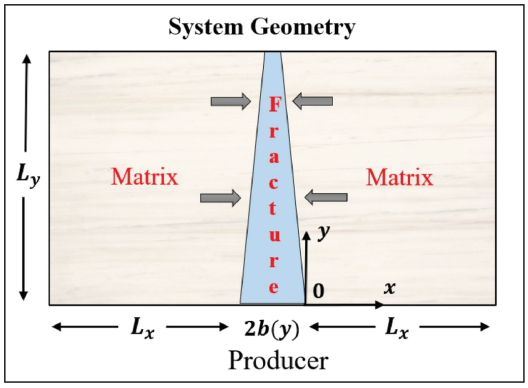

Fig. 1. System geometry: the near well reservoir is seen from above where a fracture with variable width extends from a well perforation with length L_y. Shale matrix surrounds the fracture on both sides with total length $2L_x$ (typical perforation interval) (Berawala et al., 2019).

2. Mathematical model

2.1. System geometry

Assume a hydraulic fracture extending perpendicularly from a well, along which we define the positive y-axis, starting from the well perforation. The fracture has width $2b(y)$ and it is assumed the width can vary from the perforation until its length L_y. The fracture width is assumed to vary linearly and recover gas from the matrix only in its perpendicular direction (x-direction). The matrix is assumed to behave identically on both sides of the fracture. This results in a net no-flow boundary at $x = L_x$ (the matrix half length). In the following we study the matrix and fracture only on the right-hand side of the symmetric system ($-b < x < L_x$).

2.2. Mass conservation equation

Consider a domain with volume V containing gas in free and adsorbed form. The mass of gas in the porous media volume changes due to flow in and out of the interface $\partial\Omega$ with area A as expressed by the mass balance equation (LeVeque, 2002):

$$\partial_t \int_{\Omega} \left(\varphi\rho_g + (1-\varphi)a_g\right) dV = -\int_{\partial\Omega} (\rho_g \boldsymbol{u})\cdot \boldsymbol{n}\, dA, \tag{1}$$

where ϕ is porosity, $\rho_g(p_g)$ gas density, a_g adsorbed gas (mass per solid volume), $\boldsymbol{u}$ Darcy mass flux vector, $\boldsymbol{n}$ is the unit normal vector pointing out of Ω, and p_g is the gas pressure.

2.2.1. Fracture domain

In the fracture, gas adsorption is negligible, i.e., $a_g^f = 0$. The fracture width, denoted $2b(y)$, can vary with distance from the well. Considering a volume $dV = 2b(y)\, h\, dy \to 0$ we get from (1):

$$\partial_t\left(\varphi\rho_g 2b\right) = \partial_y\left(\rho_g u 2b\right) + \left(\rho_g u\right)_{x=-2b,y} - \left(\rho_g u\right)_{x=0,y}. \tag{2}$$

Since the fracture is surrounded by matrix symmetrically, the two source terms contribute identically:

$$\left(\rho_g u\right)_{x=-2b,y} = -\left(\rho_g u\right)_{x=0,y}, \tag{3}$$

and we obtain:

$$\partial_t(\varphi\rho_g b) = -\partial_y(\rho_g u b) - (\rho_g u)_{x=0,y}. \tag{4}$$

2.2.2. Matrix domain

In the matrix, it is assumed that all flow is directed in the x-direction (towards the fracture), while flow in the y-direction is ignored. Considering a volume $dV = dx\,h\,dy \to 0$ we get from (1):

$$\partial_t(\varphi\rho_g + (1-\varphi)a_g) = -\partial_x(\rho_g u). \tag{5}$$

2.3. Non-Darcy flow

Forchheimer's equation is defined by (Forchheimer, 1901):

$$\partial_x p = -u\left(\frac{\mu}{k} + \gamma\rho|u|\right), \tag{6}$$

where γ is Forchheimer's constant. When $\gamma = 0$ the formula reduces to Darcy's equation: $\partial_x p = -u\frac{\mu}{k}$).

$$\partial_x p = -u\frac{\mu}{k} \tag{7}$$

This coefficient is usually obtained from experimental data. However, there are several correlations available in the literature to evaluate the Forchheimer's constant. In this paper, we use the correlation given by Tek et al. (1962):

$$\gamma = \frac{C_\beta}{k^{1.25}\varphi^{0.75}}, \tag{8}$$

where C_β is non-Darcy flow constant and k is the apparent permeability. It is useful that:

$$u|u| = s(u)u^2 \tag{9}$$

where $s(\cdot)$ denotes the sign function with value ± 1. We further have that:

$$\partial_x p = s(\partial_x p)|\partial_x p|, \quad s(u) = -s(\partial_x p) \tag{10}$$

To get velocity in a form comparable with Darcy's law $\left(u = -\frac{k}{\mu}\partial_x p\right)$ we write:

$$u = -\frac{k}{\mu}\partial_x p\left(\frac{-1+\sqrt{1+4\frac{k^2}{\mu^2}\gamma\rho|\partial_x p|}}{2\frac{k^2}{\mu^2}\gamma\rho|\partial_x p|}\right) \tag{11}$$

The latter term is in the form:

$$f(z) = \frac{-1+\sqrt{1+2z}}{z}, \tag{12}$$

where

$$z = \frac{k^2}{\mu^2}\gamma\rho|\partial_x p|, \tag{13}$$

which has a limit $f \to 1$ when $z \to 0$ and $f \to 0$ when $z \to \infty$. We name $f(z)$ the transition factor as it denotes the transition of flow from Darcy to non-Darcy. In other words, the velocity is always less or equal to the velocity from Darcy's law. The value of $f(z) = 1$ would indicate Darcy flow and $f(z) < 1$ would mean non-Darcy flow.

2.4. The volume factor and density relation

Introduce the inverse volume factor b_g, using the real gas law:

$$b_g(p) = \frac{1}{B_g(p)} = \frac{T^{atm}}{Z(p)Tp^{atm}}p, \tag{14}$$

which implies:

$$\rho_g(p) = \rho_{gs}b_g, \tag{15}$$

Assuming that the gas is ideal $Z = 1$, we get:

$$\rho_g(p) = \rho_{gs}b_g^{`}p, \quad b_g^{`} = \frac{T^{atm}}{Tp^{atm}}. \tag{16}$$

where $b_g^{`}$ is the inverse volume factor differentiated with respect to pressure. We note that $b_g^{`}$ is constant and has unit of inverse pressure.

2.5. Shale gas adsorption

From (14-16) we have:

$$\varphi\rho_g + (1-\varphi)a_g = \varphi\rho_{gs}b_g^{`}p + (1-\varphi)a_g = \varphi\rho_{gs}b_g^{`}\left(p + \frac{(1-\varphi)}{\varphi\rho_{gs}b_g^{`}}a_g\right) = \varphi\rho_{gs}b_g^{`}(p + \widehat{a}_g(p)), \tag{17}$$

where we have defined:

$$\widehat{a}_g(p) = \frac{(1-\varphi)}{\varphi\rho_{gs}b_g^{`}}a_g(p). \tag{18}$$

The pressure dependency is related through a Langmuir adsorption relation:

$$\widehat{a}_g(p) = \widehat{a}_{max}\frac{p}{p+p_L}, \tag{19}$$

where $\widehat{a}_{max}$ is the max capacity of the shale (in units of pressure) to store gas on the surface and p_L is the pressure at which half this capacity has been obtained.

2.6. Apparent permeability correction

Due to the nano-pore structure of the shale matrix, Darcy's law cannot describe the actual gas behavior and transport phenomena. Fluid flow departs from the continuum flow regime, in favour of other flow mechanisms such as slip flow, transition flow and free molecular conditions. The Knudsen number (Knudsen, 1909) which is a dimensionless parameter is used to differentiate between these flow regimes, for conduit with effective radius r_e, it is defined as:

$$K_n = \frac{\mu_g Z}{p_g r_e}\sqrt{\frac{\pi RT}{2M}}, \tag{20}$$

where T is absolute temperature, Z is gas compressibility factor, r_e is effective radius of flow path, R is the universal gas constant and M is gas molecular weight.

The apparent permeability of shale matrix can be represented by the following general form that relies only on Knudsen number K_n, and the effective intrinsic permeability $k_{\infty e}$ (Karniadakis and Beşkök, 2001):

$$k = k_{\infty e} f(K_n) \tag{21}$$

Florence et al. (2007) extended this derivation to characterize the non-Darcy gas flow in shale formations:

$$k = k_{\infty e}(1+\alpha_K K_n)\left(1+\frac{4K_n}{1+K_n}\right) \tag{22}$$

where α_K is the rarefraction parameter:

$$\alpha_K = \frac{128}{15\pi^2}\tan^{-1}\left(4K_n^{0.4}\right) \tag{23}$$

Considering the effect of matrix compaction and adsorbed layer on the nanopore geometry, the effective intrinsic permeability is given as (Jiang and Yang, 2018):

$$k_{\infty e} = \frac{r_e^2}{8}\frac{\varphi}{\tau} \tag{24}$$

where r_e is the effective radius of flow path and τ is the tortuosity of rock.

Huang and Ghassemi (2015) and Cao et al. (2016) gave generalized formulation that incorporates the overall contribution from effective stress, adsorption and flow regimes for the apparent gas permeability:

$$k = \frac{r_e^2}{8}\frac{\varphi}{\tau}(1+\alpha_K K_n)\left(1+\frac{4K_n}{1+K_n}\right) \tag{25}$$

2.7. Summary of model

Substituting (6-25) into (4) and (5), we summarize the system for the flow of gas in the fracture-matrix system:

$$\varphi^f b(y)\partial_t(p) = -\partial_y(pub(y)) - (pu)_{x=0,y}, \quad (x,y\in\Omega^f) \tag{26}$$

$$\varphi^m \partial_t\left(p+\hat{a}_g(p)\right) = -\partial_x(pu) \quad (x,y\in\Omega^m) \tag{27}$$

$$u = -\frac{k}{\mu_g} f\,\partial_x P \tag{28}$$

These flow equations must be solved together with the initial and boundary conditions.

2.7.1. Initial conditions

Initially, the fracture and matrix have the same reservoir pressure p_{init}. The adsorbed gas content in the matrix is defined from the isotherm at this pressure:

$$p_g(t=0) = p_{init}, \quad \hat{a}_g(t=0) = \hat{a}_{max}\frac{p_{init}}{p_{init}+p_L}. \tag{29}$$

2.7.2. Boundary conditions

The well is perforated at $y = 0$ with a known pressure:

$$p_g(y=0) = p_{well}, \quad (x\in\Omega^f). \tag{30}$$

There is pressure and mass flux continuity across the fracture-matrix boundary. The fracture is closed (or has negligible production) from the matrix in y-direction. Similarly, the matrix has, due to symmetry, no flow at its outer boundary:

$$\partial_y p_g|_{y=L_y} = 0, \quad \partial_x p_g|_{x=L_x} = 0. \tag{31}$$

2.8. Scaling of the model

We now scale the system by introducing the following dimensionless variables:

$$P = \frac{p_{well}-p_g}{\Delta p},\ Y = \frac{y}{L_y},\ X = \frac{x}{L_x},\ B = \frac{b}{b_0},\ D = \frac{p}{p_{avr}},\ \hat{A}_g = \frac{\hat{a}_g}{\Delta p},$$
$$K^m = \frac{k^m}{k^m_{ref}},\ F^m = \frac{f^m}{f^m_{ref}},\ K^f = \frac{k^f}{k^f_{ref}},\ F^m = \frac{f^f}{f^f_{ref}} \tag{32}$$

where

$$\Delta p = p_{init}-p_{well}, \quad p_{avr} = \frac{1}{2}(p_{init}+p_{well}) \tag{33}$$

$2b_0$ is the average width of the fracture. D is the gas diffusion coefficient resulting from the absolute pressure, scaled by the average pressure. The scaled coordinates obey $0 \le X, Y \le 1$. The scaled pressure P ranges between 0 and 1 (corresponding to the well pressure in absolute terms). The apparent permeability is scaled using a reference permeability defined as:

$$k^i_{ref} = \frac{2}{\left(\frac{1}{k^i(p_{init})}+\frac{1}{k^i(p_{well})}\right)}, \quad (i=m,f). \tag{34}$$

Accordingly, we scale the transition factor $f(z)$ using the k_{ref} and Δp:

$$f^i_{ref} = \frac{-1+\sqrt{1+2z^i_{ref}}}{z^i_{ref}}, \tag{35}$$

$$z^i_{ref} = 2\frac{\left(k^i_{ref}\right)^2}{\mu^2 L_i}\gamma^i_{ref}\rho_{gs}b_g^{`}p_{avr}|\Delta p|, \quad (i=m,f) \tag{36}$$

where:

$$\gamma^i_{ref} = \frac{C_\beta}{\left(k^i_{ref}\right)^{1.25}\varphi_i^{0.75}}, \quad (i=m,f) \tag{37}$$

Applying these dimensionless variables to (32-37), we can define two time scales (extending those defined in Berawala et al. (2019) to include non-Darcy effects):

- τ^f representing diffusion of gas from the fracture to the well,
- τ^m representing diffusion of free and adsorbed gas from the matrix to the fracture, given as follows:

$$\tau^f = \frac{\mu_g\varphi^f L_y^2}{f^f_{ref}k^f_{ref}p_{avr}}, \quad \tau^m = \frac{\mu_g\varphi^m(G^{`})_{ref}L_x^2}{f^m_{ref}k^m_{ref}p_{avr}} \tag{38}$$

Note that we have introduced the parameter $(G^{`})_{ref}$, motivated as follows: Let the quantity of gas in free and adsorbed form be represented by $G = P + \hat{A}_g$. A typical retardation factor is then:

$$(G^{`})_{ref} = \frac{\Delta G}{\Delta p} = 1+\frac{\hat{A}_g(p_{init})-\hat{A}_g(p_{well})}{\Delta p} \tag{39}$$

$(G^{`})_{ref} \ge 1$ denotes both the factor of increased time to produce gas from the matrix due to adsorption, but also the increased quantity of gas released from adsorption during the pressure depletion. Further, we scale time with respect to the fracture diffusion time scale:

$$t^{`} = \frac{t}{\tau^f}. \tag{40}$$

After scaling, the coupled transport system (26) and (27) can be expressed in the following form:

$$B\partial_t P = \partial_y\left(DBK^f F^f\partial_y P\right) + \alpha\beta(DK^m F^m\partial_X P)_{x=0,y}, \quad (x,y\in\Omega^f) \tag{41}$$

$$\frac{1}{(G^{'})_{ref}}\partial_T\left(P+\widehat{A}_g(P)\right) = \alpha\beta\partial_X(DK^mF^m\partial_X P), \quad (x,y\in\Omega^m) \tag{42}$$

All the constant terms are collected into the two following dimensionless variables α and β:

$$\alpha = \frac{\tau^f}{\tau^m} = \frac{\varphi^f L_y^2}{f_{ref}^f k_{ref}^f}\frac{f_{ref}^m k_{ref}^m}{(G^{'})_{ref}L_x^2\varphi^m},\ \beta = \frac{(G^{'})_{ref}L_x^2\varphi^m}{\varphi^f b_0},\ \alpha\beta = \frac{f_{ref}^m k_{ref}^m L_y^2}{f_{ref}^f k_{ref}^f L_x b_0}. \tag{43}$$

Physically, α represents the ratio of the time scales involved in gas diffusion from the fracture and gas diffusion from the matrix (including desorption), respectively. β denotes the pore volume ratio of the matrix relative to the fracture and consists of the additional amount of gas produced from the matrix due to adsorption, indicated by $(G^{'})_{ref}$.

Comparing to Berawala et al. (2019), the updated model represented by (26-29) now consists of non-Darcy flow velocity u represented in a form comparable to Darcy flow through a transition factor f. It also accounts for permeability variation in the matrix due to gas slippage effects, adsorption and effective stresses. The scaling of model also leads to new definitions of dimensionless variables. However, it is important to note that diffusion time scale of matrix τ_m comprises of reference transition factor f_{ref}^m whose value changes with matrix non-Darcy flow constant from case to case.

3. Simulation results

In this section, we study the behavior of the model (Eqs. (39)–(41)) by considering Marcellus shale Langmuir isotherm parameters defined in Table 2. We also perform sensitivity analysis to various input parameters to identify the conditions under which the non-Darcy effect becomes significant. In particular, we plot overall gas recovery vs time and show distributions of scaled pressure, transition factor and the relative amount of total mass in the system at 15% production of the mass initially in the reservoir, denoted by RF_{ob}.

The system is solved by an operator-splitting approach, similar to that described by Andersen et al. (2014, 2015), Berawala et al. (2019) and Berawala and Andersen, (2020). In this approach, we alternatively solve for flow in the y-direction (fracture diffusion) and flow in the x-direction (fracture/matrix diffusion and desorption). We refer to Appendix A for a detailed solution procedure. In total 600 cells were used with 20 equal cells in y-direction and 30 equal cells in positive x-direction. The numerical solution was validated by Berawala et al. (2019) by comparing the model with the established industry software Eclipse (GeoQuest, 2009) for a case with negligible amount of adsorbed gas in the matrix, a fracture with uniform width and gas transportation driven by Darcy flow. The full system (both sides of matrix surrounded by fracture) was then modelled using $80{\cdot}20{\cdot}1 = 1600$ blocks and solved fully implicit. Using gas recovery and pressure vs time profiles at different locations relative to the fracture and well, the numerical solution was found consistent with that of Eclipse.

Mean pore radius of shale matrix is usually in the range of 1–100 nm (Javadpour et al., 2007; Loucks et al., 2009; Zou et al., 2012; Yao et al., 2013), we use a representative value 14 nm for simulation. Using the input parameters defined in Table 2, we get Knudsen number (K_n) in the range of 0.01–0.1 which indicates slip-flow or transition flow regime (refer Table 1). This implies the mean-free path of gas molecule is less or of the same magnitude as pore size of the matrix. In this regime, the gas transport is mainly governed by Knudsen diffusion and the conventional Darcy's law equation with no-slip boundary conditions cannot be applied. The permeability described by Eq. (25) takes into account this slippage effect. The corresponding apparent permeability for the reference case parameters is shown in Fig. 2(b).

Table 1
Classification of gas-flow regimes according to Knudsen number, K_n (Roy et al., 2003).

$K_n < 10^{-3}$	$0.001 < K_n < 0.1$	$0.1 < K_n < 10$	$K_n > 10$
Continuum flow regime	Slip flow regime	Transition- flow regime	Free molecular regime

Eq. (12) described in **2.3** denotes the transition factor f which is a function of non-Darcy flow velocity z. The transition factor will always be less or equal to 1. $f(z) = 1$ indicates Darcy flow and a value less than 1 would indicate how significant the non-Darcy effect is. We plot the transition factor f against z as shown in Fig. 3. We see that the gas transport is governed by non-Darcy effects when $z > 10^{-1}$. To establish the conditions under which this can happen, we perform sensitivity analyses (**3.1**) on various input parameters such as non-Darcy flow constant (C_β), pore size (r_m), fracture permeability (k^f), and shape (b_0) and size. Further, we also compare how each of these parameters affect gas recovery with/without non-Darcy flow in the matrix and fracture.

3.1. Sensitivity analysis

3.1.1. Reference case demonstration

Using the reference case parameters listed in Table 2, we present scaled average gas pressure and recovery profiles against time for four systematically varied non-Darcy flow constants C_β, see Fig. 4. The same values are applied to fracture and matrix. The $C_\beta = 0$ case indicates that Darcy flow is considered both in matrix and fracture. As seen from Fig. 4, the recovery process goes much faster for Darcy flow $C_\beta = 0$ compared to the non-Darcy cases $C_\beta = 1e-6,\ 3e-6$ and $9e-6\ \mathrm{m}^{-2.5}$. This indicates that with increasing the magnitude of non-Darcy flow constant, the gas is produced at a much slower rate. To report how significant the non-Darcy effect for individual cases is, we report the reference transition factor f_{ref} values for both fracture and matrix, denoted by f_{ref}^f and f_{ref}^m in Table 3. The reference values are calculated using the pressure gradient between initial reservoir and well pressure divided over the entire length of the matrix (refer to Eq. (35)). For $C_\beta = 1e-6\ \mathrm{m}^{-2.5}$, we get $f_{ref}^f = 0.11$ and $f_{ref}^m = 0.87$, which indicates that the flow is reduced by 89% and 13% compared to Darcy flow for the same pressure gradient in fracture and matrix respectively. Also, from Eq. (11), we see that for the same pressure gradient, non-Darcy flow will give lower velocities than Darcy. In general, both Darcy and non-Darcy Forchheimer models predict the same behavior at low velocity. But at high velocities like in fracture, non-Darcy models results in reduced velocities limiting the overall gas recovery.

To further understand as to why non-Darcy effects limits the production, we plot in Fig. 5 distributions of scaled pressure, total mass and transition factor after $RF_{ob} = 15\%$ for three values $C_\beta = 0,\ 1e-6$ and $3e-6\ \mathrm{m}^{-2.5}$. Scaled total mass is defined as the relative amount of gas currently in place to initial mass of gas in matrix and fracture (refer to Appendix C, Eq. (68)). If $C_\beta = 0$ (Darcy flow), we see that the gas entering the fracture is instantly produced to the well. A zero-scaled pressure in the fracture for this case and uniform pressure and total mass distribution surrounding the fracture is observed. The flow here is mainly governed by matrix and we are in a *matrix-controlled regime*. In the case with $C_\beta = 1e-6,\ 3e-6\ \mathrm{m}^{-2.5}$ (non-Darcy flow), the gas requires some time to leave the fracture and a significant pressure is observed in the fracture. This high-pressure gradient reduces the production rate from the matrix and leads to more non-uniform production around the fracture. We can thus say that non-Darcy effects leads to significant residence time in the fracture and controls the rate of recovery. The flow becomes more fracture-dominated or *fracture-controlled regime*. Inspired by works on spontaneous imbibition (Rangel-German and Kovscek, 2002; Andersen et al., 2014); Berawala et al. (2019) showed that also the production of shale gas can be classified into matrix- or fracture-controlled. A similar approach is applied here with respect to the role of non-Darcy flow.

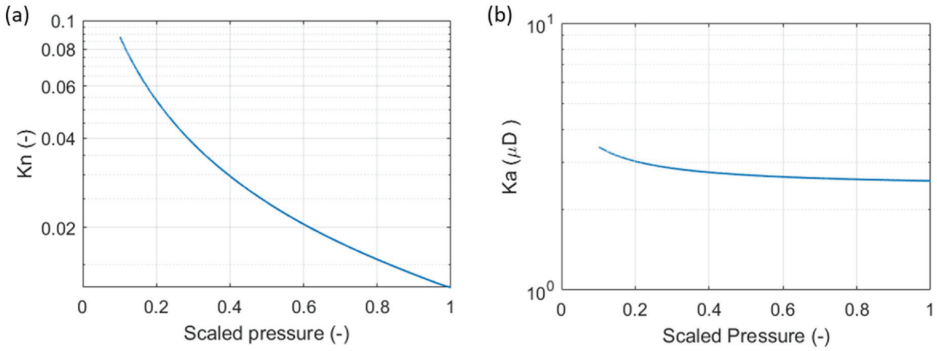

Fig. 2. Knudsen number (a) and apparent permeability (b) vs scaled pressure for reference case input parameters defined in Table 2.

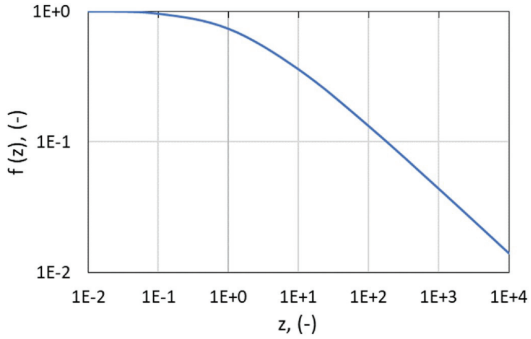

Fig. 3. Transition factor $f(z)$ vs z indicating Darcy to non-Darcy flow transition.

Table 2
Input parameters used for reference case simulations.

Parameters	Value	Units
Average fracture half-width, b_0 [b]	0.02	m
Bottom hole well pressure, p_{well} [a]	17.24	Bar
Fracture length, L_y [b]	7	m
Fracture permeability, k^f [b]	10	mD
Fracture porosity, φ^f [b]	0.60	–
Fracture height, h [b]	1	m
Gas compressibility factor (ideal gas), Z	1	–
Gas constant, R	8.314	J/mol
Gas density at standard condition, ρ_{gs} [b]	0.7	kg/Sm^3
Gas viscosity, μ_g [b]	0.0184	cP
Initial reservoir pressure, p_{init} [a]	344.7	Bar
Langmuir max adsorption capacity, a_{max} [a]	5.023	kg/m^3
Langmuir half capacity pressure, p_L [a]	27.58	Bar
Matrix half length, L_x	15	m
Matrix porosity, φ^m [b]	0.15	–
Mean pore radius, r_e	14	nm
Molar mass of methane, M	16.04	g/mol
Max-to-min fracture width ratio, $\frac{b_{max}}{b_{min}}$	1	–
Reservoir temperature, T [a]	323.15	K
Non-Darcy flow constant, C_β	$1e-6$	m$^{-2.5}$

[a] Yu et al. (2016).
[b] Berawala et al. (2019).

3.1.2. Role of individual fracture and matrix non-Darcy flow constants

In order to understand the importance of non-Darcy flow in the fracture and matrix domains, we consider two cases where we turn off the non-Darcy effect alternately in each domain and plot scaled pressure and gas recovery versus time. These two cases are compared against Darcy flow denoted by dashed line in Fig. 6 and against the reference case where we used same $C_\beta = 1e-6$ m$^{-2.5}$ for both fracture and matrix.

For the case where non-Darcy flow is considered only in the matrix ($C^f_\beta = 0,\ C^m_\beta = 1e-6$ m$^{-2.5}$, green line), we obtain similar recovery as in the case of Darcy flow. This shows that for the input parameters mentioned in Table 2, non-Darcy effects in the matrix do not play a significant role. When $C^f_\beta = 1e-6,\ C^m_\beta = 0$ m$^{-2.5}$ (orange line), we get much lower recovery compared to the Darcy flow. The gas transport from matrix to the well is then fracture dominated, i.e. the time scale of transporting gas through the fracture limits the gas production compared to producing the gas from the matrix. This also follows from the mathematical formulation of diffusion time scale for fracture (Eq. (38)). High C_β in fracture and its intrinsic properties give very low f^f_{ref} resulting in higher diffusion time for gas in fracture compared to matrix.

3.1.3. Effect of pore size

In this section, we investigate the role of matrix pore size r_m on gas recovery. We consider four pore radii $r_m = 10,\ 20,\ 40,\ 80$ nm and plot Knudsen number, apparent permeability in Fig. 7(a) & **(b)**. As seen from the figure, increasing pore radii in the matrix, increases the Knudsen number. For higher pore radii, pore size becomes comparatively larger than the mean-free path of gas molecules and gas is mainly driven by viscous forces. Apparent permeability is proportionally linked to the Knudsen number (refer Eq. (25)). Increase in Knudsen number with increasing pore size gives higher apparent permeability as shown in Fig. 7(b).

Fig. 7(c) shows the recovery profile when only Darcy flow is considered in the system. It can be seen that at higher pore radii, gas travels from matrix to the fracture at much faster rate due to high apparent permeability, which is then produced from the fracture instantaneously. However, when the same cases are plotted in presence of non-Darcy effects both in matrix and fracture (Fig. 7(d)), we see delay in production. As seen in **3.1.1**, non-Darcy effect also here cause a shift from matrix-controlled flow regime towards fracture-controlled flow regime. A high-pressure gradient is created in the matrix due to which gas is not uniformly produced from fracture surroundings. The fracture then limits the flow of gas and thus; the gas is not instantaneously produced to the well. Interestingly, for cases with sufficiently low pore radii ($r_m < 40$ nm), gas recovery seems to be less sensitive in the

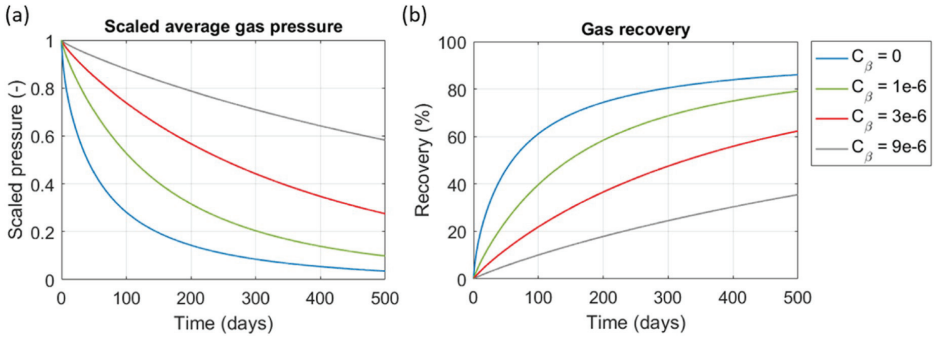

Fig. 4. Scaled average pressure (a) and gas recovery (b) profiles for four systematically varied non-Darcy flow constant C_β.

Table 3
Reference transition factor values of fracture and matrix for systematically varied four non-Darcy flow constants.

$C_\beta(\mathrm{m}^{-2.5})$	$f^f_{ref}(-)$	$f^m_{ref}(-)$
0	1	1
$1e-6$	0.11	0.87
$3e-6$	0.07	0.73
$9e-6$	0.04	0.54

presence of non-Darcy effects as compared to Darcy flow in the system. This is because non-Darcy effects incurs residence time in the fracture in addition to increase travel time for gas to flow from matrix to the fracture.

3.1.4. Effect of fracture permeability

In the following, we consider the role of fracture permeability k^f by plotting gas recovery for the system with/without non-Darcy effects. The fracture permeability is varied between 1 mD and 1000 mD. As seen in Fig. 8(a), fracture permeability barely has any influence on gas recovery for Darcy flow. The effect is dominant only when k^f is very low (~1mD). Low fracture permeability gives lower matrix-to-fracture pressure gradient, resulting in lower recovery rate compared to the

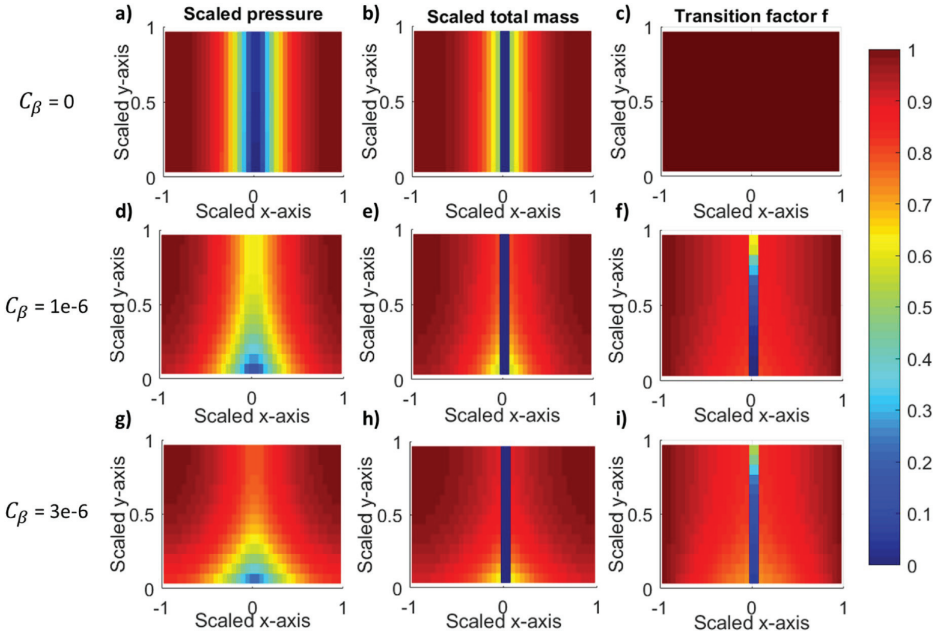

Fig. 5. Scaled pressure, scaled total mass and transition factor distribution for different non-Darcy flow constants after $RF_{ob} = 15\%$.

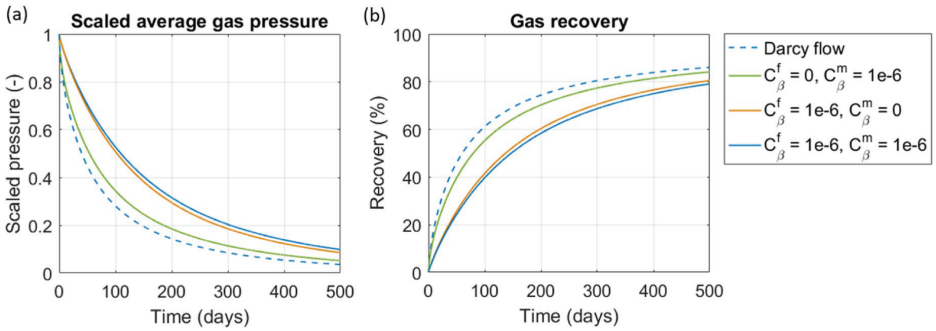

Fig. 6. Scaled gas pressure (a) and gas recovery (b) vs time for different C_β in fracture and matrix.

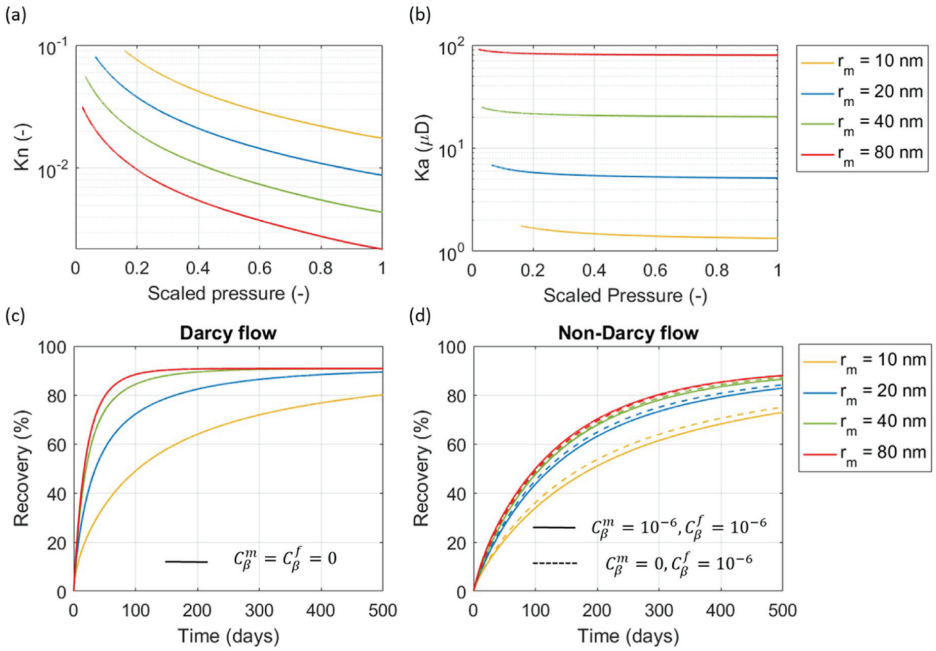

Fig. 7. Effect of matrix pore size on Knudsen number (a), apparent permeability (b), gas recovery with only Darcy flow (c) and with non-Darcy flow (d) in the system.

case with much higher recovery (1000 mD). This was also observed by Berawala et al. (2019).

For non-Darcy flow (Fig. 8(b)), we see that fracture permeability becomes very important and the production is limited by the fracture until k^f~100 mD, a fracture controlled regime. However, when non-Darcy effects are turned off in the matrix, the recovery becomes more sensitive with increasing fracture permeability. The effect of non-Darcy flow in matrix becomes more important at higher fracture permeability.

3.1.5. Effect of fracture shape and size

We compare three cases with average fracture width (b_0) 0.05 m, 0.02 m (reference), and 0.09 m to evaluate the effect of fracture size. The fracture width in all the cases above was assumed to have constant width. Here, we also consider cases where the fracture shape varies. The fracture width decreases linearly with distance from the well and is defined by three parameters; the length L_y, the average half-width b_o and the max-to-min width ratio b_{max}/b_{min} :

$$b(y) = 2b_0\left(\frac{b_{max}/b_{min}}{(b_{max}/b_{min}+1)} - \frac{(b_{max}/b_{min}-1)}{(b_{max}/b_{min}+1)}\frac{y}{L_y}\right) \tag{44}$$

For a uniform fracture width, i.e. $b_{max}/b_{min} = 1$, we get $b(y) = 2b_0$. For each of the fracture widths considered, we use two subcases with $\frac{b_{max}}{b_{min}}$ ratio of 1 and 10 to evaluate the effect of fracture shape. The $\frac{b_{max}}{b_{min}}$ ratio of 10 indicates that the fracture is 10 times narrower at the tip of the fracture ($y = L_x$) compared to at the well ($y = 0$), as illustrated in Fig. 1. Fig. 9 shows the simulated gas recovery for all cases with Darcy flow (a) and with non-Darcy flow (b) ($C_\beta^f = C_\beta^m = C_\beta = 10^{-6}$ m$^{-2.5}$) in the system.

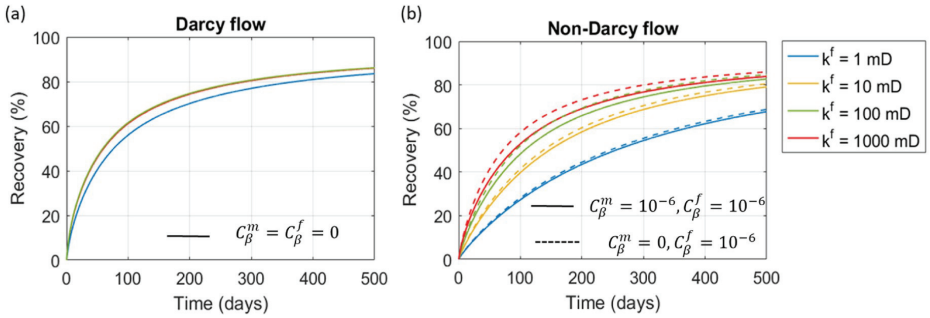

Fig. 8. Effect of fracture permeability on gas recovery with Darcy flow (a) and with non-Darcy flow (b) in the system.

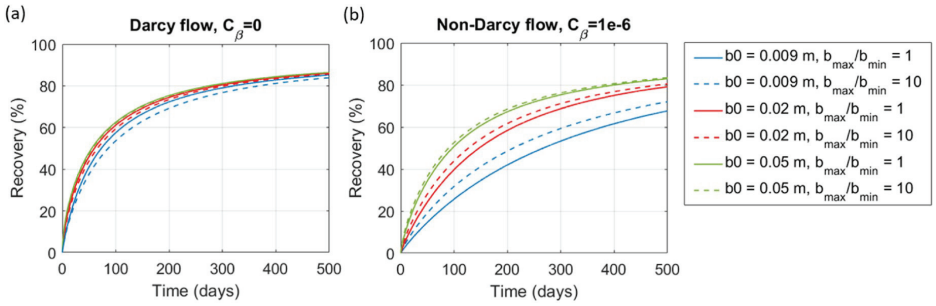

Fig. 9. Effect of fracture shape and size on gas recovery with Darcy flow (a) and with non-Darcy flow (b) in the system.

We see that for Darcy flow, gas recovery is very weakly sensitive to fracture shape and size, i.e. very similar profiles are seen. This indicates that the flow is mainly dominated by the matrix. However, at lower fracture width ($b_0 = 0.009$ m), we observe that the shape of the fracture becomes more important.

For the gas transport with non-Darcy effects in matrix and fracture (Fig. 9(b)), gas recovery becomes strongly sensitive to fracture shape. The flow of gas is delayed with decreasing fracture size and is controlled by fracture properties. This is reasonable as we have high k^f compared to the matrix. Moreover, for each fracture width, we note that gas is recovered at a faster rate with high $\frac{b_{max}}{b_{min}}$ ratio. Berawala et al. (2019) explained that the narrower the fracture is at the end; the less space does the gas have to diffuse towards the well resulting in a local pressure buildup. In such case, more gas is produced from the matrix in the near well region compared to th regions at the far end of the fracture. For the cases with widest fractures ($b_0 = 0.05$ m), the difference is not significant and a close to uniform production is seen along the fracture.

3.2. Interpretation using dimensionless numbers

In the above discussion, we have demonstrated how non-Darcy flow constants, matrix pore radius and fracture properties affect the production of shale gas with/without non-Darcy effects. In particular, we observed that non-Darcy effects typically shifts the flow towards

Table 4
Input parameters for simulation cases shown in Fig. 10, selected such that $\omega = \alpha\beta$ is nearly constant for 4 values: $\omega_i = 10^{-3}, 10^{-2}, 10^{-1}$ **and** 10^0. Other unspecified parameters are given by reference case values in Table 2.

	$\omega = \alpha\beta(-)$	$\alpha(-)$	$\beta(-)$	$f^m_{ref}(-)$	$f^f_{ref}(-)$	$c^m_\beta\,\mathrm{m}^{-2.5}(-)$	$c^f_\beta\mathrm{m}^{-2.5}(-)$	$k^f(\mathrm{mD})(-)$	$L_x(\mathrm{m})(-)$	$L_v(\mathrm{m})(-)$	$\varphi_m(-)$	$\varphi_f(-)$	$r_m(\mathrm{nm})(-)$
—	1e-3	5.2e-5	22.4	0.18	0.018	1.5e-4	1.5e-4	2000	15	6	0.01	0.6	10
- - -	6e-3	3.9e-5	30	1	0.018	0	9e-6	2000	15	6	0.01	0.6	10
—	1e-2	4e-4	22.4	0.16	0.005	9e-6	9e-6	1500	15	4	0.01	0.8	100
- - -	6e-2	2.8e-4	22.4	1	0.005	0	9e-6	1500	15	4	0.01	0.8	100
—	1e-1	5.4e-3	19.5	0.15	0.016	9e-6	9e-6	150	13	7	0.01	0.8	100
- - -	7e-1	3.6e-3	19.5	1	0.016	0	9e-6	150	13	7	0.01	0.8	46
—	1e0	0.014	70	0.26	0.037	9e-6	9e-6	10	10	5	0.1	0.8	34
- - -	4e0	0.056	70	1	0.037	0	9e-6	10	10	5	0.1	0.8	34

fracture-controlled regime as compared to matrix-controlled regime with Darcy flow. In this section, we demonstrate the cases where matrix properties become dominant as compared to fracture properties in the presence of non-Darcy effects. We do this by interpreting the results with the help of two dimensionless numbers α and β defined in Eq. (43).

Berawala et al. (2019) showed that the production of shale gas can be classified into matrix-controlled or fracture-controlled based on the magnitude of the product of α and β (this was first demonstrated for advection-spontaneous imbibition flow in Andersen et al. (2014)). They coined the parameter ω given by:

$$\omega = \frac{(\beta+1)\tau^f}{\tau^m} \approx \alpha\beta \tag{45}$$

From (42), we get:

$$\omega = \frac{(\beta+1)\tau^f}{\tau^m} \approx \alpha\beta = \frac{f^m_{ref} k^m_{ref} L_y^2}{f^f_{ref} k^f_{ref} L_x b_0}. \tag{46}$$

If $\omega \ll 1$, the flow of gas is completely controlled by the time scale of diffusion from the matrix. For larger ω, the residence time in the fracture is significant and further delays the process. Thus, when gas recovery is plotted for the cases with low ω and high non-Darcy flow constant for matrix and fracture, we expect to see matrix-controlled flow regime. To perform this test, we present eight simulation cases of gas recovery to give approximate values of the product $\omega = \alpha\beta = 1e-3, 1e-2, 1e-1, 1e0$. Both linear and non-linear parameters are varied as explained in Table 4. Other parameters are kept constant as listed in Table 2 unless otherwise is specified. All the simulation cases are presented in terms of gas recovery vs time in Fig. 10.

In particular, we compare two scenarios: 1) Increased non-Darcy flow effects both in matrix and fracture by considering high C^m_β and C^f_β values. This will give low f^m_{ref} indicating significantly high non-Darcy effect in the matrix (indicated by solid lines). 2) Compare 1) with non-Darcy effects only in the fracture, by assigning $C^m_\beta = 0$ giving $f^m_{ref} = 1$ (indicated by dashed lines). We do this for all values of $\omega = 1e-3, 1e-2, 1e-1, 1e0$. Note: assigning $C^m_\beta = 0$ would affect the ω value. In such cases, all the other parameters defined in Table 4 are kept constant so that the recovery is only affected by the matrix non-Darcy effect.

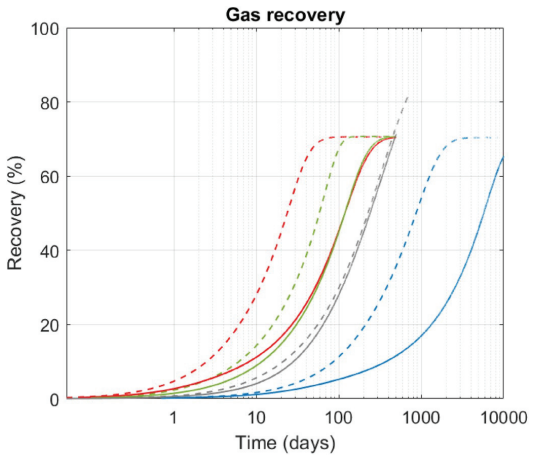

Fig. 10. Absolute gas recovery vs scaled time. Comparative test where $\boldsymbol{\omega = \alpha\beta}$ is approximately for 4 values: $\boldsymbol{\omega_i = 1e-3, 1e-2, 1e-1}$ **and** $\boldsymbol{1e0}$. Input parameters are varied in 8 tests as described in Table 4. $\boldsymbol{\omega}$ seems to characterize the flow regime of the fracture-matrix system. Unspecified parameters are given by reference case values in Table 2.

Logarithmic time axis is used in Fig. 10 since the simulations span over a wide range of time scale.

We observe that for cases with low value of ω (1e-1), gas recovery is strongly sensitive to non-Darcy effects in the matrix. Only at high $\omega = 1$ (grey lines), we see negligible effect of non-Darcy flow in matrix. This is because at high ω, flow is dominated by fracture properties and residence time for the flow of gas in fracture plays a key role. On the other hand, for high ω, flow is controlled by the residence time in matrix and the recovery only depends on matrix properties.

We repeat the simulation cases described in Table 4 and plot them against the time scaled against τ_m. However, this time for cases with no non-Darcy effect in matrix, we vary the other input parameters and adjust them in such a way that we get same ω as their corresponding pair with non-Darcy effect in both fracture and matrix. These changes are reflected in Table 5. As demonstrated by Berawala et al. (2019), we expect that the different simulation cases group well according to the value of ω. However, from Fig. 11, we see that a unique behavior with completely overlapping curve is not observed. This discrepancy is due to the fact that diffusion time scale of matrix τ_m comprises of reference transition factor f^m_{ref} whose value changes with matrix non-Darcy flow constant from case to case. Thus, the case with $\omega = 1e-2, 1e-1$ (red and green lines) show similar trend as they have similar f^m_{ref} values. The cases with $\omega < 1e-1$ still show similar behavior and maximum recovery is obtained for those cases compared to $\omega = 1e0$.

The extended 1D+1D model is a useful tool to evaluate sensitivity of input parameters, to understand the role of non-Darcy effects in matrix and fracture and to qualitatively study the shale gas production system. However, the model does not consider changes in effective stresses during production. The resulting changes in fracture or matrix porosity and permeability due to geomechanical effects might alter some of the results discussed in this paper. Moreover, the model considers flow of gas only from stimulated reservoir volume, i.e. the domain affected by the hydraulic fracture. However, flow of gas from beyond the tip of fracture and cross-flow could also contribute to overall recovery. These effects should be evaluated before extending the model to field scale application.

4. Conclusions

In this paper, we have presented a model for production of shale gas by incorporating non-Darcy and gas slippage effects. The system consists of a single fractured extended vertically from a well perforation and is surrounded symmetrically by shale matrix. The model presented is derived in such a way that it helps us to investigate the transition from Darcy to non-Darcy flow. With the help of Forchheimer's equation, the role of non-Darcy effects were for different conditions of geometry and intrinsic properties of the fracture-matrix system. The results were further interpreted by dimensionless numbers. From the numerical investigations presented, we draw the following conclusions:

- Non-Darcy flow shifts the flow regime towards fracture dominated. The non-Darcy effects are more pronounced in fracture than matrix and cause greater increase in fracture diffusion time than matrix diffusion time.
- Theoretical and numerical results indicated that the model cases could be classified according to *matrix-dominated* for $\omega \ll 1$ (the matrix then limits the gas production) and *fracture-dominated* where $\omega \approx 1$ (the fracture limits the gas production).
- Non-Darcy flow in the matrix is significant when the flow regime is matrix dominated and non-Darcy flow in matrix significantly reduces matrix flow rate. When any of these conditions is not met, non-Darcy flow in the matrix is not relevant. This is mathematically equivalent to the dimensionless number $\omega \ll 1$ and $f^m_{ref} \ll 1$ as expressed in our model.

Table 5
Input parameters for simulation cases shown in Fig. 11, selected such that $\omega = \alpha\beta$ is constant for 4 values: $\omega_i = 10^{-3}, 10^{-2}, 10^{-1}$ **and** 10^{0}. Other unspecified parameters are given by reference case values in Table 2.

	$\omega = \alpha\beta(-)$	$\alpha(-)$	$\beta(-)$	$f^m_{ref}(-)$	$f^f_{ref}(-)$	$c^m_\beta\,\mathrm{m}^{-2.5}(-)$	$c^f_\beta\mathrm{m}^{-2.5}(-)$	$k^f(\mathrm{mD})(-)$	$L_x(\mathrm{m})(-)$	$L_v(\mathrm{m})(-)$	$\varphi_m(-)$	$\varphi_f(-)$	$r_m(\mathrm{nm})(-)$
—	1e-3	5.2e-5	22.4	0.49	0.005	9e-6	9e-6	1500	15	5	0.01	0.6	14
- - -	1e-3	4.6e-5	30	1	0.005	0	9e-6	1500	15	5	0.01	0.6	10
—	1e-2	4e-4	22.4	0.16	0.005	9e-6	9e-6	1500	15	4	0.01	0.8	100
- - -	1e-2	2.8e-4	30	1	0.005	0	9e-6	2000	20	4	0.01	0.8	50
—	1e-1	5.4e-3	19.5	0.15	0.016	9e-6	9e-6	150	13	7	0.01	0.8	100
- - -	1e-1	3.6e-3	30	1	0.016	0	9e-6	150	20	7	0.01	0.8	46
—	1e0	0.0l	100	0.09	0.564	9e-6	9e-6	10	10	5	0.1	0.8	34
- - -	1e0	0.01	176	1	0.564	0	9e-6	10	25	5	0.1	0.6	27

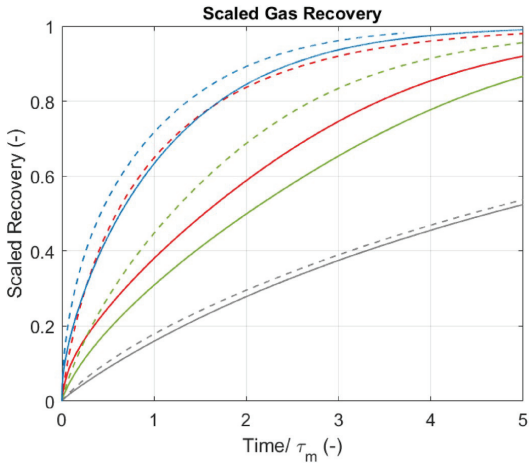

Fig. 11. Scaled gas recovery vs scaled time. Comparative test where $\omega = \alpha\beta$ is constant for 4 values: $\omega_i = 1e-3,\ 1e-2,\ 1e-1$ ***and*** $1e0$. Input parameters are varied in 8 tests as described in Table 5. ω seems to characterize the flow regime of the fracture-matrix system. Unspecified parameters are given by reference case values in Table 2.

- The gas recovery is more sensitive to the size and shape of the fracture in presence of non-Darcy flow compared to Darcy flow.
- At sufficiently high fracture permeability ($k^f > 100$ mD for our base case), diffusion time in the fracture reduces. Recovery profiles then become very similar and unchanging with permeability both for Darcy and non-Darcy flow. The impact of non-Darcy flow in the matrix becomes more sensitive at high fracture permeability.
- The magnitude of the f-factor helps to quantify the transition of Darcy flow to non-Darcy flow. At high non-Darcy flow constant C_β, non-Darcy effects in the matrix show greater sensitivity due to lower f^m_{ref} value and should be considered for evaluation of shale gas production.
- Because of the parameters appearing in ω, we can conclude that matrix properties will control the production if f^m_{ref} is low, matrix is much less permeable than fracture, the fracture volume is low and the fracture spacing is large.

Declaration of interests

The authors declare that they have no known competing financial interests or personal relationships that could have appeared to influence the work reported in this paper.

CRediT authorship contribution statement

Dhruvit S. Berawala: Conceptualization, Data curation, Formal analysis, Investigation, Methodology, Validation, Writing - original draft, Writing - review & editing. **Pål Ø. Andersen:** Conceptualization, Data curation, Formal analysis, Investigation, Methodology, Validation, Writing - original draft, Writing - review & editing.

Acknowledgments

The authors acknowledge the Research Council of Norway and the industry partners, ConocoPhillips Skandinavia AS, Aker BP ASA, Eni Norge AS, Total E&P Norge AS, Equinor ASA, Neptune Energy Norge AS, Lundin Norway AS, Halliburton AS, Schlumberger Norge AS, Wintershall Norge AS, and DEA Norge AS, of The National IOR Centre of Norway for support. The authors acknowledge Prof. Zhixin Yu (University of Stavanger) for administrative support of Mr. Berawala's PhD project.

Appendix

A. Operator Splitting

The transport system described by Eqs. (41) and (42) is solved numerically using an operator splitting approach like that presented in Andersen et al. (2014, 2015), Berawala et al. (2019) and Berawala and Andersen, (2020). The coupled system is split into two subsystems, one for the flow in y-direction (fracture diffusion) and second, for the flow in x-direction (fracture/matrix diffusion). We then apply the Strang splitting approach where system 1 is solved for the time $\frac{\Delta T}{2}$, then system 2 is solved for the time ΔT. This is then again followed by solving system 1 for time $\frac{\Delta T}{2}$.

System 1- *Fracture diffusion in y-direction.*

We set $\partial_X P = 0$ and $\partial_T \widehat{A}_g = 0$ indicating no adsorption. This gives:

$$\begin{aligned} B_D \partial_T P &= \partial_Y \left(DB_D \; K^f F^f \partial_Y P \right), \quad \left(X, Y \in \Omega^f \right) \\ \partial_T \left(P + \widehat{A}_g \right) &= 0, \quad \left(X, Y \in \Omega^m \right) \end{aligned} \tag{47}$$

System 2- Fracture/Matrix diffusion and desorption and flow in the x-direction.

Here, we assume no flow in *y*-direction and set $\partial_y P = 0$, we get:

$$\begin{aligned} B_D \partial_T P &= \alpha\beta \left(D\, K^f F^f \partial_X P \right)_{x=0,y}, \quad \left(X, Y \in \Omega^f \right) \\ \frac{1}{(G^{'})_{ref}} \partial_T P &= \alpha \partial_X \left(D\, K^m F^m \partial_X P \right), \quad \left(X, Y \in \Omega^m \right) \end{aligned} \tag{48}$$

The system is further split into two subsystems: 1) We only consider diffusion of free gas with adsorbed mass held fixed and 2) equilibrate adsorbed gas with free gas in the matrix.

Fracture matrix diffusion. With no desorption, we set $\partial_T \widehat{A}_g = 0$ and solve the diffusion system:

$$B \partial_t P = \alpha\beta \left(DK^f F^f \partial_X P \right)_{x=0,y}, \quad \left(x, y \in \Omega^f \right) \tag{49}$$

$$\frac{1}{(G^{'})_{ref}} \partial_T (P) = \alpha\beta \partial_X (DK^m F^m \partial_X P), \quad (x, y \in \Omega^m) \tag{50}$$

Desorption. No flow is considered.

$$B \partial_t P = 0 \quad \left(x, y \in \Omega^f \right) \tag{51}$$

$$\partial_T \left(P + \widehat{A}_g \right) = 0, \quad (x, y \in \Omega^m) \tag{52}$$

The conserved property here is $P + \widehat{A}_g$. From the definition of the Langmuir isotherm and mass conservation we obtain:

$$p_{eq} = -\frac{1}{2}(p_L + \widehat{a}_{max} - G) + \frac{1}{2}\sqrt{(p_L + \widehat{a}_{max} - M)^2 + 4 p_L G} \tag{53}$$

where p_{eq} is the equilibrium pressure adjusted for $\widehat{a}_g$ after fracture-matrix diffusion of free gas. G denotes conserved property with units of pressure, $G = p_g + \widehat{a}_g(p_g)$. The equilibrium pressure p_{eq} is then scaled and returned from the adsorption-correction. Refer to Berawala et al. (2019) for detailed procedure.

B. Discretization

Let the *y*-axis be discretized into $j = 1 : N_y$ cells and the matrix into $i = 1 : N_x$ cells.

System 1- Fracture diffusion

The scaled (half) width $B(y)$ is constant for a given cell j denoted by B_j. The conserved property is P, which is integrated over the grid cell gives:

$$\frac{B_j \left(P_j^{n+1} - P_j^n \right)}{\Delta T} = \frac{\left(DBK^f F^f \partial_Y P \right)_{j+\frac{1}{2}} - \left(DB_D \, K^f F^f \partial_Y P \right)_{j-\frac{1}{2}}}{\Delta Y} \tag{54}$$

The flux is further discretized as:

$$\left(DB \, K^f F^f \partial_Y P \right)_{j+\frac{1}{2}} = \frac{D_{j+1} + D_j}{2} \; \frac{B_{j+1} + B_j}{2} \; \frac{K^f{}_{j+1} + K^f{}_j}{2} \; \frac{F^f{}_{j+1} + F^f{}_j}{2} \; \frac{P_{j+1} + P_j}{\Delta Y} \tag{55}$$

At the fracture boundaries we set:

$$P_0 = 0, \quad \left(DB(y) K^f F^f \partial_y P \right)_{N_y + \frac{1}{2}} = 0. \tag{56}$$

System 2- Fracture-Matrix Diffusion.

For central cells in the matrix, we have:

$$\frac{1}{(G^{'})_{ref}} \frac{P_j^{n+1} - P_j^n}{\Delta T} = \alpha \frac{(DK^m F^m \partial_X P)_{i+\frac{1}{2}} - (DK^m F^m \partial_X P)_{i-\frac{1}{2}}}{\Delta X} \tag{57}$$

with the flux defined by:

$$(DK^m F^m \partial_x P)_{i+1/2} = \frac{D_{i+1} + D_i}{2} \; \frac{K^m{}_{i+1} + K^m{}_i}{2} \; \frac{F^m{}_{i+1} + F^m{}_i}{2} \; \frac{P_{i+1} - P_i}{\Delta X}. \tag{58}$$

At the fracture-matrix interface we have:

$$B_j \frac{P_0^{n+1} - P_0^n}{\Delta T} = \alpha\beta \left(DK^f F^f \partial_x P \right)_{i=1/2 \; j}, \quad \left(x, y \in \Omega^f \right), \tag{59}$$

$$\frac{P_1^{n+1} - P_1^n}{\Delta T} = \alpha \frac{(DK^m F^m \partial_x P)_{i=3/2 j} - (DK^m F^m \partial_x P)_{i=1/2 j}}{\Delta X}, \; (x, y \in \Omega^m). \tag{60}$$

The fracture-matrix flux term at this interface is evaluated by:

$$(DK^m F^m \partial_x P)_{i=1/2,j} = \frac{D_0 + D_1}{2} \frac{K^m{}_0 + K^m{}_1}{2} \frac{F^m{}_0 + F^m{}_1}{2} \frac{P_1 - P_0}{(\Delta X/2)}, \tag{61}$$

similar to the central fluxes except that the pressure gradient assumes the fracture pressure is given at the interface and not the fracture centre. Finally, the flux is set to 0 at the matrix outer boundary:

$$(D\partial_x P)_{i=N_x+1/2,j} = 0. \tag{62}$$

C. Initial and Current Gas in Place and Recovery Factor

The gas currently in place (*GCIP*) is given by the addition of the mass of gas adsorbed in the matrix (M_1), free gas in the fracture (M_2) and free gas in the matrix (M_3). These masses are calculated over both sides of the fracture.

$$GCIP = M_1 + M_2 + M_3 \tag{63}$$

$$GCIP = 2h \sum_{i=1}^{n_x} \sum_{j=1}^{n_y} (1-\varphi^m) a_g\left(p_g\left(x_i, y_j\right)\right) \Delta x \Delta y + \varphi^f \rho_{gs} b_g^{'} h \sum_{j=1}^{n_y} p_g\left(y_j\right) 2b\left(y_j\right) \Delta y + 2\varphi^m \rho_{gs} b_g^{'} h \sum_{j=1}^{n_y} p_g\left(x_i, y_j\right) \Delta x \Delta y. \tag{64}$$

The gas originally in place (*GOIP*) can be evaluated by using gas currently in place at initial reservoir pressure p_{init}:

$$GOIP = GCIP(p_{init}) \tag{65}$$

The recovery factor *RF* is then evaluated as:

$$RF = 1 - \frac{GCIP}{GOIP} = 1 - \frac{GCIP}{GCIP(p_{init})}. \tag{66}$$

The obtainable recovery is defined by:

$$RF_{ob} = \frac{RF}{RF_{\infty}} = \frac{GCIP(p_{init}) - GCIP}{GCIP(p_{init}) - GCIP(p_{well})}. \tag{67}$$

Scaled total mass in the matrix and fracture is mathematically defined as:

$$M_T = \frac{GCIP}{GOIP(p_{init})} = \frac{M1 + M3}{M1(P_{init}) + M3(P_{init})} + \frac{M2}{M2(P_{init})} \tag{68}$$

Nomenclature

Roman

a_g	Adsorbed gas, kg/m^3
a_{max}	Max capacity adsorbed gas, kg/m^3
$\hat{a}_g$	Adsorbed gas, Pa
$\hat{a}_{max}$	Max capacity adsorbed gas, Pa
b	Fracture half-width, m
b_0	Average fracture half-width, m
b_{max}	Max half width (at well), m
b_{min}	Min half width (end of fracture), m
b_g	Inverse gas volume factor,
C_β	Non-Darcy flow constant, m$^{-2.5}$
f	Transition factor,
h	Fracture height, m
K	Absolute permeability, m^2
k	Apparent permeability, m^2
k_f	Fracture permeability, m^2
K_n	Knudsen number,
L_x	Matrix half-length, m
L_y	Fracture length, m
M	Gas molecular weight, g/mol
p_g	Gas pressure, Pa
p_L	Langmuir half capacity pressure, Pa
R	Gas constant, J/mol
r_e	Pore radius, nm
T	Temperature, K
u	Gas velocity, m/s
V	Volume, m^3

Z	Gas compressibility factor,

Greek

α_K	Rarefraction parameter,
γ	Forchheimer's constant,
μ_g	Gas viscosity, Pa s
ρ_g	Gas molar density, mol/m3 gas
$\rho_{g,sc}$	Surface gas molar density, mol/m3 gas
τ	Tortuosity,
φ^m	Matrix Porosity,
φ^f	Fracture porosity,

Indices

atm	Atmospheric conditions
f	Fracture
init	Initial conditions
m	Matrix
well	Well conditions

Abbreviations

GOIP	Gas originally in place
GCIP	Gas currently in place

Appendix A. Supplementary data

Supplementary data to this article can be found online at https://doi.org/10.1016/j.petrol.2020.107114.

References

Al-Rbeawi, S., 2019. Flow-regime-based inflow-performance relationships of unconventional fractured reservoirs. SPE Prod. Oper. In press.

Al-Rbeawi, S., 2018. Performance-based comparison for hydraulically fractured tight and shale-gas reservoirs with and without non-Darcy-flow effect. SPE Reservoir Eval. Eng. 21 (4), 981-1.

Andersen, P.Ø., Evje, S., Kleppe, H., 2014. A model for spontaneous imbibition as a mechanism for oil recovery in fractured reservoirs. Transport Porous Media 101 (2), 299–331.

Andersen, P.Ø., Evje, S., Kleppe, H., Skjaeveland, S.M., 2015. A model for wettability alteration in fractured reservoirs. SPE J. 20 (6), 1–261.

Barree, R.D., Conway, M.W., 2005. Reply to Discussion of' Beyond Beta factors: A complete model for Darcy, Forchheimer, and Trans-Forchheimer flow in porous media. Journal of Petroleum Technology 57 (8), 73-73.

Belhaj, H.A., Agha, K.R., Nouri, A.M., Butt, S.D., Vaziri, H.F., Islam, M.R., 2003. Numerical simulation of non-Darcy flow utilizing the new Forchheimer's diffusivity equation. In: Paper Presented at Middle East Oil Show, Bahrain.

Berawala, D.S., Andersen, P., 2020. Evaluation of multicomponent adsorption kinetics for carbon dioxide enhanced gas recovery from tight shales. SPE Reservoir Eval. Eng. In press.

Berawala, D.S., Andersen, P.Ø., Ursin, J.R., 2019. Controlling parameters during continuum flow in shale-gas production: a fracture/matrix-modeling approach. SPE J. 24 (3), 1378–1394.

Beskok, A., Karniadakis, G.E., 1999. Report: a model for flows in channels, pipes, and ducts at micro and nano scales. Microscale Thermophys. Eng. 3 (1), 43–77.

Bird, R.B., 2002. Transport phenomena. Appl. Mech. Rev. 55 (1), R1–R4.

Blasingame, T.A., 2008. The characteristic flow behavior of low-permeability reservoir systems. In: Paper Presented at the SPE Unconventional Reservoirs Conference, USA.

Bybee, K., 2006. Non-Darcy flow in hydraulic fractures. J. Petrol. Technol. 58 (3), 58–59.

Cao, P., Liu, J., Leong, Y.K., 2016. Combined impact of flow regimes and effective stress on the evolution of shale apparent permeability. J. Unconv. Oil Gas Resour. 14, 32–43.

Cipolla, C.L., Lolon, E.P., Erdle, J.C., Rubin, B., 2010. Reservoir modeling in shale-gas reservoirs. SPE Reservoir Eval. Eng. 13 (4), 638–653.

Civan, F., 2010. Effective correlation of apparent gas permeability in tight porous media. Transport Porous Media 82 (2), 375–384.

Civan, F., Rai, C.S., Sondergeld, C.H., 2011. Shale-gas permeability and diffusivity inferred by improved formulation of relevant retention and transport mechanisms. Transport Porous Media 86 (3), 925–944.

Fan, M., McClure, J., Han, Y., Ripepi, N., Westman, E., Gu, M., Chen, C., 2019. Using an experiment/simulation-integrated approach to investigate fracture-conductivity evolution and non-Darcy flow in a proppant-supported hydraulic fracture. SPE J. 24 (4), 1912–1928.

Florence, F.A., Rushing, J., Newsham, K.E., Blasingame, T.A., 2007. Improved Permeability Prediction Relations for Low Permeability Sands. Paper presented at Rocky Mountain Oil & Gas Technology Symposium, USA.

Forchheimer, P., 1901. Wasserbewegung durch boden. Z. Ver. Deutsch, Ing. 45, 1782–1788.

GeoQuest, S., 2009. ECLIPSE Reservoir Simulator. Technical description.

Hagoort, J., 2004. Non-Darcy flow near hydraulically fractured wells. SPE J. 9 (2), 180–185.

Huang, J., Ghassemi, A., 2015. A poroelastic model for evolution of fractured reservoirs during gas production. J. Petrol. Sci. Eng. 135, 626–644.

Javadpour, F., 2009. Nanopores and apparent permeability of gas flow in mudrocks (shales and siltstone). J. Can. Petrol. Technol. 48 (8), 16–21.

Javadpour, F., Fisher, D., Unsworth, M., 2007. Nanoscale gas flow in shale gas sediments. J. Can. Petrol. Technol. 46 (10).

Jiang, J., Yang, J., 2018. Coupled fluid flow and geomechanics modeling of stress-sensitive production behavior in fractured shale gas reservoirs. Int. J. Rock Mech. Min. Sci. 101, 1–12.

Jones, S.C., 1987. Using the inertial coefficient, β, to characterize heterogeneity in reservoir rock. In: Paper Presented at SPE Annual Technical Conference and Exhibition, USA.

Klewiah, I., Berawala, D.S., Walker, H.C.A., Andersen, P.Ø., Nadeau, P.H., 2019. Review of experimental sorption studies of CO2 and CH4 in shales. J. Nat. Gas Sci. Eng. 73, 103045.

Knudsen, M., 1909. Die Gesetze der Molekularströmung und der inneren Reibungsströmung der Gase durch Röhren (The Laws of Molecular and Viscous Flow of Gases Through Tubes). Ann. Phys. 333 (1), 75–130.

Karniadakis, G., Beşkök, A., 2001. Microflows: Fundamentals and Simulation. Springer.

LeVeque, R.J., 2002. Finite Volume Methods for Hyperbolic Problems, vol. 31. Cambridge university press.

Li, D., Engler, T.W., 2001. Literature review on correlations of the non-Darcy coefficient. In: Paper Presented in SPE Permian Basin Oil and Gas Recovery Conference, USA.

Ling, K., He, J., Wu, X., Shen, Z., 2013. Determining Coefficient of Quadratic Term in Forchheimer Equation. International Petroleum Technology Conference, China.

Loucks, R.G., Reed, R.M., Ruppel, S.C., Jarvie, D.M., 2009. Morphology, genesis, and distribution of nanometer-scale pores in siliceous mudstones of the Mississippian Barnett Shale. J. Sediment. Res. 79 (12), 848–861.

Luo, W., Tang, C., 2015. A semianalytical solution of a vertical fractured well with varying conductivity under non-Darcy-flow condition. SPE J. 20 (5), 1–28.

Mainguy, M., Ulm, F.J., 2001. Coupled diffusion-dissolution around a fracture channel: the solute congestion phenomenon. Transport Porous Media 45 (3), 479–495.

Moridis, G.J., Blasingame, T.A., Freeman, C.M., 2010. Analysis of mechanisms of flow in fractured tight-gas and shale-gas reservoirs. In: Paper Presented at the SPE Latin American and Caribbean Petroleum Engineering Conference, Argentina.

Mustapha, H., Langavant, L., Giddins, M., 2015. Darcy and non-Darcy flows in fractured gas reservoirs. In: Paper Presented at SPE Reservoir Characterisation and Simulation Conference and Exhibition, UAE.

Pang, Y., Soliman, M.Y., Sheng, J., 2018. Investigating gas-adsorption, stress-dependence, and non-Darcy-flow effects on gas storage and transfer in nanopores by use of Simplified Local Density Model. SPE Reservoir Eval. Eng. 21 (1), 73–95.

Rangel-German, E.R., Kovscek, A.R., 2002. Experimental and analytical study of multidimensional imbibition in fractured porous media. J. Petrol. Sci. Eng. 36 (1–2), 45–60.
Roy, S., Raju, R., Chuang, H.F., Cruden, B., Meyyappan, M., 2003. Modeling gas flow through microchannels and nanopores. J. Appl. Phys. 93 (8), 4870–4879.
Tek, M.R., Coats, K.H., Katz, D.L., 1962. The effects of turbulence on flow of natural gas through porous reservoirs. J. Pet. Technol. Trans. AIME 222, 799–806.
Wang, J., Luo, H., Liu, H., Cao, F., Li, Z., Sepehrnoori, K., 2017. An integrative model to simulate gas transport and production coupled with gas adsorption, non-Darcy flow, surface diffusion, and stress dependence in organic-shale reservoirs. SPE J. 22 (1), 244–264.
Wang, H., Marongiu-Porcu, M., 2015. Impact of shale-gas apparent permeability on production: combined effects of non-Darcy flow/gas-slippage, desorption, and geomechanics. SPE Reservoir Eval. Eng. 18 (4), 495–507.
Yao, J., Sun, H., Fan, D.Y., Wang, C.C., Sun, Z.X., 2013. Numerical simulation of gas transport mechanisms in tight shale gas reservoirs. Petrol. Sci. 10 (4), 528–537.
Yu, W., Sepehrnoori, K., Patzek, T.W., 2016. Modeling gas adsorption in Marcellus shale with Langmuir and bet isotherms. SPE J. 21 (2), 589–600.
Zeng, F., Zhao, G., 2008. SemiAnalytical model for reservoirs with Forchheimer's non-Darcy flow. SPE Reservoir Eval. Eng. 11 (2), 280–291.
Zou, C.N., Zhu, R.K., Wu, S.T., Yang, Z., Tao, S.Z., Yuan, X.J., Bai, B., 2012. Types, characteristics, genesis and prospects of conventional and unconventional hydrocarbon accumulations: taking tight oil and tight gas in China as an instance. Acta Pet. Sin. 33 (2), 173–187.

Paper III

Berawala, D. S., & Andersen, P. Ø. (2020). Evaluation of Multicomponent Adsorption Kinetics for Carbon Dioxide Enhanced Gas Recovery from Tight Shales. *SPE Reservoir Evaluation & Engineering*, 23(03), 1060-1076. https://doi.org/10.2118/195536-PA

Paper IV

Journal of Natural Gas Science and Engineering 73 (2020) 103045

Contents lists available at ScienceDirect

Journal of Natural Gas Science and Engineering

journal homepage: http://www.elsevier.com/locate/jngse

Review of experimental sorption studies of CO_2 and CH_4 in shales

Isaac Klewiah [a,*], Dhruvit S. Berawala [b,c], Hans Christian Alexander Walker [a], Pål Ø. Andersen [a,b,c], Paul H. Nadeau [a]

[a] Department of Energy Resources, University of Stavanger, 4036, Norway
[b] Department of Energy and Petroleum Engineering, University of Stavanger, 4036, Norway
[c] The National IOR Centre of Norway, University of Stavanger, 4036, Norway

ARTICLE INFO

Keywords:
Gas sorption
Shale reservoirs
Enhanced gas recovery
Carbon storage and sequestration
Adsorption isotherms

ABSTRACT

In recent years CO_2 injection in shale has been investigated with aim to enhance shale gas recovery (ESGR) and permanently sequester CO_2. This paper reviews the state of research on CH_4 and CO_2 sorption in shale. We present the interaction of CO_2 and CH_4 with shale rocks and discuss the dependence of gas sorption on shale properties including organic matter content, kerogen type, mineralogy, moisture and temperature as well as shale selectivity for either species. Dynamic CO_2-CH_4 exchange studies are also summarized together with the geochemical and mechanical impact of gas sorption in shales. We note that most experimental work is still performed on crushed samples rather than whole cores. Also, CO_2 is preferentially adsorbed over CH_4 when both species co-exist in shale. Both gases are in supercritical state at typical reservoir conditions. Especially CO_2 adsorption is not well described by standard isotherm models in this state.

1. Introduction

Natural gas production from shales has become exceedingly important in satisfying the ever-growing global energy demands. This unconventional hydrocarbon system is globally abundant, with large technically recoverable resources reported in China (1115 tcf), Argentina (802 tcf), US (665 tcf) and Canada (573 tcf) (EIA, 2013). Commercial exploitation of shale resources has led to a shale energy revolution in the last decade. Successful implementation of large-scale horizontal drilling and hydraulic fracturing techniques (Wang and Krupnick, 2015) made this possible and is attributed to collaborative efforts by the natural gas industry (notably Mitchell Energy) and the U.S. Department of Energy (DOE) from the 1980s.

A typical gas shale system is a blend of organic-rich deposition and complex mineralogy that forms a fine-grained clastic sedimentary rock with a unique geological framework where the shale independently exists as source, trap and reservoir. Common types are black shale (rich in organic matter), carbonaceous shale (rich in organic matter that has been carbonized), siliceous shale (high amount of quartz), iron shale (having some fractions of iron oxides, hydroxides, etc.) and oil shale (containing a certain amount of bitumen/asphalt) (Curtis, 2002; Wang et al., 2012). Shale rocks have grains with sizes often less than 62.5 μm with pore body and throat sizes ranging from micropores (<0.1 μm) to nanopores (nm) (Sondergeld et al., 2010; Chen et al., 2019). The pores in shale are associated with both organic and mineral matter (Tang et al., 2016). Loucks et al. (2012) presented a descriptive classification of shale matrix-related pore types, differentiating between interparticle (located between particles and crystals) and intraparticle (existing within particles) pores affiliated with the mineral matrix and intraparticle organic matter pores. The hydrocarbons are generated in-situ through biogenic and thermogenic processes (Krooss et al., 1995) and are stored in three different states; as free compressed gas in the open pores and microcracks; as adsorbed gas on the nanopore/micropore inner surfaces of shale organic and inorganic components; or as solution gas absorbed within the solid organic matter and connate water (Bustin et al., 2008). Natural gas in shale is predominantly methane (>94%) with minor fractions of ethane, propane and butane plus traces of CO_2 and N_2 (Kalkreuth et al., 2013).

Low intrinsic matrix permeability (e.g. 0.1 μD for Huron shales (Soeder, 1988)) coupled with structural heterogeneity and complex pore networks complicates fluid transport and storage within the formation and poses tremendous challenges to technical evaluation and effective development. Although current technological advancements in horizontal drilling and fluid fracturing have contributed to primary production, only 5–10% of the original gas in place (OGIP) is estimated to be recovered economically (Rassenfoss, 2017) leaving a high potential

* Corresponding author.
E-mail addresses: isaacklewiah@gmail.com, isaacklewiah@yahoo.com (I. Klewiah).

https://doi.org/10.1016/j.jngse.2019.103045
Received 3 June 2019; Received in revised form 26 October 2019; Accepted 26 October 2019
Available online 31 October 2019

for enhanced recovery methods. The gas stored by sorption in the shale matrix is estimated to account for 20–80% of the total gas fraction (Lane et al., 1989; Bruner and Smosna, 2011; Edwards et al., 2015). Desorption is triggered by pressure reduction and/or presence of a favourably adsorbing gas.

Experimental results have shown that shales have greater adsorption affinity for CO_2 than CH_4 (Weniger et al., 2010; Heller and Zoback, 2014). CO_2 is also favourably adsorbed over CH_4 when both gas species co-exist within the shale (Pino et al., 2014; Cancino et al., 2017; Ma et al., 2018). A huge potential for enhanced shale gas recovery (ESGR) is therefore feasible through injection of CO_2 (Blok et al., 1997; Oldenburg et al., 2001) which can stimulate the desorption of pre-adsorbed methane through an in-situ molecular swapping mechanism at the sorption sites, releasing the otherwise trapped methane into the porous system to increase the rate and volume of CH_4 recovered (Regan, 2007). This technique is referred to as CO_2 enhanced shale gas recovery, CO_2-ESGR and is considered a viable means for simultaneous CO_2 storage in the shale formations with recent reviews provided by Liu et al. (2019) and Rani et al. (2019). This concept of CO_2 utilization in shales is illustrated in Fig. 1. Godec et al. (2013) demonstrated through simulation that at optimal operational conditions, 7% incremental CH_4 production could be obtained through CO_2 injection in the Marcellus Shale in Eastern United States. They estimated 12 trillion cubic meters of methane to be technically recoverable with an associated storage of 55 billion tonnes of CO_2. Khosrokhavar (2015) demonstrated that for an approximate storage of 12 kg of CO_2 in a characteristic gas shale system, 1 kg of CH_4 can be produced and yield 55 MJ energy while spending 12 MJ energy for compression. They noted that the energy gain was still substantial when accounting for CO_2 capture and storage (CCS) as quantified by Iijima et al. (2011). Logistically, in most cases, a surface gas pipeline distribution network could easily be modified to transport CO_2 to the wellhead whereas the cost of CO_2 injection into the subsurface formation is drastically minimized by repurposing the available well infrastructure to accommodate CO_2 injection (Tao et al., 2014).

2. Objectives and scope

The mechanisms in the CO_2-ESGR system are complex, many and coupled. Key parameters include storage capacity and form of CH_4 and CO_2, CO_2-CH_4 competitive sorption, isotherms and diffusion; chemical and geomechanical impact of gas sorption and desorption (shrinkage and swelling); CO_2 injectivity and trapping integrity. Many of these parameters are interrelated, further coupled to the intricate petrographic nature of shales, inherent structural heterogeneities and variation of pressure and temperature. To limit our scope, our objectives are:

- Evaluate the state of experimental findings regarding gas sorption in shales
- Determine gaps in experimental research that should be addressed

Detailed theories of adsorption phenomena, experimental tools and associated uncertainties are not specifically addressed. For such aspects we refer to Polanyi (1932); Steele (1974); Sing et al. (1985); Sircar (1985); Malbrunot et al. (1997); Neimark and Ravikovitch (1997); Cavenati et al. (2004); Ross and Bustin (2007b); Busch and Gensterblum (2011); Rudzinski and Everett (2012).

The paper is organized as follows:

- Mechanisms for gas sorption on shale and relevant isotherm models (3.1), definition of useful thermodynamical parameters (3.2) and adsorption behavior of individual gas species (3.3).
- Dependence of CO_2 and CH_4 sorption capacity on shale physico-chemical parameters such as organic matter (4.1), thermal maturity (4.2), kerogen type (4.3), inorganic content (4.4), moisture content (4.5) and temperature (4.6).
- CO_2 versus CH_4 comparative adsorption capacity on shale (5.0).
- Recent advances in experimental work related to dynamic CO_2-CH_4 exchange and transport in gas shales (5.1).
- Experimental work on geomechanical (5.2) and geochemical (5.3) impact of gas adsorption-desorption on shale.
- Brief discussion of presented findings
- Conclusions and recommendations

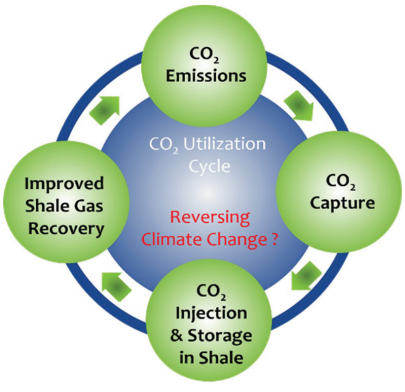

Fig. 1. Concept of CO_2 capture and utilization for enhanced shale gas recovery and carbon sequestration.

3. Gas sorption on shale

Gas sorption in shales is a comprehensive term for surface accumulation onto organic and mineral surfaces (adsorption), absorption (soaking or imbibition) into organic molecular (kerogen) openings and capillary condensation within the pores. Gas adsorption on shale matrix surfaces is governed by physisorption (Brunauer et al., 1940). This is a result of weak van der Waals and electrostatic interaction forces between the gas molecules (adsorbates) and the shale surface (the adsorbent). This is enhanced by the abundant nano-microscale pores (Nelson, 2009) that provide a large internal surface area and restrictions that force the fluid-solid phases closely enough for weak dipole-dipole interaction to occur and bind the gas species to the shale surfaces. Physisorption is deemed reversible, due to the absence of adsorbate-adsorbent covalent bonds.

Sorption of CO_2 or CH_4 onto shale matrix is frequently examined in the laboratory by construction of sorption isotherms, which involves measuring the uptake or release of either gas species on a shale sample at controlled temperature and pressure conditions. The measured sorption is a combination of adsorption, absorption or capillary condensation which individually are difficult to distinguish. Although these mechanisms are characteristically different, the net result is a storage of gas molecules in a denser phase relative to the bulk (free gas) phase in the open pores (Ross and Bustin, 2009). The experimental procedures to measure sorption vary but can be categorized into mass-based or volumetric-based. In the mass-based method the change in sample mass associated with adsorption at each fixed pressure and temperature condition is measured with a microbalance of high accuracy. The volumetric technique is based on Boyle's law, where the adsorption isotherms are constructed by computing the amount of adsorbed gas using the real gas equation, which accounts for the gas compressibility factor at each equilibrium pressure (Heller and Zoback, 2014). The former approach is limited to the use of very small sample sizes whereas the latter can satisfactorily accommodate different sample sizes.

The reviewed literature depicts tremendous challenge with performing experimental flow-through tests due to the characteristically

ultra-low permeability of shale rocks. Hence most experimental evaluations of gas sorption have been conducted with crushed samples as opposed to whole cores. Likely sources of experimental errors and uncertainties in these tests are discussed by Fraissard and Conner (1997); Busch and Gensterblum (2011). In general, high-pressure isotherm experiments determine sorption capacity, whereas structural properties (e.g. specific surface area, pore size distribution, nano-, micro- or mesopore volumes) are evaluated via low-pressure (<1 MPa) sorption tests.

3.1. Gas sorption isotherm models

The quantity obtained in laboratory measurements is excess sorption (also called Gibbs sorption) (Burwell, 1977). It is the amount sorbed in excess of the molecular gas volume that would be present in the sample if the sorbed-phase volume were filled with bulk gas (Heller and Zoback, 2014). The total or absolute amount sorbed is computed by mathematical modelling, before fitting the data to one of many available mathematical isotherm models (e.g. Henry, Langmuir, BET, DR, Pore-filling). It is suspected that adsorption occurs as a monolayer at low pressures and as multilayers at higher pressures. The Langmuir model, which assumes monolayer adsorption, is widely reported as the most suitable fit for gas adsorption on shales (Lu et al., 1995; Nuttal et al., 2005; Chalmers and Bustin, 2008; Ji et al., 2012; Yuan et al., 2014; Hong et al., 2016).

This isotherm is reasonably simple and can be fit to data with a two-parameter equation (Langmuir, 1916, 1918) given as:

$$V_p = \frac{V_L P}{P_L + P} \tag{1}$$

where V_p is the adsorbed volume at pressure P, V_L is the Langmuir volume (total adsorption volume at infinite pressure), and P_L is the Langmuir pressure (the pressure at which half the Langmuir volume is adsorbed). Some authors (e.g. Duan et al., 2016) have also found the BET model (which accounts for multilayer adsorption) as a satisfactory choice. Indeed, the acceptance of a single model for universal description of sorption in shales is still contended amongst researchers. A review by Tang et al. (2017) presents some widely used adsorption models with comparisons and distinctive applications. Besides revealing the adsorptive potential for a material, the magnitude and shape of the sorption isotherm suggests the relation between pore accessibility and pressure, information regarding adsorption/desorption, sorption capacity, rates, pore structure, as well as surface properties of the shale matrix. This is primarily because the physical sorption process is inextricably linked to the effects that the confined pore space exerts on the state and thermodynamic stability of the gas species held onto the nano-pores (Thommes, 2010).

3.2. Adsorption thermodynamics

Sorption isotherms are frequently employed as basis for applying thermodynamical principles to interpretation of adsorption phenomena. This often implies the computation of parameters such as adsorption energy, binding energy, activation energy or heat of adsorption. The latter has especially been applied in the evaluation of CH_4 and CO_2 adsorption on shales (Chikatamarla and Crosdale, 2001; Rexer et al., 2014; Xiong et al., 2017; Chen et al., 2019). The isosteric heat of adsorption indicates the strength of interaction between the adsorbent and adsorbate (in this case the shale surfaces and the gas species; greater values indicative of stronger adsorbate-adsorbent bonding). By classical definition, it reflects the energy evolved when one molecule of adsorbate is added to an adsorption system. It depends on the gas type, surface chemistry and pore structure. It is a strong function of adsorbate density and surface coverage. The heat of adsorption for CO_2 is reportedly greater than for CH_4 in gas shales; indicative of greater affinity of shale for CO_2 over methane (Luo et al., 2015; Duan et al., 2016). In adsorption, activation energy is the minimum energy needed (to overcome the adsorbate-adsorbent repulsion) for the gas molecules to react/interact with adsorption sites in the shale rock formation. Also, when adsorbate (gas) molecules interact with surfaces of an adsorbent (i.e. shale, in this case), the adsorption energy (E_{ads}) is defined as:

$$E_{ads} = E_{sys} - \left(E_{mol} + E_{surf}\right) \tag{2}$$

where E_{sys}, E_{mol} and E_{surf} represents the energy of the total adsorbate-adsorbent system, the gas phase molecules and the shale surface respectively. E_{ads} also equals sum of the binding energy (E_b, characterizing the interaction between a single isolated gas molecule with the shale surface) and adsorbate stabilization energy ($E_{inter\text{-}ad}$) which accounts for intermolecular interactions between the gas molecules (Bocquet et al., 2005)

$$E_{ads} = E_b + E_{inter-ad} \tag{3}$$

CO_2, CH_4 adsorption is an exothermic process, making E_{ads} a negative variable. On the other hand, a negative (or positive) binding energy implies that the adsorption is favorable (or unfavorable) (Scaranto et al., 2011). The nature of these parameters, interrelationship and theoretical variance has been discussed by Saha and Chowdhury (2011) and Inglezakis and Zorpas (2012).

3.3. Single component sorption of CO_2 or CH_4 at reservoir conditions

The majority of shale formations have temperatures ranging from 96 to 122 °C, with pore pressures in the range of 15–25 MPa (Lu et al., 2016). The subsurface sorption phenomenon will most likely proceed as a supercritical adsorption-desorption process (Menon, 1968) since both CH_4 and CO_2 will typically exist in the supercritical state (CH_4: $T_{cr} = -82$ °C and $P_{cr} = 4.64$ MPa; CO_2: $T_{cr} = 31$ °C and $P_{cr} = 7.38$ MPa). A peculiar feature in adsorption isotherms of supercritical fluids is the possible occurrence of a peak in adsorption with pressure (Aranovich and Donohue, 1995, 1996). Its occurrence will depend on the gas type, the proximity of pressure and temperature conditions to the supercritical ('sc') state of the gas, the void volume determination technique, and the sample properties (e.g, pore size distribution) (Murata et al., 2001; Gumma and Talu, 2003; Herrera et al., 2011; Gasparik et al., 2012). Laboratory experiments thus should be performed at relevant subsurface pressure and temperature conditions, but often the experimental literature is restricted to lower pressures due to available equipment and experimental constraints.

In that context, CH_4-CO_2-shale adsorption processes are conveniently divided into three stages owing to the pressure range and adsorption rate: low pressure (<3 MPa; below supercritical conditions), intermediate pressure (3–10 MPa; transition into supercritical conditions) and high-pressure (>10 MPa; supercritical state) adsorption stages that vary depending on the gas species and sample properties. The low-pressure stage is characterized by sorption on the sites with highest adsorption energy (i.e. the smallest pores) first, and progression towards larger pores (as pressure increases) which causes gradual reduction in the isosteric heat of adsorption (Stoeckli, 1990). This is indicative of physisorption by pore-filling as originally suggested by Dubinin (1975) for gas sorption in microporous materials. Further increase in pressure will eventually cause only small changes in the adsorption content. The isosteric heat of adsorption reduces with pressure until equilibrium is established, and no more gas can adsorb.

In the reviewed literature, CH_4 excess adsorption on gas shales is reported to increase monotonously with pressure (in both gaseous and supercritical states) and gradually reach a constant value at high pressures (Bi et al., 2016; Wang et al., 2016; Li et al., 2017). Gas-phase CO_2 adsorption also increases monotonously with pressure to the supercritical transition point, however adsorption of CO_2 in supercritical state causes the adsorption profile to reach a maximum, after which further increase in pressure will cause CO_2 to desorb monotonically. Typical

sorption behavior for both CH_4 and CO_2 is depicted in Fig. 2 for sorption experiments on crushed Devonian shale samples at a fixed temperature of 45 °C and pressures ranging up to 25 MPa. The characteristic difference in the adsorption of either gas is clearly revealed, with maxima observed only for CO_2. The same trend in experimental profiles of CO_2-CH_4 sorption is reported by Strubinger et al. (1991); Sudibandriyo et al. (2003); Busch et al. (2008); Weniger et al. (2010); Schaef et al. (2013); Gasparik et al. (2014); Schaef et al. (2014); Lu et al. (2016); Merey and Sinayuc (2016) on either gas shale samples of original composition or pure inorganic minerals.

In shales, the gradual increase in CO_2 adsorption near supercritical conditions has been attributed to the sharp change (i.e. increase) in fluid density when gaseous CO_2 is converted to supercritical fluid. This favors overall CO_2-shale interaction by increased (binding) energy and more molecular layers are attached onto the surfaces. For CO_2, Schaef et al. (2013) observed that with continued adsorption, the cross-over point (Fig. 2b) is reached because the stabilization energy ($E_{inter\text{-}ad}$) of the supercritical CO_2 molecules increases as the pressurized system brings the gas molecules closely together. Meanwhile, the adsorbate-adsorbent adsorption energy (E_{ads}) decreases (becomes less negative). This could drive the adsorbent-adsorbent binding energy (E_b) to negative ranges (see equation (3)) and thereafter desorption dominates as the principal mechanism and a decline is observed in the isotherm curve. Recently, Jia et al. (2018) reported a similar trend of CO_2 adsorption behavior, where a crossover region was observed before and after the critical pressure point, through sorption measurements from low-to high-pressure conditions (temperature was kept constant at 30 °C) in a shale core from the Green River Formation in Colorado. The discontinuity of CO_2 adsorption at pressures above CO_2-P_{cr} may have crucial implications on CO_2-ESGR and CO_2 storage. It must be noted that the occurrence of an adsorption peak has also been reported in some cases for CH_4, although mostly for dried overmatured gas shales (Moffat and Weale, 1955; Gasparik et al., 2012; Merkel et al., 2015; Zhou et al., 2018) and pure carbon adsorbents (Xiong et al., 2017). Most single- and multi-component adsorption isotherms are monotonous; showing no distinct peaks even at relatively high pressures (e.g. the Langmuir type). Capturing physical behavior at reservoir conditions may require more general isotherm approaches, especially when significant peaks and declines are demonstrated in lab measurements.

4. Dependence of gas sorption on shale properties

Most sorption studies are available on gas shale samples of original composition or pure individual shale components. The literature indicates that shale adsorption capacity correlates directly to factors that can generate more micropores, but inversely to factors that reduce or plug micropores. This is because small pores generate larger surface area and stronger adsorbate-adsorbent interaction energy which results in greater adsorption. Sorption experiments on samples from across the world (see Fig. 3) have been reviewed in this section to gain insight into the relationship between sorption, rock compositional and geological features to outline the major factors that controls gas sorption capacity of shales.

4.1. Influence of organic matter (richness) on gas sorption

The shale organic matter (OM), also known as kerogen, is associated with the in-situ generation of hydrocarbons. The organic richness is frequently expressed by the Total Organic Carbon (TOC). It is primarily responsible for the microporous nature of shale and is the main contributor to the surface area and total pore volume (Cao et al., 2015; Zhou et al., 2018). The TOC wt% of the shale varies substantially among shale reservoirs and within a formation itself. Table 1 shows the TOC content reported for some shale gas plays. Although these values may not exactly be large, the microporosity associated with the organic fraction is the principal control on CH_4 and CO_2 sorption; there the trapping forces are enhanced due to coalescing of molecules and overlap of interaction energies between the sorbed gas molecules (Thommes, 2010). In stark contrast, immature gas shales with appreciable matrix bituminite can store gas by dissolution and may demonstrate large sorbed gas capacities that are unrelated to micropore volume (Ross and Bustin, 2009). Bituminite, originally described by Teichmüller (1971), could be considered as a semi-solid portion of degrading organic matter that lacks definite shape or form (Kus et al., 2017). It is often present in immature source rocks and may have a dominantly fluidal or granular internal structure within which gases could be stored by dissolution.

The reviewed literature confirms that CH_4 and CO_2 sorption capacities on shale is strongly correlated with TOC. A strong positive linearity is observed for CH_4 and CO_2 sorption datasets (Ross and Bustin, 2007a, 2008; 2009; Zhang et al., 2012; Wang et al., 2013; Heller and Zoback, 2014; Hong et al., 2016; Cancino et al., 2017; Zhou et al., 2018) sourced from experimental measurements on a wide range of shale samples (Fig. 4). The regression factors for both CH_4 and CO_2 are relatively high under both dry and moist conditions and demonstrate the shale TOC to have primary control on adsorption of either gas species. It is interesting to note that the regression constants for both species is higher for moisture-equilibrated samples relative to dry samples. This implies a much stronger correlation of gas adsorption to TOC in the presence of water and could infer that water adsorbs primarily to water-wet inorganic (i.e. clay) mineral phases within the shale formation.

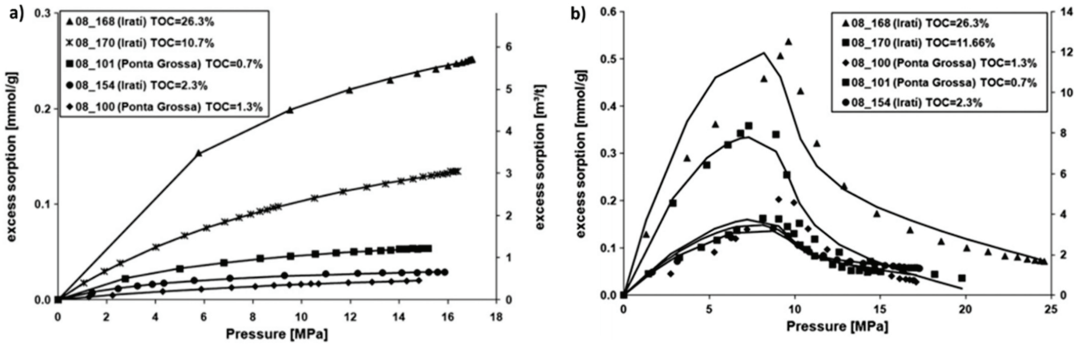

Fig. 2. Comparison of adsorption isotherm (excess sorption vs pressure) for CH_4 (a) and CO_2 (b) on gas shale samples of the Paraná Basin in Brazil (Weniger et al., 2010). Experiment was conducted on crushed dry samples at a fixed temperature of 45 °C.

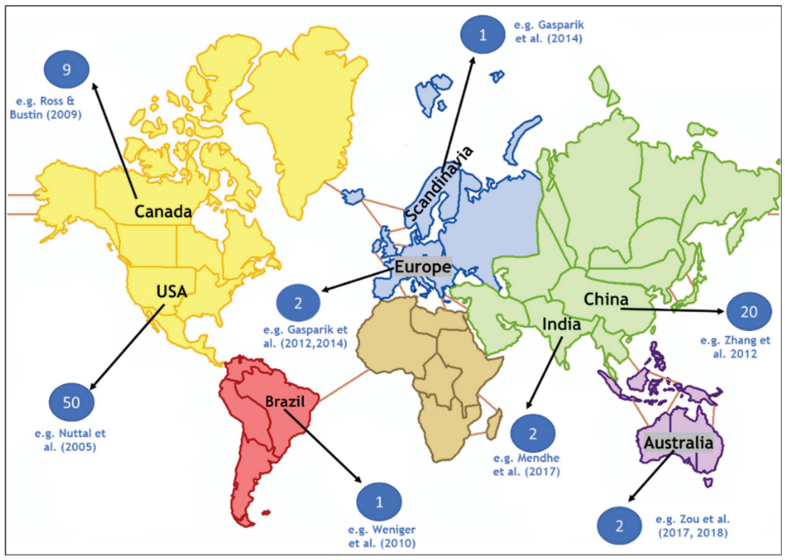

Fig. 3. Worldwide illustration of shale formations actively investigated by researchers. The numbers are purely based on the literature reviewed in this study with focus particularly on CH_4 and CO_2, sorption tests and auxiliary evaluations relevant to CO_2-ESGR.

Table 1
Typical TOC of some shale plays and formations (fm.) adapted from Chalmers and Bustin (2007); Ross and Bustin (2007a, 2008); Ambrose et al. (2010); Zhang et al. (2012); Wang et al. (2013).

Region	Shale/Play	TOC (wt %)
North – American Shale systems, U.S	Barnett	2.5–7.9
	Marcellus	1–10
	Haynesville	0–8
	Horn River	3
	Woodford	5
Northeastern British Columbia region, Canada	Lower Jurassic fm.	0.8–11.8
	Lower cretaceous fm.	0.53–17
	Poker Chip fm.	0.8–2.2
Western Canada Basin	Besa River fm.	0.9–5.7
	Horn River fm.	2.5–3.5
	Muskwa fm.	0.4–3.6
	Fort Simpson fm.	<1
	Mattson	<1.2
Sichuan Basin, China	Qiong-zhu-si fm.	0.5–4
	Long-ma-xi fm.	0.5–2.3
	Da-long and Long-tan fm.	1.0–10

It is noted that extrapolating the regression lines to TOC concentrations of zero reveals the influence of other non-organic adsorption sites, hence significant deviations from this trend could be observed for individual samples depending on the compositional makeup. High-pressure gas sorption isotherms reported by Tan et al. (2014) showed sorption capacities of samples with similar clay content, thermal maturity and moisture content to exhibit even stronger positive linear correlations with TOC. The dependence of gas adsorption on TOC content has been reported by many other researchers (Manger et al., 1991; Schettler and Parmely, 1991; Lancaster and Hill, 1993; Lu et al., 1995; Zuber et al., 2002; Chalmers & Bustin, 2007, 2008; Ross and Bustin, 2007a; Ruppel and Loucks, 2008; Beaton et al., 2010; Strapoc et al., 2010; Weniger et al., 2010; Chareonsuppanimit et al., 2012; Wei et al., 2012; Gasparik et al., 2014; Rexer et al., 2014; Bi et al., 2016; Wang et al., 2016; Yang et al., 2016; Chang et al., 2017; Mendhe et al., 2017; Xia et al., 2017; Sharma and Galvis-Portilla, 2018). There are however existing studies that have reported little to no correlation between TOC and adsorption capacity (Gasparik et al., 2012; Zou et al., 2017). This trend is particularly notable in shales with low organic matter content and high clay content.

4.2. Influence of thermal maturity

Thermal maturity describes the heat-driven diagenetic changes of organic matter in sedimentary source rocks to generate hydrocarbons. Vitrinite reflectance, V_r, is widely used as indication of thermal maturity in shale analysis. It is measured by optical microscopy and reported by % R_o (where high $\%R_o$ indicates high maturity), the percentage of incident light reflected from the surface of vitrinite particles in the shale rock. In shales, thermal maturity of organic matter can generate additional micropores (Bae and Bhatia, 2006; Jarvie et al., 2007; Chalmers and Bustin, 2008; Loucks et al., 2009; Ambrose et al., 2010; Sondergeld et al., 2010; Curtis et al., 2011; Bernard et al., 2012; Ma et al., 2015; Wu et al., 2017; Delle Piane et al., 2018; Zheng et al., 2018). This is due to the structural transformation of organic matter during maturation that generates smaller (nano-micro scale) pores as kerogen is thermally converted. The generation of more micropores with organic matter maturity increases the adsorption capacity.

It was previously suggested (Ramos, 2004) that the strong correlation between sorption and TOC masks the relationship between adsorption capacity and thermal maturation. However, Ross and Bustin (2009) found the sorption capacities of low TOC (0.2–4.9 wt%) overmature D-M shale samples ($1.6\% < R_o < 2.5\%$) to be higher than for high TOC (1.4–11.8) immature Jurassic shales ($R_o < 1.2\%$). This was qualitatively attributed to creation of sorption sites, and/or opening up microporosity onto which gas could sorb from structural transformations of the organic matter during thermal maturation. Nonetheless, other researchers have found concomitant decrease in CH_4 sorption capacity with increasing maturity (Chalmers and Bustin, 2007, 2008). This suggests, as previously pointed out by Schieber (2010) that

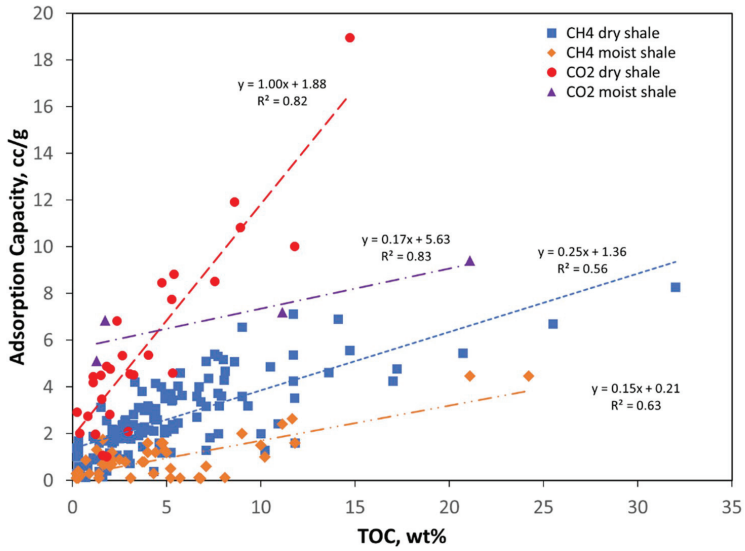

Fig. 4. Correlation between TOC and CH_4, CO_2 sorption capacity of dry and moisture equilibrated shales. Data points are representative of langmuir volume reported in the evaluations of (Nuttal et al., 2005; Ross and Bustin, 2009; Weniger et al., 2010; Zhang et al., 2012; Wang et al., 2013; Gasparik et al., 2014; Heller and Zoback, 2014; Luo et al., 2015; Hong et al., 2016; Cancino et al., 2017; Pozo et al., 2017; Zhou et al., 2018). The regression constants of both species are relatively high and extrapolation to zero TOC content shows impact of auxillary sorption sites.

intraparticle OM pore generation in thermally matured rocks may depend on the OM type. Loucks et al. (2012) also reported absence of OM pores in a matured (R_o of 0.89%) shale sample from the Atoka formation in the Midland Basin. The relationships established for any specific shale system, therefore, may not be directly applied elsewhere. But in general, the reviewed literature indicates that overmature and high TOC samples will show higher sorption capacity for both CH4 and CO_2 than the low mature and low TOC shales.

Some literature also reports thermal maturity to have noticeable effect on the shape of excess isotherms. Zhang et al. (2012) reported the methane Langmuir pressure, P_L of three Barnett shale samples (% $R_o = 0.58, 0.81, 2.01$) to distinctly shift towards lower pressures from the immature to overmature gas shale samples under the same temperature conditions. Similar trends have been reported by Gasparik et al. (2014) and Tan et al. (2014). In a related study, Gasparik et al. (2012) also found positive correlation between TOC-normalized sorption capacities and maturity for black shales, but the trend became negative for over matured samples with R_o in a range of 2.8–3.3%.

4.3. Influence of kerogen type

Although TOC content has a superior control on gas sorption in shales, another key factor is kerogen type. Kerogen is the fraction of organic matter in sedimentary rocks (in this case, shale rocks) that is insoluble in organic solvents. It is formed from the decomposition of organic matter and is the precursor of hydrocarbon generation in source rocks. Kerogen is categorized as either Type I, which consists mainly of algal and amorphous kerogen and is highly likely to generate oil; Type II, which is formed from mixed terrestrial and marine source materials and can generate both oil and gas (but mostly waxy oil); and Type III, which is formed from terrestrial plant debris and typically generates gas upon maturation. In essence, the kerogen type depends on the source rock material and the deposition environment (Seewald, 2003; Boyer et al., 2006; Vandenbroucke and Largeau, 2007; Glorioso and Rattia, 2012).

Chalmers and Bustin (2008) investigated CH_4 sorption capacity for the Lower Cretaceous Buckinghorse Formation in Canada and found that per unit TOC volume basis, the capacity trend was Type II/III mixtures > Type III > Type II > Type I. They attributed this to Type III kerogen being more mature and generating more hydrocarbons and micropores at a given temperature compared to the other kerogen types. Zhang et al. (2012) conducted high pressure (0–16 MPa) methane sorption tests on organic-rich bulk shale samples and their isolated kerogens, with thermal maturity and kerogen type being the main variation in the samples. At all temperature conditions (35, 50, 65 °C), the CH_4 sorption capacity was in the order of Type III > Type II > Type I (Fig. 5). The trend was attributed to extensive aromatization from immature (Type I) to overmature (Type III) organic matter. They indicated that the progression from kerogen Type I to Type III, represents an increase in the relative fraction of aromatic hydrocarbons compared to the aliphatic and naphthenic hydrocarbons, as reported by other researchers (Tissot and Welte, 1984; Helgeson et al., 2009). The findings of Zhang et al. (2012) depict methane adsorption to be influenced by the chemical structure of the organic matter. The details and concept of the effects exerted by organic functional groups on gas adsorption, particularly CO_2 is not well addressed in the literature and deserves further investigation. We also note, as indicated by Loucks et al. (2012) that different kerogen types exhibit differing propensities to the development of intraparticle OM pores. The storage capacity trend reported for a shale Basin system based on kerogen types may therefore not be applicable to shales from different Basins. This complicates the generalization of the effects that kerogen type exerts on adsorption capacity. We recommend further studies on the association of OM pores and kerogen type to elucidate this phenomenon.

4.4. Influence of inorganic components

Shale usually contains clay, quartz or carbonate mineral phases with trace amounts of albite and pyrite. These inorganic constituents contribute enormously to the surface area and influence pore size, cumulative porosity and sorption properties. Particularly, the clay minerals are reported (Slatt and O'Brien, 2011; Milliken et al., 2013) to contribute to the shale micropore volume. In contrast to coals, where mineral matter seems to have little influence on CH_4 sorption capacity (e.g. Faiz et al., 1992; Rice et al., 1993; Bustin and Clarkson, 1998) but significantly affects CO_2 sorption (e.g. Karacan and Mitchell, 2003; Weniger et al., 2010), mineral components in gas shale systems have

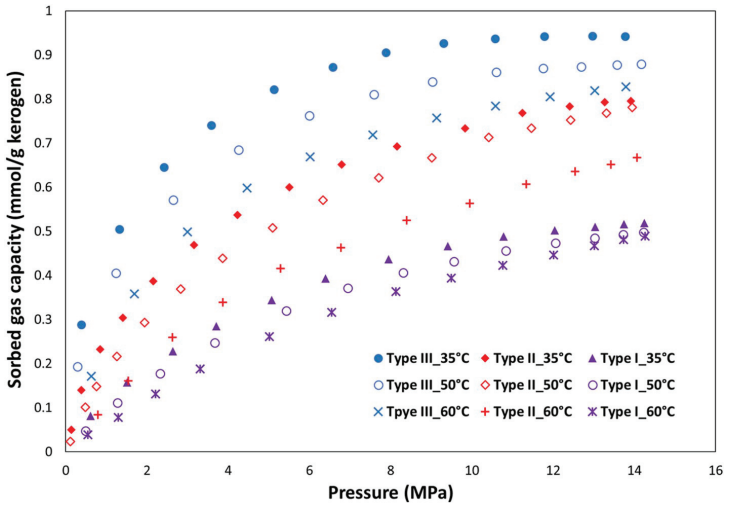

Fig. 5. Effect of kerogen type on methane sorption capacity at different temperatures (Zhang et al., 2012).

been proven to have appreciable sorption capacity for both gases (Aylmore, 1974; Heller and Zoback, 2014).

Preliminary adsorption studies on Devonian gas shale samples by Schettler and Parmely (1991); Lu et al. (1995) exclusively highlighted the inorganic clay minerals to contribute as sorption sites in shale systems due to their microporous nature. Schettler and Parmely (1990) originally postulated TOC to be of secondary importance in shale systems with low organic content. This conclusion was later reiterated by Busch et al. (2008) who attributed the high CO_2 sorption capacity of Muderong shales (TOC < 0.5%) entirely to its clay mineral constituents. The strong positive correlation of shale clay content to sorption capacity is emphasized in other reports (Chalmers and Bustin, 2008; Gasparik et al., 2012; Luo et al., 2015; Wang and Yu, 2016; Lutyński et al., 2017) where low TOC shale samples demonstrated high sorption due to their high clay contents. The specific influence of clay on shale sorption, however, is less evident in shales with high TOC content (Wang et al., 2013; Gasparik et al., 2014; Tan et al., 2014; Bi et al., 2016).

The microporous crystal layers of clay serve as ideal adsorption sites due to the large surface area (Aringhieri, 2004; Cheng and Huang, 2004; Venaruzzo et al., 2002). The contributions differ with clay type. Ross and Bustin (2009) reported clay-rich (low Si/Al ratio) shales to have superior gas storage capacities over their silica-rich (high Si/Al ratio) counterparts. Ji et al. (2012) conducted sorption experiments (up to 15 MPa) on dried clay-rich rocks at varying temperatures (35–65 °C) to shed light on the relative influence of clay type on methane adsorption. They established physisorption as the dominant mechanism for CH_4 adsorption on clay and noted sorption capacity to proceed in the order of montmorillonite > illite/smectite mixed layers > kaolinite > chlorite > illite. High-pressure CO_2 sorption experiments on pure clay minerals showed Ca-rich montmorillonite to have greater storage capacity than Na-rich montmorillonite (Busch et al., 2008). Gas shale reservoirs are dominated by illite (Jarvie et al., 2001; Gasparik et al., 2012), possibly due to the illitization of kaolinite and smectite which occurs at temperatures between 80 and 120 °C (Pytte and Reynolds, 1989). The temperatures of high organic content shale systems is in the range 96–277 °C (Lu et al., 2016). It is likely that at adequate conditions (especially in tropical zones) a blend of chemical and temperature gradient change could trigger a transition from illite to smectite (Eberl, 1984). This may occur particularly for uplifted shales exposed to weathering (e.g. shallow reservoir sections and outcrops). Since smectite has larger surface area (Šucha et al., 2001) and thus greater sorption, this could lead to potential overestimation of gas storage capacity during shale gas exploration. Additional study is recommended to understand the possibility of illite-smectite reversal transformation in clays found in shale formations.

It must be pointed out that clays are naturally hydrophilic and may present experimental challenges when correlating shale sorption capacity to clay content. For example, Chalmers and Bustin (2008) observed that the TOC-normalized CH_4 sorption capacity in dry samples from the Bucking horse formation in Canada positively correlated with clay content whereas no correlation existed for moisture equilibrated samples. Data obtained from as received or moisture equilibrated, and dried samples should therefore be evaluated carefully to accommodate this fundamental clay-water affiliation.

4.5. Influence of moisture

Moisture is reported to correlate positively with organic matter and clay content in shale formations (Chalmers and Bustin, 2007; Passey et al., 2010) which makes it a crucial subsurface component to be analyzed in sorption experimental procedures. Many authors have addressed the effect of moisture on gas adsorption by comparing the adsorption capacity of dry samples and moisture equilibrated samples (Lu et al., 1995; Ross & Bustin, 2007a, 2009; Busch et al., 2008; Gasparik et al., 2012, 2014; Aljamaan, 2013; Tan et al., 2014; Yuan et al., 2014; Yang et al., 2016; Zou et al., 2018) The result indicates that sorption capacity decreases with increasing moisture content until a certain equilibrium (critical) moisture content is attained for the sample. This equilibrium moisture content is representative of the maximum moisture saturation that can adsorb on the shale surfaces.

When present, water sorbs strongly on organic functional groups containing oxygen via hydrogen bonding (Dubinin, 1980) and has secondary tendencies to interact with pre-adsorbed water and charged surfaces of mineral matter (especially chemisorptive clay). Thus, besides attaching to primary (water-wet) sorption sites in the clay matrix, molecular water also competes with CO_2 and CH_4 for adsorption sites and causes a reduction in the gas sorption capacity. In shales, besides attaching onto surfaces, water molecules can condense in inorganic pores, occupying the smaller capillaries first before filling the larger pores as relative humidity increases (Zolfaghari et al., 2017a, 2017b).

The water molecules can also aggregate as clusters at high pressure (Aljamaan, 2013; Yang et al., 2016; Huang et al., 2018) to block gas-enterable pores and serves as an added negative effect on gas sorption capacity.

The equilibrium moisture content depends on the shale maturity, organic richness and organic type (Chalmers and Bustin, 2008). The value for selected European gas shale samples was estimated (Gasparik et al., 2014) to be at or below 75% relative humidity (RH). Merkel et al. (2015) reported similar values for the moisture saturation threshold (50–75% RH) of Bossier and Haynesville shales from the U.S. A recent report by Fan et al. (2018) indicated that the methane sorption capacity versus moisture content exhibited three distinct decreasing stages separated by two threshold moisture contents (Fig. 6). They performed CH_4 sorption experiments on gas shale samples from the Sichuan Basin in China at 35, 45 and 55 °C and pressures up to 10 MPa. They attributed the initial reduction (stage I) to competitive adsorption between water and methane until an extended stagnant period (stage II) where all possible hydrophilic sites are filled. They postulated that water condensation in the clay pores and some organic hydrophobic pores was responsible for the late convex-like decrease (stage III) in the adsorption capacity. The moisture effect is however reported to be masked in high TOC and over mature gas shales (Ross and Bustin, 2007a; Wang and Yu, 2016).

4.6. Influence of temperature

Thermodynamically, adsorption is an exothermic process and the effect of changing the equilibrium temperature is hinged to the Le Châtelier principle. Therefore, less adsorption is expected with increasing temperature. This relation was first reported for shales by Lu et al. (1995) who investigated sorption as a function of both pressure and temperature on Devonian shales and showed the sorption capacity to decrease with temperature. Recently, Merey and Sinayuc (2018) confirmed through adsorption measurements at 25, 50 and 75 °C that adsorption capacity increases for both CH_4 and CO_2 when temperature is decreased. This concurs with other experimental evaluations (Guo, 2013; Guo et al., 2013; Hao et al., 2013; Fan et al., 2014; Duan et al., 2016; Chang et al., 2017; Pozo et al., 2017; Zou et al., 2017; Liu et al., 2018).

Zhang et al. (2012) reported that the decrease in sorptive capacity with temperature occurred on both bulk gas shale samples (of original composition) and their isolated kerogens. Gasparik et al. (2014) constructed methane isotherms at experimental temperatures ranging up to 100 °C for immature ($V_r = 0.5$) and mature ($V_r = 0.9$) shale samples and up to 150 °C for over-mature ($V_r = 1.5$) samples and reported that besides reduction in sorptive capacity, this sorption capacity was reached at a higher pressure when the temperature was increased. This implies that for the same sample, adsorption capacity decreases with temperature and that less gas can adsorb at lower pressures. The interrelation of adsorbed gas amount with temperature and pressure is depicted in Fig. 7.

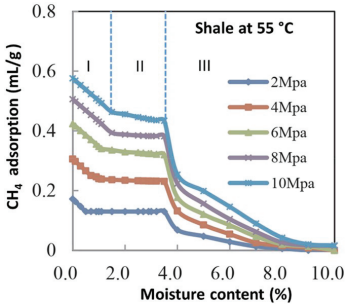

Fig. 6. Effects of moisture content on methane maximum sorption capacity at 55 °C (Fan et al., 2018).

5. CO_2 versus CH_4 sorption on shale

The first investigation of CO_2 and CH_4 sorption on the same shale material was conducted by Nuttal et al. (2005). They measured isothermal CH_4 and CO_2 adsorption on several Devonian black shales from Kentucky and found CO_2 absolute mass adsorption to be approximately 5 times greater than that of CH_4 at the same pressure. Following their report, several authors (Weniger et al., 2010; Kang et al., 2011; Chareonsuppanimit et al., 2012; Aljamaan, 2013; Heller and Zoback, 2014; Luo et al., 2015; Charoensuppanimit et al., 2016; Hong et al., 2016; Cancino et al., 2017; Pozo et al., 2017) have performed CO_2 and CH_4 gas sorption measurements on the same gas shale sample under controlled experimental conditions and reported consistently higher CO_2 sorption relative to CH_4. The reported CO_2/CH_4 absolute mass sorption ratio ranges between 1.3 and 10 for dry shale samples (Fig. 8). The ratio is expected to be relatively lower at moist conditions for the same shale sample since sorption capacity in general is lower for moist shales (see Fig. 4). There is limited data in the literature that compares the CO_2/CH_4 sorption ratio for the same sample at dry and moist conditions. Such an experimental study would be relevant to confirm this trend.

The relative sorption capacity of gas shale materials for either CO_2 or CH_4 is controlled by the respective interaction energy (thermodynamic forces), molecular size and accessibility of each gas type to the microporous network of the shale matrix system (steric forces). The tetrahedral molecular geometry of CH_4 is somewhat rounded, compared to CO_2 which has a linear molecular geometry. The dynamic diameter of CO_2 is about 0.33 nm as compared to 0.38 for CH_4 (Duan et al., 2016). The effective size of CO_2 is therefore smaller and can access narrower pores in the shale matrix and contacts a greater volume of the shale system (Kang et al., 2011). The reviewed experimental results depict that the steric and thermodynamic controlling parameters favor adsorption of CO_2 over CH_4 in gas shales. The mechanism of CO_2 accessibility is reportedly enhanced at supercritical conditions where gaseous CO_2 transitions to supercritical CO_2 (Sc-CO_2). Sc-CO_2 is completely wetting to the shale rock, with liquid-like density, but with viscosity and diffusive properties close to gas behavior (Wang et al., 2012). This unique physicochemical feature can improve the volumetric sweep during CO_2 injection and potentially increase the CO_2 subsurface storage amount by allowing Sc-CO_2 to contact more available sorption sites deeper within the formation.

Binary CO_2-CH_4 and mixed-gas sorption experiments evaluating the selectivity of gas shales for either gas species under the same pressure and temperature conditions have also been recently reported on the same shale sample in the literature. In these tests, a gas detection device (e.g. gas chromatograph) supplements the conventional sorption experimental setup that allows the determination of the gas mole fraction of each species in the mixture. During the tests, the shale samples are initially saturated with varied molar ratios of CO_2 and CH_4 at the desired experimental conditions. The majority of these authors (Pusch et al., 2012; Luo et al., 2015; Duan et al., 2016; Cancino et al., 2017; Huang et al., 2018; Ma et al., 2018) observed preferential adsorption of CO_2 over CH_4. It is reported that the selectivity of CO_2 in a gas mixture experiment evolves with pressure and is significantly higher at low pressures (Cancino et al., 2017) most likely due to the dominance of micropore filling associated with low temperatures. The adsorption selectivity parameter (represented as α) is frequently used to evaluate the competitive adsorption between CO_2 and CH_4 and given as (Duan et al., 2016):

$$\propto_{CO_2/CH_4} = \frac{x_{CO_2}\, y_{CH_4}}{x_{CH_4} y_{CO_2}} = \frac{V_{LCO_2}/P_{LCO_2}}{V_{LCH_4}/P_{LCH_4}} \quad (4)$$

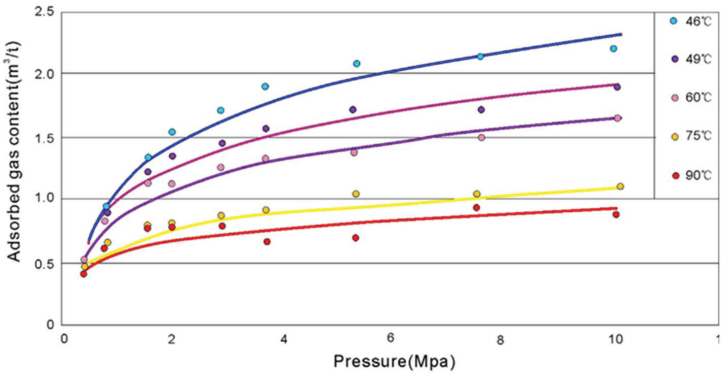

Fig. 7. Variation of adsorbed CH_4 amount with temperature performed on gas shale samples of the Ordos Basin in China (Guo, 2013).

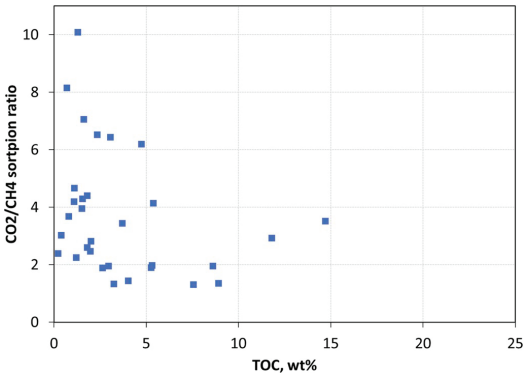

Fig. 8. CO_2/CH_4 sorption ratio for different dry shale samples as a function of total organic carbon content. Data sets are taken from Langmuir volumes reported in the evaluations of Nuttal et al. (2005); Heller and Zoback (2014); Luo et al. (2015); Hong et al. (2016); Cancino et al. (2017); Pozo et al. (2017).

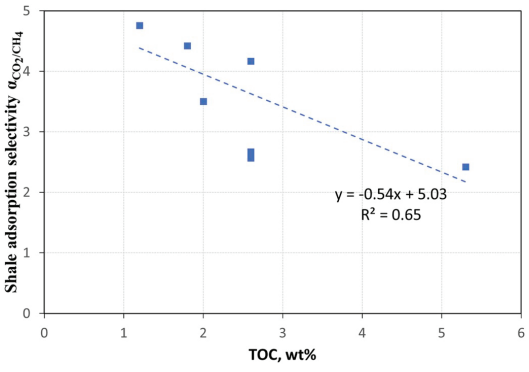

Fig. 9. Variation of shale adsorption selectivity $\propto_{CO_2/CH_4}$ different dry shale samples from China and the U.S. as a function of total organic carbon content (Heller and Zoback, 2014; Pei et al., 2015; Duan et al., 2016; Cancino et al., 2017).

where x and y variables are the molar fractions of the gas species in the adsorbed phase and free gas phase respectively for gas mixture evaluations and V_L, P_L are the Langmuir parameters. A value of $\propto_{CO_2/CH_4} > 1$ suggests that adsorbed CH_4 can be displaced by CO_2. Larger values represent stronger displacement capacity of CO_2 over CH_4. The CO_2 selectivity over CH_4 depends on shale matrix composition and pore structure. For iso-TOC samples, high clay content and micropores favours higher $\propto_{CO_2/CH_4}$ (Duan et al., 2016). The variation of $\propto_{CO_2/CH_4}$ for some selected shales in China and the U.S are shown in Fig. 9 where the selectivity is seen to decrease with increasing TOC.

In coals, preferential adsorption of CH_4 over CO_2 in mixed-gas sorption experiments has been reported, particularly at low pressures (Crosdale, 1999; Busch et al., 2003, 2006; Majewska et al., 2009). In shale samples, however, consistent CO_2 preferential adsorption in the entire pressure range has been experimentally proven and verified by simulation studies (e.g Merey and Sinayuc, 2016). These experiments are however limited, and further studies of multi-component sorption in gas shales is recommended to validate the trend.

6. Current practice of dynamic CO_2-CH_4 exchange

In gas shales, the experimental approaches to evaluate CO_2-CH_4 exchange and gas recovery have been conducted implicitly by measuring how effectively CO_2 can replace already adsorbed CH4 in a closed system. The procedures differentiate between the CO_2 and CH_4 molecules existing as adsorbed or free phase throughout the dynamic CO_2-CH_4 exchange within the shale sample at specific time steps. During these tests, usually shale material (which is often crushed) is initially saturated with CH_4 at desired experimental conditions and allowed to equilibrate before CO_2 is injected at specified criteria. The CH_4 recovery yield is quantified by the resulting amount of originally adsorbed CH_4 released from the adsorbed state.

Some authors have employed the usual Gibbsian surface excess (GSE) variable for computations through the application of conventional sorption techniques (see Section 3), whereas others have used fluid detection techniques, like Nuclear Magnetic Resonance (NMR), for evaluation. NMR characterizes the existing states of hydrogen (^{1}H) proton-containing fluids existing within a porous media (Coates et al., 1999). NMR-based techniques have been used successfully for petrophysical characterization of nano-porous structures in coal and gas shale (Mullen, 2010; Jin et al., 2017; Yin et al., 2017b; Zhou et al., 2018), monitoring flow and dispersion in porous media (Manz et al., 1999), evaluating CO_2 and CH_4 self-diffusion (Pusch et al., 2012) and CO_2 sorption on rock surfaces (Bernin and Hedin, 2018). A summary of the various findings from CO_2-CH_4 exchange tests are presented in Table 2.

7. Discussion and key research issues

A vast amount of investigations have been carried out to study the effectiveness and feasibility of CO_2- ESGR. However, some key research issues should be looked into:

- The majority of experimental work reported in the literature is conducted on crushed samples. To our knowledge, only Nuttal et al. (2003) reported adsorption data acquisition using an intact core. Their report highlighted the experimental difficulty involved since they only managed to capture CO_2 adsorption isotherm data for a single whole core out of twenty-six Devonian black shale samples. Using crushed samples is a quick and convenient means to perform measurements on shales, but an obvious trade-off is uncertainty in whether the data would be representative of actual reservoir conditions since it alters the structure of the porous medium (e.g. micro-fractures) and could lead to misrepresentative estimates of formation characteristics.
- The impact on gas sorption (i.e. isotherm shape) from organic matter content (TOC) and maturity, temperature and pressure and clay and moisture content are all relations that deserve attention. Particularly, lowered P_L values (associated with decreasing temperature or higher maturity) indicate that CH_4 will desorb more readily at lower pressures on higher maturity shales. Such affinity to remain sorbed in matured shales indicates that a greater reduction in CH_4 partial pressure will be required to desorb CH_4 during production. The selectivity of the surface towards CO_2 can be the solution to release the strongly sorbed CH_4 and is in such cases even more important to measure. The question of how significant adsorbed gas will be to overall production is a key concept and further investigation is required to properly correlate the P_L reduction to these parameters. Furthermore, measuring the density of the adsorbed gas phases is a key parameter in the commonly used modelling approaches that has not received much attention in experimental assessments.
- A notable concern for CO_2-ESGR is the impact of moisture which preferentially binds to hydrophilic clay surfaces and reduces sorption (and hence CO_2 sequestration) potential. Dried samples may overestimate the adsorption capacity. Although water in principle like CO_2 can substitute CH_4 by adsorbing to hydrophilic surfaces and give EGR, water will usually exist also in aqueous phase and cause mobility issues related to presence of multiple phases and water blocking effects near the wellbore or macro-fractures. Pressurized fracking fluids are essential for creating flow paths in the reservoir. The standard is use of water, but there is potential in using water-free fracking methods (e.g. propane-gel, supercritical CO_2). Gas soluble fracking fluids should be positive for recovery as well as the environment (reduction of produced water).
- Reports (Heller and Zoback, 2014; Lu et al., 2016; Yin et al., 2016) indicate crushed shale to swell (especially for high clay-content shales) during gas adsorption which changes both the pore structure and roughness. The degree of adsorption-induced swelling is shown to vary depending on the shale composition and pore characteristics and achieves a stable state when adsorption equilibrium is attained. The extent to which swelling during CO_2 injection impacts sorption isotherms, rock mechanical and hydrological (permeability, porosity) properties is crucial. In particular, Guo et al. (2017) observed through series of experiments that adsorption effects had substantial impact on shale permeability both at low and high pressures.
- Mechanical weakening of organic-rich gas shales by CO_2 saturation has been reported, especially for supercritical CO_2 (Lyu et al., 2016a, 2016b, 2018a, 2018b; Yin et al., 2017a) This is attributed to the modification of in-situ acid-base equilibria that triggers precipitation and dissolution of minerals (Liu et al., 2012; Carroll et al., 2013) and the ability of supercritical CO_2 to act as an organic solvent to extract non-polar aliphatic and polycyclic aromatic hydrocarbons from shale (Jiang et al., 2016; Yin et al., 2016). This could expand originally present gas seepage channels or generate flow channels with influence on the safety of sequestered CO_2. Most of the experimental results are reported for gas saturated shale samples monitored over a couple of days.
- Geochemical alterations of Australian Muderong shales were suggested to explain differences in specific surface areas before and after CO_2 sorption experiments conducted at reservoir conditions ($T = 45–50\,^{\circ}C$; $P < 20$ MPa) (Busch et al., 2008). The inferred geochemical changes however could not be quantified and seemed to occur only at high pressures. In a subsequent study, Busch et al. (2009) assessed the interrelation of CO_2-mediated reactions and transport properties in the Muderong shale by exposing crushed samples to CO_2 in the presence of water at 15 MPa and 50 °C for different equilibration time periods. They reported significant changes (equilibration times < 1 month) in mineralogical composition, particularly with the increase of smectite and K-feldspar contents and reduction in illite content. Mineral changes in shale sample

Table 2
Experimental studies of CO_2-CH_4 dynamic exchange conducted on shales.

Author (s)	Location	Procedure	Operating Conditions	Findings	Cons
Huo et al. (2017)	Longmaxi shales, China	Volumetric-based method applied to dried crushed samples	Fixed temperature of 45 °C. Constant initial equilibrium pressure of CH4 of 4.5 MPa CO_2 injection at varied pressures of 5.2, 6.3, 7.3, 8.4, and 9.3 MPa. Final system equilibrium pressures ranged were 4.7, 5.6, 6.5, 7.5 and 8.4 MPa respectively	The amounts of recovered CH_4 and stored CO_2 increase with CO_2 injection pressure. CH_4 recovery yield was higher for shales with smaller micropores (i.e. having lower CH_4 adsorption performance)	Inherent uncertainties of evaluating excess sorption measurements. Final system equilibrium pressure not allowed to reach injection value. It is unclear what determined when to stop the test for each injection pressure step
Liu et al. (2017)	Longmaxi shales, China	Nuclear Magnetic Resonance (NMR) based method on dried crushed samples	Fixed temperature of 35 °C. Varied initial equilibrium pressure of CH_4-saturated sample of 0.1 MPa and 1.5 MPa CO_2 injected at constant pressure of 4.5 MPa	CO_2 injection improved recovery yield of CH_4 in the adsorbed phase by an additional ~25%.	Rather simplified laboratory conditions devoid of relevant in situ reservoir complexities (e.g High temperature, high pressure, presence of water). Uncertainties in NMR detection capabilities, particularly in the presence of e.g. moisture, pyrite
Zhao and Wang (2018)	Longmaxi shales, China	NMR-based technology on dried crushed samples	Fixed temperature of 25 °C. Initial equilibrium pressures of the CH_4-saturated sample was ~10 MPa CO_2 injection pressure not specified. Final equilibrium system pressures varied between 11.8 and 12.5 MPa.	Decreased adsorbed molar amounts of CH_4 due to CO_2 injection. They suggested the inclusion of secondary stimulating (e.g. hydraulic fracturing) methods in the design of shale CO_2 injection since the CH_4 was predominantly restricted to the pore centre after desorption by CO_2 exchange.	

plugs have also been reported in the literature (Wollenweber et al., 2009; Battistutta et al., 2010). The extent to which these changes could influence storage integrity needs further investigation. Available data (Angeli et al., 2009; Busch et al., 2010; Wollenweber et al., 2010; Edlmann et al., 2013) indicates shale cap rocks to be adequately resilient towards CO_2 leakage and demonstrates an encouraging note for the sequestration of CO_2 in gas shale systems.

As seen, production and enhanced recovery of gas from shales is a complex process. Sorption is a central mechanism in this interplay. Despite this complexity, promising results have been achieved at lab and field scales (Louk et al., 2017) and CO_2 injection for ESGR is becoming a better understood process.

8. Conclusions

- Both CH_4 and CO_2 exist in critical thermodynamical state for most relevant reservoir conditions. CH_4 sorption increases monotonously with pressure from pressures near ambient to reservoir and can in most cases be described by a Langmuir isotherm. CO_2 however changes sorption behavior at the critical pressure. At lower pressures, the sorption increases monotonously, while near the critical pressure a peak in adsorption is reached and desorption occurs with increased pressure. This is not captured in low pressure experiments and standard isotherm models, e.g. multicomponent Langmuir models, are not sufficient. Extended isotherms or PVT-relations that treat both the gas and sorbed phases accurately should be applied.
- CH_4 and CO_2 adsorption storage capacity have a strong positive correlation with Total Organic Carbon, where a greater capacity is measured for CO_2.
- More mature shales tend to have higher storage capacity, but also lower Langmuir pressure indicating that the gas desorbs less easily on pressure reduction.
- Kerogen type also influences storage capacity of CH_4 with capacity trend as Type III > Type II > Type I. More experimental data is suggested to fully support this trend. Especially, there seems to be little or no data on the correlation between CO_2 storage capacity and kerogen type.
- Clays can increase the storage capacity for gas adsorption, but they strongly associate with water. Measurements on dry samples are therefore likely to yield higher capacity than original state or moisture equilibrated samples.
- Adsorption is an exothermic process and the heat of adsorption for CO_2 is greater than for CH_4 in shales. CO_2 is therefore more favourably adsorbed. Increased temperature opposes the adsorption reaction and explains observed trends; both gases adsorb less at higher temperature.
- Recent advances have allowed NMR studies to track and distinguish gaseous and sorbed CH_4 and CO_2 in shale.

Acknowledgments

The authors acknowledge the Research Council of Norway and the industry partners, ConocoPhillips Skandinavia AS, Aker BP ASA, Vår Energi AS, Equinor ASA, Neptune Energy Norge AS, Lundin Norway AS, Halliburton AS, Schlumberger Norge AS, and Wintershall DEA, of The National IOR Centre of Norway for support.

References

Aljamaan, H., 2013. Petrophysical investigation on gas transport properties of the Barnett. In: Paper Presented at the SPE Annual Technical Conference and Exhibition.
Ambrose, R.J., Hartman, R.C., Diaz Campos, M., Akkutlu, I.Y., Sondergeld, C., 2010. New pore-scale considerations for shale gas in place calculations. In: Paper Presented at the SPE Unconventional Gas Conference, Pittsburgh, Pennsylvania, USA.
Angeli, M., Soldal, M., Skurtveit, E., Aker, E., 2009. Experimental percolation of supercritical CO2 through a caprock. Energy Procedia 1 (1), 3351–3358. https://doi.org/10.1016/j.egypro.2009.02.123.
Aranovich, G.L., Donohue, M.D., 1995. Adsorption isotherms for microporous adsorbents. Carbon 33 (10), 1369–1375. https://doi.org/10.1016/0008-6223(95)00080-W.
Aranovich, G.L., Donohue, M.D., 1996. Adsorption of supercritical fluids. J. Colloid Interface Sci. 180 (2), 537–541. https://doi.org/10.1006/jcis.1996.0334.
Aringhieri, R., 2004. Nanoporosity characteristics of some natural clay minerals and soils. Clay Clay Miner. 52 (6), 700–704. https://doi.org/10.1346/ccmn.2004.0520604.
Aylmore, L.A.G., 1974. Gas sorption in clay mineral systems. Clay Clay Miner. 22 (2), 175–183. https://doi.org/10.1346/ccmn.1974.0220205.
Bae, J.-S., Bhatia, S.K., 2006. High-pressure adsorption of methane and carbon dioxide on coal. Energy Fuels 20 (6), 2599–2607. https://doi.org/10.1021/ef060318y.
Battistutta, E., van Hemert, P., Lutynski, M., Bruining, H., Wolf, K.-H., 2010. Swelling and sorption experiments on methane, nitrogen and carbon dioxide on dry Selar Cornish coal. Int. J. Coal Geol. 84 (1), 39–48. https://doi.org/10.1016/j.coal.2010.08.002.
Beaton, A.P., Pawlowicz, J.G., Anderson, S.D.A., Berhane, H., Rokosh, C.D., 2010. Total Organic Carbon and Adsorption Isotherms of the Duvernay and Muskwa Formations in Alberta: Shale Gas Data Release. Energy Resources Conservation Board /Alberta Geological Survey, Edmonton, Alberta, Canada.
Bernard, S., Horsfield, B., Schulz, H.-M., Wirth, R., Schreiber, A., Sherwood, N., 2012. Geochemical evolution of organic-rich shales with increasing maturity: a STXM and TEM study of the Posidonia Shale (Lower Toarcian, northern Germany). Mar. Pet. Geol. 31 (1), 70–89. https://doi.org/10.1016/j.marpetgeo.2011.05.010.
Bernin, D., Hedin, N., 2018. Perspectives on NMR studies of CO2 adsorption. Curr. Opin. Colloid Interface Sci. 33, 53–62. https://doi.org/10.1016/j.cocis.2018.02.003.
Bi, H., Jiang, Z., Li, J., Li, P., Chen, L., Pan, Q., Wu, Y., 2016. The Ono–Kondo model and an experimental study on supercritical adsorption of shale gas: a case study on Longmaxi shale in southeastern Chongqing, China. J. Nat. Gas Sci. Eng. 35, 114–121. https://doi.org/10.1016/j.jngse.2016.08.047.
Blok, K., Williams, R.H., Katofsky, R.E., Hendriks, C.A., 1997. Hydrogen production from natural gas, sequestration of recovered CO2 in depleted gas wells and enhanced natural gas recovery. Energy 22 (2), 161–168. https://doi.org/10.1016/S0360-5442(96)00136-3.
Bocquet, M.L., Rappe, A.M., Dai, H.L., 2005. A density functional theory study of adsorbate-induced work function change and binding energy: olefins on Ag(111). Mol. Phys. 103 (6–8), 883–890. https://doi.org/10.1080/00268970412331333609.
Boyer, C., Kieschnick, J., Suarez-Rivera, R., Lewis, R.E., Waters, G., 2006. Producing gas from its source. Oilfield Rev. 18 (3), 36–49.
Brunauer, S., Deming, L.S., Deming, W.E., Teller, E., 1940. On a theory of the van der Waals adsorption of gases. J. Am. Chem. Soc. 62 (7), 1723–1732. https://doi.org/10.1021/ja01864a025.
Bruner, K.R., Smosna, R., 2011. A Comparative Study of the Mississippian Barnett Shale, Fort Worth Basin, and Devonian Marcellus Shale, Appalachian Basin. Report to US Dept. of Energy (US DOE), National Technology Laboratory.
Burwell, R.L., 1977. Advances in Catalysis. Elsevier.
Busch, A., Krooss, B.M., Gensterblum, Y., Van Bergen, F., Pagnier, H.J.M., 2003. High-pressure adsorption of methane, carbon dioxideand their mixtures on coals with a special focus on the preferential sorption behaviour. J. Geochem. Explor. 78–79, 671–674. https://doi.org/10.1016/S0375-6742(03)00122-5.
Busch, A., Gensterblum, Y., Krooss, B.M., Siemons, N., 2006. Investigation of high-pressure selective adsorption/desorption behaviour of CO2 and CH4 on coals: an experimental study. Int. J. Coal Geol. 66 (1), 53–68. https://doi.org/10.1016/j.coal.2005.07.003.
Busch, A., Alles, S., Gensterblum, Y., Prinz, D., Dewhurst, D.N., Raven, M.D., Stanjek, H., Krooss, B.M., 2008. Carbon dioxide storage potential of shales. Int. J. Greenh. Gas Contr. 2 (3), 297–308. https://doi.org/10.1016/j.ijggc.2008.03.003.
Busch, A., Alles, S., Krooss, B.M., Stanjek, H., Dewhurst, D., 2009. Effects of physical sorption and chemical reactions of CO2 in shaly caprocks. Energy Procedia 1 (1), 3229–3235. https://doi.org/10.1016/j.egypro.2009.02.107.
Busch, A., Amann-Hildenbrand, A., Bertier, P., Waschbuesch, M., Krooss, B.M., 2010. The significance of caprock sealing integrity for CO2 storage. In: Paper Presented at the SPE International Conference on CO2 Capture, Storage, and Utilization, New Orleans, Louisiana, USA.
Busch, A., Gensterblum, Y., 2011. CBM and CO2-ECBM related sorption processes in coal: a review. Int. J. Coal Geol. 87 (2), 49–71. https://doi.org/10.1016/j.coal.2011.04.011.
Bustin, R.M., Clarkson, C.R., 1998. Geological controls on coalbed methane reservoir capacity and gas content. Int. J. Coal Geol. 38 (1–2), 3–26. https://doi.org/10.1016/s0166-5162(98)00030-5.
Bustin, R.M., Bustin, A.M.M., Cui, A., Ross, D., Pathi, V.M., 2008. Impact of shale properties on pore structure and storage characteristics. In: Paper Presented at the SPE Shale Gas Production Conference, Fort Worth, Texas, USA.
Cancino, O.P.O., Pérez, D.P., Pozo, M., Bessieres, D., 2017. Adsorption of pure CO2 and a CO2/CH4 mixture on a black shale sample: manometry and microcalorimetry measurements. J. Pet. Sci. Eng. 159, 307–313. https://doi.org/10.1016/j.petrol.2017.09.038.
Cao, T., Song, Z., Wang, S., Cao, X., Li, Y., Xia, J., 2015. Characterizing the pore structure in the silurian and permian shales of the Sichuan Basin, China. Mar. Pet. Geol. 61, 140–150. https://doi.org/10.1016/j.marpetgeo.2014.12.007.
Carroll, S.A., McNab, W.W., Dai, Z., Torres, S.C., 2013. Reactivity of mount simon sandstone and the Eau Claire shale under CO2 storage conditions. Environ. Sci. Technol. 47 (1), 252–261. https://doi.org/10.1021/es301269k.

Cavenati, S., Grande, C.A., Rodrigues, A.E., 2004. Adsorption equilibrium of methane, carbon dioxide, and nitrogen on Zeolite 13X at high pressures. J. Chem. Eng. Data 49 (4), 1095–1101. https://doi.org/10.1021/je0498917.

Chalmers, G.R., Bustin, R.M., 2007. The organic matter distribution and methane capacity of the Lower Cretaceous strata of Northeastern British Columbia, Canada. Int. J. Coal Geol. 70 (1–3), 223–239. https://doi.org/10.1016/j.coal.2006.05.001.

Chalmers, G.R., Bustin, R.M., 2008. Lower Cretaceous gas shales in northeastern British Columbia, Part I: geological controls on methane sorption capacity. Bull. Can. Petrol. Geol. 56 (1), 1–21. https://doi.org/10.2113/gscpgbull.56.1.1.

Chang, T., Shu, Y., Ma, Y., Xu, X., Niu, Y., 2017. Isothermal adsorption and desorption properties of marine shales on Longmaxi shale in south China. , 7(12), 1819–1835.

Chareonsuppanimit, P., Mohammad, S.A.R., Robert, L., Robinson, R.L., Gasem, K.A.M., 2012. High-pressure adsorption of gases on shales: measurements and modeling. Int. J. Coal Geol. 95, 34–46. https://doi.org/10.1016/j.coal.2012.02.005.

Charoensuppanimit, P., Mohammad, S.A., Gasem, K.A.M., 2016. Measurements and modeling of gas adsorption on shales. Energy Fuels 30 (3), 2309–2319. https://doi.org/10.1021/acs.energyfuels.5b02751.

Chen, L., Zuo, L., Jiang, Z., Jiang, S., Liu, K., Tan, J., Zhang, L., 2019. Mechanisms of shale gas adsorption: evidence from thermodynamics and kinetics study of methane adsorption on shale. Chem. Eng. J. 361, 559–570. https://doi.org/10.1016/j.cej.2018.11.185.

Cheng, A.-L., Huang, W.-L., 2004. Selective adsorption of hydrocarbon gases on clays and organic matter. Org. Geochem. 35 (4), 413–423. https://doi.org/10.1016/j.orggeochem.2004.01.007.

Chikatamarla, L., Crosdale, P., 2001. Heat of methane adsorption of coal: implications for pore structure development. In: Paper Presented at the Proceedings of the International Coalbed Methane Symposium.

Coates, G.R., Xiao, L., Prammer, M.G., 1999. NMR Logging: Principles and Applications, vol. 234. Haliburton Energy Services, Houston.

Crosdale, P.J., 1999. Mixed methane/carbon dioxide sorption by coal: new evidence in support of pore-filling models. In: Paper Presented at the Proceedings of the 1999 International Coalbed Methane Symposium, Tuscaloosa, Alabama.

Curtis, J.B., 2002. Fractured shale-gas systems. AAPG Bull. 86 (11), 1921–1938. https://doi.org/10.1306/61eeddbe-173e-11d7-8645000102c1865d.

Curtis, M.E., Ambrose, R.J., Sondergeld, C.H., Rai, C.S., 2011. Investigation of the relationship between organic porosity and thermal maturity in the Marcellus Shale. In: Paper Presented at the North American Unconventional Gas Conference and Exhibition.

Delle Piane, C., Bourdet, J., Josh, M., Clennell, M.B., Rickard, W.D., Saunders, M., Sherwood, N., Li, Z., Dewhurst, D.N., Raven, M.D., 2018. Organic matter network in post-mature Marcellus Shale: effects on petrophysical properties. AAPG Bull. 102 (11), 2305–2332. https://doi.org/10.1306/04121817180.

Duan, S., Gu, M., Du, X., Xian, X., 2016. Adsorption equilibrium of CO2 and CH4 and their mixture on Sichuan Basin shale. Energy Fuels 30 (3), 2248–2256. https://doi.org/10.1021/acs.energyfuels.5b02088.

Dubinin, M.M., 1975. Physical adsorption of gases and vapors in micropores. In: Progress in Surface and Membrane Science, vol. 9. Elsevier, pp. 1–70.

Dubinin, M.M., 1980. Water vapor adsorption and the microporous structures of carbonaceous adsorbents. Carbon 18 (5), 355–364. https://doi.org/10.1016/0008-6223(80)90007-X.

Eberl, D., 1984. Clay mineral formation and transformation in rocks and soils. Philos. Trans. R. Soc. Lond. Ser. A Math. Phys. Sci. 311 (1517), 241–257. https://doi.org/10.1098/rsta.1984.0026.

Edlmann, K., Haszeldine, S., McDermott, C.I., 2013. Experimental investigation into the sealing capability of naturally fractured shale caprocks to supercritical carbon dioxide flow. Environ. Earth sci. 70 (7), 3393–3409. https://doi.org/10.1007/s12665-013-2407-y.

Edwards, R.W., Celia, M.A., Bandilla, K.W., Doster, F., Kanno, C.M., 2015. A model to estimate carbon dioxide injectivity and storage capacity for geological sequestration in shale gas wells. Environ. Sci. Technol. 49 (15), 9222–9229.

EIA, 2013. Technically Recoverable Shale Oil and Shale Gas Resources: an Assessment of 137 Shale Formations in 41 Countries outside the United States. https://www.eia.gov/analysis/studies/worldshalegas/archive/2013/pdf/fullreport_2013.pdf.

Faiz, M., Aziz, N., Hutton, A., Jones, B., 1992. Porosity and gas sorption capacity of some eastern Australian coals in relation to coal rank and composition. In: Paper presented at the Coalbed Methane Symposium, Townsville.

Fan, E., Tang, S., Zhang, C., Guo, Q., Sun, C., 2014. Methane sorption capacity of organics and clays in high-over matured shale-gas systems. Energy Explor. Exploit. 32 (6), 927–942. https://doi.org/10.1260/0144-5987.32.6.927.

Fan, K., Li, Y., Elsworth, D., Dong, M., Yin, C., Li, Y., Chen, Z., 2018. Three stages of methane adsorption capacity affected by moisture content. Fuel 231, 352–360. https://doi.org/10.1016/j.fuel.2018.05.120.

Fraissard, J.P., Conner, C.W., 1997. Physical Adsorption: Experiment, Theory, and Applications, vol. 491. Springer Science & Business Media.

Gasparik, M., Ghanizadeh, A., Bertier, P., Gensterblum, Y., Bouw, S., Krooss, B.M., 2012. High-pressure methane sorption isotherms of black shales from The Netherlands. Energy Fuels 26 (8), 4995–5004. https://doi.org/10.1021/ef300405g.

Gasparik, M., Bertier, P., Gensterblum, Y., Ghanizadeh, A., Krooss, B.M., Littke, R., 2014. Geological controls on the methane storage capacity in organic-rich shales. Int. J. Coal Geol. 123, 34–51. https://doi.org/10.1016/j.coal.2013.06.010.

Glorioso, J.C., Rattia, A.J., 2012. Unconventional reservoirs: basic petrophysical concepts for shale gas. In: Paper Presented at the SPE/EAGE European Unconventional Resources Conference and Exhibition, Vienna, Austria.

Godec, M., Koperna, G., Petrusak, R., Oudinot, A., 2013. Potential for enhanced gas recovery and CO2 storage in the Marcellus Shale in the Eastern United States. Int. J. Coal Geol. 118, 95–104. https://doi.org/10.1016/j.coal.2013.05.007.

Gumma, S., Talu, O., 2003. Gibbs dividing surface and helium adsorption. Adsorption 9 (1), 17–28. https://doi.org/10.1023/a:1023859112985.

Guo, S., 2013. Experimental study on isothermal adsorption of methane gas on three shale samples from Upper Paleozoic strata of the Ordos Basin. J. Pet. Sci. Eng. 110, 132–138. https://doi.org/10.1016/j.petrol.2013.08.048.

Guo, W., Xiong, W., Gao, S., Hu, Z., Liu, H., Yu, R., 2013. Impact of temperature on the isothermal adsorption/desorption of shale gas. Pet. Explor. Dev. 40 (4), 514–519. https://doi.org/10.1016/S1876-3804(13)60066-X.

Guo, W., Hu, Z., Zhang, X., Yu, R., Wang, L., 2017. Shale gas adsorption and desorption characteristics and its effects on shale permeability. Energy Explor. Exploit. 35 (4), 463–481. https://doi.org/10.1177/0144598716684306.

Hao, F., Zou, H., Lu, Y., 2013. Mechanisms of shale gas storage: implications for shale gas exploration in China mechanisms of Shale Gas Storage. AAPG Bull. 97 (8), 1325–1346. https://doi.org/10.1306/02141312091.

Helgeson, H.C., Richard, L., McKenzie, W.F., Norton, D.L., Schmitt, A., 2009. A chemical and thermodynamic model of oil generation in hydrocarbon source rocks. Geochem. Cosmochim. Acta 73 (3), 594–695. https://doi.org/10.1016/j.gca.2008.03.004.

Heller, R., Zoback, M., 2014. Adsorption of methane and carbon dioxide on gas shale and pure mineral samples. J. Unconv. Oil Gas Resour. 8, 14–24. https://doi.org/10.1016/j.juogr.2014.06.001.

Herrera, L., Fan, C., Do, D., Nicholson, D., 2011. A revisit to the Gibbs dividing surfaces and helium adsorption. Adsorption 17 (6), 955–965. https://doi.org/10.1007/s10450-011-9374-y.

Hong, L., Jain, J., Romanov, V., Lopano, C., Disenhof, C., Goodman, A., Hedges, S., Soeder, D., Sanguinito, S., Dilmore, R., 2016. An investigation of factors affecting the interaction of CO 2 and CH 4 on shale in Appalachian Basin. J. Unconv. Oil Gas Resour. 14, 99–112. https://doi.org/10.1016/j.juogr.2016.02.003.

Huang, L., Ning, Z., Wang, Q., Zhang, W., Cheng, Z., Wu, X., Qin, H., 2018. Effect of organic type and moisture on CO 2/CH 4 competitive adsorption in kerogen with implications for CO 2 sequestration and enhanced CH 4 recovery. J. Appl. Energy 210, 28–43. https://doi.org/10.1016/j.apenergy.2017.10.122.

Huo, P., Zhang, D., Yang, Z., Li, W., Zhang, J., Jia, S., 2017. CO 2 geological sequestration: displacement behavior of shale gas methane by carbon dioxide injection. Int. J. Greenh. Gas Contr. 66, 48–59. https://doi.org/10.1016/j.ijggc.2017.09.001.

Iijima, M., Nagayasu, T., Kamijyo, T., Nakatani, S., 2011. MHI's energy efficient flue gas CO2 capture technology and large scale ccs demonstration test at coal-fired power plants in USA. Mitsubishi Heavy Ind. Tech. Rev. 48 (1), 26–32. https://www.mhi.co.jp/technology/review/pdf/e481/e481026.pdf.

Inglezakis, V.J., Zorpas, A.A., 2012. Heat of adsorption, adsorption energy and activation energy in adsorption and ion exchange systems. Desalination Water Treat. 39 (1–3), 149–157. https://doi.org/10.5004/dwt.2012.3000.

Jarvie, D.M., Claxton, B.L., Henk, F., TBJ, 2001. Oil and shale gas from the Barnett shale, Ft. Worth basin, Texas. In: Paper Presented at the AAPG Annual Meeting Program.

Jarvie, D.M., Hill, R.J., Ruble, T.E., Pollastro, R.M., 2007. Unconventional shale-gas systems: the Mississippian Barnett Shale of north-central Texas as one model for thermogenic shale-gas assessment. AAPG Bull. 91 (4), 475–499. https://doi.org/10.1306/12190606068.

Ji, L., Zhang, T., Milliken, K.L., Qu, J., Zhang, X., 2012. Experimental investigation of main controls to methane adsorption in clay-rich rocks. Appl. Geochem. 27 (12), 2533–2545. https://doi.org/10.1016/j.apgeochem.2012.08.027.

Jia, B., Tsau, J.-S., Barati, R., 2018. Different flow behaviors of low-pressure and high-pressure carbon dioxide in shales. SPE J. 23 (04), 1452–1468. https://doi.org/10.2118/191121-pa.

Jiang, Y., Luo, Y., Lu, Y., Qin, C., Liu, H., 2016. Effects of supercritical CO2 treatment time, pressure, and temperature on microstructure of shale. Energy 97, 173–181. https://doi.org/10.1016/j.energy.2015.12.124.

Jin, X., Wang, X., Liu, X., Jiao, H., Sun, L., Su, L., Bi, L., Chen, Y., 2017. Low field cryoporometry NMR for mesopores distribution in shale. In: Paper Presented at the SPE/IATMI Asia Pacific Oil & Gas Conference and Exhibition, Jakarta, Indonesia.

Kalkreuth, W., Holz, M., Levandowski, J., Kern, M., Casagrande, J., Weniger, P., Krooss, B., 2013. The coalbed methane (CBM) potential and CO2 storage capacity of the santa Terezinha coalfield, Paraná Basin, Brazil–3D modelling, and coal and carbonaceous shale characteristics and related desorption and adsorption capacities in samples from exploration Borehole CBM001-ST-RS. Energy Explor. Exploit. 31 (4), 485–527. https://doi.org/10.1260/0144-5987.31.4.485.

Kang, S.M., Fathi, E., Ambrose, R.J., Akkutlu, I.Y., Sigal, R.F., 2011. Carbon dioxide storage capacity of organic-rich shales. SPE J. 16 (04), 842–855. https://doi.org/10.2118/134583-pa.

Karacan, C.Ö., Mitchell, G.D., 2003. Behavior and effect of different coal microlithotypes during gas transport for carbon dioxide sequestration into coal seams. Int. J. Coal Geol. 53 (4), 201–217. https://doi.org/10.1016/s0166-5162(03)00030-2.

Khosrokhavar, R., 2015. Sorption of CH4 and CO2 on Belgium carboniferous shale using a manometric set-up. In: Mechanisms for CO2 Sequestration in Geological Formations and Enhanced Gas Recovery. Springer International Publishing, pp. 49–66.

Krooss, B.M., Littke, R., Müller, B., Frielingsdorf, J., Schwochau, K., Idiz, E.F., 1995. Generation of nitrogen and methane from sedimentary organic matter: implications on the dynamics of natural gas accumulations. Chem. Geol. 126 (3), 291–318. https://doi.org/10.1016/0009-2541(95)00124-7.

Kus, J., Araujo, C.V., Borrego, A.G., Flores, D., Hackley, P.C., Hámor-Vidó, M., Kalaitzidis, S., Kommeren, C.J., Kwiecińska, B., Mastalerz, M., Mendonça Filho, J.G., Menezes, T.R., Misz-Kennan, M., Nowak, G.J., Petersen, H.I., Rallakis, D., Suárez-Ruiz, I., Sýkorová, I., Životić, D., 2017. Identification of alginite and bituminite in rocks other than coal. 2006, 2009, and 2011 round robin exercises of the ICCP

Identification of Dispersed Organic Matter Working Group. Int. J. Coal Geol. 178, 26–38. https://doi.org/10.1016/j.coal.2017.04.013.
Lancaster, D., Hill, D., 1993. A multi-laboratory comparison of isotherm measurements of Antrim shale samples. In: Paper Presented at the SCA Conference, Otsego County, Michigan.
Lane, H., Watson, A., Lancaster, D., 1989. Identifying and estimating desorption from Devonian shale gas production data. In: Paper Presented at the SPE Annual Technical Conference and Exhibition.
Langmuir, I., 1916. Langmuir, I., 1916. The constitution and fundamental properties of solids and liquids: Part I, Solids. J. Am. Chem. Soc. 38 (11), 2221–2295. https://doi.org/10.1021/ja02268a002.
Langmuir, I., 1918. The adsorption of gases on plane surfaces of glass, mica and platinum. J. Am. Chem. Soc. 40 (9), 1361–1403. https://doi.org/10.1021/ja02242a004.
Li, A., Ding, W., Zhou, X., Cao, X., Zhang, M., Fu, F., Chen, E., 2017. Investigation of the methane adsorption characteristics of marine shale: a case study of lower cambrian Qiongzhusi shale in eastern Yunnan province, south China. Energy Fuels 31 (3), 2625–2635. https://doi.org/10.1021/acs.energyfuels.6b03168.
Liu, D., Li, Y., Yang, S., Agarwal, R.K., 2019. CO2 sequestration with enhanced shale gas recovery. Energy Sources, Part A Recovery, Util. Environ. Eff. 1–11. https://doi.org/10.1080/15567036.2019.1587069.
Liu, F., Lu, P., Griffith, C., Hedges, S.W., Soong, Y., Hellevang, H., Zhu, C., 2012. CO2–brine–caprock interaction: reactivity experiments on Eau Claire shale and a review of relevant literature. Int. J. Greenh. Gas Contr. 7, 153–167. https://doi.org/10.1016/j.ijggc.2012.01.012.
Liu, J., Yao, Y., Liu, D., Elsworth, D., 2017. Experimental evaluation of CO2 enhanced recovery of adsorbed-gas from shale. Int. J. Coal Geol. 179, 211–218. https://doi.org/10.1016/j.coal.2017.06.006.
Liu, Y., Li, H.A., Tian, Y., Jin, Z., Deng, H., 2018. Determination of the absolute adsorption/desorption isotherms of CH4 and n-C4H10 on shale from a nano-scale perspective. Fuel 218, 67–77. https://doi.org/10.1016/j.fuel.2018.01.012.
Loucks, R.G., Reed, R.M., Ruppel, S.C., Hammes, U., 2012. Spectrum of pore types and networks in mudrocks and a descriptive classification for matrix-related mudrock pores. AAPG Bull. 96 (6), 1071–1098. https://doi.org/10.1306/08171111061.
Loucks, R.G., Reed, R.M., Ruppel, S.C., Jarvie, D.M., 2009. Morphology, genesis, and distribution of nanometer-scale pores in siliceous mudstones of the mississippian Barnett shale. J. Sediment. Res. 79 (12) https://doi.org/10.2110/jsr.2009.092, 1527-1404.
Louk, K., Ripepi, N., Luxbacher, K., Gilliland, E., Tang, X., Keles, C., Schlosser, C., Diminick, E., Keim, S., Amante, J., Michael, K., 2017. Monitoring CO2 storage and enhanced gas recovery in unconventional shale reservoirs: results from the Morgan County, Tennessee injection test. J. Nat. Gas Sci. Eng. 45, 11–25. https://doi.org/10.1016/j.jngse.2017.03.025.
Lu, X.C., Li, F.C., Watson, A.T., 1995. Adsorption studies of natural gas storage in Devonian shales. SPE Form. Eval. 10 (02), 109–113. https://doi.org/10.2118/26632-pa.
Lu, Y., Ao, X., Tang, J., Jia, Y., Zhang, X., Chen, Y., 2016. Swelling of shale in supercritical carbon dioxide. J. Nat. Gas Sci. Eng. 30, 268–275. https://doi.org/10.1016/j.jngse.2016.02.011.
Luo, X., Wang, S., Wang, Z., Jing, Z., Lv, M., Zhai, Z., Han, T., 2015. Adsorption of methane, carbon dioxide and their binary mixtures on Jurassic shale from the Qaidam Basin in China. Int. J. Coal Geol. 150–151, 210–223. https://doi.org/10.1016/j.coal.2015.09.004.
Lutyński, M., Waszczuk, P., Słomski, P., Szczepański, J., 2017. CO2 sorption of Pomeranian gas bearing shales – the effect of clay minerals. Energy Procedia 125, 457–466. https://doi.org/10.1016/j.egypro.2017.08.153.
Lyu, Q., Long, X., Ranjith, P.G., Kang, Y., 2016. Unconventional gas: experimental study of the influence of subcritical carbon dioxide on the mechanical properties of black shale. Energies 9 (7), 516. https://doi.org/10.3390/en9070516.
Lyu, Q., Ranjith, P.G., Long, X., Ji, B., 2016. Experimental investigation of mechanical properties of black shales after CO2-water-rock interaction. Materials 9 (8), 663. https://doi.org/10.20944/preprints201608.0056.v1.
Lyu, Q., Long, X., Ranjith, P., Tan, J., Zhou, J., Wang, Z., Luo, W., 2018. A laboratory study of geomechanical characteristics of black shales after sub-critical/super-critical CO 2+ brine saturation. Geomech. Geophys. Geo-Energy Geo-Resour. 1–16. https://doi.org/10.1007/s40948-018-0079-5.
Lyu, Q., Long, X., Ranjith, P.G., Tan, J., Kang, Y., Wang, Z., 2018. Experimental investigation on the mechanical properties of a low-clay shale with different adsorption times in sub-/super-critical CO2. Energy 147, 1288–1298. https://doi.org/10.1016/j.energy.2018.01.084.
Ma, Y., Zhong, N., Li, D., Pan, Z., Cheng, L., Liu, K., 2015. Organic matter/clay mineral intergranular pores in the Lower Cambrian Lujiaping Shale in the north-eastern part of the upper Yangtze area, China: a possible microscopic mechanism for gas preservation. Int. J. Coal Geol. 137, 38–54. https://doi.org/10.1016/j.coal.2014.11.001.
Ma, Y., Yue, C., Li, S., Xu, X., Niu, Y., 2018. Study of CH4 and CO2 competitive adsorption on shale in Yibin, sichuan province of China. Carbon Resour. Convers. https://doi.org/10.1016/j.crcon.2018.11.005.
Majewska, Z., Ceglarska-Stefańska, G., Majewski, S., Ziętek, J., 2009. Binary gas sorption/desorption experiments on a bituminous coal: simultaneous measurements on sorption kinetics, volumetric strain and acoustic emission. Int. J. Coal Geol. 77 (1), 90–102. https://doi.org/10.1016/j.coal.2008.09.009.
Malbrunot, P., Vidal, D., Vermesse, J., Chahine, R., Bose, T.K., 1997. Adsorbent helium density measurement and its effect on adsorption isotherms at high pressure. Langmuir 13 (3), 539–544. https://doi.org/10.1021/la950969e.
Manger, K.C., Oliver, S.J.P., Curtis, J., B, Scheper, R.J., 1991. Geologic influences on the location and production of Antrim shale gas, Michigan Basin. In: Paper Presented at the Low Permeability Reservoirs Symposium.
Manz, B., Gladden, L.F., Warren, P.B., 1999. Flow and dispersion in porous media: Lattice-Boltzmann and NMR studies. AlChE J. 45 (9), 1845–1854. https://doi.org/10.1002/aic.690450902.
Mendhe, V.A., Mishra, S., Varma, A.K., Kamble, A.D., Bannerjee, M., Sutay, T., 2017. Gas reservoir characteristics of the lower gondwana shales in Raniganj basin of eastern India. J. Pet. Sci. Eng. 149, 649–664. https://doi.org/10.1016/j.petrol.2016.11.008.
Menon, P.G., 1968. Adsorption at high pressures. Chem. Rev. 68 (3), 277–294. https://pubs.acs.org/doi/abs/10.1021/cr60253a002.
Merey, S., Sinayuc, C., 2016. Analysis of carbon dioxide sequestration in shale gas reservoirs by using experimental adsorption data and adsorption models. J. Nat. Gas Sci. Eng. 36, 1087–1105. https://doi.org/10.1016/j.jngse.2016.02.052.
Merey, S., Sinayuc, C., 2018. Adsorption behaviour of shale gas reservoirs. Int. J. Oil Gas Coal Technol. 17, 172. https://doi.org/10.1504/ijogct.2018.089941.
Merkel, A., Fink, R., Littke, R., 2015. The role of pre-adsorbed water on methane sorption capacity of Bossier and Haynesville shales. Int. J. Coal Geol. 147–148, 1–8. https://doi.org/10.1016/j.coal.2015.06.003.
Milliken, K.L., Rudnicki, M., Awwiller, D.N., Zhang, T., 2013. Organic matter–hosted pore system, Marcellus formation (Devonian), PennsylvaniaGeohorizon. AAPG Bull. 97 (2), 177–200. https://doi.org/10.1306/07231212048.
Moffat, D.H., Weale, K.E., 1955. Sorption by coal of methane at high pressures, 34 (4), 449–462.
Mullen, J., 2010. Petrophysical characterization of the Eagle Ford shale in south Texas. In: Paper Presented at the Canadian Unconventional Resources and International Petroleum Conference, Calgary, Alberta, Canada.
Murata, K., El-Merraoui, M., Kaneko, K., 2001. A new determination method of absolute adsorption isotherm of supercritical gases under high pressure with a special relevance to density-functional theory study. J. Chem. Phys. 114 (9), 4196–4205. https://doi.org/10.1063/1.1344926.
Neimark, A.V., Ravikovitch, P.I., 1997. Calibration of pore volume in adsorption experiments and theoretical models. Langmuir 13 (19), 5148–5160. https://doi.org/10.1021/la970266s.
Nelson, P.H., 2009. Pore-throat sizes in sandstones, tight sandstones, and shales. AAPG Bull. 93 (3), 329–340. https://doi.org/10.1306/10240808059.
Nuttal, B.C., Eble, C., Bustin, R.M., Drahovzal, J.A., 2003. Analysis of Devonian Black Shales in Kentucky for Potential Carbon Dioxide Sequestration and Enhanced Natural Gas Production. UNT Libraries Government Documents Department. digital.library.unt.edu/ark:/67531/metadc786289/.
Nuttal, B.C., Eble, C., Bustin, R.M., Drahovzal, J.A., 2005. Analysis of Devonian black shales in Kentucky for potential carbon dioxide sequestration and enhanced natural gas production. In: Greenhouse Gas Control Technologies, vol. 7. Elsevier, pp. 2225–2228.
Oldenburg, C.M., Pruess, K., Benson, S.M., Fuels, 2001. Process modeling of CO2 injection into natural gas reservoirs for carbon sequestration and enhanced gas recovery. Energy Fuels 15 (2), 293–298. https://doi.org/10.1021/ef000247h.
Passey, Q.R., Bohacs, K., Esch, W.L., Klimentidis, R., Sinha, S., 2010. From oil-prone source rock to gas-producing shale reservoir-geologic and petrophysical characterization of unconventional shale gas reservoirs. In: Paper Presented at the International Oil and Gas Conference and Exhibition in China.
Pei, P., Ling, K., He, J., Liu, Z., 2015. Shale gas reservoir treatment by a CO2-based technology. J. Nat. Gas Sci. Eng. 26, 1595–1606. https://doi.org/10.1016/j.jngse.2015.03.026.
Pino, D., Plantier, F., Bessieres, D., 2014. Experimental determination of the adsorption isotherms in gas mixtures under extended pressure and temperature range. J. Therm. Anal. Calorim. 117 (3), 1469–1477. https://doi.org/10.1007/s10973-014-3931-z.
Polanyi, M., 1932. Section III.—theories of the adsorption of gases. A general survey and some additional remarks. Introductory paper to section III. Trans. Faraday Soc. 28, 316–333. https://doi.org/10.1039/TF9322800316.
Pozo, M., Pino, D., Bessieres, D., 2017. Effect of thermal events on maturation and methane adsorption of Silurian black shales (Checa, Spain). Appl. Clay Sci. 136, 208–218. https://doi.org/10.1016/j.clay.2016.11.026.
Pusch, A.-K., Splith, T., Moschkowitz, L., Karmakar, S., Biniwale, R., Sant, M., Suffritti, G. B., Demontis, P., Cravillon, J., Pantatosaki, E.J.A., 2012. NMR studies of carbon dioxide and methane self-diffusion in ZIF-8 at elevated gas pressures. , 18(5–6), 359–366.
Pytte, A.M., Reynolds, R.C., 1989. The thermal transformation of smectite to illite. In: Thermal History of Sedimentary Basins. Springer, pp. 133–140.
Ramos, S., 2004. The Effect of Shale Composition on the Gas Sorption Potential of Organic-Rich Mudrocks in the Western Canadian Sedimentary Basin. University of British Columbia. Retrieved from.
Rani, S., Padmanabhan, E., Prusty, B.K., 2019. Review of gas adsorption in shales for enhanced methane recovery and CO2 storage. J. Pet. Sci. Eng. 175, 634–643. https://doi.org/10.1016/j.petrol.2018.12.081.
Rassenfoss, S., 2017. Shale EOR works, but will it make a difference? SPE-1017-0034-JPT 69 (10), 34–40. https://doi.org/10.2118/1017-0034-JPT.
Regan, M., 2007. A Review of the Potential for Carbon Dioxide (CO2) Enhanced Gas Recovery in Australia.
Rexer, T.F., Mathia, E.J., Aplin, A.C., Thomas, K.M., 2014. High-pressure methane adsorption and characterization of pores in Posidonia shales and isolated kerogens. Energy Fuels 28 (5), 2886–2901. https://doi.org/10.1021/ef402466m.
Rice, D.D., Law, B.E., Clayton, J.L., 1993. Coalbed gas: an undeveloped resource. U. S. Geol. Surv. Prof. Pap. 1570, 389–404.

Ross, D.J.K., Bustin, R.M., 2007. Shale gas potential of the lower Jurassic Gordondale member, northeastern British Columbia, Canada. Bull. Can. Petrol. Geol. 55 (1), 51–75. https://doi.org/10.2113/gscpgbull.55.1.51.
Ross, D.J.K., Bustin, R.M., 2007. Impact of mass balance calculations on adsorption capacities in microporous shale gas reservoirs. Fuel 86 (17), 2696–2706. https://doi.org/10.1016/j.fuel.2007.02.036.
Ross, D.J.K., Bustin, R.M., 2008. Characterizing the shale gas resource potential of Devonian–Mississippian strata in the Western Canada sedimentary basin: application of an integrated formation evaluation. AAPG Bull. 92 (1), 87–125. https://doi.org/10.1306/09040707048.
Ross, D.J.K., Bustin, R.M., 2009. The importance of shale composition and pore structure upon gas storage potential of shale gas reservoirs. Mar. Pet. Geol. 26 (6), 916–927. https://doi.org/10.1016/j.marpetgeo.2008.06.004.
Rudzinski, W., Everett, D.H., 2012. Adsorption of Gases on Heterogeneous Surfaces. Academic Press.
Ruppel, S., Loucks, R., 2008. Black mudrocks: lessons and questions from the mississippian Barnett shale in the southern midcontinent. Sediment. Rec. 6 (2), 4–8. https://doi.org/10.2110/sedred.2008.2.4.
Saha, P., Chowdhury, S., 2011. Insight into adsorption thermodynamics. In: Thermodynamics. InTechOpen.
Scaranto, J., Mallia, G., Harrison, N.M., 2011. An efficient method for computing the binding energy of an adsorbed molecule within a periodic approach. The application to vinyl fluoride at rutile TiO2(110) surface. Comput. Mater. Sci. 50 (7), 2080–2086. https://doi.org/10.1016/j.commatsci.2011.02.011.
Schaef, H.T., Glezakou, V.-A., Owen, A.T., Ramprasad, S., Martin, P.F., McGrail, B.P., 2013. Surface condensation of CO2 onto kaolinite. Environ. Sci. Technol. Lett. 1 (2), 142–145. https://doi.org/10.1021/ez400169b.
Schaef, H.T., Davidson, C.L., Owen, A.T., Miller, Q.R., Loring, J.S., Thompson, C.J., Bacon, D.H., Glezakou, V.A., McGrail, B.P., 2014. CO2 utilization and storage in shale gas reservoirs: experimental results and economic impacts. Energy Procedia 63, 7844–7851. https://doi.org/10.1016/j.egypro.2014.11.819. PNNL-SA-105772).
Schettler Jr., P., Parmely, C., 1990. The measurement of gas desorption isotherms for Devonian shale. GRI Devonian Gas Shale Technol. Rev. 7 (1), 4–9.
Schettler Jr., P., Parmely, C., 1991. Contributions to total storage capacity in Devonian shales. In: Paper Presented at the SPE Eastern Regional Meeting.
Schieber, J., 2010. Common themes in the formation and preservation of intrinsic porosity in shales and mudstones - illustrated with examples across the phanerozoic. In: Paper Presented at the SPE Unconventional Gas Conference.
Seewald, J.S., 2003. Organic–inorganic interactions in petroleum-producing sedimentary basins. Nature 426, 327. https://doi.org/10.1038/nature02132.
Sharma, G., Galvis-Portilla, H., 2018. Impact of total organic carbon on adsorption capacity, in-place hydrocarbons, and ultimate recovery: a case study of the duvernay formation in alberta, Canada. In: Paper Presented at the Abu Dhabi International Petroleum Exhibition & Conference.
Sing, K.S.W., Everett, D.H., Haul, R.A.W., Moscou, L., Pierotti, L.A., Rouquerol, J., Siemieniewska, T., 1985. International union of pure and applied chemistry physical chemistry division reporting physisorption data for gas/soils systems with special reference to the determination of surface area and porosity. Pure Appl. Chem. 57, 603–619. https://doi.org/10.1515/iupac.54.0530.
Sircar, S., 1985. Excess properties and thermodynamics of multicomponent gas adsorption. J. Chem. Soc., Faraday Trans. 1: Phys. Chem. Condens. Phases 81 (7), 1527–1540. https://doi.org/10.1039/F19858101527.
Slatt, R.M., O'Brien, N.R., 2011. Pore types in the Barnett and Woodford gas shales: contribution to understanding gas storage and migration pathways in fine-grained rocks geohorizon. AAPG Bull. 95 (12), 2017–2030. https://doi.org/10.1306/03301110145.
Soeder, D.J., 1988. Porosity and permeability of eastern Devonian gas shale. SPE Form. Eval. 3 (01), 116–124. https://doi.org/10.2118/15213-PA.
Sondergeld, C.H., Ambrose, R.J., Rai, C.S., Moncrieff, J., 2010. Micro-structural studies of gas shales. In: Paper Presented at the SPE Unconventional Gas Conference.
Steele, W.A., 1974. The Interaction of Gases with Solid Surfaces. Pergamon, Oxford.
Stoeckli, H.F., 1990. Microporous carbons and their characterization: the present state of the art. Carbon 28 (1), 1–6. https://doi.org/10.1016/0008-6223(90)90086-E.
Strapoc, D., Mastalerz, M., Schimmelmann, A., Drobniak, A., Hasenmueller, N.R., 2010. Geochemical constraints on the origin and volume of gas in the new Albany shale (Devonian–Mississippian), eastern Illinois basin. AAPG Bull. 94 (11), 1713–1740. https://doi.org/10.1306/06301009197.
Strubinger, J.R., Song, H., Parcher, J.F., 1991. High-pressure phase distribution isotherms for supercritical fluid chromatographic systems. 1. Pure carbon dioxide. Anal. Chem. 63 (2), 98–103. https://doi.org/10.1021/ac00002a003.
Sudibandriyo, M., Pan, Z., Fitzgerald, J.E., Robinson, R.L., Gasem, K.A.M., 2003. Adsorption of methane, nitrogen, carbon dioxide, and their binary mixtures on dry activated carbon at 318.2 K and pressures up to 13.6 MPa. Langmuir 19 (13), 5323–5331. https://doi.org/10.1021/la020976k.
Šucha, V., Środoń, J., Clauer, N., Elsass, F., Eberl, D., Kraus, I., Madejová, J., 2001. Weathering of smectite and illite-smectite under temperate climatic conditions. Clay Miner. 36 (3), 403–419. https://doi.org/10.1180/000985501750539490.
Teichmüller, M., 1971. Anwendung kohlenpetrographischer Methoden bei der Erdöl-und Erdgasprospektion. Erdöl Kohle 24, 69–76.
Tan, J., Weniger, P., Krooss, B., Merkel, A., Horsfield, B., Zhang, J., Boreham, C.J., van Graas, G., Tocher, B.A., 2014. Shale gas potential of the major marine shale formations in the Upper Yangtze Platform, South China, Part II: methane sorption capacity. Fuel 129, 204–218. https://doi.org/10.1016/j.fuel.2014.03.064.
Tang, X., Ripepi, N., Luxbacher, K., Pitcher, E., 2017. Adsorption models for methane in shales: review, comparison, and application. Energy Fuels 31 (10), 10787–10801. https://doi.org/10.1021/acs.energyfuels.7b01948.
Tang, S., Zhang, J., Elsworth, D., Tang, X., Li, Z., Du, X., Yang, X., 2016. Lithofacies and pore characterization of the lower permian shanxi and Taiyuan shales in the southern north China basin. J. Nat. Gas Sci. Eng. 36, 644–661. https://doi.org/10.1016/j.jngse.2016.11.013.
Tao, Z., Bielicki, J.M., Clarens, A.F., 2014. Physicochemical factors impacting CO2 sequestration in depleted shale formations: the case of the Utica shale. Energy Procedia 63, 5153–5163. https://doi.org/10.1016/j.egypro.2014.11.545.
Thommes, M., 2010. Physical adsorption characterization of nanoporous materials. Chem. Ing. Tech. 82 (7), 1059–1073. https://doi.org/10.1002/cite.201000064.
Tissot, B.P., Welte, D.H., 1984. Petroleum formation and occurrence. In: Springer-verlag, Berlin-Heideslberg.
Vandenbroucke, M., Largeau, C., 2007. Kerogen origin, evolution and structure. Org. Geochem. 38 (5), 719–833. https://doi.org/10.1016/j.orggeochem.2007.01.001.
Wang, H., Li, G., Shen, Z., 2012. A feasibility analysis on shale gas exploitation with supercritical carbon dioxide. Energy Sources, Part A Recovery, Util. Environ. Eff. 34 (15), 1426–1435. https://doi.org/10.1080/15567036.2010.529570.
Wang, L., Yu, Q., 2016. The effect of moisture on the methane adsorption capacity of shales: a study case in the eastern Qaidam Basin in China. J. Hydrol. 542, 487–505. https://doi.org/10.1016/j.jhydrol.2016.09.018.
Wang, S., Song, Z., Cao, T., Song, X., 2013. The methane sorption capacity of Paleozoic shales from the Sichuan Basin, China. Mar. Pet. Geol. 44, 112–119. https://doi.org/10.1016/j.marpetgeo.2013.03.007.
Wang, Y., Zhu, Y., Liu, S., Zhang, R., 2016. Methane adsorption measurements and modeling for organic-rich marine shale samples. Fuel 172, 301–309. https://doi.org/10.1016/j.fuel.2015.12.074.
Venaruzzo, J.L., Volzone, C., Rueda, M.L., Ortiga, J., 2002. Modified bentonitic clay minerals as adsorbents of CO, CO_2 and SO_2 gases. Microporous Mesoporous Mater. 56 (1), 73–80. https://doi.org/10.1016/S1387-1811(02)00443-2.
Wang, Z., Krupnick, A., 2015. A retrospective review of shale gas development in the United States: what led to the boom? Econ. Energy Environ. Pol. 4 (1), 5–18. https://doi.org/10.2139/ssrn.2286239.
Wei, X., Wei, G., Honglin, L., Shusheng, G., Zhiming, H., Farong, Y., 2012. Shale reservoir characteristics and isothermal adsorption properties. Nat. Gas. Ind. 32 (1), 113–116.
Weniger, P., Kalkreuth, W., Busch, A., Krooss, B.M., 2010. High-pressure methane and carbon dioxide sorption on coal and shale samples from the Paraná Basin, Brazil. J. Int. J. Coal Geol. 84 (3–4), 190–205. https://doi.org/10.1016/j.coal.2010.08.003.
Wollenweber, J., Alles, S., Kronimus, A., Busch, A., Stanjek, H., Krooss, B.M., 2009. Caprock and overburden processes in geological CO2 storage: an experimental study on sealing efficiency and mineral alterations. Energy Procedia 1 (1), 3469–3476. https://doi.org/10.1016/j.egypro.2009.02.138.
Wollenweber, J., Alles, S., Busch, A., Krooss, B.M., Stanjek, H., Littke, R., 2010. Experimental investigation of the CO2 sealing efficiency of caprocks. Int. J. Greenh. Gas Contr. 4 (2), 231–241. https://doi.org/10.1016/j.ijggc.2010.01.003.
Wu, C., Tuo, J., Zhang, L., Zhang, M., Li, J., Liu, Y., Qian, Y., 2017. Pore characteristics differences between clay-rich and clay-poor shales of the Lower Cambrian Niutitang Formation in the Northern Guizhou area, and insights into shale gas storage mechanisms. Int. J. Coal Geol. 178, 13–25. https://doi.org/10.1016/j.coal.2017.04.009.
Xia, J., Song, Z., Wang, S., Zeng, W., 2017. Preliminary study of pore structure and methane sorption capacity of the Lower Cambrian shales from the north Gui-zhou Province. J. Nat. Gas Sci. Eng. 38, 81–93. https://doi.org/10.1016/j.jngse.2016.12.021.
Xiong, J., Liu, X., Liang, L., Zeng, Q., 2017. Adsorption of methane in organic-rich shale nanopores: an experimental and molecular simulation study. Fuel 200, 299–315. https://doi.org/10.1016/j.fuel.2017.03.083.
Yang, F., Xie, C., Ning, Z., Krooss, B., 2016. High-pressure methane sorption on dry and moisture-equilibrated shales. Energy Fuels 31 (1), 482–492. https://doi.org/10.1021/acs.energyfuels.6b02999.
Yin, H., Zhou, J., Jiang, Y., Xian, X., Liu, Q., 2016. Physical and structural changes in shale associated with supercritical CO2 exposure. Fuel 184, 289–303. https://doi.org/10.1016/j.fuel.2016.07.028.
Yin, H., Zhou, J., Xian, X., Jiang, Y., Lu, Z., Tan, J., Liu, G., 2017. Experimental study of the effects of sub- and super-critical CO2 saturation on the mechanical characteristics of organic-rich shales. Energy 132, 84–95. https://doi.org/10.1016/j.energy.2017.05.064.
Yin, T., Liu, D., Cai, Y., Zhou, Y., Yao, Y., 2017. Size distribution and fractal characteristics of coal pores through nuclear magnetic resonance cryoporometry. Energy Fuels 31 (8), 7746–7757. https://doi.org/10.1021/acs.energyfuels.7b00389.
Yuan, W., Pan, Z., Li, X., Yang, Y., Zhao, C., Connell, L.D., Li, S., He, J., 2014. Experimental study and modelling of methane adsorption and diffusion in shale, 117, 509–519.
Zhang, T., Ellis, G.S., Ruppel, S.C., Milliken, K., Yang, R., 2012. Effect of organic-matter type and thermal maturity on methane adsorption in shale-gas systems, 47, 120–131.
Zhao, G., Wang, C., 2018. Influence of CO2 on the adsorption of CH4 on shale using low-field nuclear magnetic resonance technique. Fuel 238, 51–58. https://doi.org/10.1016/j.fuel.2018.10.092.
Zheng, X., Zhang, B., Sanei, H., Bao, H., Meng, Z., Wang, C., Li, K., 2018. Pore structure characteristics and its effect on shale gas adsorption and desorption behavior. Mar. Pet. Geol. 100, 165–178. https://doi.org/10.1016/j.marpetgeo.2018.10.045.
Zhou, S., Xue, H., Ning, Y., Guo, W., Zhang, Q., 2018. Experimental study of supercritical methane adsorption in Longmaxi shale: insights into the density of adsorbed methane. Fuel 211, 140–148. https://doi.org/10.1016/j.fuel.2017.09.065.

Zolfaghari, A., Dehghanpour, H., Holyk, J., 2017. Water sorption behaviour of gas shales: I. Role of clays. Int. J. Coal Geol. 179, 130–138. https://doi.org/10.1016/j.coal.2017.05.008.

Zolfaghari, A., Dehghanpour, H., Xu, M., 2017. Water sorption behaviour of gas shales: II. Pore size distribution. Int. J. Coal Geol. 179, 187–195. https://doi.org/10.1016/j.coal.2017.05.009.

Zou, J., Rezaee, R., Liu, K., 2017. Effect of temperature on methane adsorption in shale gas reservoirs. Energy Fuels 31 (11), 12081–12092. https://doi.org/10.1021/acs.energyfuels.7b02639.

Zou, J., Rezaee, R., Xie, Q., You, L., Liu, K., Saeedi, A., 2018. Investigation of moisture effect on methane adsorption capacity of shale samples. Fuel 232, 323–332. https://doi.org/10.1016/j.fuel.2018.05.167.

Zuber, M.D., Williamson, J.R., Hill, D.G., Sawyer, W.K., Frantz Jr., J.H., 2002. A comprehensive reservoir evaluation of a shale reservoir-the New Albany shale. In: Paper Presented at the SPE Annual Technical Conference and Exhibition.